

Effect Of Dasher Design on Residence Time and Microstructure of Frozen Desserts Produced
with a Continuous Scraped Surface Freezer

By

Lauren R. Gallagher

A dissertation submitted in partial fulfillment of
the requirements for the degree of

Doctor of Philosophy

(Food Science)

at the

UNIVERSITY OF WISCONSIN-MADISON

2024

Date of final oral examination: 01/19/2024

The dissertation is approved by the following members of the Final Oral Committee:

Richard W. Hartel, Professor, Food Science

Scott A. Rankin, Professor, Food Science

Arnoldo Lopez-Hernandez, Teaching Faculty, Food Science

Christopher Choi, Professor, Biological Systems Engineering

© Copyright by Lauren Gallagher 2024

All Rights Reserved

DEDICATION

To my best friend and life partner, Leo,
and to all of my fellow women in STEM. Rock on.

ACKNOWLEDGEMENTS

First and foremost, I need to thank Rich Hartel and the UW-Madison Department of Food Science for giving me the opportunity to pursue my PhD. There are a multitude of people who I need to thank for making this research possible. I would especially like to thank Tetra Pak for their generosity by providing the continuous freezer and dasher designs used in this study. A special thanks to Robert Bohn, Steen Gyldenloev, and Bjarke Kristensen of Tetra Pak for your technical support and insights. Thank you to Galloway, especially Hank Sweeney, for taking an interest in this study and for supplying the ice cream mix. Thank you to Graciela Alvarez and her colleagues at INRAE who provided invaluable guidance that helped me develop the methodology and complete the analyses in this dissertation. Thank you to Nick Krueger, Susan Glenn, and Ajinkya Kokandakar with CALS Statistical Consulting. Finally, thank you to the rest of my committee members, including Scott Rankin, Arnoldo Lopez-Hernandez, and Chris Choi, for your guidance.

Completion of this research took a village. I would like to extend my gratitude to Katherine Grosz (Helbig) for completing the initial phase of this research. Thank you to the ice cream dream team, Dieyckson Friere, Sam VanWees, Jasmine Wu, and CJ Wicks, as well as the rest of the Hartel lab. I could not have reached this point without your comradery, patience, and support. Thank you to the small army of undergraduates that helped me over the years as well, including Liz James, Sami LeFever, Zoe Atkins, Payton Gladem, Lauren Smith, Claire Sipple, Sydney Camp, and Aly Farrar. Together, you helped me freeze over 3,000 gallons of ice cream mix, image and trace over 250,000 ice crystals and 100,000 air cells, and discover the joy that mentoring young scientists brings me. A special thank you to Ray Van Cleve for helping me to manage the general chaos involved with conducting an experiment of this scale.

There were many people that supported me outside of the lab as well. I need to thank my therapist and my psychiatrist for helping me get here in one piece. Thank you to my friends and family, especially my parents, who cheered me on and took an interest in my research. It was also such a joy that I got to spend time with my sister, Claire, as she helped me complete my research. Lastly, thank you to my husband, Leo, for your unwavering encouragement and patience. I am beyond grateful to have a partner who is so supportive of my ambitions and willing to care for me in every way possible as I chase them. I love you more than words can express.

ABSTRACT

Most frozen desserts produced for retail sale are manufactured using continuous scraped surface freezers (SSFs). SSFs contain a dasher assembly that includes a dasher, knives, and sometimes a beater. The purpose of the dasher assembly is to mix the working fluid, scrape ice off the freezer wall as it forms, destabilize fat globules, and whip air into the product as it is dynamically frozen. These processes occur simultaneously and impact the structure of the frozen dessert. Equipment manufacturers of SSFs employ a variety of dasher assembly designs based on desired product attributes; however, to date these assemblies have largely been constructed based on proprietary findings, and trial and error. The objective of this study was to elucidate the effect of dasher design on product microstructure and fluid behavior in the freezer and to determine if processing conditions are predictive of microstructural attributes.

Preliminary experiments were conducted to understand how freeze concentration and temperature influence rheological properties of the serum phase of ice cream. A model system was generated by removing water from ice cream mix to simulate the unfrozen serum phase at levels of freeze concentration from 0% – 50%. As freeze concentration increased, shear stress and viscosity also increased. Samples representing high levels of freeze concentration were more susceptible to increases in shear stress and viscosity with decreasing temperature. The evolution of microstructural properties after start-up of a SSF was also investigated to understand how long it takes for microstructure to stabilize during freezing. Ice crystal size and air cell size stabilized quickly, while the amount of fat destabilization took longer to stabilize. A ‘steady state’ for microstructure was achieved within ~6x of the theoretical residence time assuming plug flow.

To improve the understanding of SSF operation, a Tetra Pak CF700 continuous freezer was used in a series of pilot scale experimental studies encompassing 5 commercially available dasher

assemblies with varying geometries and ranging from 26 to 64% volume displacement. Residence time distribution (RTD) profiles and microstructural attributes (ice crystal, air cell, and fat globule size distributions) were characterized for sorbet and ice cream made under constant processing conditions, while varying dasher assembly. For selected dashers, we also investigated how processing parameters, (including product throughput, dasher rotational speed, and overrun), interact with dasher design to influence RTD and microstructural attributes of ice cream.

Generally, increased volume displacement of the dasher assembly resulted in a shorter RTD. Although it was expected that RTD would influence ice crystal size, no practical effect of dasher was observed in hardened samples. However, differences in ice crystal size at draw suggested increased subcooling for samples made with higher displacement dashers. Dasher designs and freezing parameters that increased shear forces (more displacement, increased overrun, increased dasher speed) generally resulted in smaller air cells and more fat globule destabilization. Fat destabilization was also increased with increased residence time. Microstructure generally did not correlate well with the processing conditions measured in this study (i.e., torque on dasher motor and RTD), suggesting that shear forces are also important in determining microstructure. This would indicate the dasher geometry, not just displacement, is important in determining microstructure, as different geometries would cause different shear forces.

This study furthers our understanding of how dasher design influences heat transfer, fluid flow, and shear forces in SSFs. It will enable frozen dessert manufacturers to select a dasher based on desired structural characteristics and inform SSF manufacturers on how to design dashers more efficiently by using engineering principles.

TABLE OF CONTENTS

Dedication	i
Acknowledgements	ii
Abstract	iv
List of Tables	xiii
List of Figures	xviii
1 Introduction	1
2 Literature Review	3
2.1 Composition of Frozen Desserts	3
2.1.1 Sorbet	3
2.1.2 Ice Cream	3
2.2 Microstructure of Frozen Desserts	5
2.2.1 Ice Crystals	5
2.2.2 Air Cells	6
2.2.3 Fat Globules & Partially Coalesced Fat	7
2.2.4 Serum Phase	9
2.3 Scraped Surface Freezers	9
2.3.1 Design of Scraped Surface Freezers	9
2.3.1.1 Refrigeration System and the Freezing Cylinder	9
2.3.1.2 Dasher Assembly	11
2.4 Phenomena in Scraped Surface Freezers	13
2.4.1 Ice Crystallization	14
2.4.1.1 Nucleation	17

2.4.1.2	Growth	20
2.4.1.3	Recrystallization	22
2.4.2	Fat Destabilization	25
2.4.2.1	Theoretical Mechanisms of Partial Coalescence	29
2.4.2.2	Effect of Processing Parameters on Partial Coalescence	31
2.4.3	Aeration/Foaming	33
2.4.3.1	Effect of Shear on Air Incorporation and Size Reduction	34
2.4.3.2	Stabilization of Air by Fat Structures	37
2.5	Residence Time Distribution in Scraped Surface Freezers.....	38
2.5.1	Ideal Plug Flow	38
2.5.2	Deviations from Ideal Flow	38
2.5.3	Experimental Determination of RTD.....	39
2.6	Effects of Freezer Conditions on Frozen Dessert Manufacture.....	41
2.6.1	Residence Time Distribution	42
2.6.1.1	Throughput Rate	42
2.6.1.2	Dasher Geometry	43
2.6.1.3	Dasher Speed	44
2.6.1.4	Draw/Refrigerant Temperature	44
2.6.2	Ice Crystal Size	45
2.6.2.1	Residence Time/Throughput Rate	45
2.6.2.2	Draw/Refrigerant Temperature	46
2.6.2.3	Overrun	47
2.6.2.4	Dasher Speed	47

2.6.2.5	Dasher Assembly Design.....	48
2.6.3	Air Cell Size Distribution	48
2.6.3.1	Residence Time/Throughput Rate	48
2.6.3.2	Draw/Refrigerant Temperature.....	49
2.6.3.3	Overrun	50
2.6.3.4	Dasher Speed	51
2.6.3.5	Dasher Assembly Design.....	51
2.6.4	Fat Globule Destabilization	51
2.6.4.1	Residence Time/Throughput Rate	51
2.6.4.2	Draw/Refrigerant Temperature.....	52
2.6.4.3	Overrun	52
2.6.4.4	Dasher Speed	53
2.6.4.5	Dasher Assembly Design.....	53
2.7	Summary	53
3	Materials & Methods	55
3.1	Freezing Equipment.....	55
3.1.1	Continuous Scraped Surface Freezer	55
3.1.2	Dasher Designs	56
3.2	Working Fluid.....	58
3.2.1	Sorbet Experiment	58
3.2.2	Ice Cream Experiments.....	58
3.3	Effect of Dasher Design on Residence Time Distribution and Ice Crystal Size of Un aerated Sorbet Made with a Continuous Scraped Surface Freezer	59

3.3.1	Experimental Design.....	59
3.3.2	Sample Collection and Measurements.....	59
3.4	Rheological Characterization of a Model for the Freeze Concentrated Serum Phase of Ice Cream.....	60
3.4.1	Preparation of Freeze Concentrated Serum Phase Model Samples.....	60
3.4.2	Freezing Point and Freezing Point Depression Curve.....	60
3.4.3	Rheological Characterization.....	61
3.5	Microstructural Evolution of Ice Cream after Start-up of a Continuous Scraped Surface Freezer.....	62
3.5.1	Experimental Overview.....	62
3.5.2	Sample Collection and Measurements.....	62
3.6	Effect of Dasher Design and Processing Parameters on Residence Time Distribution and Microstructural Characteristics of Ice Cream Made with a Continuous Scraped Surface Freezer.....	63
3.6.1	Experimental Overview.....	63
3.6.1.1	Dasher Speed Experiment.....	64
3.6.1.2	Overrun Experiment.....	64
3.6.1.3	Throughput Rate Experiment.....	65
3.6.2	Sample Collection and Measurements.....	65
3.7	Residence Time Distribution Methodology.....	66
3.7.1	Sorbet Residence Time Trials.....	66
3.7.2	Ice Cream Residence Time Trials.....	68
3.7.3	RTD Data Treatment.....	69

3.8	Microstructural Analysis Methodology	70
3.8.1	Ice Crystal Size Distribution.....	70
3.8.2	Air Cell Size Distribution	71
3.8.3	Fat Destabilization	72
3.9	Statistical Analysis.....	72
4	Results & Discussion	73
4.1	Effect of Dasher Design on Residence Time Distribution and Ice Crystal Size of Unaerated Sorbet.....	73
4.1.1	Processing Conditions.....	73
4.1.2	Residence Time Distributions.....	74
4.1.3	Ice Crystal Size Distributions	80
4.1.4	Summary	84
4.2	Rheological Characterization of a Model for the Freeze Concentrated Serum Phase of Ice Cream	85
4.2.1	Moisture and Freezing Point.....	85
4.2.2	Rheological Characteristics	86
4.2.3	Summary	93
4.3	Microstructural Evolution of Ice Cream after Start-up in a Continuous Freezer	95
4.3.1	Processing Conditions.....	95
4.3.2	Microstructural Evolution Over Time	98
4.3.2.1	Ice Crystal Size	98
4.3.2.2	Air Cell Size.....	103
4.3.2.3	Fat Destabilization	106

4.3.3	Practical Considerations.....	109
4.4	Effect of Dasher Design and Processing Parameters on Residence Time Distribution and Microstructural Characteristics of Ice Cream Made with a Continuous Scraped Surface Freezer.....	111
4.4.1	Dasher Speed Experiment.....	111
4.4.1.1	Processing Conditions.....	111
4.4.1.2	Residence Time Distribution	113
4.4.1.3	Microstructure.....	119
4.4.1.3.1	Ice Crystal Size – Draw	119
4.4.1.3.2	Ice Crystal Size – Hardened.....	124
4.4.1.3.3	Air Cell Size.....	127
4.4.1.3.4	Fat Destabilization	131
4.4.1.4	Correlations.....	135
4.4.2	Overrun Experiment.....	140
4.4.2.1	Processing Conditions.....	140
4.4.2.2	Residence Time Distribution	141
4.4.2.3	Microstructure.....	150
4.4.2.3.1	Ice Crystal Size – Draw	150
4.4.2.3.2	Ice Crystal Size – Hardened.....	152
4.4.2.3.3	Air Cell Size.....	157
4.4.2.3.4	Fat Destabilization	160
4.4.2.4	Correlations.....	164
4.4.3	Throughput Rate Experiment.....	170

4.4.3.1	Processing Conditions.....	170
4.4.3.2	Residence Time Distribution	172
4.4.3.3	Microstructure.....	180
4.4.3.3.1	Ice Crystal Size – Draw	180
4.4.3.3.2	Ice Crystal Size – Hardened.....	185
4.4.3.3.3	Air Cell Size.....	189
4.4.3.3.4	Fat Destabilization	192
4.4.3.4	Correlations.....	195
4.4.4	Summary.....	203
5	Conclusions and Recommendations	204
5.1	Conclusions.....	204
5.2	Recommendations.....	207
6	References.....	209
A	Appendix.....	221

LIST OF TABLES

Table 2.1. Effect of scraped surface freezer parameters on microstructure of frozen desserts.....	41
Table 2.2. Previous studies on residence time distribution in SSFs used to make frozen desserts...	42
Table 3.1. Tetra Pak CF700 A2 dasher assembly designs and specifications. Total volume of freezing cylinder without dasher assembly = 12.54 L	57
Table 3.2. Theoretical residence times (s) for ice cream experimental parameters under plug flow model assumption in Tetra Pak CF700 continuous freezer	69
Table 4.1.1. Effects of dasher assembly on viscosity (torque on dasher motor as a percentage of its total capacity) for unaerated sorbet made at throughput rate = 190 L/h, dasher speed = 300 RPM (unless noted), and draw temperature = -6°C.....	74
Table 4.1.2. Effects of dasher assembly on residence time distribution parameters for nonaerated sorbet made at a throughput rate = 190 L/h, dasher speed = 300 RPM (unless noted), and draw temperature = -6°C as determined by pulse injection study	75
Table 4.1.3. Effect of dasher assembly on ice crystal size for hardened sorbet. Throughput rate = 190 L/h, overrun = 0%, dasher speed = 300 RPM (unless noted), and draw temperature = -6°C	80
Table 4.2.1. Moisture content and calculated freezing point for ice cream mix with water removed to create models of unfrozen phase as a result of freeze concentration.....	86
Table 4.4.1. Effects of dasher assembly and dasher speed on processing conditions for ice cream made at a throughput rate = 300 L/h, overrun = 75%, and target draw temperature = -5.5°C.....	112

Table 4.4.2. Effects of dasher assembly and dasher speed on residence time distribution parameters for ice cream made at a throughput rate = 300 L/h, overrun = 75%, and target draw temperature = -5.5°C as determined by pulse injection study.	114
Table 4.4.3. ANOVA table assessing factors affecting residence time distribution parameters	114
Table 4.4.4. Effects of dasher assembly and dasher speed on microstructural attributes of ice cream made at a throughput rate = 300 L/h, overrun = 75%, and target draw temperature = -5.5°C.....	120
Table 4.4.5. ANOVA table assessing factors affecting ice crystal size at draw (target = -5.5°C) ...	121
Table 4.4.6. ANOVA table assessing factors affecting ice crystal size in hardened ice cream.....	124
Table 4.4.7. ANOVA table assessing factors affecting air cell size in hardened ice cream	128
Table 4.4.8. ANOVA table assessing factors affecting fat destabilization.....	132
Table 4.4.9. Overall correlation coefficient R^2 between processing conditions and microstructural attributes.	137
Table 4.4.10. Correlation coefficient R^2 between viscosity and microstructural attributes as a function of dasher assembly.....	137
Table 4.4.11. Correlation coefficient R^2 between mean residence time and microstructural attributes as a function of dasher assembly.....	138
Table 4.4.12. Correlation coefficient R^2 between standard deviation in residence time and microstructural attributes as a function of dasher assembly.	139

Table 4.4.13. Effects of dasher assembly and overrun on viscosity (measured as the torque placed on the dasher motor as a percentage of its total capacity) for ice cream made at a throughput rate = 300 L/h, dasher speed = 200 RPM, and draw temperature = $-5.5\pm 0.1^{\circ}\text{C}$	141
Table 4.4.14. Effects of dasher assembly and overrun on residence time distribution parameters for ice cream made at a throughput rate = 300 L/h, dasher speed = 200 RPM, and draw temperature = $-5.5\pm 0.1^{\circ}\text{C}$ as determined by pulse injection study	144
Table 4.4.15. ANOVA table assessing factors residence time distribution parameters.....	144
Table 4.4.16. Effects of dasher assembly and overrun on microstructural attributes of ice cream made at a throughput rate = 300 L/h, dasher speed = 200 RPM, and draw temperature = $-5.5\pm 0.1^{\circ}\text{C}$	151
Table 4.4.17. ANOVA table assessing factors affecting ice crystal size at draw ($-5.5\pm 0.1^{\circ}\text{C}$).....	152
Table 4.4.18. ANOVA table assessing factors affecting ice crystal size in hardened ice cream.....	157
Table 4.4.19. ANOVA table assessing factors affecting air cell size in hardened ice cream	160
Table 4.4.20. ANOVA table assessing factors affecting fat destabilization	161
Table 4.4.21. Overall correlation coefficient R^2 between processing conditions and microstructural attributes	164
Table 4.4.22. Correlation coefficient R^2 between viscosity and microstructural attributes as a function of dasher assembly.....	165
Table 4.4.23. Correlation coefficient R^2 between mean residence time and microstructural attributes as a function of dasher assembly.....	167

Table 4.4.24. Correlation coefficient R^2 between standard deviation in residence time and microstructural attributes as a function of dasher assembly	169
Table 4.4.25. Effects of dasher assembly and throughput rate on processing conditions for ice cream made at a dasher speed = 200 RPM, target overrun = 75%, and draw temperature = $-5.5 \pm 0.1^\circ\text{C}$	172
Table 4.4.26. Effects of dasher assembly and throughput rate on residence time distribution parameters for ice cream made at a dasher speed = 200 RPM, target overrun = 75%, and draw temperature = $-5.5 \pm 0.1^\circ\text{C}$ as determined by pulse injection study	174
Table 4.4.27. ANOVA table assessing factors residence time distribution parameters.....	174
Table 4.4.28. Effects of dasher assembly and throughput rate on microstructural attributes of ice cream made at a dasher speed = 200 RPM, target overrun = 75%, and draw temperature = $-5.5 \pm 0.1^\circ\text{C}$	181
Table 4.4.29. ANOVA table assessing factors affecting ice crystal size at draw ($-5.5 \pm 0.1^\circ\text{C}$).....	182
Table 4.4.30. ANOVA table assessing factors affecting ice crystal size in hardened ice cream.....	186
Table 4.4.31. Percentage of ice crystals $> 50 \mu\text{m}$ in diameter as a function of dasher assembly and throughput rate for hardened ice cream made at dasher speed = 200 RPM, target overrun = 75%, and draw temperature = $-5.5 \pm 0.1^\circ\text{C}$	186
Table 4.4.32. ANOVA table assessing factors affecting air cell size in hardened ice cream	189
Table 4.4.33. ANOVA table assessing factors affecting fat destabilization	192
Table 4.4.34. Overall correlation coefficient R^2 between processing conditions and microstructural attributes.	197

Table 4.4.35. Correlation coefficient R^2 between viscosity and microstructural attributes as a function of dasher assembly.....	197
Table 4.4.36. Correlation coefficient R^2 between mean residence time and microstructural attributes as a function of dasher assembly.....	200
Table 4.4.37. Correlation coefficient R^2 between standard deviation in residence time and microstructural attributes as a function of dasher assembly	200

LIST OF FIGURES

Figure 2.1. Schematic of the microstructure of ice cream. (Adapted from Goff and Hartel, 2013).	5
Figure 2.2. Effect of mean ice crystal size on ice detectability on smoothness of ice cream (from Russell et al., 1999).....	6
Figure 2.3. Fat globule size distribution of initial homogenized ice cream mix versus frozen ice cream containing partially coalesced fat globules	8
Figure 2.4. Vapor-compression refrigeration cycle in a scraped surface freezer. 1) Evaporation – liquid refrigerant absorbs heat from the product in the freezing cylinder and is vaporized. 2) Compression – vaporized refrigerant is compressed, causing a rise in temperature. 3) Condensation – the superheated vapor is cooled by an external heat sink, causing the refrigerant to condense to a liquid. 4) Expansion – the high-pressure liquid refrigerant passes through an expansion (throttling) device which further decreases the refrigerant temperature. The refrigerant is ready to re-enter the refrigeration cycle in the evaporator (Adapted from Goff and Hartel, 2013 and Dincer, 2017).....	10
Figure 2.5. Schematic of the components of a dasher assembly. The primary components of the dasher assembly include the dasher itself (1); the beater (8), which is only used inside of open dashers; and knives (2) that are supported on the outside of the dasher (Courtesy of Tetra Pak).....	12
Figure 2.6. Examples of commercially available dasher and beater designs (courtesy of Tetra Pak)	13

Figure 2.7. Example of a freezing point depression curve, which demonstrates how freeze concentration of solutes in the unfrozen phase decreases the freezing point. From Goff and Hartel (2013).....	15
Figure 2.8. Cross section of freezer barrel. Ice nucleation occurs at the freezer wall, and growth of dendritic crystals forms a slush layer at the freezer wall. The slush is removed by rotating scraper blades in the form of ice flocs, which are broken down by mixing and shear inside the freezer. As the ice melts due to warmer temperatures in the center of the barrel, ice discs are formed and may recrystallize/ripen after residing in the freezer for a period of time (From Cook and Hartel, 2010)	17
Figure 2.9. Homogeneous and heterogeneous nucleation of ice crystals. Embryos of ice (β) are formed from water (α). Homogeneous nucleation (a) occurs in the bulk phase, whereas heterogenous nucleation (b) occurs at a surface (κ), either of a particle or at a surface, such as the freezer wall. Adapted from Walstra (2003)	18
Figure 2.10. Effect of shear on growth rate R_g of ice crystals in pure water with a degree of supercooling $\Delta T = 30^\circ\text{C}$. Results from molecular dynamics simulation. From Luo et al., 2019.....	21
Figure 2.11. Ice crystal growth at -0.4°C (A) develops more slowly and is more rounded than the dendritic shaped crystal formed at -3.0°C (B) supercooling (From Teraoka et al., 2002)	22
Figure 2.12. Proposed fat destabilization mechanisms circa 2010 (from Fredrick et al., 2010). The mechanism of partial coalescence has not yet been fully elucidated. Studies have demonstrated that crystallized fat protruding from fat globule is not necessary for partial coalescence to occur	26

Figure 2.13. Partial coalescence of fat globules, with varying contact angles (from center of mass) and packing efficiencies (from Dahiya et al., 2017).....	29
Figure 2.14. Coalescence behavior based on the energy balance model, where the degree of partial coalescence, or strain (ϵ) is based on balance of elastic modulus energy and interfacial energy (From Pawar et al., 2012).....	31
Figure 2.15. Example of bubble deformation in shear flow. From Janssen et al., 1994.....	35
Figure 2.16. Mechanisms of bubble break up in turbulent flow. From Risso and Fabre (1998).....	36
Figure 2.17. Stimulus-response input, ideal response, and real response for tubular reactors using the (a) step function or (b) pulse injection techniques. w_0 and w_E indicate the weight concentration of tracer in the inlet and effluent streams, respectively. (From Hill, 1977).....	39
Figure 2.18. Effect of rotor type on RTD for (a) a 0.4% Carbopol system and (b) ice cream made using a scraped surface freezer. Throughput rate was 0.111 kg/s and rotor/dasher speed was 250 RPM. For ice cream, product was frozen to -5°C , but Carbopol system was not cooled. (From Russell et al., 1997).....	43
Figure 3.1. Schematic of Tetra Pak CF700 A2 continuous freezer. Courtesy of Tetra Pak, adapted	56
Figure 3.2. Schematic of pulse injection of methylene blue into Tetra Pak CF700 continuous freezer during manufacture of nonaerated sorbet for determination of residence time distribution. Processing parameters were set at throughput = 190 L/h, draw temperature = -6.0°C , dasher speed = 300 RPM, and cylinder pressure = 0 bar	67
Figure 3.3. Standard curve for methylene blue (MB) in sorbet mix at 5°C . absorbance was measured using a spectrophotometer at a wavelength of 664 nm	67

Figure 3.4. Standard curve of methylene blue (MB) in melted ice cream. Samples were diluted 20:1 in a 1% SDS solution and absorbance was measured using a spectrophotometer at a wavelength of 664 nm.....	69
Figure 4.1.1. Cumulative residence time distribution $F(t)$ curves as a function of dasher assembly for unaerated sorbet made at throughput = 190 L/h, dasher speed = 300 RPM (unless noted), and draw temperature = -6°C (n=3).....	76
Figure 4.1.2. Images of samples collected during pulse injection experiment for evaluating residence time distribution of unaerated sorbet as a function of dasher assembly. Throughput rate = 190 L/h, dasher speed = 300 RPM (unless noted), draw temperature = -6°C . Top left cup in each image was collected at $t = 0\text{s}$ when 20 mL of tracer (0.5% methylene blue in sorbet mix) was injected into freezer	77
Figure 4.1.3. A) $E(t)$ curves and B) $E(\theta)$ curves as a function of dasher assembly for unaerated sorbet made at a throughput rate = 190 L/h, dasher speed = 300 RPM (unless noted), and draw temperature = -6°C (n=3).....	78
Figure 4.1.4. Mean residence time t_s as a function of dasher assembly for unaerated sorbet made at a throughput rate = 190 L/h, dasher speed = 300 RPM (unless noted), and draw temperature = -6°C . Means without a common letter differ ($P < 0.05$).....	79
Figure 4.1.5. Correlation between dasher displacement and mean residence time t_s for unaerated sorbet made at a throughput rate = 190 L/h, dasher speed = 300 RPM (unless noted), and draw temperature = -6°C	79
Figure 4.1.6. Cumulative ice crystal size distributions as a function of dasher assembly for hardened sorbet. Throughput rate = 190 L/h, overrun = 0%, dasher speed = 300 RPM (unless noted), draw temperature = -6°C	81

Figure 4.1.7. Correlation between dasher displacement and ice crystal size distribution as a function of dasher assembly for hardened sorbet	81
Figure 4.1.8. Correlation between viscosity, (measured as the torque on the dasher motor as a percentage of its total capacity), and ice crystal size distribution as a function of dasher assembly for hardened sorbet	82
Figure 4.1.9. Correlation between ice crystal size distribution and A) mean residence time and B) standard deviation in residence time as a function of dasher assembly for hardened sorbet....	83
Figure 4.2.1. Freezing curve for ice cream mix calculated using method detailed by Goff and Hartel (2013).....	85
Figure 4.2.2. Shear sweep curves for model unfrozen phase of ice cream at 5°C as a function of % water removed. Error bars represent standard deviation for 3 replicates	88
Figure 4.2.3. Shear sweep curves for model unfrozen phase of ice cream at 2.5°C as a function of % water removed. Error bars represent standard deviation for 3 replicates.....	88
Figure 4.2.4. Shear sweep curves for model unfrozen phase of ice cream at 0°C as a function of % water removed. Error bars represent standard deviation for 3 replicates	89
Figure 4.2.5. Shear sweep curves for model unfrozen phase of ice cream at -2.5°C as a function of % water removed. Error bars represent standard deviation for 3 replicates.....	89
Figure 4.2.6. Viscosity as a function of shear rate and temperature for model unfrozen phase of ice cream mix (0% water removed). Error bars represent standard deviation for 3 replicates.....	90
Figure 4.2.7. Viscosity as a function of shear rate and temperature for model unfrozen phase of ice cream at 10% freeze concentration (ice cream mix with 10% of water removed). Error bars represent standard deviation for 3 replicates	90

- Figure 4.2.8.** Viscosity as a function of shear rate and temperature for model unfrozen phase of ice cream at 20% freeze concentration (ice cream mix with 20% of water removed). Error bars represent standard deviation for 3 replicates91
- Figure 4.2.9.** Viscosity as a function of shear rate and temperature for model unfrozen phase of ice cream at 30% freeze concentration (ice cream mix with 30% of water removed). Error bars represent standard deviation for 3 replicates91
- Figure 4.2.10.** Viscosity as a function of shear rate and temperature for model unfrozen phase of ice cream at 40% freeze concentration (ice cream mix with 40% of water removed). Error bars represent standard deviation for 3 replicates92
- Figure 4.2.11.** Viscosity as a function of shear rate and temperature for model unfrozen phase of ice cream at 50% freeze concentration (ice cream mix with 50% of water removed). Error bars represent standard deviation for 3 replicates92
- Figure 4.2.12.** Apparent viscosity at shear rate of 50 s^{-1} for ice cream mix as a function of % water removed and temperature. Error bars represent standard deviation for 3 replicates.....93
- Figure 4.3.1.** Draw temperature over time, where $t = 0 \text{ min}$ is freezer start-up. Target processing conditions were throughput rate = 200 L/h, draw temperature = -5.5°C , overrun = 75%, and dasher speed = 200 RPM97
- Figure 4.3.2.** Viscosity, measured as torque on dasher motor as percentage of total capacity, over time where $t = 0$ is freezer start-up. Target processing conditions were throughput rate = 200 L/h, draw temperature = -5.5°C , overrun = 75%, and dasher speed = 200 RPM.....97
- Figure 4.3.3.** Overrun over time, where $t = 0$ is freezer start-up. Target processing conditions were throughput rate = 200 L/h, draw temperature = -5.5°C , overrun = 75%, and dasher speed = 200 RPM.....98

Figure 4.3.4. Evolution of ice crystal size in ice cream immediately after draw, where $t = 0$ min is freezer start-up. Target processing conditions were throughput rate = 200 L/h, draw temperature = -5.5°C , overrun = 75%, and dasher speed = 200 RPM. Draw ice crystal size analyzed at -5.5°C99

Figure 4.3.5. Optical microscopy images of ice crystals in hardened ice cream over time, where $t = 0$ min is freezer start-up. Samples collected every minute for the first 20 min of freezing. Target processing conditions were throughput rate = 200 L/h, draw temperature = -5.5°C , overrun = 75%, and dasher speed = 200 RPM. Hardened ice crystal size analyzed at -15°C101

Figure 4.3.6. Optical microscopy images of ice crystals in hardened ice cream over time, where $t = 0$ min is freezer start-up. Samples collected every 6 min for 78 min. Target processing conditions were throughput rate = 200 L/h, draw temperature = -5.5°C , overrun = 75%, and dasher speed = 200 RPM. Hardened ice crystal size analyzed at -15°C 102

Figure 4.3.7. Evolution of ice crystal size of hardened ice cream, where $t = 0$ min is freezer start-up. Target processing conditions were throughput rate = 200 L/h, draw temperature = -5.5°C , overrun = 75%, and dasher speed = 200 RPM. Hardened ice crystal size analyzed at -15°C103

Figure 4.3.8. Optical microscopy images of air cells in hardened ice cream over time, where $t = 0$ min is freezer start-up. Samples collected every minute for the first 20 min of freezing. Target processing conditions were throughput rate = 200 L/h, draw temperature = -5.5°C , overrun = 75%, and dasher speed = 200 RPM. Hardened air cell size analyzed at -6°C104

Figure 4.3.9. Optical microscopy images of air cells in hardened ice cream over time, where $t = 0$ min is freezer start-up. Samples collected every 6 min for 78 min. Target processing conditions were throughput rate = 200 L/h, draw temperature = -5.5°C , overrun = 75%, and dasher speed = 200 RPM. Hardened air cell size analyzed at -6°C105

Figure 4.3.10. Evolution of air cell size of hardened ice cream, where $t = 0$ min is freezer start-up. Target processing conditions were throughput rate = 200 L/h, draw temperature = -5.5°C , overrun = 75%, and dasher speed = 200 RPM. Hardened air cell size analyzed at -6°C 106

Figure 4.3.11. Optical microscopy images of fat destabilization over time, where $t = 0$ min is freezer start-up. Samples collected every minute for the first 20 min of freezing. Target processing conditions were throughput rate = 200 L/h, draw temperature = -5.5°C , overrun = 75%, and dasher speed = 200 RPM. Melted ice cream samples diluted 1:20 in deionized water for imaging.....107

Figure 4.3.12. Optical microscopy images of fat destabilization over time, where $t = 0$ min is freezer start-up. Samples collected every 6 min for 78 min. Target processing conditions were throughput rate = 200 L/h, draw temperature = -5.5°C , overrun = 75%, and dasher speed = 200 RPM. Melted ice cream samples diluted 1:20 in deionized water for imaging108

Figure 4.3.13. Evolution of fat destabilization in ice cream, where $t = 0$ min is freezer start-up. Target processing conditions were throughput rate = 200 L/h, draw temperature = -5.5°C , overrun = 75%, and dasher speed = 200 RPM109

Figure 4.4.1. Cumulative residence time distribution $F(t)$ curves as a function of dasher assembly and dasher speed for ice cream made at 300 L/h throughput rate, 75% overrun, and -5.5°C target draw temperature ($n=3$).....115

Figure 4.4.2. A) $E(t)$ curves and B) $E(\theta)$ curves as a function of dasher assembly for ice cream made at 200 RPM dasher speed. Throughput rate = 300 L/h, overrun = 75%, target draw temperature = -5.5°C ($n=3$).....116

- Figure 4.4.3.** A) $E(t)$ curves and B) $E(\theta)$ curves as a function of dasher assembly for ice cream made at 300 RPM dasher speed. Throughput rate = 300 L/h, overrun = 75%, target draw temperature = -5.5°C (n=3).....117
- Figure 4.4.4.** Images of samples collected during pulse injection experiment for evaluating residence time distribution of ice cream as a function of dasher assembly and dasher speed. Throughput rate = 300 L/h, overrun = 75%, target draw temperature = -5.5°C . Top left cup in each image was collected at $t = 0\text{s}$ when 20 mL of tracer (1% methylene blue in ice cream mix) was injected into freezer118
- Figure 4.4.5.** Cumulative ice crystal size distributions immediately after draw (-5.5°C) as a function of dasher assembly for ice cream made at a dasher speed of A) 200 RPM and B) 300 RPM. Throughput rate = 300 L/h, overrun = 75%, target draw temperature = -5.5°C 122
- Figure 4.4.6.** A) Mean ice crystal size and B) standard deviation in ice crystal size of ice cream immediately after draw (-5.5°C) as a function of dasher assembly and dasher speed. Values represent the modeled averages for three replicates. Throughput rate = 300 L/h, overrun = 75%, target draw temperature = -5.5°C 123
- Figure 4.4.7.** Cumulative ice crystal size distributions as a function of dasher assembly for hardened ice cream samples made at a dasher speed of A) 200 RPM and B) 300 RPM. Throughput rate = 300 L/h, overrun = 75%, target draw temperature = -5.5°C . Samples were evaluated at -15°C125
- Figure 4.4.8.** A) Mean ice crystal size and B) standard deviation in ice crystal size of hardened ice cream samples as a function of dasher assembly and dasher speed. Throughput rate = 300 L/h, overrun = 75%, target draw temperature = -5.5°C . Samples were evaluated at -15°C . Values represent the modeled averages for three replicates126

Figure 4.4.9. Cumulative air cell size distributions as a function of dasher assembly for hardened ice cream samples made at a dasher speed of A) 200 RPM and B) 300 RPM. Samples were evaluated at -6°C . Throughput rate = 300 L/h, overrun = 75%, target draw temperature = -5.5°C ..

.....129

Figure 4.4.10. A) Mean air cell size and B) standard deviation in air cell size of hardened ice cream samples as a function of dasher assembly and dasher speed. Throughput rate = 300 L/h, overrun = 75%, target draw temperature = -5.5°C . Samples were evaluated at -6°C . Values represent the modeled averages for three replicates

130

Figure 4.4.11. Fat globule size distributions as a function of dasher assembly for ice cream samples made at a dasher speed of A) 200 RPM and B) 300 RPM. Throughput rate = 300 L/h, overrun = 75%, target draw temperature = -5.5°C . Curves represent the averages for three replicates

133

Figure 4.4.12. Optical microscopy images (20x magnification) of destabilized fat clusters as a function of dasher speed and dasher assembly

134

Figure 4.4.13. Mean % fat destabilization values for ice cream samples as a function of dasher assembly and dasher speed. Throughput rate = 300 L/h, overrun = 75%, target draw temperature = -5.5°C . Values represent the modeled averages for three replicates

135

Figure 4.4.14. Cumulative residence time distribution $F(t)$ curves as a function of dasher assembly and overrun for ice cream made at 300 L/h throughput, 200 RPM dasher speed, and -5.5°C draw temperature (n=3).....

145

Figure 4.4.15. A) $E(t)$ curves and B) $E(\theta)$ curves as a function of dasher assembly for ice cream made at 50% overrun. Throughput = 300 L/h, dasher speed = 200 RPM, draw temperature = $-5.5 \pm 0.1^{\circ}\text{C}$ (n=3).....

146

Figure 4.4.16. A) E(t) curves and B) E(θ) curves as a function of dasher assembly for ice cream made at 75% overrun. Throughput = 300 L/h, dasher speed = 200 RPM, draw temperature = $-5.5 \pm 0.1^\circ\text{C}$ (n=3).....147

Figure 4.4.17. A) E(t) curves and B) E(θ) curves as a function of dasher assembly for ice cream made at 100% overrun. Throughput = 300 L/h, dasher speed = 200 RPM, draw temperature = $-5.5 \pm 0.1^\circ\text{C}$ (n=3).....148

Figure 4.4.18. Images of samples collected during pulse injection experiment for evaluating residence time distribution of ice cream as a function of dasher assembly and overrun. Throughput = 300 L/h, dasher speed = 200 RPM, draw temperature = $-5.5 \pm 0.1^\circ\text{C}$. Top left cup in each image was collected at $t = 0\text{s}$ when 20 mL of tracer (1% methylene blue in ice cream mix) was injected into freezer149

Figure 4.4.19. Mean residence time t_s as a function of dasher assembly and overrun. Throughput = 300 L/h, dasher speed = 200 RPM, draw temperature = $-5.5 \pm 0.1^\circ\text{C}$. Values represent averages for three replicates.....150

Figure 4.4.20. Cumulative ice crystal size distributions immediately after draw (-5.5°C) as a function of dasher assembly for ice cream made at an overrun of A) 50%, B) 75% and C) 100%. Throughput = 300 L/h, dasher speed = 200 RPM, draw temperature = $-5.5 \pm 0.1^\circ\text{C}$ 153

Figure 4.4.21. A) Mean ice crystal size and B) standard deviation in ice crystal size of ice cream immediately after draw (-5.5°C) as a function of dasher assembly and overrun. Throughput = 300 L/h, dasher speed = 200 RPM, draw temperature = $-5.5 \pm 0.1^\circ\text{C}$. Values represent the modeled averages for three replicates.....154

Figure 4.4.22. Cumulative ice crystal size distributions as a function of dasher assembly for hardened ice cream samples made at an overrun of A) 50%, B) 75% and C) 100%. Throughput = 300 L/h, dasher speed = 200 RPM, draw temperature = $-5.5 \pm 0.1^\circ\text{C}$155

Figure 4.4.23. A) Mean ice crystal size and B) standard deviation in ice crystal size of hardened ice cream samples as a function of dasher assembly and overrun. Throughput = 300 L/h, dasher speed = 200 RPM, draw temperature = $-5.5 \pm 0.1^\circ\text{C}$. Samples were evaluated at -15°C . Values represent the modeled averages for three replicates156

Figure 4.4.24. Cumulative air cell size distributions as a function of dasher assembly for hardened ice cream samples made at an overrun of A) 50%, B) 75% and C) 100%. Throughput = 300 L/h, dasher speed = 200 RPM, draw temperature = $-5.5 \pm 0.1^\circ\text{C}$. Samples were evaluated at -6°C158

Figure 4.4.25. A) Mean air cell size and B) standard deviation in air cell size of hardened ice cream samples as a function of dasher assembly and overrun. Throughput = 300 L/h, dasher speed = 200 RPM, draw temperature = $-5.5 \pm 0.1^\circ\text{C}$. Samples were evaluated at -6°C . Values represent the modeled averages for three replicates159

Figure 4.4.26. Mean fat destabilization (%) for ice cream samples as a function of dasher assembly and overrun. Throughput = 300 L/h, dasher speed = 200 RPM, draw temperature = -5.5°C . Values represent the modeled averages for three replicates.....161

Figure 4.4.27. Fat globule size distributions as a function of dasher assembly for ice cream samples made at an overrun of A) 50%, B) 75%, and C) 100%. Throughput = 300 L/h, dasher speed = 200 RPM, draw temperature = $-5.5 \pm 0.1^\circ\text{C}$. Curves represent averages for three replicates162

- Figure 4.4.28.** Optical microscopy images (20x magnification) of destabilized fat clusters as a function of overrun and dasher assembly163
- Figure 4.4.29.** Correlation between fat destabilization and viscosity (i.e., torque on dasher motor as % of total capacity) as a function of dasher. Dotted lines indicate correlation for individual dashers.....166
- Figure 4.4.30.** Correlation between fat destabilization and A) mean residence time and B) standard deviation in residence time as a function of dasher. Solid black line denotes the overall correlation and dotted lines indicate correlation for individual dashers168
- Figure 4.4.31.** Viscosity as a function of dasher assembly and throughput rate. Viscosity was measured as a percentage of the total torque capacity on the motor turning the dasher (n=3)....171
- Figure 4.4.32.** Cumulative residence time distribution $F(t)$ curves as a function of dasher assembly and throughput rate for ice cream made at 200 RPM dasher speed, 75% target overrun, and $-5.5 \pm 0.1^\circ\text{C}$ draw temperature (n=3).....175
- Figure 4.4.33.** Images of samples collected during pulse injection experiment for evaluating residence time distribution of ice cream as a function of dasher assembly and throughput rate. Average time of cup collection at 200 L/h = 16s, 300 L/h = 10s, and 400 L/h = 8s. Dasher speed = 200 RPM, target overrun = 75%, draw temperature = $-5.5 \pm 0.1^\circ\text{C}$. Top left cup in each image was collected at $t = 0\text{s}$ when 20 mL of tracer (1% methylene blue in ice cream mix) was injected into freezer176
- Figure 4.4.34.** A) $E(t)$ curves and B) $E(\theta)$ curves as a function of dasher assembly for ice cream made at a throughput rate of 200 L/h. Dasher speed = 200 RPM, target overrun = 75%, draw temperature = $-5.5 \pm 0.1^\circ\text{C}$ (n=3)177

- Figure 4.4.35.** A) E(t) curves and B) E(θ) curves as a function of dasher assembly for ice cream made at a throughput rate of 300 L/h. Dasher speed = 200 RPM, target overrun = 75%, draw temperature = $-5.5 \pm 0.1^\circ\text{C}$ (n=3)178
- Figure 4.4.36.** A) E(t) curves and B) E(θ) curves as a function of dasher assembly for ice cream made at a throughput rate of 400 L/h. Dasher speed = 200 RPM, target overrun = 75%, draw temperature = $-5.5 \pm 0.1^\circ\text{C}$ (n=3)179
- Figure 4.4.37.** Mean residence time t_s as a function of dasher assembly and throughput rate. Dasher speed = 200 RPM, target overrun = 75%, draw temperature = $-5.5 \pm 0.1^\circ\text{C}$. Values represent averages for three replicates180
- Figure 4.4.38.** Cumulative ice crystal size distributions immediately after draw as a function of dasher assembly for ice cream made at a throughput rate of A) 200 L/h, B) 300 L/h, and C) 400 L/h. Dasher speed = 200 RPM, target overrun = 75%, draw temperature = $-5.5 \pm 0.1^\circ\text{C}$183
- Figure 4.4.39.** A) Mean ice crystal size and B) standard deviation in ice crystal size of ice cream immediately after draw as a function of dasher assembly and throughput rate. Dasher speed = 200 RPM, target overrun = 75%, draw temperature = $-5.5 \pm 0.1^\circ\text{C}$. Values represent the modeled averages for three replicates.....184
- Figure 4.4.40.** Cumulative ice crystal size distributions as a function of dasher assembly for hardened ice cream samples made at a throughput rate of A) 200 L/h, B) 300 L/h, and C) 400 L/h. Dasher speed = 200 RPM, target overrun = 75%, draw temperature = $-5.5 \pm 0.1^\circ\text{C}$. Samples were evaluated at -15°C 187

Figure 4.4.41. A) Mean ice crystal size and B) standard deviation in ice crystal size of hardened ice cream samples as a function of dasher assembly and throughput rate. Dasher speed = 200 RPM, target overrun = 75%, draw temperature = $-5.5 \pm 0.1^\circ\text{C}$. Samples were evaluated at -15°C . Values represent the modeled averages for three replicates188

Figure 4.4.42. Cumulative air cell size distributions as a function of dasher assembly for hardened ice cream samples made at a throughput rate of A) 200 L/h, B) 300 L/h, and C) 400 L/h. Dasher speed = 200 RPM, target overrun = 75%, draw temperature = $-5.5 \pm 0.1^\circ\text{C}$. Samples were evaluated at -6°C 190

Figure 4.4.43. A) Mean air cell size and B) standard deviation in air cell size of hardened ice cream samples as a function of dasher assembly and throughput rate. Dasher speed = 200 RPM, target overrun = 75%, draw temperature = $-5.5 \pm 0.1^\circ\text{C}$. Samples were evaluated at -6°C . Values represent the modeled averages for three replicates191

Figure 4.4.44. Fat globule size distributions as a function of dasher assembly for ice cream samples made at a throughput rate of A) 200 L/h, B) 300 L/h, and C) 400 L/h. Dasher speed = 200 RPM, target overrun = 75%, draw temperature = $-5.5 \pm 0.1^\circ\text{C}$. Curves represent the modeled averages for three replicates.....193

Figure 4.4.45. Optical microscope images (20x magnification) of destabilized fat clusters as a function of throughput rate and dasher assembly194

Figure 4.4.46. Mean fat destabilization (%) for ice cream samples as a function of dasher assembly and throughput rate. Dasher speed = 200 RPM, target overrun = 75%, draw temperature = $-5.5 \pm 0.1^\circ\text{C}$. Values represent the modeled averages for three replicates195

Figure 4.4.47. Correlation between fat destabilization and viscosity (i.e., torque on dasher motor as % of total capacity) as a function of dasher. Solid black line denotes the overall correlation and dotted lines indicate correlation for individual dashers199

Figure 4.4.48. Correlation between fat destabilization and A) mean residence time and B) standard deviation in residence time as a function of dasher. Solid black line denotes the overall correlation and dotted lines indicate correlation for individual dashers201

Figure A.1. Shear sweep curves for ice cream mix (0% water removed) as a function of temperature. Error bars represent standard deviation for 3 replicates221

Figure A.2. Shear sweep curves for ice cream mix with 10% of water removed as a function of temperature. Error bars represent standard deviation for 3 replicates221

Figure A.3. Shear sweep curves for ice cream mix with 20% of water removed as a function of temperature. Error bars represent standard deviation for 3 replicates222

Figure A.4. Shear sweep curves for ice cream mix with 30% of water removed as a function of temperature. Error bars represent standard deviation for 3 replicates222

Figure A.5. Shear sweep curves for ice cream mix with 40% of water removed as a function of temperature. Error bars represent standard deviation for 3 replicates223

Figure A.6. Shear sweep curves for ice cream mix with 50% of water removed as a function of temperature. Error bars represent standard deviation for 3 replicates223

1 INTRODUCTION

In the United States, frozen desserts are a universally beloved treat with 94% of consumers purchasing products within this category (Mintel, 2023). Continuous scraped surface freezers (SSFs) were introduced around 1926, and today are widely used to manufacture frozen desserts on an industrial scale (Goff and Hartel, 2013). One of the key components of continuous SSFs is the dasher assembly, which rotates inside of the freezing cylinder. Important roles of the dasher include mixing, incorporation of air, destabilization of fat, and carrying blades that remove ice as it forms along the cylinder walls. Despite this, dashers are typically designed through trial and error based on the proprietary knowledge of individual manufacturers of SSFs.

The quality and acceptability of frozen desserts is determined by microstructural properties. The effect of processing parameters, including throughput rate, draw/refrigerant temperature, overrun, and even dasher rotational speed, on microstructure has been the topic of many studies. Very few studies have investigated the effect of dasher design on microstructure, and those studies have only considered the displacement of the dasher (i.e., the percentage of volume that the dasher occupies inside of the freezing cylinder) and not the geometry of the dasher, though several geometries are commercially available.

The goal of this research was to understand how dasher design modulates the microstructure of frozen desserts by characterizing processing conditions, namely residence time distribution and the amount of torque placed on the dasher motor, as a function of dasher assembly. Uniquely, this research also included dasher designs with similar displacements but different geometries.

The first phase of this study focused on unaerated sorbet, which is perhaps the simplest frozen dessert system. In this phase, ice crystal size was characterized as a function of dasher

assembly. The second phase of this study focused on ice cream, which is a complex system composed of fat, air, and ice distributed in a serum phase containing milk-solids-not-fat, sucrose, stabilizers, and emulsifiers. The rheological properties of the serum phase throughout the freezing process were studied by removing water from ice cream mix to model varying degrees of freeze concentration. Then, microstructural evolution of ice cream was characterized to determine how long after start-up of a SSF it takes to achieve a microstructural 'steady state'. Finally, the effect of dasher assembly on the ice crystal size, air cell size, and fat destabilization in ice cream was studied. Dasher speed, overrun, and throughput rate were also modulated to understand if the effect of dasher design on microstructure interrelates with the effect of these processing parameters. Correlations between processing conditions and microstructural attributes were also evaluated to determine how dasher design might modulate microstructural attributes.

Ultimately, this research is intended to enable frozen dessert manufacturers to make informed decisions about which dasher assembly is best suited to achieve the desired microstructural attributes in their products. Additionally, it provides valuable insights for improving the engineering of dashers and SSFs.

2 LITERATURE REVIEW

2.1 COMPOSITION OF FROZEN DESSERTS

2.1.1 Sorbet

Sorbet, also known as water ice, is the simplest legally defined frozen dessert (in the United States, defined by 21 CFR 135.160). Sorbet contains water, fruit or fruit juice, and nutritive carbohydrate sweeteners. It can also include stabilizers such as egg white, pectin, or gums, but it cannot include food fats. Unlike sherbet, sorbet cannot contain milk- or egg-derived ingredients (other than egg white). Sorbet mix need not be pasteurized prior to freezing. The final product should weigh not less than 6 lbs per gallon.

2.1.2 Ice Cream

The legal definition of ice cream can vary by jurisdiction. According to US Standards as described in 21 CFR 135.110, ice cream is “a food produced by freezing, while stirring, a pasteurized mix consisting of one or more [...] dairy ingredients”. Ice cream must contain a minimum of 10% milkfat and 20% total milk solids. The finished product must contain 1.6 lbs of total solids and weigh not less than 4.5 lbs per gallon. Although there are technically no regulations on the maximum overrun (a measure of air content) in ice cream, these parameters constrict the maximum overrun to approximately 100%. The primary ingredients of ice cream mix include:

- *Dairy fat* – The forms of dairy fat commonly used include cream, butter, or anhydrous milkfat. These provide flavor, lubrication (both during dynamic freezing and in the mouth), and structural integrity by fat destabilization.
- *Milk-solids-not-fat (MSNF)* – MSNF ingredients may include milk, concentrated milk, milk powders, or dairy-derived protein powders, which bring up the solids content of the mix. These

solids include lactose and salts/minerals, which contribute to freezing point depression and flavor. Additionally, the protein amassed by these ingredients helps with emulsification of the mix, increases mix viscosity, and foam development during freezing (Goff, 2016).

- *Sweeteners* – Sweeteners are used for their flavor, contribution to total solids, building of mix viscosity, and freezing point depression. Nutritive sweeteners, commonly sucrose and corn syrup solids, are typically used in standard ice cream. Sugar alcohols, especially erythritol and maltitol, are nutritive sugar substitutes commonly used in ice cream. While sugar alcohols are typically not as sweet, they have reduced calorie content relative to other nutritive sweeteners. Using non-nutritive sweeteners may be desirable for decreasing calorie content as they are undigestible to humans. Commonly used artificial non-nutritive sweeteners include aspartame, acesulfame K, and sucralose, while commonly used natural non-nutritive sweeteners include monk fruit and stevia extracts. These non-nutritive sweeteners are sweeter in taste than sucrose, meaning a smaller amount can be used to achieve an equivalent level of sweetness with sucrose. This can cause problems, as non-nutritive sweeteners will not contribute to viscosity or freezing point depression like nutritive sweeteners. To counteract these effects, bulking agents such as sugar alcohols and polydextrose must be added when non-nutritive sweeteners are used to replace sucrose.
- *Stabilizers* – The key functions of stabilizers are to increase mix viscosity and prevent mix separation. In ice cream, stabilizers delay ice crystal growth and provide resistance to melting. A wide variety of stabilizers may be used in ice cream, including starches, gums, carrageenan, agar and alginates, gelatin, and pectin.
- *Emulsifiers* – Emulsifiers are used to improve foaming properties and fat destabilization. Today, the most commonly used emulsifiers are mono- and di-glycerides, polysorbate 80, and

lecithin. Traditionally, however, egg yolk was used as an emulsifier. In contrast with custard, ice cream must contain less than 1.4 percent egg yolk solids by weight.

2.2 MICROSTRUCTURE OF FROZEN DESSERTS

The microstructure of frozen desserts is developed during the dynamic step of freezing. Major microstructural components include ice crystals, air cells, and (in the case of ice cream) fat globules, all of which are dispersed in an unfrozen serum phase (Figure 2.1).

2.2.1 Ice Crystals

Ice crystals are only formed in the dynamic freezing step, as subsequently described in section 2.4.1. During dynamic freezing, approximately 50% of the water in the mix is frozen. The mean size of ice crystals is about 15-35 μm upon exiting the freezer (Donhowe and Hartel, 1996b; Muse and Hartel, 2004; Drewett and Hartel, 2007, Hernández-Parra et al., 2018a).

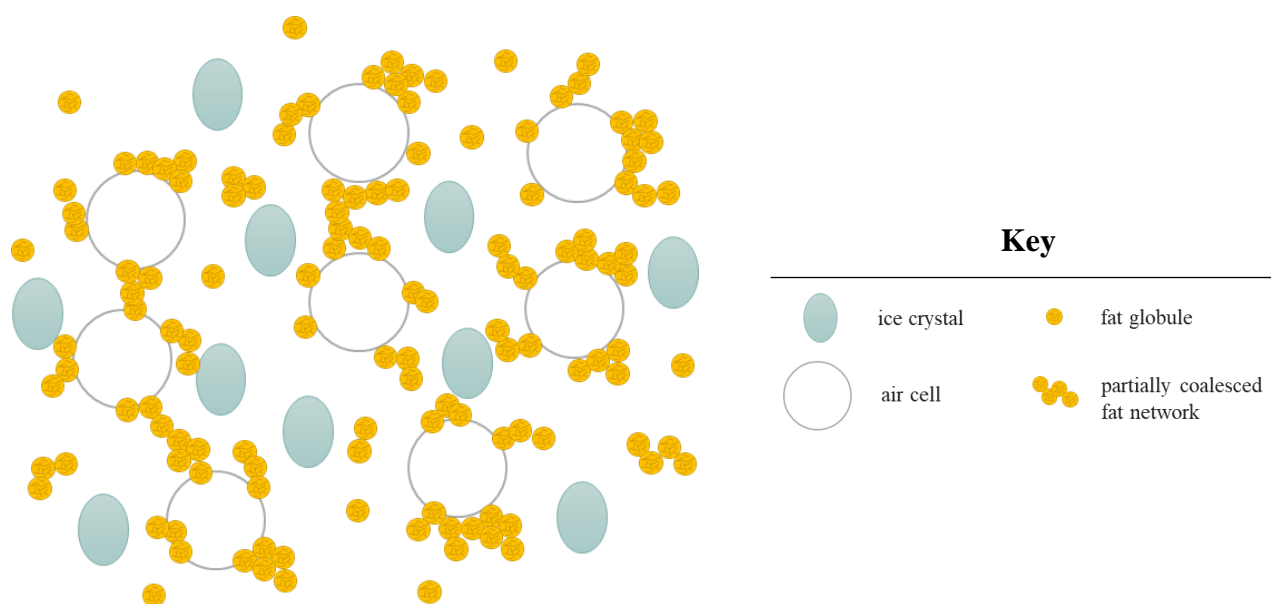


Figure 2.1. Schematic of the microstructure of ice cream. (Adapted from Goff and Hartel, 2013).

During hardening, approximately 75%-80% of water is frozen. However, only the volume of water frozen can increase, the number of ice crystals cannot increase in the product. Therefore, average ice crystal size will grow in the hardened product. In a survey of commercial ice cream products in the United States, Warren and Hartel (2014) found that the average hardened ice crystal size ranged from approximately 26-67 μm . Ice crystal size plays a critical role in the texture of ice cream, with small ice crystals contributing to a smooth mouthfeel (Russell et al., 1999; Amador et al., 2017). However, large ice crystals ($>50 \mu\text{m}$) can result in icy texture (Figure 2.2).

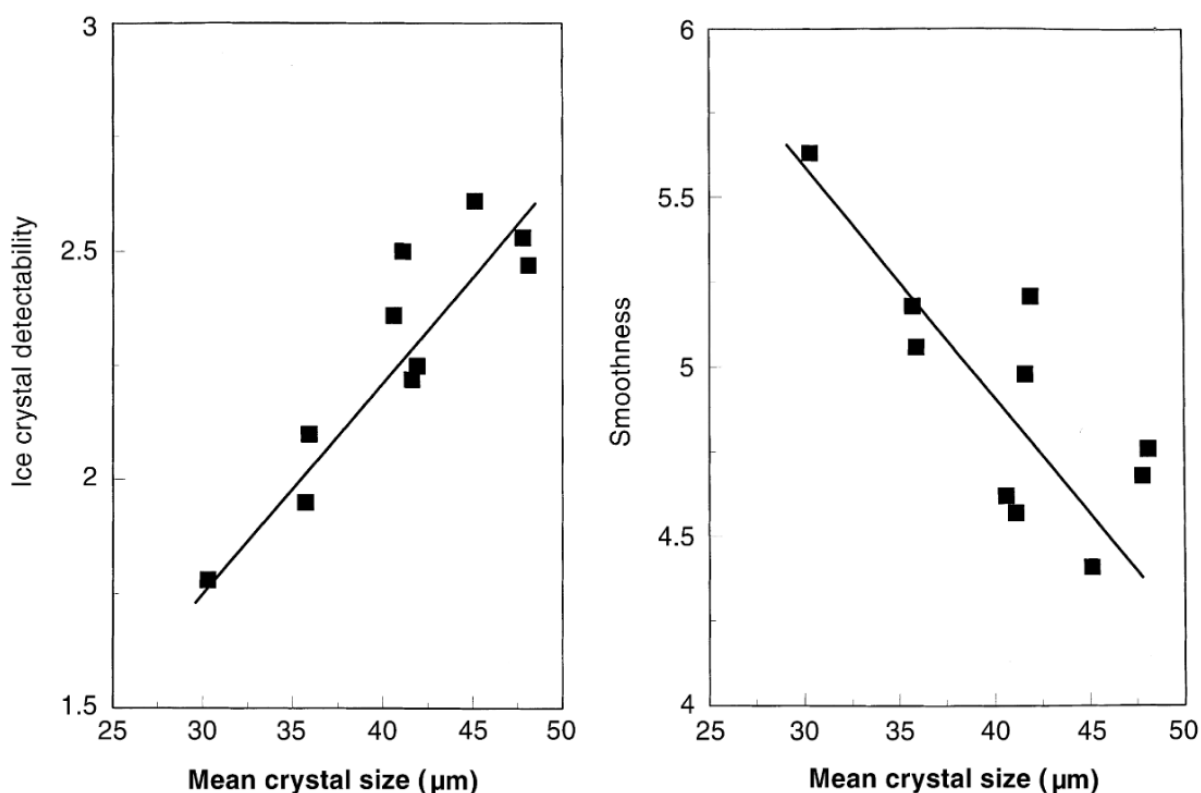


Figure 2.2. Effect of mean ice crystal size on ice detectability on smoothness of ice cream (from Russell et al., 1999).

2.2.1 Air Cells

Air is a critical component of frozen desserts as it influences hardness and melting properties (Muse and Hartel, 2004; Sofjan and Hartel, 2004; Warren and Hartel, 2018). Air content

in frozen desserts is measured as overrun, or the increase in volume that occurs during freezing as a result of whipping. Overrun in frozen desserts can range from 25-150%. Overrun is calculated as:

$$\text{Overrun} = \frac{\text{Wt. of mix} - \text{Wt. of same vol. of ice cream}}{\text{Wt. of same vol. of ice cream}} * 100 \quad (\text{Eqn. 2.1})$$

Formation of ice is necessary for proper air incorporation into frozen desserts. Ice formation during dynamic freezing increases the viscosity of the product by freeze concentration, which helps stabilize air cells (Chang and Hartel, 2002a). Air cell size at draw is approximately 15-35 μm (Chang and Hartel, 2002a, 2002b; Muse and Hartel, 2004; Hernández-Parra et al., 2018a). Air cell size in commercial (hardened) products is approximately 27-40 μm (Warren and Hartel, 2014). Growth of air cells may occur by disproportionation, coalescence, drainage, or distortion (Chang and Hartel, 2002b).

2.2.2 Fat Globules & Partially Coalesced Fat

Prior to freezing, the diameter of fat globules in homogenized ice cream mix is approximately 1 μm . Upon freezing, the fat globules are partially coalesced into a fat network (Figure 2.1). Instead of reporting the size of the partially coalesced fat clusters, the extent of partial coalescence is typically characterized as the percentage of fat destabilization. Percent fat destabilization is the ratio (by volume) of fat clusters above initial emulsion size to the volume of fat globules at the initial mix emulsion size (Figure 2.3).

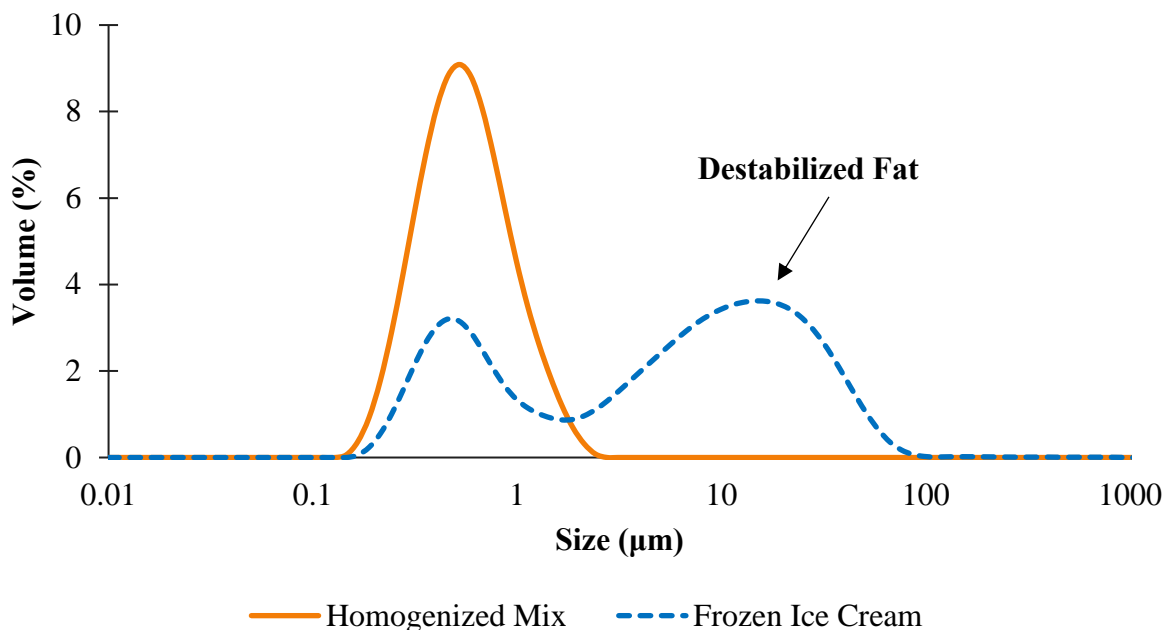


Figure 2.3. Fat globule size distribution of initial homogenized ice cream mix versus frozen ice cream containing partially coalesced fat globules.

Fat destabilization can vary greatly, ranging from approximately 3-55% in a survey of commercial samples (Warren and Hartel, 2014), although fat destabilization above 80% has been reported (Goff and Jordan, 1989). The extent of fat destabilization is important as the partially-coalesced fat network provides structural integrity, which is particularly important for shape retention when ice melts. Fat globule destabilization has often been inversely correlated with melting rate (Bolliger et al., 2000a; Koxholt et al., 2001; Muse and Hartel, 2004; Warren and Hartel, 2014; Wu et al., 2019), although this correlation does not exist under all conditions (Warren and Hartel, 2018; Wu et al., 2019) because meltdown occurs as a result of complex interactions. While fat destabilization can reduce melting rate and contribute to the smooth and creamy mouthfeel of ice cream, a high level of fat destabilization may result in churning, visible fat globules, or a greasy mouthfeel (Berger and White, 1971; Amador et al., 2017). Therefore, achieving the appropriate level of fat destabilization for the desired product properties is critical.

2.2.3 Serum Phase

The serum phase is the continuous phase in which the ice crystals, air cells, and fat globules/clusters are dispersed. It is composed of unfrozen water with dissolved solutes, as well as suspended proteins and stabilizers. In the frozen product, the serum phase will often be present as thin lamella where proteins may adsorb to the fat or air interfaces (Caldwell et al., 1992, Goff et al., 1999; Zhang and Goff, 2004). Due to freeze concentration, the serum phase becomes more viscous as ice is formed and the proportion of solutes and suspended molecules to unfrozen water increases.

2.3 SCRAPED SURFACE FREEZERS

The freezing of ice cream occurs in two steps: dynamic freezing and hardening. Dynamic freezing is critical for the microstructural development of ice cream, as discussed in section 2.4. The dynamic freezing step utilizes specialized heat exchangers commonly called scraped surface freezers (SSFs). SSFs may be batch or continuous, although continuous freezers are used in industrial scale operations. Continuous SSFs will be the focus of this review.

2.3.1 Design of Scraped Surface Freezers

2.3.1.1 Refrigeration System and the Freezing Cylinder

The freezing cylinder is arguably the most important part of SSFs as this is where all freezing and microstructural development takes place. The freezing cylinder is a tube-in-tube heat exchanger with refrigerant in the jacket. Refrigerants typically include ammonia or hydrofluorocarbons. A vapor-compression refrigeration system is utilized to remove heat from the product as it moves through the SSF. A vapor-compression refrigeration cycle (Figure 2.4) consists of four processes: 1) evaporation, 2) compression, 3) condensation, and 4) expansion.

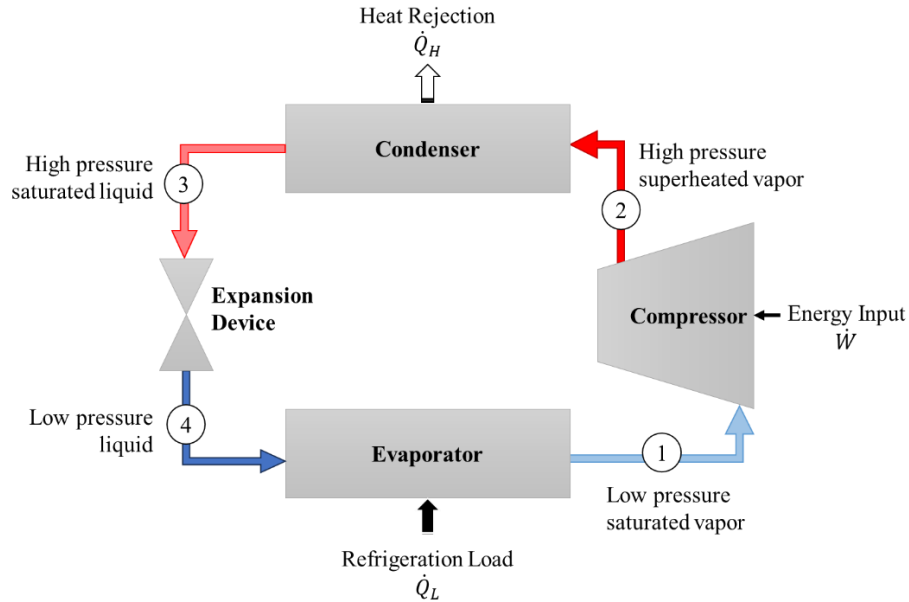


Figure 2.4. Vapor-compression refrigeration cycle in a scraped surface freezer. 1) Evaporation – liquid refrigerant absorbs heat from the product in the freezing cylinder and is vaporized. 2) Compression – vaporized refrigerant is compressed, causing a rise in temperature. 3) Condensation – the superheated vapor is cooled by an external heat sink, causing the refrigerant to condense to a liquid. 4) Expansion – the high-pressure liquid refrigerant passes through an expansion (throttling) device which further decreases the refrigerant temperature. The refrigerant is ready to re-enter the refrigeration cycle in the evaporator (Adapted from Goff and Hartel, 2013 and Dincer, 2017).

In the case of scraped surface freezers, the evaporator is the freezing cylinder. Low-pressure liquid refrigerant contacts the freezing cylinder wall. The refrigerant absorbs heat (\dot{Q}_L) because its temperature is lower than the temperature of the mix on the other side of the cylinder wall, and this causes the refrigerant to boil and form a low-pressure saturated vapor. The state change causes a much larger absorption of heat by latent heat. At the same time, the removal of heat from the frozen dessert mix allows for ice crystal formation and growth (Goff and Hartel, 2013).

The low-pressure vaporized refrigerant is then pumped into the compressor, where the pressure of the vapor is increased through compression, (or decreasing volume), of the gas, which requires external energy input, or work (\dot{W}). As the pressure is increased, the temperature of the refrigerant rises in accordance with the ideal gas law until it is superheated. The superheated vapor

moves to the condenser, where the heat that was absorbed in the evaporator is removed (\dot{Q}_H) and ‘rejected’ outside of the system. In freezers with self-contained refrigeration units, the heat is typically rejected to an outside source of cooling water. To complete the cycle, the throttling device, which often takes the form of an expansion valve, is used to reduce the pressure of the liquid refrigerant, which also reduces its temperature further. The low-pressure liquid refrigerant can then enter the evaporator again (Dincer, 2017).

2.3.1.2 Dasher Assembly

The dasher plays several key roles in the development of ice cream microstructure, including mixing, air incorporation and size reduction, and partial coalescence of fat, which are a result of the shear provided by the dasher. Additionally, the dasher carries knives/blades that scrape ice from the walls. As the product moves through the freezer, the dasher rotates at a constant speed, typically ranging from 100 RPM – 300 RPM. However, some freezers can operate at speeds of up to 1,000 RPM (Arellano et al., 2012). Some freezers can only operate at a fixed dasher rotational speed, whereas others have a variable drive that allows the speed to be changed by the operator to achieve the desired product attributes.

The dasher assembly is composed of 3 primary components: the dasher, beater (in open dashers only), and knives (Figure 2.5). The number of knives on an assembly varies, ranging from 2 to 4. Dasher assembly design is complex and widely variable, as it is typically based on the proprietary findings of each individual freezer manufacturer. Typically, dashers are characterized by how much of the freezer barrel volume they displace; however, dasher designs of similar displacements may have very different geometries. There are two primary types of dasher designs: solid dashers, which typically displace a high volume in the freezing cylinder, and open dashers,

which are hollow in the center and displace less volume in the freezing cylinder. Open dashers support the beater, which can also vary in design. Examples of commercially available dashers and beaters are provided in Figure 2.6. The effects of dasher design on the microstructure of frozen desserts are discussed in section 2.6.

Key

- 1: Standard Dasher
- 2: Scrape knife
- 3+5: Bushing
- 4: Beater bearing standard
- 6: Snap ring
- 7: Shaft seal
- 8: Wing beater

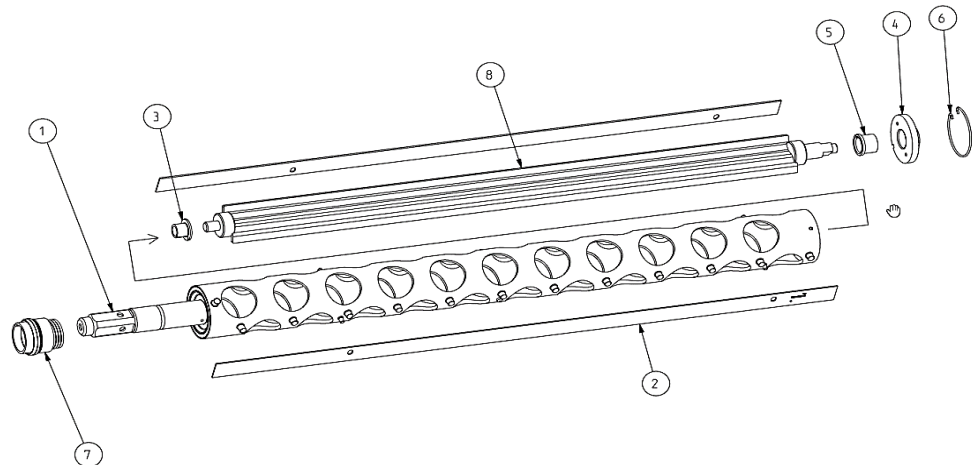
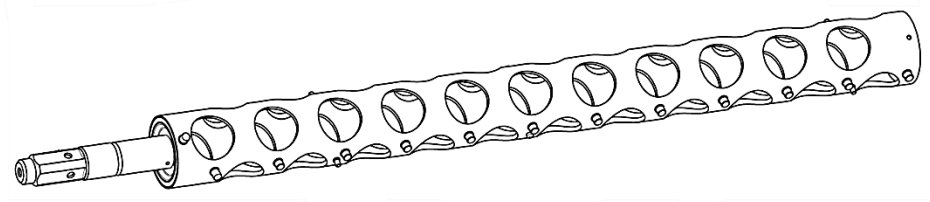


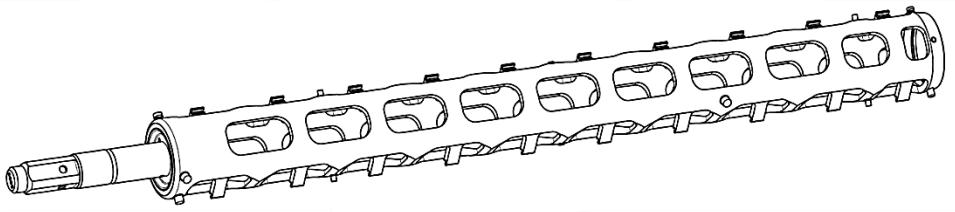
Figure 2.5. Schematic of the components of a dasher assembly. The primary components of the dasher assembly include the dasher itself (1); the beater (8), which is only used inside of open dashers; and knives (2) that are supported on the outside of the dasher (Courtesy of Tetra Pak).

Dasher Designs

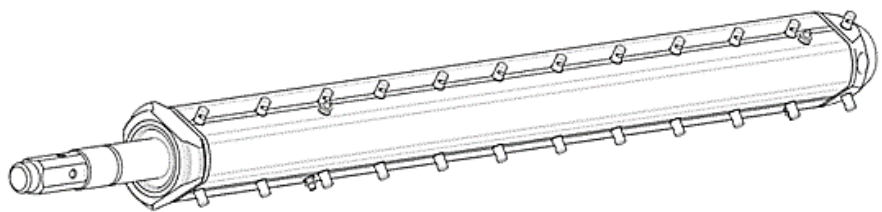
Standard Dasher



Multi Dasher

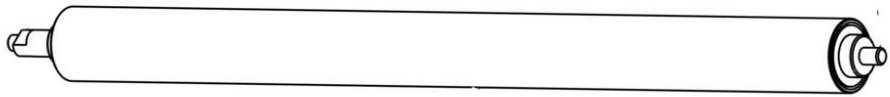


Solid Dasher



Beater Designs

Solid Beater



Wing Beater

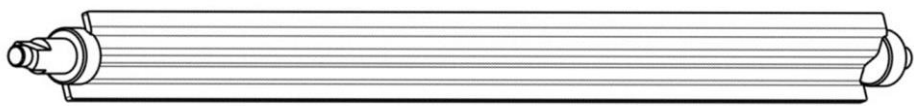


Figure 2.6. Examples of commercially available dasher and beater designs (courtesy of Tetra Pak).

2.4 PHENOMENA IN SCRAPED SURFACE FREEZERS

Several phenomena occur simultaneously during the freezing process in SSFs, including ice crystallization, freeze concentration of the serum phase, fat destabilization, and air incorporation/size reduction.

2.4.1 Ice Crystallization

Several reviews have covered the ice crystallization process in frozen desserts (Hartel, 1996; Adapa et al., 2000; Stamatiou et al., 2005; Cook and Hartel, 2010). The freezing point of pure water is 0°C; however, in a frozen dessert system such as sorbet or ice cream, low molecular weight solutes such as sugars and milk salts will be present. The presence of solutes reduces the amount of ice formed at any given temperature; a property known as freezing point depression. Freezing point depression is colligative, meaning that the size and quantity (i.e., moles) of solutes impacts the degree of depression (Reid and Fennema, 2008). Freezing point is calculated as:

$$FPD_T = FPD_{SE} + FPD_{SA} \quad (\text{Eqn. 2.2})$$

Where FPD_{SE} accounts for the mono- and disaccharides present in the product as a function of the sucrose equivalence (SE) in g/g of mix, and FPD_{SA} accounts for salts in MSNF and whey solids. These theoretical equations were developed based on experiments conducted to compare the effect of ingredients on freezing point relative to sucrose and experiments comparing predictive models to analytical freezing point values (Leighton, 1927; Smith and Bradley, 1983; Baer and Keating, 1987; Jaskulka et al., 1993; Jaskulka et al., 1995; Livney et al., 2003; Whelan et al., 2008; Goff and Hartel, 2013). SE is calculated as:

$$SE = (MSNF * 0.545) + (WS * 0.765) + S + (10DE\ CSS * 0.2) + (36DE\ CSS * 0.6) + (42DE\ CSS * 0.8) + (62DE\ CSS * 1.2) + (HFCS * 1.8) + (F * 1.9) \quad (\text{Eqn. 2.3})$$

Where MSNF = milk solids not fat, WS = whey solids, S = sucrose or other directly added disaccharides, CSS = corn syrup solids at varying dextrose equivalents (DE), HFCS = high fructose corn syrup, and F = fructose or other pure monosaccharides. The SE can then be used to find the freezing point depression based on:

$$FPD_{SA} = \frac{(MSNF+WS)*2.37}{W} \quad (\text{Eqn. 2.4})$$

When water freezes, solutes are excluded so that the ice is pure as it is formed (Reid and Fennema, 2008). This results in an increasing concentration of solutes in the unfrozen phase of water, also called freeze concentration. Therefore, the freezing point of the unfrozen phase changes as more ice is formed, and this phenomenon can be summarized by a freezing curve (Figure 2.7).

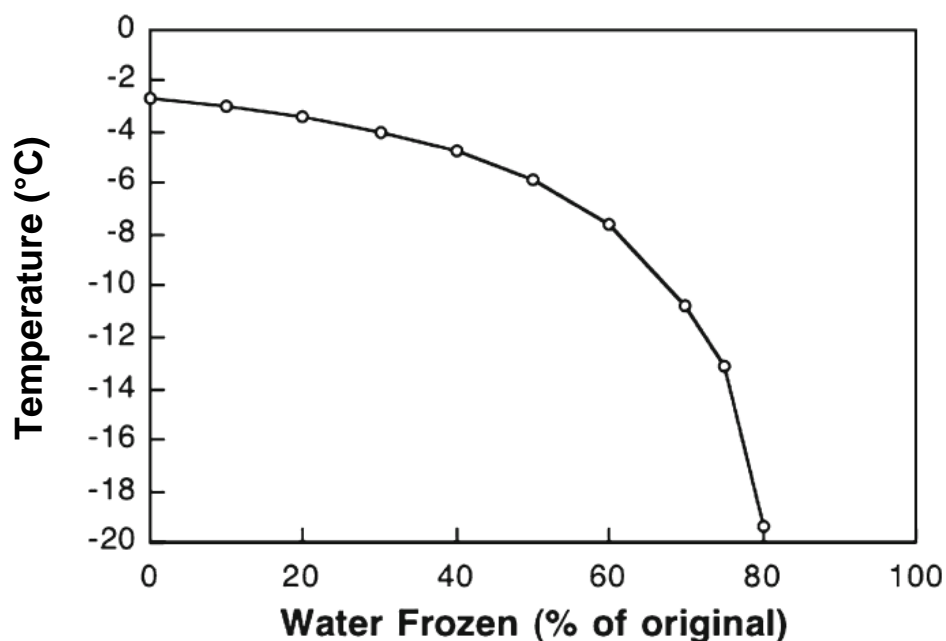


Figure 2.7. Example of a freezing point depression curve, which demonstrates how freeze concentration of solutes in the unfrozen phase decreases the freezing point. From Goff and Hartel (2013).

Freezing point can also be determined experimentally by osmometer (Baer and Keating, 1987; Jaskulka et al., 1993; Jaskulka et al., 1995) and DSC (de Cindio et al., 1995; Livney et al., 2003).

The methods for calculation of freezing point can be used to create a theoretical freezing curve by dividing SE by the total amount of unfrozen water in the product. Livney et al. (2003) compared this method of calculating freezing point curves to be suitable as a basis for comparison of different mixes, as it was able to accurately predict values for freezing point depression curves up to approximately 50% of water frozen. As approximately 50% of water is frozen during the dynamic freezing process, the method of calculation is suitable for approximation of freezing curves in

scraped surface freezers. It should be noted that freeze concentration can only occur until the point where the concentration of solutes in the unfrozen phase causes an increase in viscosity that limits diffusion. This point is called the maximum freeze concentration (C'_g). The temperature at which C'_g is reached is also the glass transition temperature (T'_g), since any decrease in temperature beyond this point will result in the unfrozen phase becoming a glass (Roos, 2021). These temperatures may become relevant during hardening or low temperature storage, but they are typically not relevant during dynamic freezing.

The ice crystallization process in a scraped surface freezer has been summarized into 4 steps: 1) supercooling, 2) nucleation, 3) growth, and 4) recrystallization (Cook and Hartel, 2010). Figure 2.8 details where each of these steps takes place axially in the freezer barrel. Supercooling occurs when the temperature of a solution drops below its freezing point, and the degree of supercooling can be summarized as the difference between the system temperature and the freezing point. This only occurs near the freezer wall, where temperatures are close to refrigerant temperature (approximately -35°C). Nucleation can only take place in areas with subcooling at or near the freezer wall. Meanwhile, growth can occur at the wall or any area with a temperature below the melting point. Cook (2010) proposed that the growth of individual, dendritic crystals form a slush layer along the freezer wall, similar to what was observed by Jacobsen (1999) in a slush freezer. As the dasher blade removes these crystals from the wall, they are incorporated into the bulk mix towards the center of the freezer barrel, and recrystallization can occur to those crystals incorporated into the bulk. This is supported by computational fluid dynamic (CFD) and population balance (PB) models that predict the ice mass fraction and number concentration of ice crystals is largest near the wall of the SSF (Lian et al., 2006). Skating may occur if there is an excessive buildup of ice at the freezer wall and dasher blades “skate” along the surface of ice rather

than removing the ice from the wall. Skating most often occurs when dasher blades are not properly maintained and become dull, and it causes a decline in freezer performance and product quality.

In addition to differences in ice crystal formation from a radial perspective, there are also likely differences in the predominant mechanisms of ice crystal formation axially in the freezer barrel. Near the freezer barrel entrance where not many ice crystals have been formed yet, nucleation is likely the primary mechanism of crystallization. Near the middle of the freezer, it is likely that growth is the primary mechanism at work, and near the end of the freezer where many crystals have already been formed and therefore growth is limited by crystal interactions, recrystallization is likely the primary mechanism (Cook and Hartel, 2011).

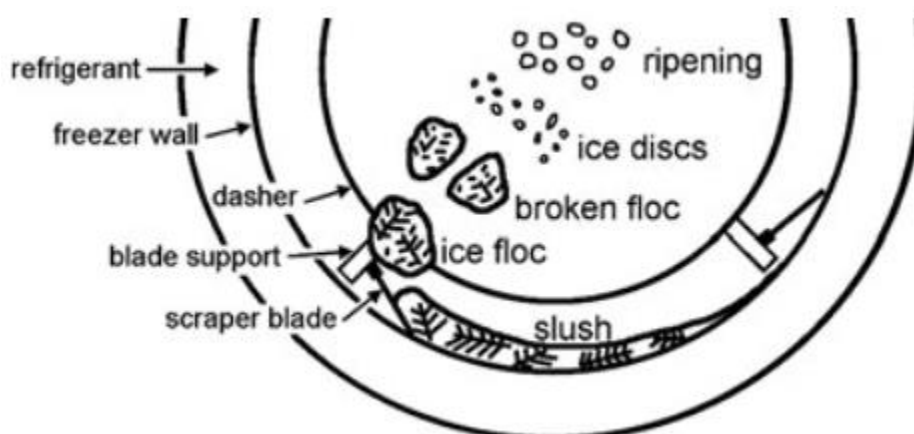


Figure 2.8. Cross section of freezer barrel. Ice nucleation occurs at the freezer wall, and growth of dendritic crystals forms a slush layer at the freezer wall. The slush is removed by rotating scraper blades in the form of ice flocs, which are broken down by mixing and shear inside the freezer. As the ice melts due to warmer temperatures in the center of the barrel, ice discs are formed and may recrystallize/ripen after residing in the freezer for a period of time (From Cook and Hartel, 2010).

2.4.1.1 Nucleation

Nucleation is the formation of a new crystal. Matsumoto et al. (2002) characterized this nucleus formation process with a molecular dynamics simulation. In water, individual ring structures are formed and destroyed by the continuous forming and breaking of hydrogen bonds. Upon supercooling, the hydrogen bonds become longer lasting, and if by chance they locally form

a tetrahedral structure, they have the potential to create a nucleus. Tetrahedral structures are more likely to appear in low-mobility regions of supercooled water (Russo et al., 2018). This cluster of molecules will then rapidly become more compact as water molecules surrounding it become less diffuse and attach themselves to that cluster (Fitzner et al., 2019). This continues until the cluster reaches the critical radius (r_c) of a nucleus, also called an embryo. The critical radius is the minimum size the nucleus must reach for it to grow spontaneously:

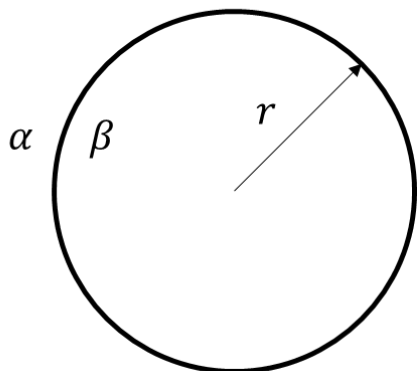
$$r_{cr} = \frac{2\gamma}{\Delta H^V \left(1 - \frac{T}{T_{eq}}\right)} \quad (\text{Eqn. 2.5})$$

where γ is the interfacial tension, T_{eq} is the temperature at which water and ice are at equilibrium between phases, and assuming a spherical embryo. Given this, it can be deduced that lower temperatures result in a smaller critical radius. If the cluster does not reach the critical radius, it will dissolve due to an unfavorable change in free energy:

$$\Delta G_{max} = \frac{4}{3}\pi r_{cr}^2 \gamma \quad (\text{Eqn. 2.6})$$

where ΔG_{max} is the activation free energy for nucleus formation. (Walstra, 2003).

a. Homogeneous Nucleation



b. Heterogeneous Nucleation

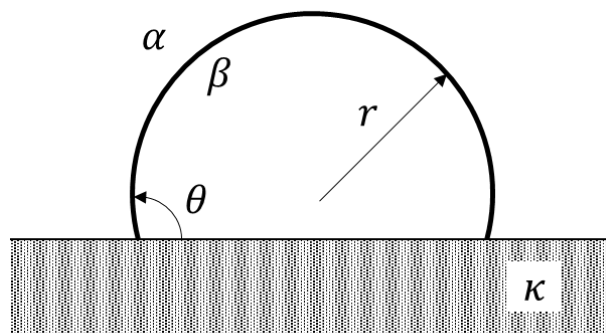


Figure 2.9. Homogeneous and heterogeneous nucleation of ice crystals. Embryos of ice (β) are formed from water (α). Homogeneous nucleation (a) occurs in the bulk phase, whereas heterogeneous nucleation (b) occurs at a surface (κ), either of a particle or at a surface, such as the freezer wall. Adapted from Walstra (2003).

There are two types of primary nucleation: homogeneous and heterogeneous (Figure 2.9). Homogeneous nucleation occurs in bulk phase of pure water, with the absence of phase boundaries, at approximately -40°C (Walstra, 2003). Given the solution and multi-phase nature of ice cream, it is more likely that the primary driver is heterogeneous nucleation. Heterogeneous nucleation occurs at impurities in water, or at any surface, such as the wall of an ice cream freezer. Heterogeneous nucleation can occur at a much higher temperature than homogeneous nucleation, due to the lowering of interfacial tension required to form a nucleus:

$$\cos \theta = \frac{\gamma_{\alpha\kappa} - \gamma_{\beta\kappa}}{\gamma_{\alpha\beta}} \quad (\text{Eqn. 2.7})$$

The curvature of the nucleus will remain the same as in homogeneous nucleation; however, the volume of the nucleus is smaller. This essentially lowers the value of ΔG_{max} by a factor of f_{cat} , meaning that heterogeneous nucleation occurs much more readily:

$$f_{cat} = \frac{1}{4}(2 + \cos \theta)(1 - \cos \theta)^2 \quad (\text{Eqn. 2.8})$$

Holden et al. (2019) successfully imaged active sites in heterogeneous nucleation and found that these active sites are driven by nanoscale topography. That is, small deviations in a surface (like cavities) may stabilize the critical nucleus through reduction of interfacial tension (Page and Sear, 2006).

The final type of nucleation that occurs in the manufacture of frozen desserts is secondary nucleation. Secondary nucleation occurs in the vicinity of an ice crystal that has already been formed. Agitation, which occurs by dasher rotation in the freezer, increases nucleation rate. This is likely due to the scraping of ice crystals off the barrel wall by scraper blades as well as breaking of newly formed crystals as they contact either the freezer parts or other solids (Walstra, 2003).

Nucleation rate is important as it determines the number of crystals present in a product, which will also affect the size to which ice crystals can grow (Cook and Hartel, 2010). Factors that

affect nucleation include temperature and surface energy (Li et al., 2017). Slower cooling rates, which are a result of smaller temperature differentials between the freezer barrel wall and the product, typically result in a lower nucleation rate as hydrogen bonds are more frequently broken (Bogdanova et al., 2022). Indeed, Haddad Amamou et al. (2010) found that in a model freezer system, nucleation was faster at lower refrigeration temperatures. However, at extremely low temperatures, (i.e., temperatures near the glass transition temperature T_g'), hydrogen bonds may not be able to reorient properly to form a nucleus due to reduced molecular mobility. Similarly, water-surface interactions can break hydrogen bonds, but they can also cause orientation of water molecules that leads to more hydrogen bonding. Therefore, nucleation is a balance between temperature and water-surface interactions, with hexagonal structuring being favored when the temperature effect and surface effect are comparable and intermediate (Li et al., 2017).

2.4.1.2 Growth

On a molecular level, ice crystal growth requires mass transfer of water molecules to the nucleus by diffusion as well as heat transfer required for the phase change of water to ice. As this occurs, hydrogen bonds are organized into a hexagonal, honeycomb-like structure. The main factor that affects the rate of ice crystal growth is the degree of subcooling, with crystals growing more rapidly at a higher degree of supercooling (Teraoka et al., 2002). This is relevant as a fraction of a second at sufficient supercooling allows for significant ice crystal growth (Cook, 2010; Luo et al., 2019). However, this is only pertinent until approximately -15°C , where increased supercooling no longer increases growth rate, likely due to a decrease in molecular mobility (Si, 2000; Cook and Hartel, 2011).

Distance between crystals can also impact growth, as ice crystals will grow significantly in directions away from neighboring crystals – that is, crystal interactions inhibit ice crystal growth (Cook, 2010). Shear also affects ice crystal growth rate. Near the freezing point, growth rate decreases with shear. In regions with sufficient supercooling, such as near the freezer wall, the effect of shear on growth rate is nonlinear (Figure 2.10, Luo et al., 2019). As shear increases from zero, the rate of growth increases. Locally, hydrogen bonds of water are broken, which gives water molecules the opportunity to re-orient into positions along ice-water interfaces, therefore contributing to growth of the ice crystal. Increasing shear also decreases heat transfer resistance (Lakhdar et al., 2005). However, after a certain point, shear can break water molecules from the ice lattice, which slows growth rate (Luo et al., 2019).

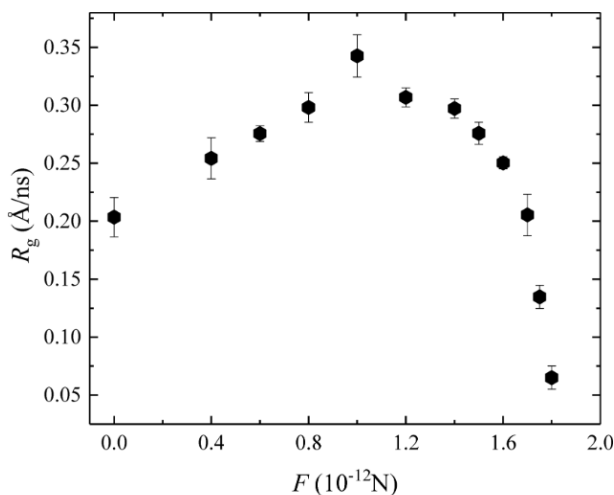


Figure 2.10. Effect of shear on growth rate R_g of ice crystals in pure water with a degree of supercooling $\Delta T = 30^\circ\text{C}$. Results from molecular dynamics simulation. From Luo et al., 2019.

The shape of ice crystals varies throughout the growth process. In a solution at a high degree of supercooling, ice crystals will initially grow dendritically (Teraoka et al., 2002; Petzold and Aguilera, 2009). The word dendrite comes from the Greek word dendron, which means ‘tree’, which underscores the branched structure of dendritic crystals. Velocity of dendrite formation is

increased with increased supercooling (Hindmarsh et al., 2005), which can also influence ice crystal morphology (Figure 2.11). In SSFs, the degree of supercooling is high, as refrigerant temperatures are approximately -30°C (Goff and Hartel, 2013)

The presence of solutes causes more dendrite-like crystals to be formed than in pure water, where crystals are smoother. This is because solutes are not able to diffuse as quickly as the ice is formed, but they are still excluded from the ice structure, meaning that they disrupt growth where they are present (Teraoka et al., 2002).

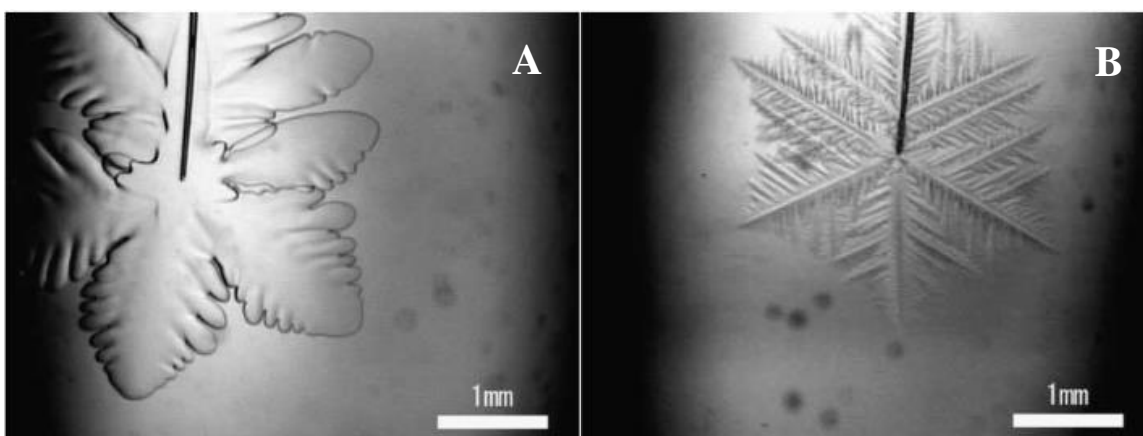


Figure 2.11. Ice crystal growth at -0.4°C (A) develops more slowly and is more rounded than the dendritic shaped crystal formed at -3.0°C (B) supercooling (From Teraoka et al., 2002).

2.4.1.3 Recrystallization

Recrystallization, also called ripening, occurs during the dynamic freezing process, but also during hardening and storage (Donhowe et al., 1991; Donhowe and Hartel, 1996a, 1996b). This is evidenced by the fact that crystals exiting a dynamic freezer are disc shaped rather than dendritic. During recrystallization, the morphology of ice crystals changes from dendritic to rounded (Smith and Schwartzberg, 1985; Cook and Hartel, 2011). Cook and Hartel (2011) simulated freezing at the freezer wall, followed by warming, which would lead to recrystallization. This study demonstrated that recrystallization led to rounded circular or oblong ice crystals, with little evidence of dendritic shape. It is likely that there is mechanical breakage of ice crystals that

contributes to the breakdown of dendrites (Cook, 2010). However, several other mechanisms are at play: isomass recrystallization, accretion, and Ostwald ripening (Donhowe and Hartel, 1996a, 1996b; Regand and Goff, 2003; Cook and Hartel, 2010). Isomass recrystallization occurs when a singular crystal changes shape, but its mass does not change. Accretion occurs when two crystals join into one after contacting each other. During Ostwald ripening, large ice crystals grow at the expense of smaller crystals through diffusion (Walstra, 2003). Smith and Swartzberg (1985) demonstrated that recrystallization occurs rapidly when the ice crystal size distribution is bimodal. Ostwald ripening is governed by the Kelvin equation:

$$\ln \frac{C_w}{C_{we}} = \frac{(T-T_0)}{(T_e-T_0)} = \frac{2B_a V_m \sigma_I}{3B_v R T D} \quad (\text{Eqn. 2.9})$$

where C_w is the equilibrium concentration of free water in contact with ice crystals of diameter D , C_{we} is the concentration of water in solution in equilibrium with ice crystals whose diameters are so large that surface free energy effects are negligible, T is temperature, T_0 is the freezing point of pure water (273.2 K), T_e is the temperature of solution in equilibrium with ice crystals whose diameter is so large that surface free energy effects are negligible, B_a is the surface shape factor (ratio of the crystal surface to D^2), V_m is the molar volume of ice crystals $\left(0.0197 \frac{m^3}{kg \cdot mol}\right)$, σ_I is the interfacial tension at the surface of ice $\left(0.02 \frac{kg}{s^2}\right)$, B_v is the volume shape factor (ratio of crystal volume to D^3), and R is the gas constant $\left(8.314 \frac{kJ}{kg \cdot mol \cdot K}\right)$ (Smith and Swartzberg, 1985). This equation highlights that small ice crystals will have high solubility due to the curvature of the particle. It also describes that when crystals have extreme features like points or pitting, their solubility will be decreased locally, causing rounding of the crystal to a disc shape. Thermodynamically, when small crystals melt, heat is removed from solution, which also provides the heat transfer (latent heat of fusion) necessary for larger ice crystals to grow.

The kinetics of recrystallization are driven by heat and mass transfer. Mass transfer, or the mass flux (J) (kg/m²s) of water to or from the surface of a growing crystal can be described by:

$$J = \frac{3B_v\rho_I dD_i}{dt} = kB_a(C_n - C_i) \quad (\text{Eqn. 2.10})$$

where B_v is a volume shape factor or the ratio of crystal volume to diameter D^3 , ρ_I is the density of ice (917 kg/m³), D_i is the mean diameter of crystals in size range i , k is the overall mass-transfer coefficient for dissolving/growing ice crystals, B_a is the surface shape factor or the ratio of crystal surface area to D^2 , C_n is the concentration of water in solution in equilibrium with ice crystals of neutral diameter, and C_i is the concentration of water in solution in equilibrium with ice crystal of diameter D_i . When J is negative, crystals are dissolving, and when J is positive crystals are growing (Smith and Schwartzberg, 1985). Recrystallization occurs at both oscillating and constant temperature, but it occurs more quickly when ice is subject to rapid temperature oscillation (Donhowe and Hartel, 1996a; Ndoye and Alvarez, 2014). Donhowe et al. (1991) identified that ice crystal size increases greatly between draw and hardening and that the first 7 weeks of storage are critical for ice recrystallization in the product. Increasing temperature increases the rate of recrystallization, especially near the freezing point of the product (Donhowe and Hartel, 1996a; Hagiwara et al., 2005, Ndoye and Alvarez, 2014). Storage below the glass transition temperature results in a halt in recrystallization, or no change in ice crystal size over time (Flores and Goff, 1999a). The power law model of kinetics (or $t^{1/3}$ kinetics), fits linearly to recrystallization rate when plotted against mean ice crystal size for temperatures from -20 to -5°C (Donhowe and Hartel, 1996a, 1996b), as described by:

$$L_{1,0} = k \times t^{1/3} \quad (\text{Eqn. 2.11})$$

where $L_{1,0}$ is the population-based mean ice crystal size (μm), t is time (days), and k is the rate constant, which is temperature dependent. This temperature dependence of recrystallization rate

fits Arrhenius and Williams-Landel-Ferry (WLF) equations (Donhowe and Hartel, 1996a, 1996b; Ben-Yoseph and Hartel, 1998). The Arrhenius equation is:

$$k = Ae^{-E_a/RT} \quad (\text{Eqn. 2.12})$$

and activation energy E_a has been identified between 45109 to 48102 kJ mol⁻¹ (Ndoye and Alvarez, 2014). Recrystallization kinetics using the WLF and the temperature dependence of k can be described as (Slade and Levine, 1988):

$$\log k = \log k_0 + \frac{a(T-T_g)}{b+(T-T_g)} \quad (\text{Eqn. 2.13})$$

where k_0 , a , and b are constants. Cook (2010) studied ice crystal maturation rates in a slush freezer at a bulk temperature of about -2°C and found that there was a linear relationship between ice crystal area and time ^{1/3}. There was also an effect of solids, with formulations containing higher solids having a slower maturation rate. For neutral sorbet base and ice cream, the maturation rate was $7,600 \frac{\mu\text{m}^2}{\text{min}^{1/3}}$ and $1,400 \frac{\mu\text{m}^2}{\text{min}^{1/3}}$, respectively.

2.4.2 Fat Destabilization

Fat destabilization occurs through several mechanisms (Figure 2.12). Ostwald ripening occurs due to differences in particle curvature which results in the growth of larger fat globules at the expense of small ones, due to the increased interfacial pressure associated with smaller particles. Creaming occurs when fat globules diffuse upward in a dispersion due to the enhanced buoyancy of fat relative to water, which is associated with fat's lower density. Aggregation, or flocculation, occurs when particles remain nearer each other much longer than they normally would, due to colloidal interactions including Van der Waals and DLVO theory electrostatic interactions (van Boekel and Walstra, 1981a). Coalescence occurs when the thin film between two fat globules in close proximity ruptures and the two globules combine, which results in a decrease

in free energy due to the reduction in the surface area/volume ratio. While these mechanisms may be relevant in ice cream mix prior to freezing, partial coalescence (also called arrested coalescence) is the main fat destabilization mechanism of interest during the freezing process (Walstra, 2003; Walstra and van Vliet, 2008).

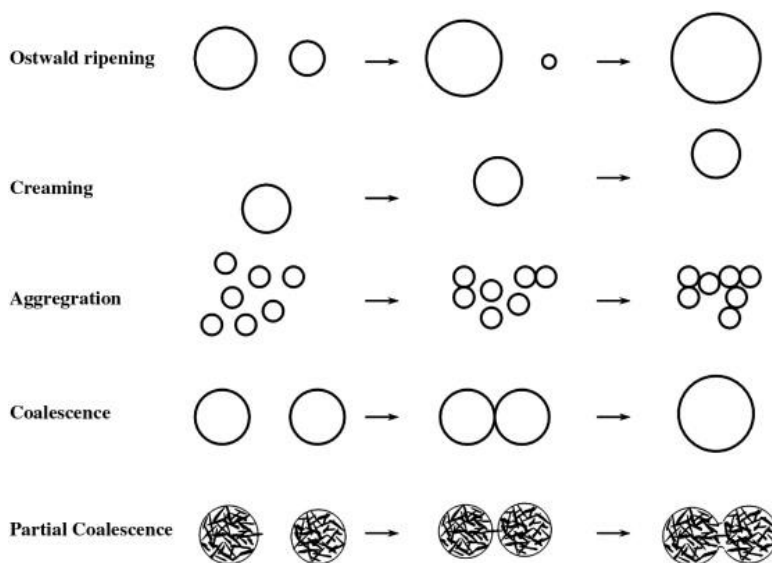


Figure 2.12. Proposed fat destabilization mechanisms circa 2010 (from Fredrick et al., 2010). The mechanism of partial coalescence has not yet been fully elucidated. Studies have demonstrated that crystallized fat protruding from fat globule is not necessary for partial coalescence to occur.

Partial coalescence of fat in ice cream can only occur when there is solid fat within individual fat globules. To understand partial coalescence, adequate knowledge of the changes that fat undergoes during mix processing and aging is required. For the purposes of this review, the following discussion will be specific to dairy milkfat as 10% milkfat is the minimum required fat content for a frozen dessert to be labeled as ice cream (FDA, 1998). It should be noted that other fat sources used in frozen desserts (like palm oil) would behave differently due to differences in their composition. Unhomogenized milkfat is $\sim 0.5\text{-}6\ \mu\text{m}$ in size, but homogenization reduces fat globule to a uniform size of $<2\ \mu\text{m}$ (Gelin et al., 1994). This uniformity is important as larger fat droplets are more susceptible to partial coalescence due to the larger contact area (Fredrick et al.,

2010). Homogenization of fat also creates a relatively stable emulsion. As the fat globule membrane is disrupted and reformed, proteins that adsorb to the newly formed membrane prevent destabilization mechanisms such as Ostwald ripening and creaming through steric repulsion (Goff and Hartel, 2013).

The variety of fatty acids that compose triacylglycerols in milkfat results in a melting range of approximately -40°C to 40°C , meaning that there is liquid fat present during every stage of the ice cream manufacturing process (Adleman and Hartel, 2001). Homogenization of ice cream mix takes place immediately following pasteurization, when the ice cream mix is at $\sim 80^{\circ}\text{C}$ (for HTST pasteurization) so that all fat is liquid and therefore spherical (Goff and Hartel, 2013). After homogenization, ice cream mix is cooled. The onset of milkfat crystallization occurs at $\sim 14.5^{\circ}\text{C}$ (Fredrick et al., 2011). The mechanism for crystallization of milkfat occurs in a similar manner to ice as detailed in the previous section. Nucleation occurs with sufficient undercooling via one of three mechanisms: primary homogeneous nucleation, primary heterogeneous nucleation, and secondary nucleation (Fredrick et al., 2010). In ice cream mix, primary heterogeneous nucleation is most likely to occur due to the presence of catalytic impurities. After cooling, the mix is stored at refrigeration temperatures of $\leq 4^{\circ}\text{C}$ for 4–24 h prior to freezing, a process known as aging (Goff and Hartel, 2013). Aging allows for partial crystallization of fat; that is, the solid fat content (SFC) of the mix increases. While most of the crystallization occurs during the first hour of aging, SFC continues to slowly increase for several hours (Barfod et al., 1991). When fat crystals are initially formed, they can move within the fat globule, and will typically orient at the oil-water interface to lower interfacial tension while being preferentially wetted by the oil phase (Walstra, 2003). However, as mix is cooled and more fat crystals are formed, the crystals will become more immobile due to the van der Waals attraction forces between them, a process that takes several

hours (Boode and Walstra, 1993; Boode et al., 1993). Crystals that form at the interface may protrude from the surface of the fat globule, causing the initially spherical fat globule to become anisometric; however, this has not always been observed to occur upon crystallization. The presence of these crystals, and the distance by which they protrude, is governed by the contact angle at the o/w interface, the size, and the shape of the crystal (Boode and Walstra, 1993). In the case of milkfat, which has a broad fatty acid profile, many small needle-like crystals are formed that can protrude from the fat globule (Moens et al., 2018).

Another purpose of aging that is relevant to fat destabilization in ice cream is the competitive adsorption of emulsifiers and proteins at the oil-water interface, which is a time-dependent process (Chen and Dickinson, 1993). The reduction in fat globule size that occurs because of homogenization causes a dramatic increase in their surface area. Surfactants adsorb to the newly created oil-water interface to create a new milkfat globule membrane. Immediately after homogenization, casein proteins are preferentially absorbed to the interface (Darling and Butcher, 1978; Gelin et al., 1994; Gelin et al., 1996). High protein coverage on fat globules prevents partial coalescence by stearic and electrostatic repulsion (Gelin et al., 1996; Pelan et al., 1997). During aging, the protein gradually desorbs from the interface. This process is accelerated and amplified by the presence of emulsifiers, which competitively displace protein (Goff et al., 1987; Barfod et al., 1991; Chen and Dickinson, 1993), a phenomenon that is positively correlated with emulsifier concentration (Bolliger et al., 2000a). For instance, Goff et al. (1987) found that the use of polysorbate 80 increased fat desorption by 8.1%. Emulsifiers lower the interfacial tension of fat globules, and therefore their adsorption to the oil-water interface is favorable. This results in higher levels of protein desorption and fat crystallization. The removal of some of the stearic repulsion by protein desorption decreases the stability of fat globules during freezing and results in more

agglomeration (Goff et al., 1987; Barfod et al., 1991; Segall and Goff, 2002; Fuller et al., 2015a). Consequently, the more effective an emulsifier is at lowering interfacial tension, the more fat destabilization it will produce (Goff and Jordan, 1989; Thiel, 2020). Formation of fat crystals at the interface may also contribute to displacement of protein from the interface, as this leaves less interfacial space for adsorption of protein (Chen and Dickinson, 1993; Sung and Goff, 2010). However, this does not have as large of an effect on fat stability as the interfacial properties (Pelan et al., 1997).

2.4.2.1 Theoretical Mechanism of Partial Coalescence

The mechanism of partial coalescence (Figure 2.13) has not yet been fully elucidated. Walstra's theory initially proposed that when two partially crystalline fat globules come into contact, a protruding fat crystal can pierce the surfactant coating between the globules. This would allow liquid oil to flow out, forming a 'neck' or 'bridge' between the two crystals, resulting in aggregation. However, recent studies have found that fat crystals that protrude from the fat globule

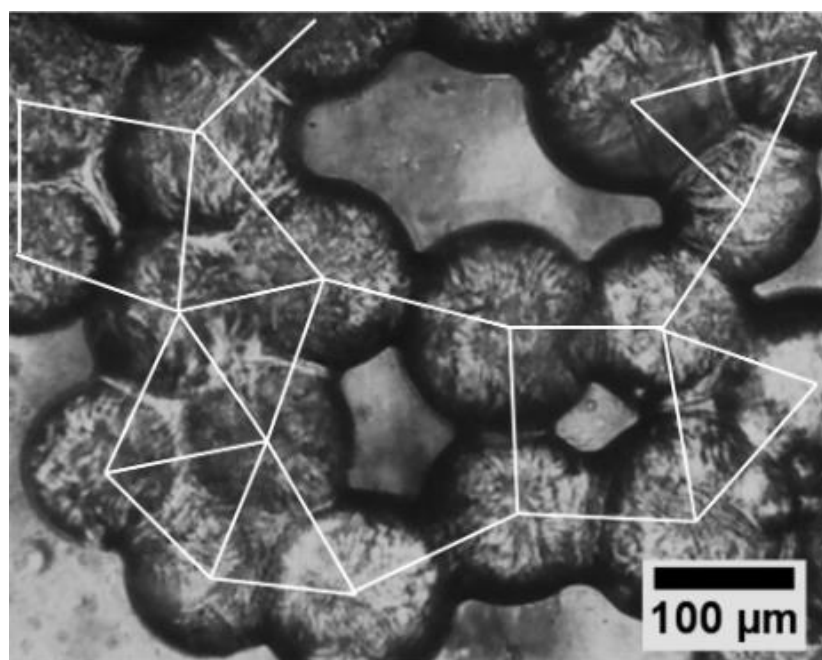


Figure 2.13. Partially-coalesced fat globules (from Dahiya et al., 2017).

may not be necessary for partial coalescence (Pawar et al., 2011; Pawar et al., 2012; Thiel et al., 2016; Thiel, 2020). These studies have observed that fat globules that lack protruding crystals can still partially coalesce, and therefore an energy balance model for partial coalescence has been put forward (Pawar et al., 2012). This model states that the degree of partial coalescence can be predicted by determining the degree of strain that two droplets must undergo to create a thermodynamically favorable system by minimizing the interfacial tension. The interfacial tension γ of a single fat globule is driven by Laplace pressure Δp , (or pressure differential between in internal and external interface), described in the Young-Laplace equation as:

$$\Delta p = \frac{2\gamma}{R} \quad (\text{Eqn. 2.14})$$

where R is the radius of the sphere. Laplace pressure drives a fat globule towards a spherical shape unless an external force is applied to deform it. The interfacial energy $E_{\text{interfacial}}$ (Eqn. 2.15) and elastic energy E_{elastic} stored in within the fat globule (Eqn. 2.16) are calculated as:

$$E_{\text{interfacial}} = A\gamma \quad (\text{Eqn. 2.15})$$

where A is the total interfacial area of the two droplets, and:

$$E_{\text{elastic}} = \frac{3}{2} G' \varepsilon^2 V \quad (\text{Eqn. 2.16})$$

where G' is the Young's modulus and V is the total volume of the coalescing droplets. The degree of force, or strain (ε), needed to achieve the minimum energy state for two coalescing droplets can be found by combining these two equations:

$$\gamma = \frac{A_2}{A_1} \exp\left(\frac{\varepsilon_{\text{min}}}{A_2}\right) G' R \varepsilon_{\text{min}} \quad (\text{Eqn. 2.17})$$

where $A_2=0.19$ and $A_1=0.23$ are empirically derived values and R is the radius of the droplet (Pawar et al., 2012). The A values are a function of the exponentially decaying interfacial area with strain and represent the non-spherical shapes that coalescing fat globules must progress through before reaching a final spherical shape. A_1 indicates the shape of coalescing globules,

which continue to hold their individual identity after merging, and A_2 indicates an elongated sphere shape (Pawar et al., 2012). This equation indicates that the degree of partial coalescence is a result of the balance of the interfacial driving force and the elastic reaction force, and the value of ϵ_{\min} is an indicator of the degree of coalescence. By plotting interfacial energy and elastic energy (Figure 2.14), we can identify that total stability (no coalescence) results when $\epsilon_{\min} = 0$, total coalescence results when $\epsilon_{\min} = 0.37$, and stable partially-coalesced states occur when ϵ_{\min} falls between those two values (Pawar et al., 2012).

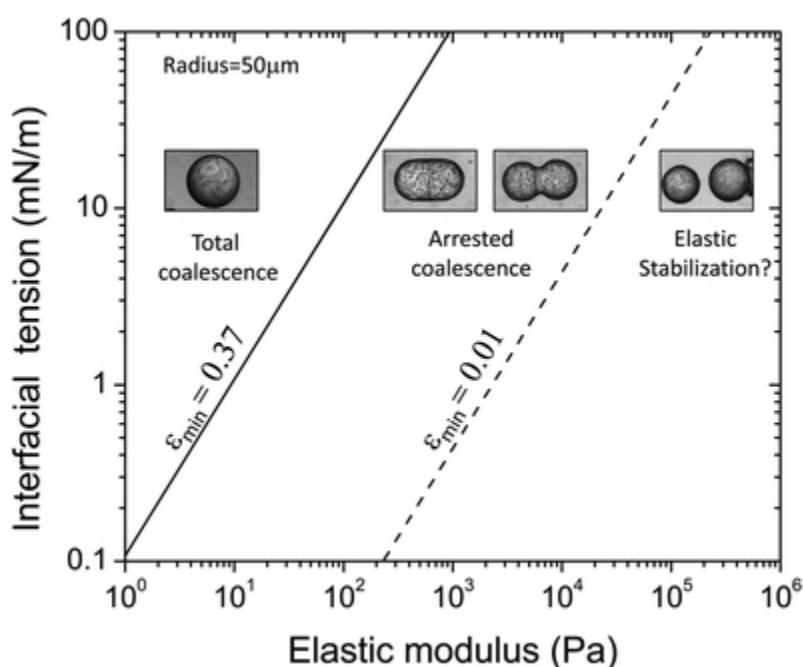


Figure 2.14. Coalescence behavior based on the energy balance model, where the degree of partial coalescence, or strain (ϵ) is based on balance of elastic modulus energy and interfacial energy (From Pawar et al., 2012).

2.4.2.2 Effect of Processing Parameters on Partial Coalescence

Regardless of the exact mechanism of partial coalescence, there are several processing factors that have been demonstrated to modulate the extent of partial coalescence in ice cream, including crystallization rate of fat, solid fat content, presence of emulsifiers, and amount of shear applied during freezing. Cooling rates affect crystallization of milkfat, with slower cooling rates

allowing high and low melting point triacylglycerols (TAGs) to crystallize separately (Ergun, 2011). At fast cooling rates, low melting point TAGs may be incorporated into the solid fat and result in less ordered crystal structure (Herrera and Hartel, 2000) and a higher solid fat content (Campos et al., 2002; Ergun, 2011). Rapid cooling also results in small crystals, whereas slower cooling creates larger crystals that grow into each other (Ergun, 2011). Rapid formation of crystals and SFC is therefore expected to increase rate and extent of network formation between crystal aggregates (Campos et al., 2002). Faster cooling rates result in a lower temperature of fat crystallization onset (Fredrick et al., 2011). This is related to the polymorphs in which the fat crystals exist. During rapid cooling, the α -polymorph is directly formed (i.e., many small nuclei), then α -polymorphs are transformed into the more stable β' polymorph at the expense of α -crystals, resulting in many small crystals and a high volume fraction of crystals in the network (Herrera and Hartel, 2000; Campos et al., 2002, Fredrick et al., 2011). At slow cooling, β' crystals can be formed because the sample will be at the temperature for induction of these crystals for a longer amount of time. The crystals will form larger aggregates with lower volume fraction composed of crystals (Campos et al., 2002). As such, slow crystallization results in softer fat system (Campos et al., 2002) due to less SFC being formed.

Generally, increasing the SFC causes earlier arrest of coalescence. Higher SFC results in higher elastic moduli and thus lower strain between fat globules (Thiel et al., 2016). Therefore, increasing the SFC results in a space-filling network of fat globules that displays resistance to restructuring (i.e., compression) after partially coalescing (Dahiya et al., 2017; Moens et al., 2018). This results in a bimodal distribution of fat globule sizes, resulting from both individual fat globules and fat aggregates (Sung and Goff, 2010). However, too much SFC (\geq approx. 60%) suppresses aggregation (Sung and Goff, 2010; Méndez-Velasco and Goff, 2012). The high SFC

results in a thicker ‘shell’ of solid fat on the outside of the fat globule, thus reducing the ability of the fat globule to destabilize as fat globules will bounce off each other upon collision (Hinrichs and Kessler, 1997; Méndez-Velasco and Goff, 2012). This may also be related to an increase in the elastic modulus with increasing SFC, which causes the strain between globules to decrease (Thiel et al., 2016). High SFC also thus limits the amount of oil available to form a bridge between two fat globules (Boode et al., 1993).

Shear is a necessary factor for partial coalescence to occur, as quiescently frozen ice cream exhibits no partial coalescence (Goff and Jordan, 1989). Aggregation increases over time at a given shear rate (Segall and Goff, 2002; Fuller et al. 2015a). The rate of partial coalescence is dependent on collision rate and collision efficiency (i.e., how many collisions result in partial coalescence). Increasing the shear rate increases the collision rate, but decreases the collision efficiency (Vanapalli and Coupland, 2001). The decrease in collision efficiency is likely due to a decrease in the duration of the collisions, which decreases the amount of time for an oil bridge to form between two fat globules (van Boekel and Walstra, 1981b; Boode et al., 1993). Still, Fuller et al. (2015b) found that increasing shear rate increased partial coalescence. Turbulent flow is more effective than shear (Couette) flow at destabilizing fat (van Boekel and Walstra, 1981b).

2.4.3 Aeration/Foaming

Ice cream is a frozen foam, meaning it contains a dispersion of air bubbles. During batch freezing, atmospheric air is incorporated through whipping action of the dasher. In a continuous SSF, air is introduced through gas injection under pressure. A foam is then generated by mechanical dispersion of the gas (Rohenkohl and Kohlus, 1999). The rheology and stability of the foam changes with bubble size, with smaller bubbles leading to a more viscous and stable foam.

Bubble size is primarily determined by shear stresses (Kroezen and Wassink, 1987). Air can help prevent melting in ice cream due to an insulating effect, as ice cream with higher overrun has a lower thermal conductivity (Cogné et al., 2003; Sofjan and Hartel, 2004).

2.4.3.1 Effect of Shear on Air Incorporation and Size Reduction

In ice cream, significant foam cannot be generated without the freezing of ice, even in a SSF that provides shear by mixing action of the dasher but no cooling. This is seemingly related to an increase in viscosity of the ice cream mix when ice is frozen and the serum phase is freeze concentrated. The increase in viscosity decreases the air cell size, as more shear stress is applied to the air bubbles (Chang and Hartel, 2002a; Silva et al., 2008; Eisner et al., 2005). The idea that shear is the main driver of air incorporation is also supported by the fact that when air is incorporated prior to freezing (i.e., pre-aeration), there is no effect on air cell size distributions (Rohenkohl and Kohlus, 1999). When air enters the freezer, it is present in large air cells that are broken down as freezing continues, also allowing for an increase in overrun (Adleman and Hartel, 2001).

In a continuous SSF, shear is generated by the mixing action of the dasher and the fluid flow through the freezing cylinder. The Weber number We describes the balance of forces between effect of shear/fluid flow and the Laplace pressure of the air bubbles by the ratio of turbulent to surface tension forces:

$$We = \frac{\dot{\gamma} d \mu}{\sigma} \quad (\text{Eqn. 2.18})$$

where $\dot{\gamma}$ is shear rate of fluid flow, d is the size of the bubble, μ is the viscosity of the fluid phase, and σ is the interfacial tension at the bubble surface. Shearing the bubble will initially result in

deformation, which enlarges the air interface (Figure 2.15) and changes the interfacial tension locally along the interface (Janssen et al., 1994).

The critical Weber number We_c determines the maximum possible air bubble size (also called the Hinze scale). In the turbulent flow regime:

$$We_c = \frac{\tau d_{\max}}{\sigma} \quad (\text{Eqn. 2.19})$$

where d_{\max} is the largest stable bubble size and τ is the shear stress. If the Weber number achieved in the freezer is higher than the critical Weber number, it will lead to deformation and bubble splitting (Hinze, 1955; Rumscheidt and Mason, 1961; Janssen et al., 1994), whereas in conditions below the critical Weber number, air bubbles will remain stable.

There are two prevailing theories for the mechanism of bubble break up in turbulent flow (Figure 2.16). The first is the action of a single strong eddy causing large deformation and bubble break up (Martínez-Bazán et al., 2010; Perrard et al., 2021). In this mechanism, some of the ‘child’ bubbles will be highly deformed upon splitting and will not recover a spherical shape.

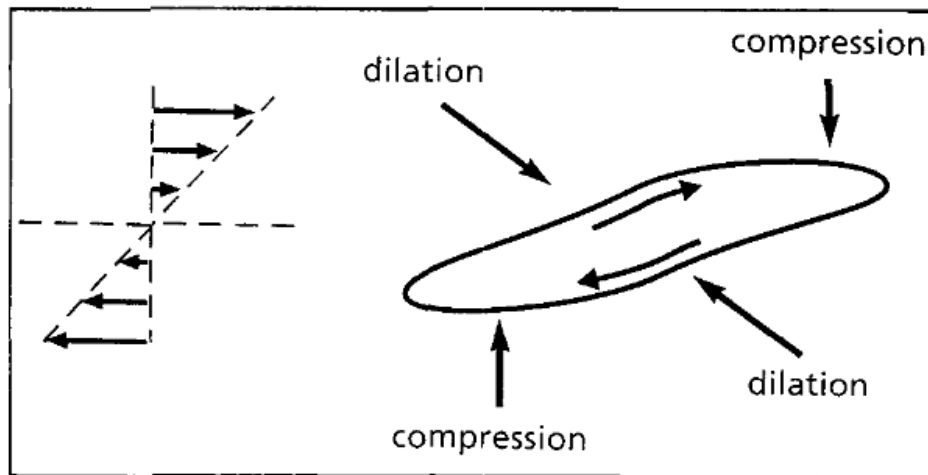
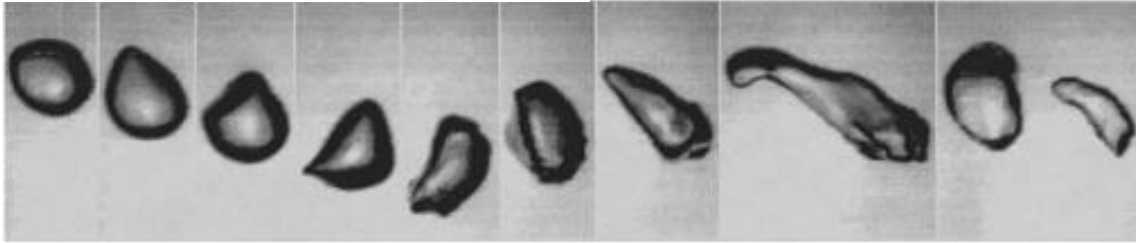


Figure 2.15. Example of bubble deformation in shear flow. From Janssen et al., 1994.

Bubble breakup at low Weber number



Bubble breakup at high Weber number

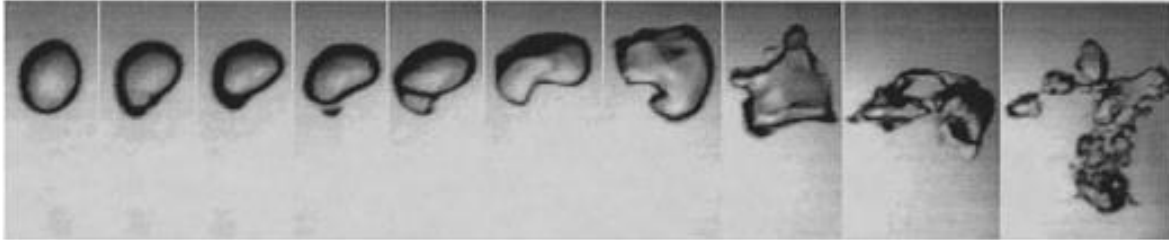


Figure 2.16. Mechanisms of bubble break up in turbulent flow. From Risso and Fabre (1998).

The instability causes the child bubbles to quickly break into numerous tiny bubbles (Rivière et al., 2021). Under this theory, if turbulence is the only cause of deformation, the critical Weber number should be about 5 (Risso and Fabre, 1998; Martínez-Bazán et al., 2010). However, several studies have demonstrated that in turbulent flow, the critical Weber number can be approximately 0.25 – 1.3 (Hinze, 1955; Sevik and Park, 1973; Kroezen and Wassink, 1987). The second proposed mechanism accounts for the time evolution of deformation of the air bubble, in that oscillation of bubbles caused by smaller eddies and the amount of time the bubble spends in turbulent flow eventually lead to bubble break-up (Risso and Fabre, 1998; Rivière et al., 2021). There is evidence that both mechanisms contribute to air bubble breakdown in turbulent flow (Perrard et al., 2021; Rivière et al., 2021).

2.4.3.2 Stabilization of Air by Fat Structures

In whipped cream, when air is initially incorporated, there is a high surface tension at the air-water interface and protein (primarily β -casein) is adsorbed (Brooker et al., 1986; Goff et al., 1999). Due to the disruption of the milkfat globule membrane during whipping, proteins may also adsorb to fat globules. This allows the fat-water interface and air-water interfaces to coalesce, thus creating a continuous interface between air cells and fat globules. (Brooker et al., 1986). Fat may then be in direct contact with air, though the protrusion of fat into air cells appears rare (Brooker et al., 1986; Goff et al., 1999). The adsorption of fat to air is increased in the presence of emulsifiers, as proteins are displaced from the surface of fat globules (Pelan et al., 1997; Goff et al., 1999; Bolliger et al., 2000a).

The effect of increasing air content on decreasing thermal conductivity does not solely account for stability of air in ice cream (Muse and Hartel, 2004). Air cells in ice cream are stabilized in part by partially-coalesced fat globules (Brooker et al., 1986; Chang and Hartel, 2002a). Partially-coalesced fat aggregates adsorb to air interfaces, more so than individual fat globules (Goff et al., 1999). Larger fat aggregates result in slower meltdown and higher shape retention properties, as they become too large to drain through the foam lamellae thus preventing collapse of air cells (Pelan et al., 1997; Bolliger et al., 2000a; Koxholt et al., 2000). Additionally, the presence of the fat networks structurally decreases the rate of air cell destabilization by coalescence and disproportionation (Chang and Hartel, 2002b; Sofjan and Hartel, 2004).

2.5 RESIDENCE TIME DISTRIBUTION IN SCRAPED SURFACE FREEZERS

Residence time distribution (RTD) describes the flow behavior in reactors. Specifically, RTD is the probability distribution of the time a particle is likely to spend in a process. This section details how real world, non-ideal reactors differ from ideal models of flow, and how this non-ideality can be quantified to derive the RTD.

2.5.1 Ideal Plug Flow

As a continuous SSF is a tubular reactor, a plug flow model may be applied to estimate residence time. Plug flow assumes that the fluid travels in an infinitely small ‘plug’ with no axial mixing (that is, no interaction with other plugs) and has infinitely rapid radial mixing (i.e., uniform temperature, composition, and pressure). In plug flow reactors, all plugs take the same amount of time to travel from the inlet of the reactor to the outlet. The residence time \bar{t} of a plug flow reactor can be easily calculated:

$$\bar{t} = \int_0^{V_R} \frac{dV_r}{\vartheta} \quad (\text{Eqn. 2.20})$$

where ϑ is volumetric flow rate and V_r is the volume physically occupied by the working fluid (Hill, 1977). While this provides an estimation of the transport of fluid through the SSF, real-world conditions are not so simple.

2.5.2 Deviations from Ideal Flow

Flow in real-world reactors exhibit various behaviors of non-ideal flow. These may include axial dispersion (i.e., back-mixing), dead zones, and channeling, all of which have been demonstrated in SSFs. This causes the fluid elements to take different lengths of time to pass through the reactor. That is, there is a RTD rather than a single residence time for all particles as

with plug flow. While computational fluid dynamics has made predicting RTDs possible, these models still need to be validated by experimental methods to determine RTD. RTD has also been demonstrated to have an impact on the microstructural properties of frozen desserts (detailed in section 2.6), which makes it important to characterize and optimize.

2.5.3 Experimental Determination of RTD

To experimentally determine RTD for a system, one must use the stimulus-response technique developed by Danckwerts (1953). Stimuli, or tracers, are non-reactive components that are added to the system and whose concentration can be quantified (e.g., by absorbance, electrical conductivity, fluorescence). The two most common stimulus techniques are the step function and the pulse injection. In a step function, the feed of the tank is switched from one concentration of tracer to another. In an ideal plug flow system, this type of stimulus would result in the tracer concentration instantaneously changing from the original concentration of the feed to the concentration of the step feed (Figure 2.17a).

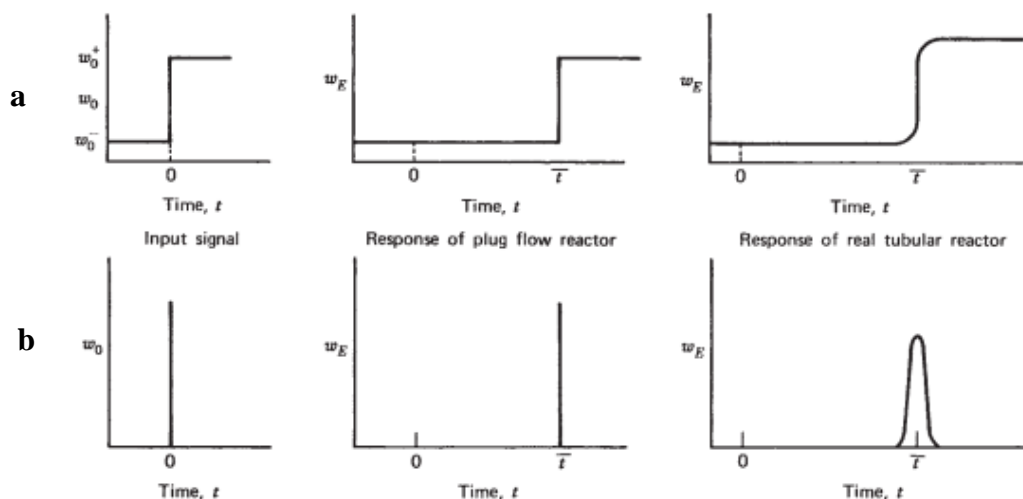


Figure 2.17. Stimulus-response input, ideal response, and real response for tubular reactors using the (a) step function or (b) pulse injection techniques. w_0 and w_E indicate the weight concentration of tracer in the inlet and effluent streams, respectively. (From Hill, 1977)

However, due to nonideality of flow, the effluent flow of tracer concentration is sigmoidal in shape. The pulse injection technique involves injecting a small volume of tracer into the feed stream in the shortest amount of time possible. In ideal plug flow, all of the tracer would be recovered from the effluent stream at the same time. Nonideality results in the response being distorted with the concentration of tracer coming out over time (Figure 2.17b).

The concentration of tracer detected in the effluent stream over time can be used to determine the RTD function $E(t)$, which can be used to describe how a system deviates from ideal flow:

$$E(t) = \frac{c_{out}(t)}{\int_0^{\infty} c_{out}(t) dt} \quad (\text{Eqn. 2.21})$$

where $E(t)$ is the volume fraction of fluid at the outlet that has remained in the system for a time less than t , and c_{out} is the outlet concentration of tracer (Danckwerts, 1953). When $E(t)$ is plotted against time, the resulting curve is called the E-curve. The E-curve is normalized, which implies that the area curve is equal to 1 and that comparisons can be made between experimental data independent of the average residence time and the initial concentration of tracer dye (Russell et al., 1997). The RTD function can also be described as the cumulative function $F(t)$:

$$F(t) = \int_0^t E(t) dt \quad (\text{Eqn. 2.22})$$

where $F(t)$ is the probability that a fluid element entering the reactor at time zero has left by time t .

The E-curve not only allows for visualization of system non-ideality, but also allows for complete quantitative characterization of the RTD. This is done by taking the first three moments of the $E(t)$ distribution. The first moment is the average residence time \bar{t} :

$$\bar{t} = \int_0^{\infty} t \cdot E(t) dt \quad (\text{Eqn. 2.23})$$

The second moment characterizes the variance σ^2 :

$$\sigma^2 = \int_0^{\infty} (t - \bar{t})^2 E(t) dt \quad (\text{Eqn. 2.24})$$

where σ^2 is the square of the standard deviation and describes the spread of the distribution.

Finally, the third moment characterizes the skewness s^3 :

$$s^3 = \frac{1}{\sigma^{3/2}} \int_0^{\infty} (t - \bar{t})^3 E(t) dt \quad (\text{Eqn. 2.25})$$

where s^3 describes the extent to which the distribution is skewed in one direction or another relative to the mean (Fogler, 2016).

2.6 EFFECTS OF FREEZER CONDITIONS ON FROZEN DESSERT MANUFACTURE

This section details how freezer parameters affect the RTD and microstructural properties (ice crystal size, air cell size, and % fat destabilization) of frozen desserts. The effects on microstructural attributes are summarized in Table 2.1.

Table 2.1. Effect of scraped surface freezer parameters on microstructure of frozen desserts.

Freezing Parameter	Ice Crystal Size	Air Cell Size	Fat Globule
↑ Throughput Rate	↓ (6, 7, 13, 14, 20) N (16)	N (5, 14)	↓ (5) N (14)
↑ Draw Temperature	↑ (5, 7, 13, 14, 15, 16, 17)	↑ (5, 8, 9, 11, 14, 17)	↓ (1, 2, 3, 5, 11, 14)
↑ Overrun	↓ (4, 9, 10, 14) N (17, 18)	↑ (8, 14) ↓ (10, 17, 18)	↑ (2, 3, 14, 18)
↑ Dasher Speed	↑ (5, 6, 13) ↓ (14, 15, 16) N (7, 12, 18, 20)	↓ (5, 14, 18, 19)	↑ (2, 5, 14, 18)
Dasher Design	N (6, 20)	No research available	↑ Displacement = ↑ Destabilization (2)

N = No significant effect. References: ¹ Berger & White, 1971; ² Kokubo et al., 1996; ³ Kokubo et al., 1998; ⁴ Flores & Goff, 1999b; ⁵ Rohenkohl & Kohlus, 1999; ⁶ Russell et al., 1999; ⁷ Koxholt et al., 2000; ⁸ Chang & Hartel, 2002a; ⁹ Caillet et al., 2003; ¹⁰ Sofjan & Hartel, 2004; ¹¹ Eisner et al., 2005; ¹² Rajesh Potineni et al., 2006; ¹³ Drewett & Hartel, 2007; ¹⁴ Inoue et al., 2008; ¹⁵ Haddad Amamou et al., 2010; ¹⁶ Arellano et al., 2012; ¹⁷ Hernández-Parra et al., 2018a; ¹⁸ Warren & Hartel, 2018; ¹⁹ Masuda et al., 2020; ²⁰ Helbig, 2021

2.6.1 Residence Time Distribution

While tubular heat exchangers have been studied extensively, studying the RTD of SSFs presents a special case as phase changes and increasing viscosity affect the way the product flows through the freezer. Additionally, most changeable processing parameters will also alter RTD. While residence time has previously been characterized in SSFs (Table 2.2), it should be noted that previous studies have focused on pilot-scale freezers.

Table 2.2. Previous studies on residence time distribution in SSFs used to make frozen desserts.

Reference	Material Studied	Cylinder Diameter (m)	Cylinder Length (m)	Dasher Geometry (% Displacement)	Dasher Diameter (m)	Dasher Speed range (RPM)
Russell et al., 1997	Carbopol, Ice cream	0.203	0.746	Open (15%) Solid (80%)	0.166 m 0.178 m	20 - 250
Arellano et al., 2013a	Non-aerated Sorbet	0.05	0.40	Solid (46%)	0.046	545 - 1000
Fayolle et al., 2013	Ice Cream	0.05	0.40	Solid (40%)	unknown	330 - 500
Ndoye et al., 2018	Aerated Sorbet	0.05	0.4	Solid (46%)	0.046	496

2.6.1.1 Throughput Rate

As is intuitive, studies have indicated that an increased throughput rate results in a narrower RTD curve, as well as a shorter residence time (Arellano et al., 2013a; Fayolle et al., 2013; Ndoye et al., 2018). Arellano et al. (2013a) attribute the reduced spread in RTD to reduced axial dispersion. However, it should be noted that in this study, refrigerant temperature was controlled rather than the product draw temperature. Therefore, as throughput rate increased the draw temperature also increased as the product received less cooling. Warmer draw temperatures are associated with decreased product viscosity, which increases the efficiency of radial mixing, another factor that would result in a narrower RTD curve.

2.6.1.2 Dasher Geometry

Only one study has characterized how dasher geometry affects RTD for both a 0.4% Carbopol model system as well as an 8% dairy fat ice cream frozen to -5°C with 50% overrun (Russell et al., 1997). This study found that an open dasher (15% displacement) had a broader RTD compared to a solid dasher (80% displacement). It should be noted that these dasher geometries had differing numbers of blades: (open=4, solid=3). The authors replaced standard blades on the solid dasher (80% displacement) with blades containing holes and found that the RTD was narrowed for both Carbopol and ice cream systems (Figure 2.18), indicating that axial dispersion was reduced. That is, fluid was not forced into the gaps between the blades but rather was able to flow through the holes at the wall, and therefore back-mixing was reduced. Similarly, the authors studied the RTD of the Carbopol system using the solid dasher (80% displacement) without blades and found that the RTD curve had a tail to the right, indicating that material at the wall was likely in the system longer due to a high viscosity without the shear of the blade to remove it (Russell et al., 1997).

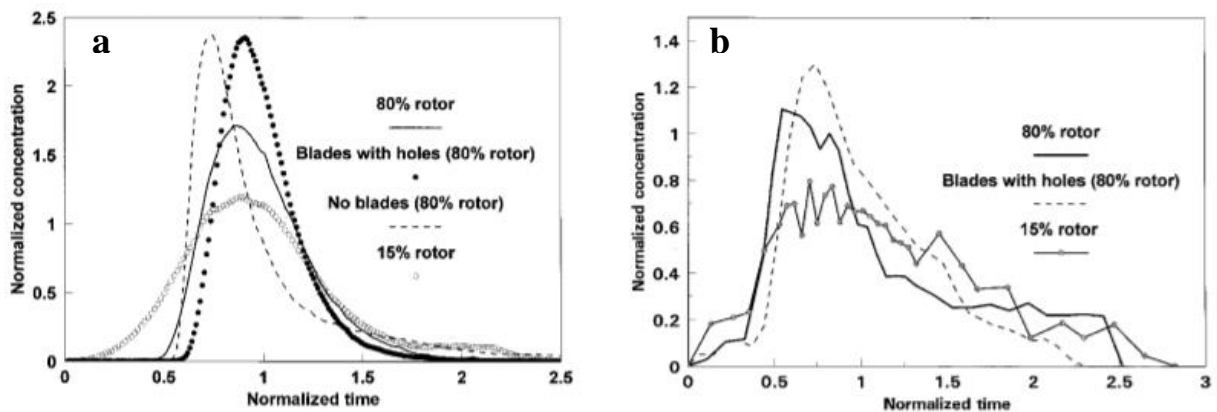


Figure 2.18. Effect of rotor type on RTD for (a) a 0.4% Carbopol system and (b) ice cream made using a scraped surface freezer. Throughput rate was 0.111 kg/s and rotor/dasher speed was 250 RPM. For ice cream, product was frozen to -5°C , but Carbopol system was not cooled. (From Russell et al., 1997).

2.6.1.3 Dasher Speed

Several studies have characterized the effect of dasher speed on RTD in SSFs, although the observed effect has varied (Russell et al., 1997; Lakhdar et al., 2005; Arellano et al., 2013a; Fayolle et al., 2013). Russell et al. (1997) and Fayolle et al. (2013) studied dasher speeds of 20-250 RPM and 240-420 RPM respectively and observed that increasing dasher speed resulted in reduced spread of the RTD, as well as a shorter mean residence time. By contrast, Arellano et al. (2013a) observed no effect of dasher speed on RTD, although the dasher speeds studied in this experiment were significantly higher at 545-1000 RPM. Lakhdar et al. (2005) found that increased dasher speed reduced internal heat transfer resistance, which became noticeable below ~500 RPM, which may explain why effects were only seen in experiments studying dasher speeds below that level.

2.6.1.4 Draw / Refrigerant Temperature

Arellano et al. (2013a) examined the RTD for unaerated sorbet frozen with a refrigerant temperature of -10.6°C, -15.3°C, and -20.1°C. Draw temperature was not controlled but decreased with refrigerant temperature. When refrigerant temperature reached -20.1°C, a widening of the RTD curve with a significantly longer tail was observed. This was attributed to increased axial dispersion caused by an increase in the radial temperature gradient from the freezer wall to the center of the freezing cylinder. This would lead to the product at the wall having a significantly higher viscosity than the product in the center of the barrel. Similarly, Ndoye et al. (2018) studied the effect of refrigerant temperature at -9.9°C, -11.7°C, and -15.8°C on RTD of aerated sorbet. Unlike the Arellano et al. (2013a) study, this study found that minimum and average residence time were reduced with decreasing refrigerant temperature, while the spread of the RTD was

increased. This related to an increase in apparent viscosity in the system, as the final draw temperature decreased with decreasing coolant temperature. While both of the aforementioned studies were carried out on the same freezer, the mix flow rate and dasher rotational speed differed between studies. Therefore, a conclusion cannot be directly drawn, but it may suggest that the insulating effect of air or its effect on viscosity play a role in the size of the effect observed in Ndyoe et al. (2018).

2.6.2 Ice Crystal Size

2.6.2.1 Residence Time / Throughput Rate

Most studies have found that a faster throughput rate (also corresponding with a shorter residence time) results in smaller average ice crystal size (Russell et al., 1999; Koxholt et al., 2000; Drewett and Hartel, 2007; Inoue et al., 2008; Helbig, 2021). When draw temperature is controlled for, a faster cooling rate is required when throughput rate is increased. This is achieved by decreasing the refrigerant temperature. Although decreasing coolant temperature does decrease ice crystal size through enhanced nucleation, Russell et al. (1999) found that average residence time had larger effect on ice crystal size than nucleation rate. This suggests that rapid recrystallization can happen in the freezing barrel, and therefore increasing throughput rate decreases the amount of time the product can recrystallize. Drewett and Hartel (2007) found that of the parameters tested, including draw temperature and dasher speed, that residence time had the most pronounced effect on ice crystal size. Inoue et al. (2008) used response surface methodology to study processing parameters on microstructural components and found that throughput rate had the second most pronounced effect on ice crystal size, with other parameters tested being draw temperature, overrun, cylinder pressure, and dasher speed.

Arellano et al. (2012) found that there was no significant effect of throughput rate on ice crystal size; however, increasing the throughput rate increased the ice mass fraction. It is important to note that focused beam reflectance measurement (FBRM) methodology was used to determine ice crystal size in this study, whereas microscopy methods were used for the other studies. FBRM would not be suitable to measure ice crystal size in aerated products as air cells may also be detected; however, Arellano et al. (2012) studied unaerated sorbet. FBRM measures chord length and does not directly measure particle size, and therefore a conversion is needed to obtain particle size data from FBRM measurements (Wynn, 2003). Chord length can also be influenced by including the optical properties and shape of the particle being measured, especially for small particles where backscattering may influence measurements (Li et al., 2005). FBRM tends to overestimate the number of small particles (Li et al., 2005; Greaves et al., 2008), which is also what was concluded in the Arellano et al. (2012) study as the range of ice crystal size in their study was 6-12 μm , a range that is significantly smaller and narrower than the aforementioned studies. This may be why an effect of throughput rate on ice crystal size was not observed.

2.6.2.2 Draw / Refrigerant Temperature

Lower SSF draw temperatures result in smaller ice crystals (Rohenkohl and Kohlus, 1999; Koxholt et al., 2000; Drewett and Hartel, 2007; Inoue et al., 2008) as do lower refrigerant temperatures (Haddad Amamou et al., 2010; Arellano et al., 2012; Hernández-Parra et al., 2018a). Of the effects they studied, Inoue et al. (2008) found that draw temperature had the largest effect on ice crystal size and that this effect was especially pronounced at draw temperatures above -5°C . At a given throughput rate, a lower coolant temperature is needed to reach a lower draw temperature, which increases nucleation due to more dramatic supercooling (Drewett and Hartel,

2007; Arellano et al., 2012). In fact, Haddad Amamou et al. (2010) and Hernández-Parra et al. (2018a) found that at lower refrigerant temperatures ($< -15^{\circ}\text{C}$), nucleation is the main mechanism governing ice crystal size. Recrystallization/growth occurs more slowly when draw temperature is decreased due to increased product viscosity, which makes water diffusion occur more slowly.

2.6.2.3 Overrun

The majority of studies have found that as overrun increases, ice crystal size decreases (Flores and Goff, 1999b; Caillet et al., 2003; Sofjan and Hartel, 2004; Inoue et al., 2008), though this relationship may also be temperature dependent (Sofjan and Hartel, 2004; Hernández-Parra et al., 2018a). Overrun had no significant effect on ice crystal size in Warren and Hartel (2018). The general reduction in ice crystal size with increased overrun is attributed to changes in heat transfer rates, as well as air acting as a physical barrier that prevents ice crystals from colliding or recrystallizing (Flores and Goff, 1999b; Inoue et al., 2008).

2.6.2.4 Dasher Speed

The effect of dasher speed on ice crystal size is uncertain. Some studies have found that increasing dasher speed decreases ice crystal size (Inoue et al., 2008; Haddad Amamou et al., 2010; Arellano et al., 2012). Haddad Ammamou et al. (2010) observed this effect once ice concentration reached 20.4%, citing increased attrition as the cause for lower crystal size, which would be a result of increased shear. Arellano et al. (2012) also suggested that the increased frequency of blades scraping along the wall results in smaller ice flocs being detached from the freezer barrel wall. Additionally, Lakhdar et al. (2005) found that increasing dasher speed lowers heat transfer resistance at the wall, allowing for more cooling of the product between scrapes. Other studies

have observed the opposite effect, in which increasing dasher speed increases ice crystal size (Rohenkohl and Kohlus, 1999; Russell et al., 1999; Drewett and Hartel, 2007). This has been attributed to increased frictional heat generated at the higher shear rates of increased dasher speed, which could lead to increased recrystallization rates (Russell et al., 1999). The effect observed by Drewett and Hartel (2007) was small, but the draw temperature was also decreased with increasing dasher speed, which may have offset the effect slightly. Still others have found that dasher speed has no impact on ice crystal size (Koxholt et al., 2000; Rajesh Potineni et al., 2006; Warren and Hartel, 2018; Helbig, 2021).

2.6.2.5 Dasher Assembly Design

There are very few studies that have investigated the effect of dasher design on ice cream structure. Russell et al. (1999) found that dasher type had no significant impact on ice crystals when comparing ice cream made using 30% and 80% displacement dashers at a constant average residence time. The study concluded that the main effect of dasher design is on the modulation of residence time. Therefore, at a constant throughput rate the dasher design could theoretically influence ice crystal size indirectly. Helbig (2021) found that dasher design did not have an influence on ice crystal size in sorbet while testing five dashers with displacements ranging from 26-64% and with varying geometries.

2.6.3 Air Cell Size Distribution

2.6.3.1 Residence Time / Throughput Rate

Inoue et al. (2008) found that increasing mix flow rate also increased air cell size, although this effect was small. When variables with no predictive ability were removed from the complete

model estimating the effects of processing parameters on air cell size, the pruned model found that mix flow rate did not have a significant effect on air cell size. Likewise, Rohenkohl and Kohlus (1999) found no significant effect of mass flow rate on air cell size. Kroezen and Wassink (1987) found that bubble size distribution reaches an equilibrium within seconds, and therefore concluded that residence time was not a key parameter for bubble size distribution for a foam generated in a rotor mixer.

2.6.3.2 Draw / Refrigerant Temperature

Freezing is necessary for incorporation of air into frozen desserts, as ice cream that is only whipped and not frozen contains minimal overrun and only large air cells (Rohenkohl and Kohlus, 1999; Chang and Hartel, 2002a; Caillet et al., 2003). Chang and Hartel (2002a) studied development of air cells in a batch freezer and found that when freezing was only applied during the first half of total processing time (final draw temperature approximately -4°C), overrun development continued, whereas overrun dropped when freezing was applied continuously (final draw temperature approximately -7°C) during the process. This study found that the final mean air cell size was smaller at the lower temperature, while simultaneously viscosity increased as draw temperature decreased. This suggests that the increase in viscosity built by the formation of ice results in higher shear, resulting in disruption of air cells (Rohenkohl and Kohlus, 1999; Chang and Hartel, 2002a). This correlation between draw temperature and air cell size has also been observed in freezing of ice cream in continuous freezers (Rohenkohl and Kohlus, 1999; Caillet et al., 2003; Inoue et al., 2008) and low temperature extruders (Eisner et al., 2005), as well as in the freezing of aerated sorbet (Hernández-Parra et al., 2018a). Inoue et al. (2008) found that draw temperature had the largest impact on air cell size of all processing parameters studied. The

increased fat destabilization that also occurs at lower draw temperatures also stabilizes the air cells (Rohenkohl and Kohlus, 1999).

2.6.3.3 Overrun

The effects of overrun on air cell size are unclear. Some studies have found that increasing overrun increases air cell size in ice cream (Chang and Hartel, 2002a; Inoue et al., 2008). Inoue et al. (2008) found that overrun was the second most important processing factor, behind draw temperature, in the determination of air cell size. Similarly, Chang and Hartel (2002) found that overrun development was greater when freezing was only applied during the first half of total processing time (~150% OR) compared to overrun development in product that was frozen during the entire processing time (~75% OR). Even though the sample frozen for half the time had a higher overrun, the air cell size was larger than in the sample frozen for the full time, supporting that draw temperature is dominant over overrun in regulating air cell size.

Contrarily, other studies have found that increasing overrun results in decreased air cell size in ice cream (Sofjan and Hartel, 2004; Warren and Hartel, 2018) and sorbet (Hernández-Parra et al., 2018a). Hernández-Parra et al. (2018a) only observed a decrease in air cell size in sorbet at a draw temperature of -10°C , and only when air flow rate was increased from 0-0.019 kg/h to 0.03 kg/h. Otherwise, there was no significant effect of overrun on air cell size at -10°C from 0-0.019 kg/h, or at any air flow rate at -15°C . A decrease in air cell size with increasing overrun may be due to an increase in product viscosity with increasing overrun (Goff et al., 1995, Sofjan and Hartel, 2004). An increase in overrun also led to increased partial coalescence of fat in the presence of emulsifiers, which can stabilize small air cells (Goff and Jordan, 1989; Warren, 2015). Ndoye et al. (2018) suggested that the presence of stagnant air in a continuous freezer, which increases

with increased air flow rate, reduces the amount of volume available for the liquid phase. This would increase the shear in the liquid phase, leading to enhanced air cell breakdown.

2.6.3.4 Dasher Speed

An increase in dasher speed has been found to decrease air cell size (Rohenkohl and Kohlus, 1999; Inoue et al., 2008; Warren and Hartel, 2018; Masuda et al., 2020), although this effect is limited to a certain range of dasher speeds and overruns (Inoue et al., 2008). This is due to increased shear that is applied to the product that results in air bubble break-up. Warren and Hartel (2018) found that in ice cream, this effect was only observed when the emulsifier polysorbate 80 was in the formulation, suggesting that the effect of dasher speed on air cell size may have a secondary effect related to the partial coalescence of fat, which is increased at higher dasher speeds. Masuda et al. (2020) found that the size distribution of air cells was also narrower at higher dasher speeds.

2.6.3.5 Dasher Assembly Design

To the author's knowledge, there is no literature available about how dasher design impacts air cell size.

2.6.4 Fat Globule Destabilization

2.6.4.1 Residence Time / Throughput Rate

Rohenkohl and Kohlus (1999) found that a decreased throughput rate, and thus a longer residence time, resulted in more fat globule destabilization due to the increased amount of shear

applied to the fat globules. However, Inoue et al. (2008) found no significant effect of mix flow rate on fat globule destabilization.

2.6.4.2 Draw / Refrigerant Temperature

Decreasing the draw temperature increases the amount of fat destabilization (Kokubo et al., 1996; Kokubo et al., 1998; Rohenkohl and Kohlus, 1999; Eisner et al., 2005; Inoue et al., 2008), as does decreasing refrigeration temperature (Berger and White, 1971). Inoue et al. (2008) found that draw temperature had the largest influence on fat destabilization of the processing parameters studied. Temperature of freezing can play a role in the shear force exerted on the product as viscosity increases with increasing ice content. This has a much more dramatic effect on extent of fat destabilization compared to minor increases in SFC that would result from the temperature drop during freezing (Goff and Jordan, 1989).

2.6.4.3 Overrun

Increasing overrun increases the amount of destabilized fat (Kokubo et al., 1996; Kokubo et al., 1998; Inoue et al., 2008; Warren and Hartel, 2018), and thus the size of fat aggregates increases with overrun. Kokubo et al. (1996) found that when there was no overrun added during the freezing process, very little fat destabilized, suggesting overrun plays an important role in fat destabilization. This result is corroborated by Inoue et al. (2008), who found that overrun had a larger influence on fat destabilization at higher values of overrun (100-120%). Air may play a role in additional crystallization of fat (as a nucleation promoter) during freezing (Herrera and Hartel, 2000). Additionally, adsorption and desorption of fat from the air interface may increase the number of collisions of fat globules, thus increasing destabilization (Warren and Hartel, 2018).

2.6.4.4 Dasher Speed

Increasing dasher speed increases destabilized fat, as more agitation/shear increases the chance of fat globule collisions (Kokubo et al., 1996; Rohenkohl and Kohlus, 1999; Inoue et al., 2008; Warren and Hartel, 2018). Additional shear also promotes enhanced fat crystallization, which promotes destabilization (Herrera and Hartel, 2000; Fuller et al., 2015b). Only one study concluded that dasher speed did not have an effect on fat destabilization (Rajesh Potineni et al., 2006). It was suggested that this may have been due to the low overrun (60%) or warmer draw temperature (-4°C) used in this study, both of which would limit the amount of fat destabilization.

2.6.4.5 Dasher Assembly Design

The only article that has been published on the effect of dasher type on fat destabilization was Kokubo et al. (1996). When dasher displacement was increased from 15% to 80%, the amount of fat destabilized during freezing increased. This was attributed to a decreased amount of mix in the freezing cylinder for the higher displacement dasher, which caused the ice cream to freeze more quickly. The early increase in ice crystal concentration provided additional shear that contributed to the destabilization of fat globules.

2.7 SUMMARY

The formation and structuring of the ice crystals, air cells, and partially-coalesced fat globules in frozen desserts is complex. While it is known that processing parameters employed during dynamic freezing affect these phenomena, these effects may be indirect. The RTD and shear applied during dynamic freezing may more directly relate to microstructure formation. Additionally, due to the proprietary nature of dasher development by freezer manufacturers, very

little research exists on the dasher designs utilized in continuous SSFs. As frozen desserts are in direct contact with the dasher assembly during the freezing process, it is likely that there are microstructural consequences of dasher design. The goal of this dissertation was to add to the body of knowledge regarding the engineering principles that guide microstructure development in continuous SSFs.

3 MATERIALS & METHODS

3.1 FREEZING EQUIPMENT

3.1.1 Continuous Scraped Surface Freezer

All freezing experiments were completed in a commercial scale Tetra Pak CF700 A2 continuous freezer (Tetra Pak, Aarhus, Denmark), a schematic representation of which is depicted in Figure 3.1. The freezing cylinder had a length of 94.7 cm and an internal diameter of 13.06 cm, giving a working volume of 0.0127 m³ (12.7 L), not including piping and pumps, and a heat exchange surface of 0.389 m². The mix pump had a capacity of 350 L/h of mix throughput. The freezer was operated under viscosity cooling control using R404A as the coolant. Under viscosity cooling control, the product “viscosity” was modulated to achieve the target draw temperature. Viscosity cooling control was used instead of draw temperature control since preliminary results indicated that draw temperature cooling control resulted in a high degree of process variability. The freezer was equipped with a variable speed dasher motor rated at 70 Hz (412 RPM).

Although commonly referred to as “viscosity” among manufacturers of SSFs, the viscosity parameter that is measured by the SSF does not actually measure apparent viscosity of the product. Rather, the “viscosity” is measured as the power drawn by the dasher motor as a percentage of the motor’s total capacity. Since the power drawn by the dasher motor is a function of the torque required to turn the dasher, the viscosity measurement is influenced by the weight, surface area, and geometry of the dasher components in addition the actual viscosity of the product in the freezing cylinder. The power will also be influenced by the dasher rotational speed. Since the viscosity parameter was used to indirectly manipulate draw temperature in this study, the viscosity measurement was also influenced by the cooling rate required to achieve that draw temperature.

3.1.2 Dasher Designs

Five dasher designs were provided by Tetra Pak (Aarhus, Denmark) including a standard dasher + wing beater, multi dasher + wing beater, standard dasher + solid beater, and multi dasher + solid beater, each with 2 scraper blades, and one solid dasher with 3 blades. Each design is detailed in Table 3.1.

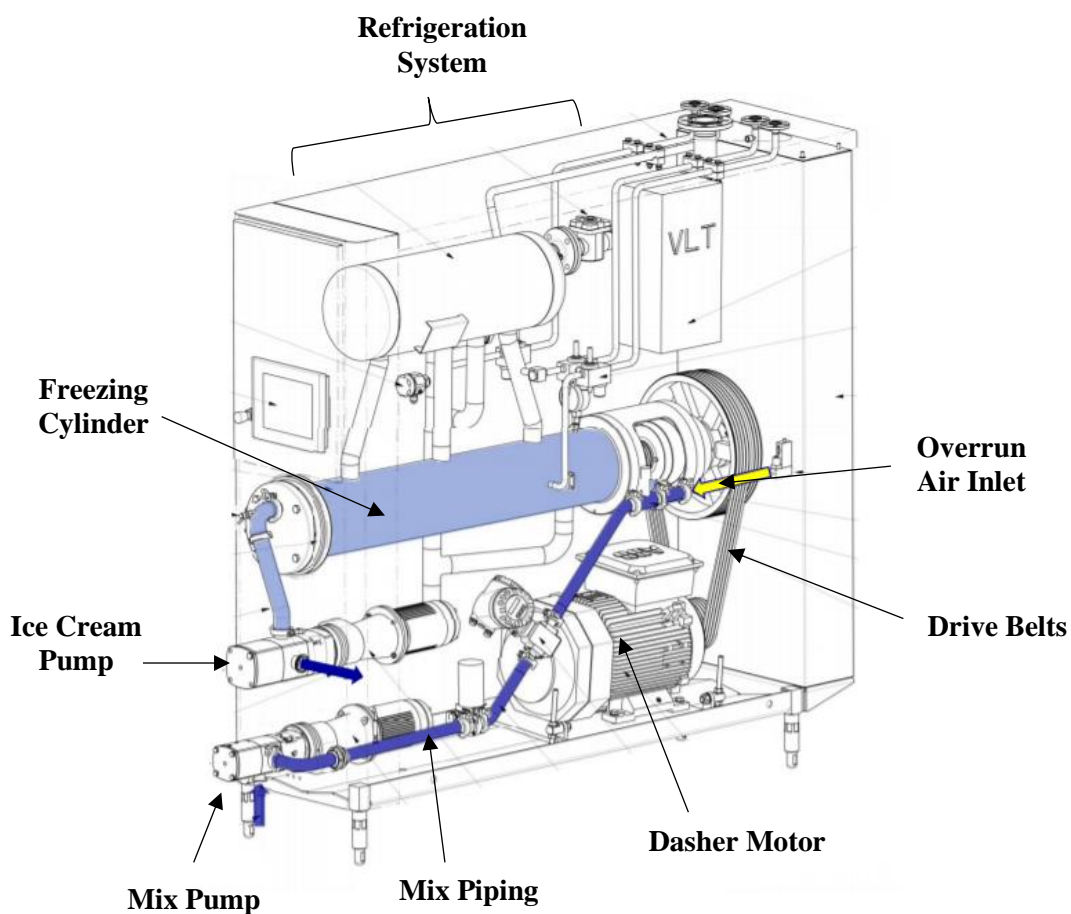
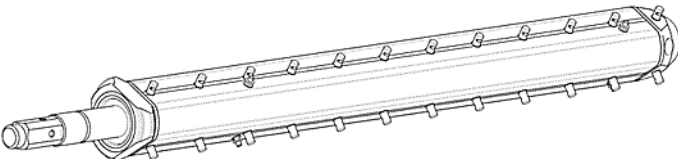
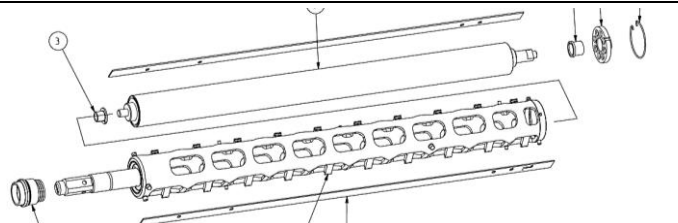
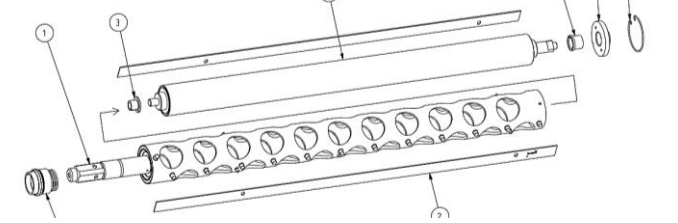
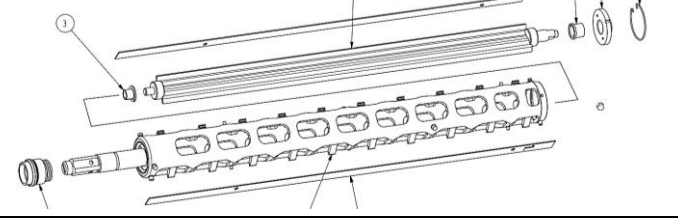
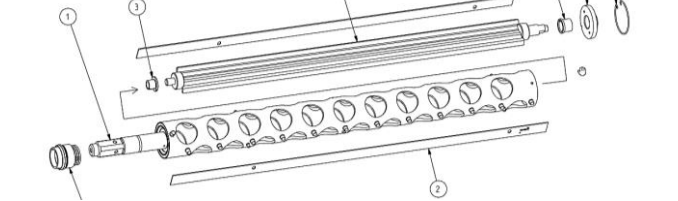


Figure 3.1. Schematic of Tetra Pak CF700 A2 continuous freezer. Courtesy of Tetra Pak, adapted.

Table 3.1. Tetra Pak CF700 A2 dasher assembly designs and specifications. Total volume of freezing cylinder without dasher assembly = 12.54 L.

Dasher Assembly	Displacement (L)	Surface Area of Dasher (m ²)	Geometry
Solid Dasher	8.06 (64.3%)	0.55	
Multi Dasher + Solid Beater	6.78 (54.1%)	0.74	
Standard Dasher + Solid Beater	6.42 (51.2%)	0.70	
Multi Dasher + Wing Beater	3.63 (28.9%)	0.66	
Standard Dasher + Wing Beater	3.29 (26.2%)	0.62	

3.2 WORKING FLUID

3.2.1 Sorbet Experiment

Sorbet mix was made as described and characterized by Helbig (2021). Sorbet mix was made with 14.6% w/w sucrose (Domino Foods; Yonkers, NY), 9.5% w/w fructose (ADM; Decatur, IL), 0.25% w/w dextrose (Ingredion, Inc.; Westchester, IL), 0.44% w/w Germantown Premium Ice Cream Stabilizer (Danisco; University Park, IL), and 74.33% water. The proprietary stabilizer blend contained locust bean gum, guar gum, carrageenan, and dextrose. Mix was made by first mixing all dry ingredients. After adding dry ingredients to water, the mixture was heated to 85°C using indirect steam under agitation in a jacketed mixer (UMC 44 E Vertical-Cutter/Mixer, Stephan Machinery Corporation; Columbus, OH). The mix was then cooled to 20°C by switching the jacketed mixer to cooling water. The mix was stored overnight at 5°C prior to freezing.

3.2.2 Ice Cream Experiments

Pasteurized and homogenized ice cream mix was obtained from Galloway (Neenah, WI). Ingredients included skim milk, milk, cream, sugar, corn syrup, mono & diglycerides, locust bean gum, guar gum, and carrageenan. Although the formulation is proprietary, the mix contained 38.55% total solids, 10.2% fat, 10% milk-solids-not-fat (MSNF), 12% sucrose, and 6% corn syrup solids (DE 42/43). Ice cream mix was stored at 5°C prior to freezing.

3.3 EFFECT OF DASHER DESIGN ON RESIDENCE TIME DISTRIBUTION AND ICE CRYSTAL SIZE OF UNAERATED SORBET MADE WITH A CONTINUOUS SCRAPED SURFACE FREEZER

3.3.1 Experimental Design

In this experiment, the effect of dasher design (5 types, Table 3.1) on residence time distribution and ice crystal size distribution of unaerated sorbet was studied. All other freezing parameters were kept constant at throughput = 190 L/h, overrun = 0%, dasher speed = 300 RPM, and cylinder pressure = 0 bar. Since the solid dasher had 3 scraper blades, unlike the other 4 dasher assemblies, which had 2 scraper blades, an additional trial was run with the solid dasher to maintain a constant scrape rate of 600 scrapes/min. The viscosity freezer setting was adjusted to maintain a constant draw temperature of $-6.0 \pm 0.1^\circ\text{C}$. The experiment was replicated in triplicate.

3.3.2 Sample Collection and Measurements

First, a residence time distribution trial was run after reaching steady state as detailed in section 3.7.1. Then, samples for ice crystal size were packed into 118 mL coated paper containers. Draw samples were immediately transferred to a refrigerated glovebox at -6°C , while the remaining samples were placed in a quiescent freezer at -27°C for hardening and storage. Ice crystal size was analyzed as described in section 3.8.1.

Although air was not injected into the product during the freezing process, it is possible that air was whipped into the product through the action of the dasher. Three samples per replicate were collected in 104 mL coated paper cups to measure the overrun of the frozen samples. The

samples were collected at least 20 min after freezer start up, which was determined to be steady state by Helbig (2021). Overrun was calculated as:

$$\% \textit{Overrun} = \frac{\textit{Wt.of mix} - \textit{Wt.of same vol.of ice cream}}{\textit{Wt.of same vol.of ice cream}} * 100 \quad (\text{Eqn. 3.1})$$

The viscosity, taken as the torque placed on the motor of the dasher (% of capacity) and draw temperature were also recorded. These parameters were measured by built-in sensors on the freezer.

3.4 RHEOLOGICAL CHARACTERIZATION OF A MODEL FOR THE FREEZE CONCENTRATED SERUM PHASE OF ICE CREAM

3.4.1 Preparation of Freeze Concentrated Serum Phase Model Samples

Samples were prepared to model freeze concentration (FC) of the serum phase to 0%, 10%, 20%, 30%, 40%, and 50% of water frozen. The moisture content of ice cream mix was measured by forced air oven drying. Water was removed from the mix via freeze drying (Genesis Pilot Freeze Dryer, SP VirTis, Warminster, PA) at -15°C and 97 mTorr for 3 days. The amount of water removed was taken as the difference in product weight before and after freeze drying. Deionized water was then added back to the freeze-dried ice cream mix to make solutions with 10%, 20%, 30%, 40%, and 50% removal of water from the original mix. The original mix was used for the 0% FC sample. The moisture content of all FC samples was confirmed by forced air oven drying.

3.4.2 Freezing Curve and Freezing Point of Model Samples

The freezing point depression was determined by calculation as described by Goff and Hartel (2013). First, the sucrose equivalents (*SE*) were calculated by:

$$SE = (MSNF * 0.545) + S + (42DE CSS * 0.8) \quad (\text{Eqn. 3.2})$$

where $MSNF$ = milk-solids-not-fat, S = sucrose, $DE CSS$ = dextrose equivalents corn syrup solids.

The SE was then used to find the freezing point depression associated with SE in water (FPD_{SE}) from data extrapolated from Leighton (1927). Next, freezing point depression associated with salts (FPD_{SA}) in °C was calculated as:

$$FPD_{SA} = \frac{MSNF * 2.37}{W} \quad (\text{Eqn. 3.3})$$

where W is the water content. Finally, the total freezing point depression (FPD_T) was calculated as:

$$FPD_T = FPD_{SE} + FPD_{SA} \quad (\text{Eqn. 3.4})$$

The freezing curve was calculated by accounting for freeze concentration, where water is removed from the serum phase as it is frozen to ice. By reducing the water content left in the mix, the FPD_T can then be recalculated. The freezing curve is then built by plotting percentage of water frozen in the mix (i.e., water removed) against the freezing temperature (Goff and Hartel, 2013).

3.4.3 Rheological Characterization

Rheology of freeze concentrated model samples was characterized using a rheometer fitted with a concentric cylinders geometry (Discovery HR-2 Hybrid rheometer, details). A shear sweep was performed from 100 s^{-1} to 1 s^{-1} on 17 mL of sample. The shear sweep was tested at 5°C , 2.5°C , 0°C , -2.5°C for all samples. Additionally, shear sweeps were run at the nearest 0.5°C above the freezing point and at 0.5°C above that temperature. The sample cup was jacketed to control temperature using a Peltier cooling system. TRIOS software (TA Instruments, New Castle, DE) was used to calculate the apparent viscosity η :

$$\eta = \frac{1}{4\pi h} \left(\frac{1}{R_i^2} - \frac{1}{R_o^2} \right) \frac{M}{\omega} \quad (\text{Eqn. 3.5})$$

where the radius of the inner cylinder $R_i = 14$ mm, the radius of the outer cylinder $R_o = 15$ mm, height of immersion of the inner cylinder in the liquid medium $h = 42$ mm, M is the torque on the cylinder surface, and ω is the angular velocity.

3.5 MICROSTRUCTURAL EVOLUTION OF ICE CREAM AFTER START-UP OF A CONTINUOUS SCRAPED SURFACE FREEZER

3.5.1 Experimental Overview

The purpose of this experiment was to characterize the evolution of the microstructural components of ice cream over time immediately following freezer start-up. The data from this experiment was also intended to inform ice cream experiments detailed in section 3.6, specifically to determine how long the continuous freezer must operate to attain microstructural steady state. Therefore, the dasher assembly and operating conditions selected for this experiment were for the longest theoretical residence time of experiments in section 3.6. The dasher assembly used was the standard + wing, and the freezer was operated at throughput = 200 L/h, overrun = 75%, dasher speed = 200 RPM, and cylinder pressure = 4 bar. The viscosity freezer setting was used for cooling control and was adjusted to reach and then maintain a draw temperature of $-5.5 \pm 0.1^\circ\text{C}$. This experiment was completed in triplicate.

3.5.2 Sample Collection and Measurements

The freezing cylinder was primed with ice cream mix prior to freezer start-up. The refrigeration compressor, throughput pumps, dasher motor, and air supply were simultaneously started at $t=0$ min, which was defined as freezer start-up. Sample collection began immediately at

t=0 min. Samples for analysis of ice crystal size at draw were collected every 6 min for 78 min. Draw samples were immediately transported to a refrigerated glovebox set at the draw temperature of -5.5°C and analyzed using the methodology detailed in section 3.8.1. Samples for microstructure analysis of the hardened product were collected every 1 min for the first 20 min after freezer start-up, and then every 6 min from 24-78 min after freezer start-up. These were immediately placed in a quiescent freezer at -27°C for hardening and storage. Hardened samples were subsequently analyzed for ice crystal size, air cell size, and fat destabilization as described in section 3.8.

One sample was collected in 104 mL coated paper ice cream cups at the same intervals as hardened samples, and this was weighed to track overrun of the frozen samples. Overrun was calculated using Eqn. 3.1. The viscosity, taken as the torque placed on the motor of the dasher (% of capacity) and draw temperature were also recorded. These parameters were measured by built-in sensors on the freezer.

3.6 EFFECT OF DASHER DESIGN AND PROCESSING PARAMETERS ON RESIDENCE TIME DISTRIBUTION AND MICROSTRUCTURAL CHARACTERISTICS OF ICE CREAM MADE WITH A CONTINUOUS SCRAPED SURFACE FREEZER

3.6.1 Experimental Overview

A full factorial (5x3x2) studying the effects of dasher design (5 types, Table 1), throughput rate, overrun (OR), and dasher speed (each at 2 levels) was initially considered. However, Inoue et al. (2008) has already elucidated the main and interaction effects for these processing parameters, excluding dasher design. By completing 3 separate experiments (in triplicate), each

focused on a different processing parameter (dasher speed, throughput rate, and OR), we can more effectively and efficiently elucidate the main effects of dasher design as well as any interaction effects.

3.6.1.1 Dasher Speed Experiment

A 5x3 (dasher assembly x dasher speed) factorial design was implemented. Dasher speeds tested included 100PRM, 200 RPM and 300 RPM. These dasher speeds represent 33, 45, and 71% of the dasher motor (rated at 70 Hz) speed capacity. Freezing parameters that were kept constant included throughput rate = 300 L/h, overrun = 75%, and cylinder pressure = 4 bar. The viscosity freezer setting was adjusted to maintain a constant draw temperature of $-5.5\pm 0.1^{\circ}\text{C}$.

3.6.1.2 Overrun Experiment

A 5x3 (dasher assembly x OR) factorial design was implemented. OR levels tested included 50, 75, and 100%. The standard of identity of ice cream requires that a gallon of ice cream should weigh not less than 4.5 lbs, which corresponds to roughly 100 % OR (21CFR135.110). Super premium products typically have ~50% OR. Warren and Hartel (2014) found that the average OR of commercial ice creams in the US is ~75%, so the selected OR range represents range typical of commercially available ice cream products. Freezing parameters that were kept constant included throughput rate = 300 L/h, dasher speed = 200 RPM, and cylinder pressure = 4 bar. The viscosity freezer setting was adjusted to maintain a constant draw temperature of $-5.5\pm 0.1^{\circ}\text{C}$.

3.6.1.3 Throughput Rate Experiment

A 5x3 (dasher assembly x throughput rate) factorial design was implemented. Throughput rates tested included 200 L/h, 300 L/h, and 400 L/h. The capacity of the CF700 is 700 L/h. At 75% OR, 200, 300, and 400 L/h of output represent 33%, 49%, and 65% of the freezer throughput capacity, respectively, allowing for investigation across the mid-range of freezer operating capacity. Freezing parameters that were kept constant included overrun = 75%, dasher speed = 200 RPM, and cylinder pressure = 4 bar. The viscosity freezer setting was adjusted to maintain a constant draw temperature of $-5.5 \pm 0.1^\circ\text{C}$.

3.6.2 Sample Collection and Measurements

First, a residence time distribution trial was run (after reaching steady state) as detailed in section 3.7.2. Then, samples for microstructural analysis were collected by packing ice cream into 118 mL coated paper ice cream containers. Draw samples were immediately transferred to a refrigerated glovebox at -5.5°C , while the remaining samples were placed in a quiescent freezer at -27°C for hardening and storage. Microstructure was analyzed as described in section 3.8.

Five samples, collected in 104 mL coated paper ice cream cups, were taken after reaching steady state to confirm the overrun of the frozen samples. Overrun was calculated using Eqn. 3.1. The viscosity, taken as the torque placed on the motor of the dasher (% of capacity) and draw temperature were also recorded. These parameters were measured by built-in sensors on the freezer.

3.7 RESIDENCE TIME DISTRIBUTION METHODOLOGY

3.7.1 Sorbet Residence Time Trials

To measure residence time distribution, a pulse injection was performed near the entrance to the freezing cylinder (Figure 3.2). Methylene blue (MB) (ThermoFischer Scientific, Fair Lawn, NJ) was chosen as a tracer as it has previously been used for residence time studies in sorbet (Arellano et al., 2013a). Based on preliminary findings, a tracer concentration of 0.5% MB in sorbet mix was chosen as it provided absorbance results within an acceptable range per the Beer-Lambert law. Once the freezer achieved steady state (after 20 min of operation as determined by Helbig, 2021), 20 mL of tracer was injected into the mix inlet with a syringe. The injection took approximately 2-5 seconds. Samples were continuously collected in 500 mL cups immediately after tracer injection. After collection, the samples were weighed, covered, and allowed to thaw overnight at 5°C.

Samples were transferred to 50 mL centrifuge tubes and centrifuged at 4,000 RPM for 10 min to remove any entrained air. Two mL of sample were then pipetted into a 4.5 mL polystyrene cuvette, and a spectrophotometer (Genesys 20, ThermoFischer Scientific, Waltham, MA) with a path length of 10 mm was used to measure the absorbance of each sample at 672 nm (Arellano et al., 2013a). The first sample collected after tracer injection was used as the blank. A pre-established standard curve for MB in sorbet was used to calculate the concentration of MB in each sample (Figure 3.3).

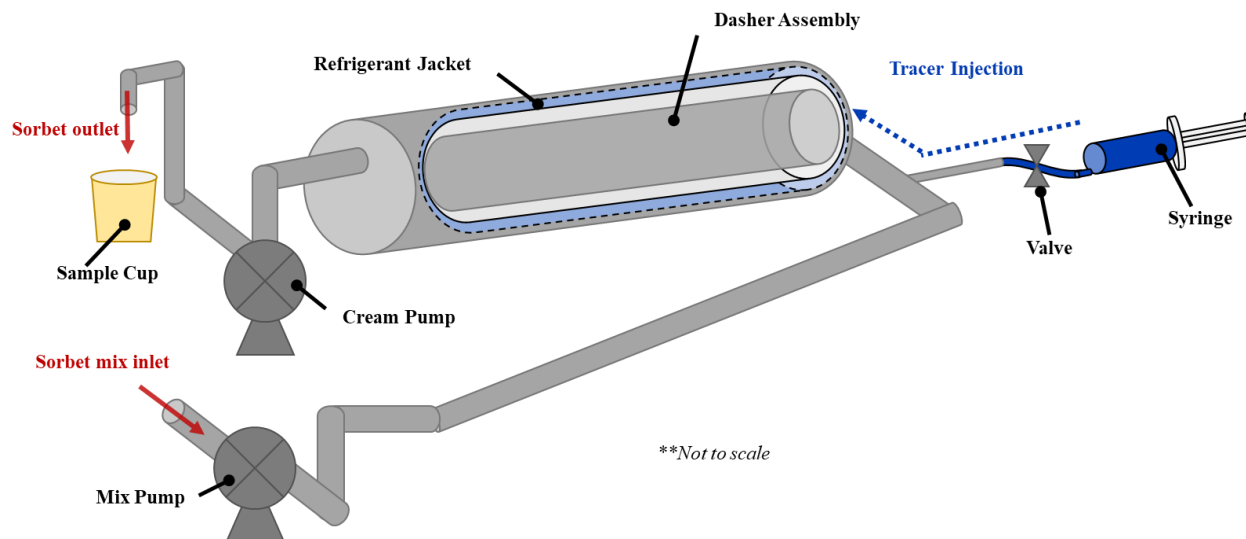


Figure 3.2. Schematic of pulse injection of methylene blue into Tetra Pak CF700 continuous freezer during manufacture of nonaerated sorbet for determination of residence time distribution. Processing parameters were set at throughput = 190 L/h, draw temperature = -6.0°C , dasher speed = 300 RPM, and cylinder pressure = 0 bar.

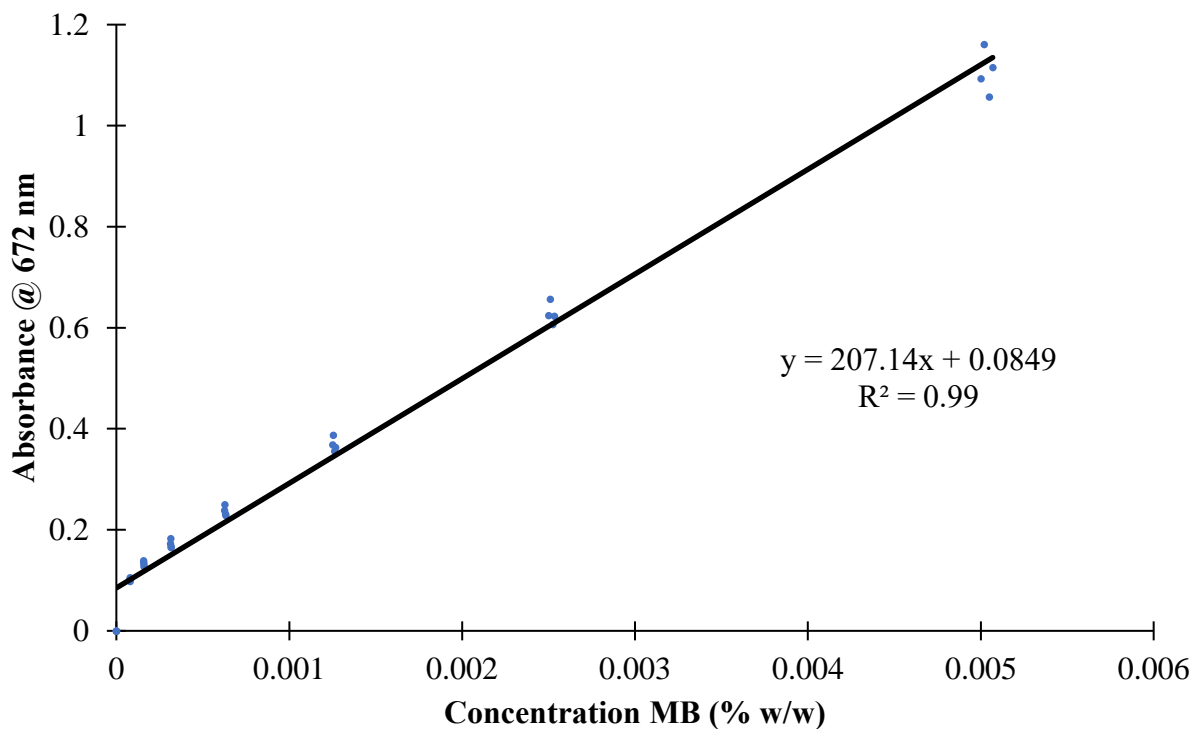


Figure 3.3. Standard curve for methylene blue (MB) in sorbet mix at 5°C . absorbance was measured using a spectrophotometer at a wavelength of 664 nm.

3.7.2 Ice Cream Residence Time Trials

For these trials, a pulse injection was performed near the entrance to the freezing cylinder, with a set-up similar to that of sorbet experiments (Figure 3.2). Methylene blue (MB) (ThermoFischer Scientific, Fair Lawn, NJ) was chosen as a tracer as it has previously been used for residence time studies in frozen desserts (Arellano et al., 2013a). Based on preliminary findings, a tracer concentration of 1% MB in ice cream mix was chosen as it provided absorbance results within an acceptable range per the Beer-Lambert law. Once the freezer achieved steady state, which was taken as 10x the theoretical residence time assuming plug flow (Table 3.2), 20 mL of tracer was injected into the mix inlet with a forced air syringe. The injection took approximately 3-5 seconds. Samples were continuously collected in 1,000 mL pre-weighed cups immediately after tracer injection. After collection, the samples were weighed, covered, and allowed to thaw overnight at 5°C. Due to the opacity of ice cream, each sample was diluted 1:20 with a 1% SDS solution. SDS was used to standardize particle size in the samples by reversing partial coalescence of fat (Méndez-Velasco and Goff, 2012). After pipetting 2 mL of sample into a 4.5 mL polystyrene cuvette, a spectrophotometer (Genesys 20, ThermoFischer Scientific, Waltham, MA) with a path length of 10 mm was used to measure the absorbance of each sample at 664 nm, the maximum absorbance wavelength for MB. The first sample collected after tracer injection should theoretically have negligible amounts of tracer in it, and therefore was used as the blank. A pre-established standard curve for MB in ice cream was used to calculate the concentration of MB in each sample (Figure 3.4).

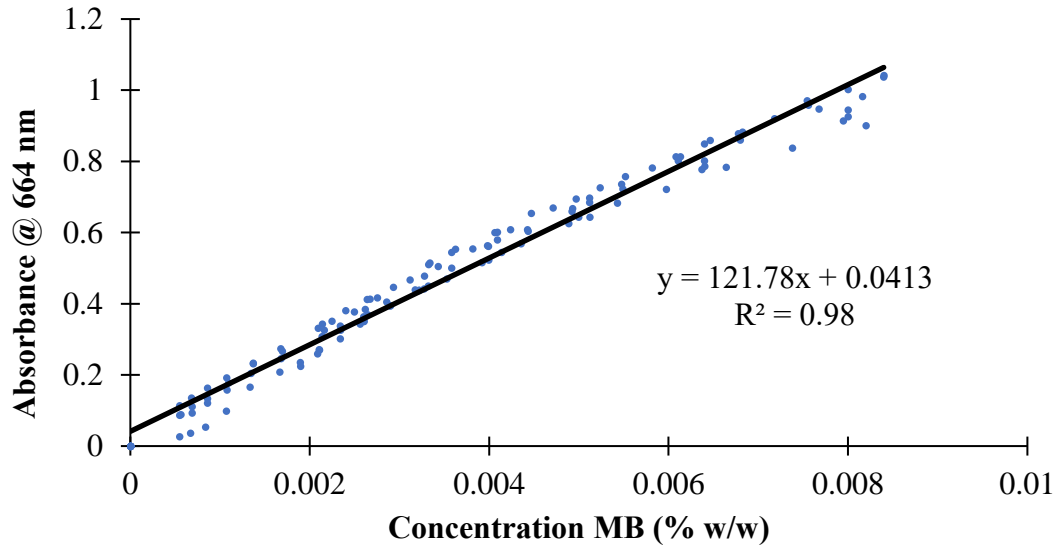


Figure 3.4. Standard curve of methylene blue (MB) in melted ice cream. Samples were diluted 20:1 in a 1% SDS solution and absorbance was measured using a spectrophotometer at a wavelength of 664 nm.

Table 3.2. Theoretical residence times (s) for ice cream experimental parameters under plug flow model assumption in Tetra Pak CF700 continuous freezer.

Overrun		50% OR	75% OR		100% OR	
Throughput Rate		300 L/h	200 L/h	300 L/h	400 L/h	300 L/h
Dasher Assembly	Solid	81	141	94	71	108
	Multi + Solid	104	181	121	91	138
	Standard + Solid	110	193	129	96	147
	Multi + Wing	160	281	187	140	214
	Standard + Wing	167	291	194	146	222

3.7.3 RTD Data Treatment

The residence time distribution (RTD) was calculated using the age distribution function $E(t)$:

$$E(t) = \frac{C(t)}{\int_0^{\infty} C(t)dt} \quad (\text{Eqn. 3.6})$$

where $C(t)$ is the concentration of MB tracer (% w/w) in the effluent stream at time t . The experimental mean residence time t_s (the first moment of the RTD) was calculated as:

$$t_s = \int_0^{\infty} t \cdot E(t) dt \quad (\text{Eqn. 3.7})$$

The variance σ^2 (the second moment of the RTD), or the spread around the average residence time was calculated as:

$$\sigma^2 = \int_0^{\infty} (t - t_s)^2 E(t) dt \quad (\text{Eqn. 3.8})$$

Finally, the skewness s^3 (the third moment of the RTD) was calculated as:

$$s^3 = \frac{1}{\sigma^{3/2}} \int_0^{\infty} (t - \bar{t})^3 E(t) dt \quad (\text{Eqn. 3.9})$$

where s^3 describes the extent to which the distribution is skewed in one direction or another relative to the mean (Fogler, 2016). Data were also normalized so that the flow performance of dasher assemblies with different working volumes or processing conditions at different throughput rates could be compared. The normalized time θ and age distribution function $E(\theta)$ were respectively calculated as:

$$\theta = \frac{t}{t_s} \quad (\text{Eqn. 3.10})$$

and

$$E(\theta) = t_s \cdot E(t) \quad (\text{Eqn. 3.11})$$

3.8 MICROSTRUCTURAL ANALYSIS METHODOLOGY

3.8.1 Ice Crystal Size Distribution

Ice crystal size distributions were determined using a method adapted from Donhowe et al. (1991). Using a refrigerated glovebox, the ice crystal size was measured immediately after draw with the glovebox set to the draw temperature (-6°C for sorbet and -5.5°C for ice cream). Ice crystal size of the hardened product was measured at -15°C after the product had been stored for

at least 2 weeks at -27°C . A small amount of sample was taken from the center of the container and placed on a glass slide along with 2 drops of 1:1 pentanol:butanol, which acted as a dispersant. A coverslip was placed over the sample, and a tweezer was used to gently manipulate the sample until ice crystals were in a single layer. The sample was viewed using an optical microscope (3000 LED Microscope Series, Accu-scope; Commack, NY) at 10x magnification, and images were taken using a Motic camera and software (Moticam 3+ with Motic Images Plus 3.1, Motic; Schertz, TX). At least 300 ice crystals were traced using Microsoft Paint, and the area was calculated using Image Pro (Version 10, Media Cybernetics, Rockville, MD). Ice crystal size was taken as the circular-area equivalent diameter. Ice crystal size measurements were taken in triplicate from 3 separate containers.

3.8.2 Air Cell Size Distribution

Air cell size distributions were determined for ice cream using a method adapted from Chang and Hartel (2002c). Hardened samples prepared for analysis in a refrigerated glovebox at -15°C after the product had been stored for at least 2 weeks at -27°C . A well was made by gluing two glass cover slips (thickness $\approx 0.22\pm 0.03$ mm) to a glass microscope slide. A thin slice of ice cream, taken from the center of the container, was placed in the well and covered with another glass cover slip. The temperature of the glovebox was then raised to -6°C to partially melt the ice cream, which allowed air cells to rise to the cover slip for observation. The sample was viewed using an optical microscope (3000 LED Microscope Series, Accu-scope; Commack, NY) at 10x magnification, and images were taken using a Motic camera and software (Moticam 3+ with Motic Images Plus 3.1, Motic; Schertz, TX). At least 300 air cells were traced using Image Pro (Version

10, Media Cybernetics, Rockville, MD). Air cell size measurements were taken in triplicate from 3 separate containers.

3.8.3 Fat Destabilization

Fat destabilization, which was taken as percentage of fat particles with a size $>3\mu\text{m}$, was determined for ice cream. This value was chosen because the particle size in the unfrozen ice cream mix was approximately $\leq 3\mu\text{m}$. Fat globule size was determined by laser diffraction using a Mastersizer 3000 (Malvern Panalytical Inc., Westborough, MA). Ice cream samples were melted overnight prior to analysis. A small amount of sample (1-2 drops) was added to deionized water in the sample cell with a stirrer speed 2,000 RPM until an obscuration level of 13-15% was achieved. The refractive index for particles (milkfat) was set at 1.47; and the refractive index of the dispersant (deionized water) was set at 1.33. Five measurements were performed on each sample. Fat destabilization was also qualitatively visualized using optical microscopy (Eclipse FN1 Microscope equipped with DS-Fi2 Camera, Nikon; Tokyo, Japan) at 20x magnification.

3.9 STATISTICAL ANALYSIS

Statistical analyses were performed using RStudio (Posit™, Boston, MA). All results were fitted to a linear model, and the effects of respective variables on responses were determined by performing one-way ANOVA followed by Tukey's HSD post-hoc tests ($\alpha < 0.05$). For ice cream experiments detailed in section 3.6, two-way ANOVA ($\alpha < 0.05$) was used to assess for interaction effects between dasher assembly and the processing parameter (dasher speed, overrun, or throughput rate). Correlations between variables and responses were evaluated to determine the R^2 value.

4 RESULTS AND DISCUSSION

4.1 EFFECT OF DASHER DESIGN ON RESIDENCE TIME DISTRIBUTION AND ICE CRYSTAL SIZE OF UNAERATED SORBET

The purpose of this experiment was to evaluate whether different dasher assemblies influence the processing conditions, residence time distribution (RTD), and microstructure of sorbet made in a scraped surface freezer (SSF). In most instances, unaerated sorbet was made under the following conditions: throughput rate = 190 L/h, draw temperature = -6.0°C , cylinder pressure = 0 bar, and dasher speed = 300 RPM. All open dasher assemblies supported two scraper blades, but the solid dasher supported 3 blades. For this reason, the solid dasher was operated at a dasher speed of 200 and 300 RPM, the former of which matched the scraping rate of 600 scrapes/min for dashers supporting only 2 blades.

4.1.1 Processing Conditions

The processing conditions for sorbet made with different dasher assemblies are given in Table 4.1.1. The draw temperature was measured at $-6.0 \pm 0.1^{\circ}\text{C}$ for all treatments. While the sorbet was not intentionally aerated, overrun was monitored as air may have been incorporated into the product through the whipping action of the dasher. The overrun ranged from 6.0 – 8.0%, indicating minimal aeration. There were not significant differences in overrun among dasher assemblies. There was a significant effect of dasher assembly on viscosity, or the torque that was placed on the motor turning the dasher as a percentage of its total capacity. The configurations containing a solid beater had the highest viscosity, but otherwise viscosity values were similar. The increased torque on the motor may be due to the increased surface area of dasher assemblies containing a

solid beater (Table 3.1) as well as a narrow annular space between the dasher and beater, both of which would increase friction.

Table 4.1.1. Effects of dasher assembly on viscosity (torque on dasher motor as a percentage of its total capacity) for unaerated sorbet made at throughput rate = 190 L/h, dasher speed = 300 RPM (unless noted), and draw temperature = -6°C.

Dasher Assembly	Viscosity (%)
Solid	67±20 ^{AB}
Solid (200 RPM)	61±4 ^B
Multi + Solid	81±6 ^{AB}
Standard + Solid	91±3 ^A
Multi + Wing	64±2 ^B
Standard + Wing	58±1 ^{AB}

^{A-B} Within a column, means without a common uppercase superscript differ ($P < 0.05$) due to dasher.
[±] Values indicate standard deviation for 3 replicates.

4.1.2 Residence Time Distributions

Cumulative residence time distributions as a function of dasher assembly are shown in Figure 4.1.1, with images of the samples collected during the pulse injection trial depicted in Figure 4.1.2. The first three moments of the residence time distribution curves are given in Table 4.1.2. As dasher displacement increased (Table 3.1), $F(t)$ and $E(t)$ curves (Figures 4.1.3a) were shifted left, indicating increased residence time, although configurations with a common beater had similar curves. Mean residence time varied from 95 – 191s. There was a significant effect of dasher assembly on mean residence time, with dasher assemblies containing a common beater having similar mean residence times (Figure 4.1.4). Additionally, there was not an effect of changing the solid dasher rotational speed to match scrape rate (200 RPM) versus dasher speed (300 RPM). When mean residence time was plotted against dasher displacement (Figure 4.1.5), there was a strong linear correlation ($R^2 = 0.96$). The variance and skew in residence time was highest for the

standard + wing assembly, though it was not significantly different from the multi + wing assembly. These two configurations had the lowest displacement. The skewness, or tailing of the distribution, can also be observed qualitatively in the RTD samples collected (Figure 4.1.2). This is likely due to increased axial mixing. However, the normalized residence time $E(\theta)$ curves (Figures 4.1.3b) were generally similar. $E(\theta)$ curves allow for comparison of flow performance in reactors of different sizes. While the freezing cylinder volume remains the same, the working volume of the reactor changes depending on dasher displacement (Table 3.1). The $E(\theta)$ curves suggest that flow performance is similar when accounting for average residence time.

Table 4.1.2. Effects of dasher assembly on residence time distribution parameters for nonaerated sorbet made at a throughput rate = 190 L/h, dasher speed = 300 RPM (unless noted), and draw temperature = -6°C as determined by pulse injection study.

Dasher Assembly	Residence Time Parameter		
	Mean Residence Time, t_s (s)	Variance, σ^2 (s^2)	Skewness, s^3
Solid	100 \pm 7 ^A	1300 \pm 774 ^{AB}	1.02 \pm 0.08 ^{AB}
Solid (200 RPM)	95 \pm 3 ^A	700 \pm 46 ^A	0.94 \pm 0.02 ^{AB}
Multi + Solid	123 \pm 5 ^B	1640 \pm 551 ^{AB}	0.94 \pm 0.14 ^{AB}
Standard + Solid	120 \pm 8 ^B	1330 \pm 496 ^{AB}	1.06 \pm 0.12 ^A
Multi + Wing	179 \pm 5 ^C	2990 \pm 68 ^{BC}	0.78 \pm 0.10 ^{BC}
Standard + Wing	191 \pm 13 ^C	4220 \pm 1720 ^C	0.67 \pm 0.05 ^C

^{A-C} Within a parameter and column, means without a common uppercase superscript differ ($P < 0.05$) due to dasher.

\pm Values indicate standard deviation for 3 replicates.

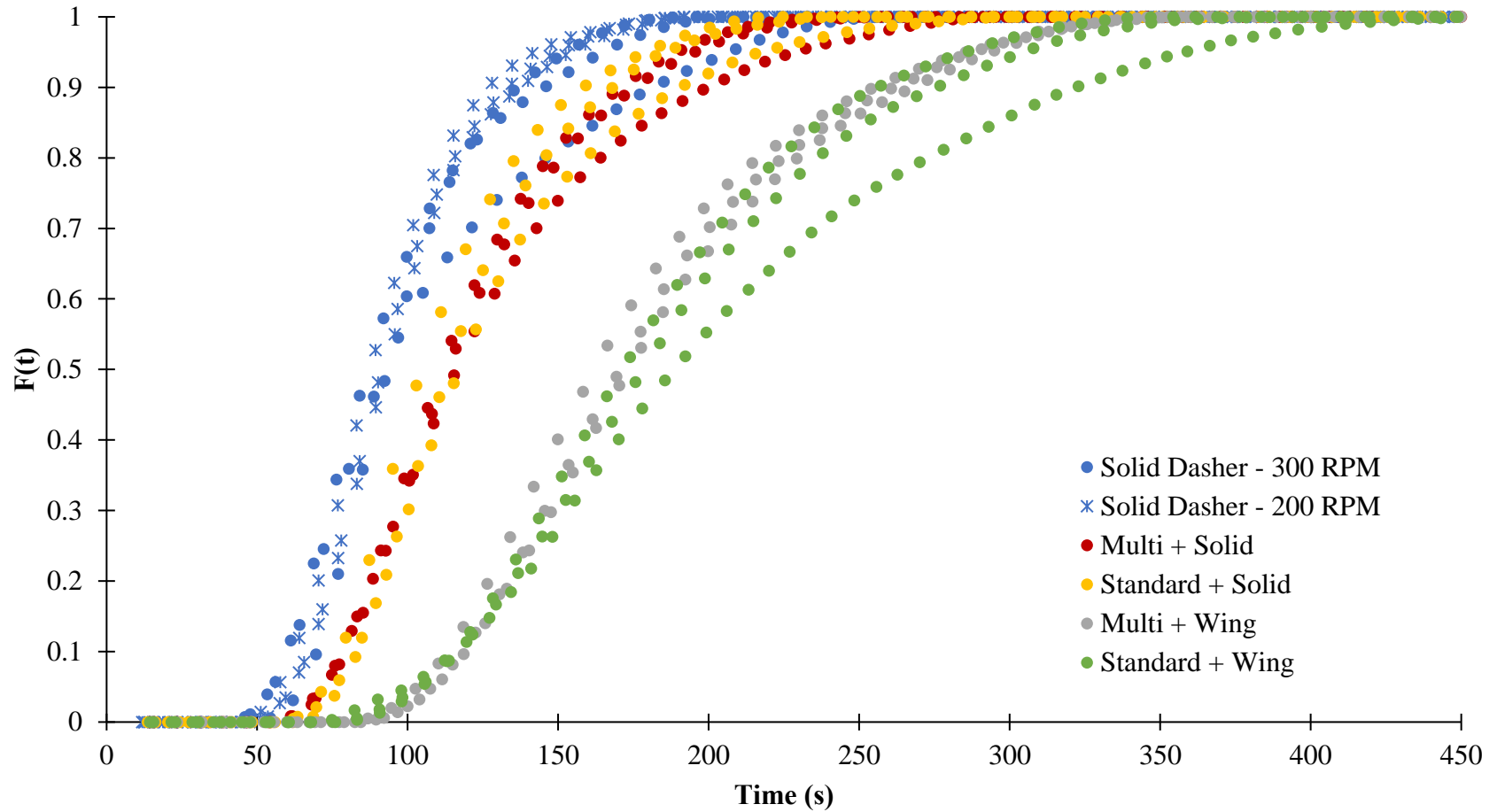


Figure 4.1.1. Cumulative residence time distribution $F(t)$ curves as a function of dasher assembly for unaerated sorbet made at throughput = 190 L/h, dasher speed = 300 RPM (unless noted), and draw temperature = -6°C ($n=3$).

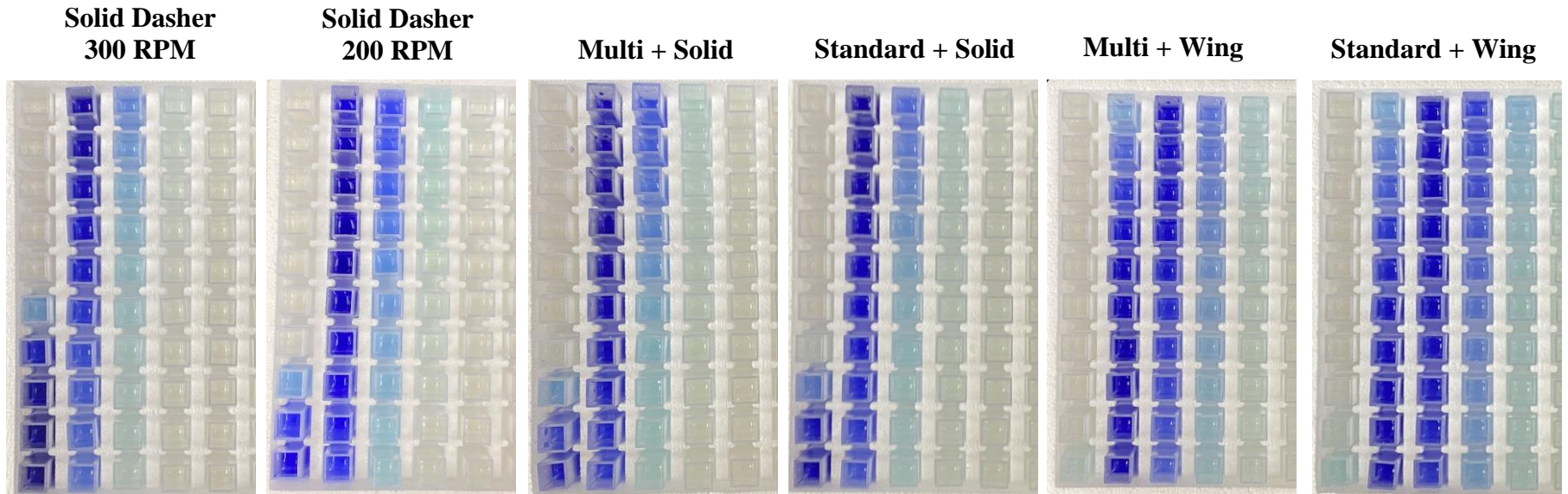


Figure 4.1.2. Images of samples collected during pulse injection experiment for evaluating residence time distribution of unaerated sorbet as a function of dasher assembly. Throughput rate = 190 L/h, dasher speed = 300 RPM (unless noted), draw temperature = -6°C . Top left cup in each image was collected at $t = 0\text{s}$ when 20 mL of tracer (0.5% methylene blue in sorbet mix) was injected into freezer.

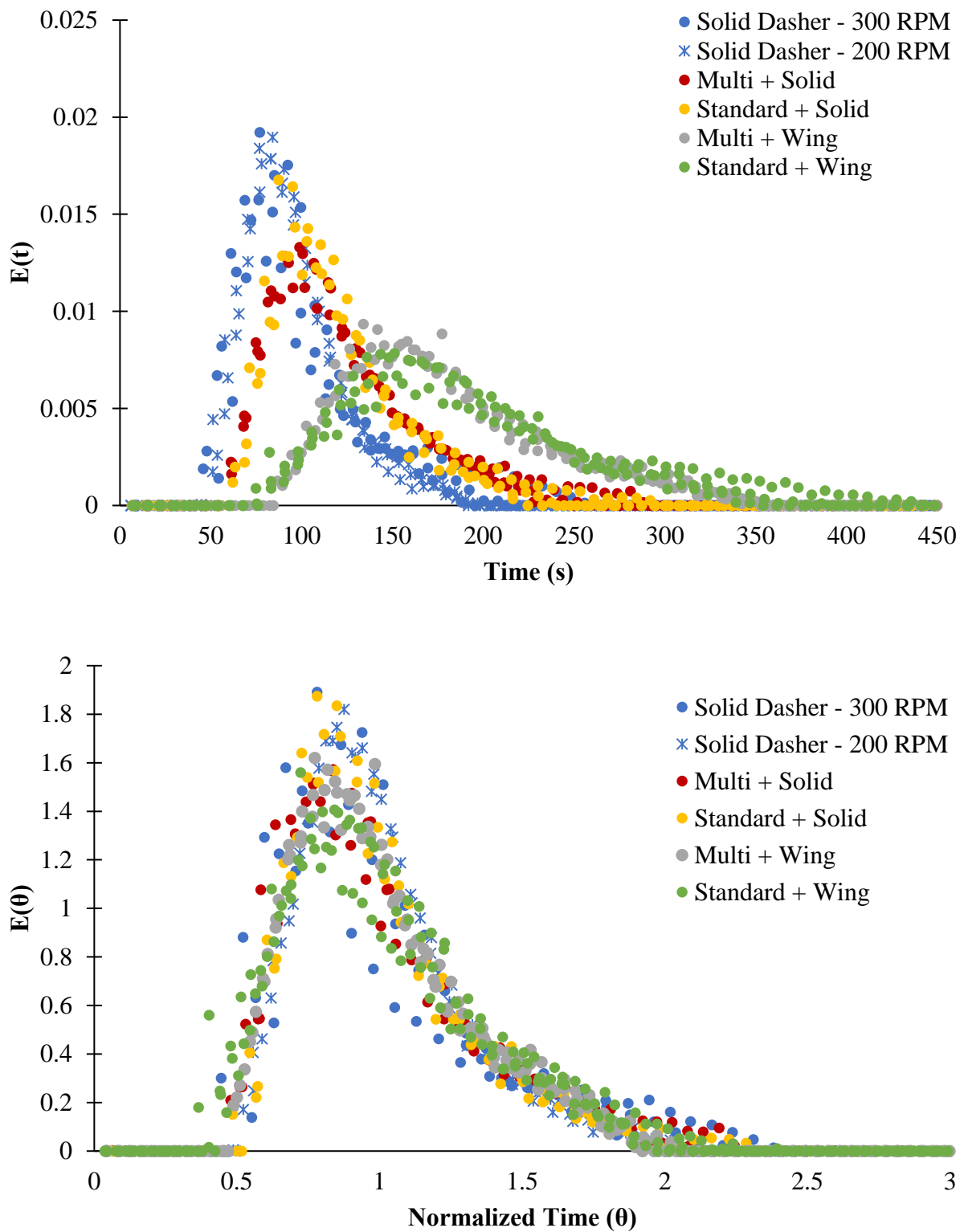


Figure 4.1.3. A) $E(t)$ curves and B) $E(\theta)$ curves as a function of dasher assembly for unaerated sorbet made at a throughput rate = 190 L/h, dasher speed = 300 RPM (unless noted), and draw temperature = -6°C ($n=3$).

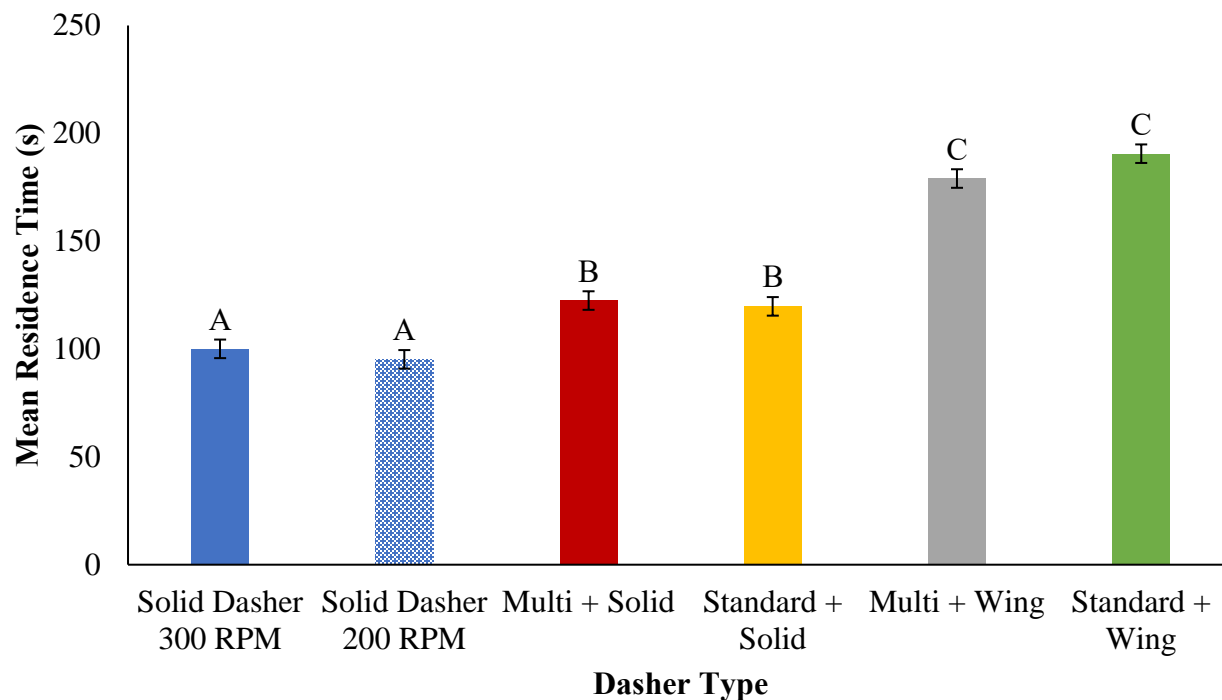


Figure 4.1.4. Mean residence time t_s as a function of dasher assembly for unaerated sorbet made at a throughput rate = 190 L/h, dasher speed = 300 RPM (unless noted), and draw temperature = -6°C . Means without a common letter differ ($P < 0.05$). Error bars represent standard deviation for 3 replicates.

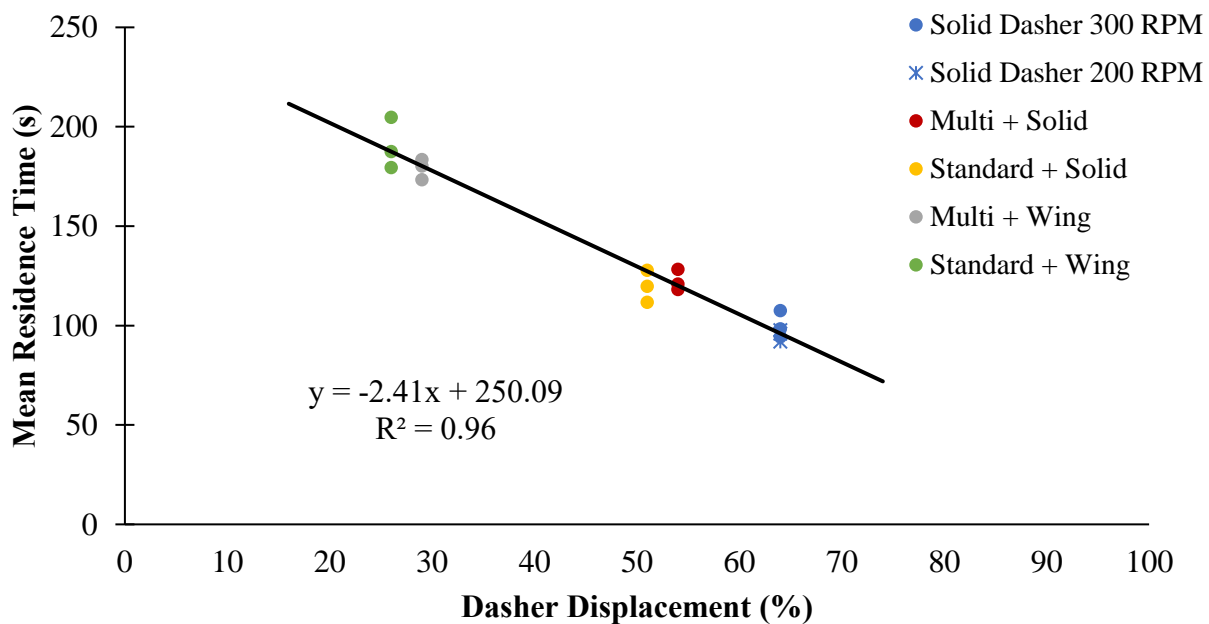


Figure 4.1.5. Correlation between dasher displacement and mean residence time t_s for unaerated sorbet made at a throughput rate = 190 L/h, dasher speed = 300 RPM (unless noted), and draw temperature = -6°C .

4.1.3 Ice Crystal Size Distributions

The average ice crystal size of hardened sorbet ranged from 33.1 – 38.7 μm . Cumulative size distributions are given in Figure 4.1.6, and mean and standard deviation in ice crystal size as a function of dasher are presented in Table 4.1.3. There were no significant differences in ice crystal size as a function of dasher. Additionally, changing the solid dasher (3 blades) rotational speed to match the scraping frequency of dashers containing two blades did not significantly affect ice crystal size. These sizes and effects are in agreement with Helbig (2021), who studied sorbet under the same conditions. To confirm that there was no relationship between processing parameters and ice crystal size, mean ice crystal size was plotted against dasher displacement (Figure 4.1.7), viscosity (Figure 4.1.8), and the mean and variance in residence time (Figure 4.1.9). All correlations were low ($R^2 \leq 0.22$).

Table 4.1.3. Effect of dasher assembly on ice crystal size for hardened sorbet. Throughput rate = 190 L/h, overrun = 0%, dasher speed = 300 RPM (unless noted), and draw temperature = -6°C .

Dasher Assembly	Mean Diameter (μm)	Standard Deviation in Diameter (μm)
Solid	35.1 \pm 4.0 ^A	12.6 \pm 1.6 ^A
Solid (200 RPM)	38.7 \pm 2.2 ^A	15.2 \pm 1.2 ^A
Multi + Solid	35.1 \pm 3.6 ^A	12.8 \pm 0.9 ^A
Standard + Solid	33.1 \pm 1.6 ^A	12.2 \pm 0.5 ^A
Multi + Wing	32.0 \pm 2.4 ^A	12.9 \pm 0.4 ^A
Standard + Wing	33.9 \pm 3.4 ^A	14.3 \pm 1.7 ^A

^A Within a column, means without a common uppercase superscript differ ($P < 0.05$) due to dasher.

* Hardened ice crystal diameter mean and variance evaluated at -15°C .

\pm Values indicate standard deviation for 3 replicates.

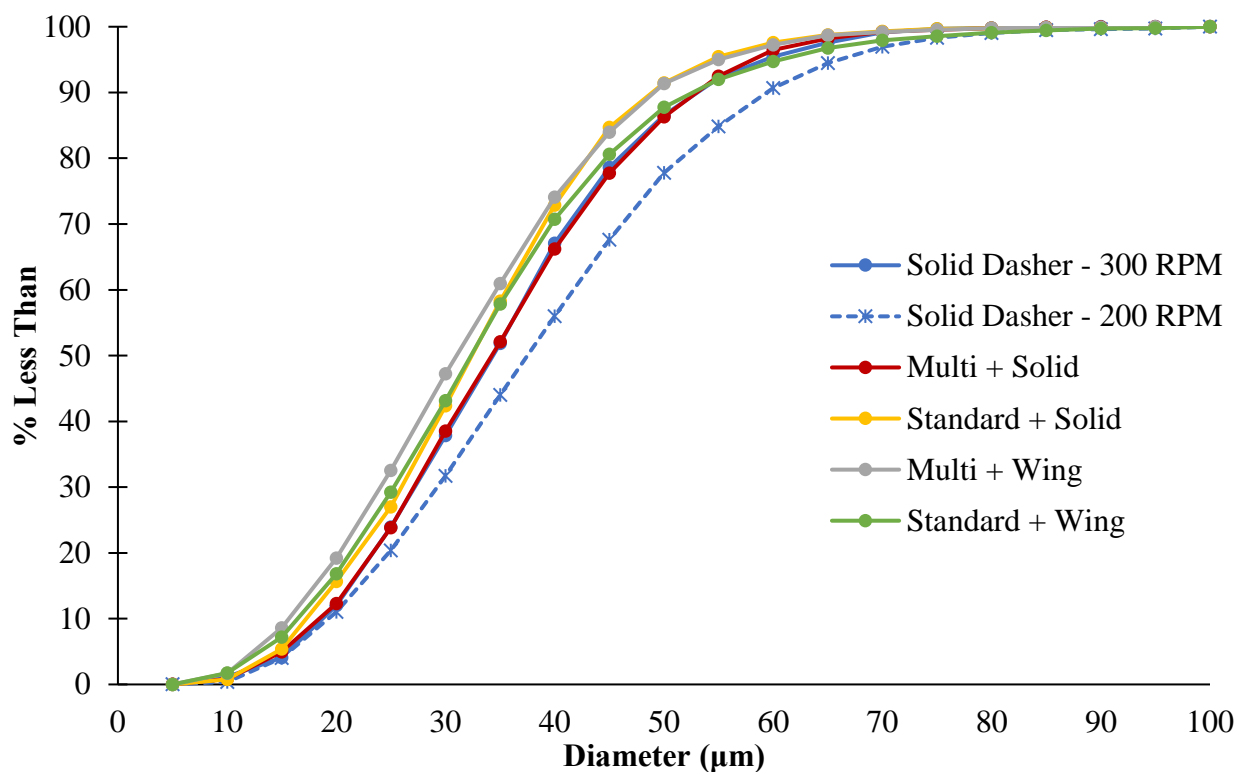


Figure 4.1.6. Cumulative ice crystal size distributions as a function of dasher assembly for hardened sorbet. Throughput rate = 190 L/h, overrun = 0%, dasher speed = 300 RPM (unless noted), draw temperature = -6°C .

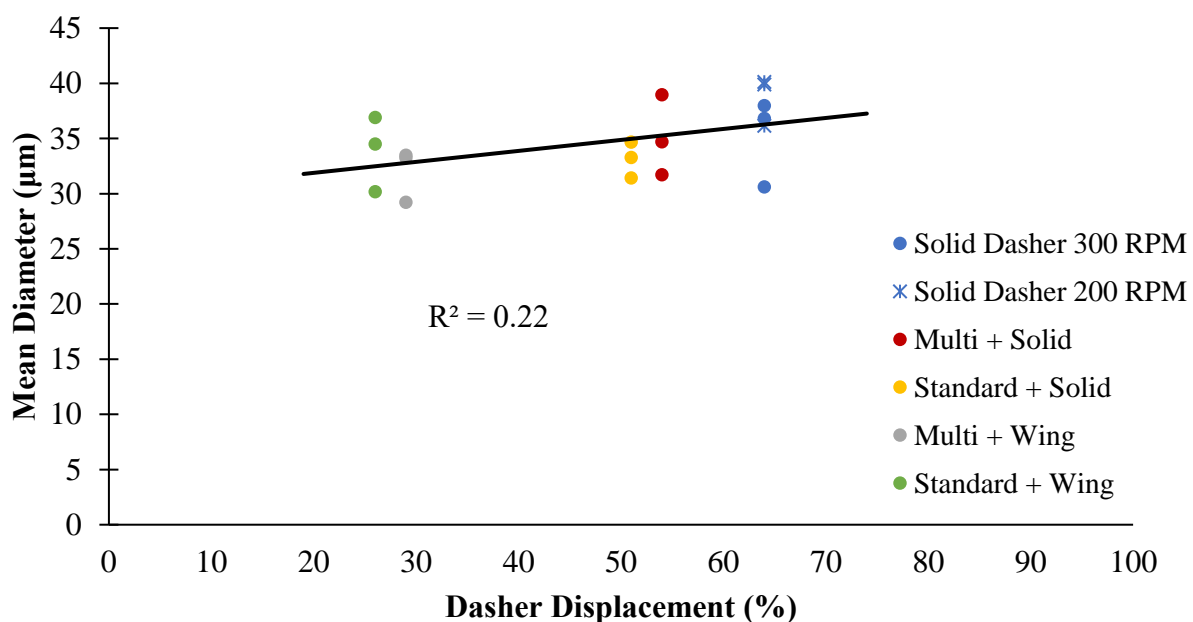


Figure 4.1.7. Correlation between dasher displacement and ice crystal size distribution as a function of dasher assembly for hardened sorbet.

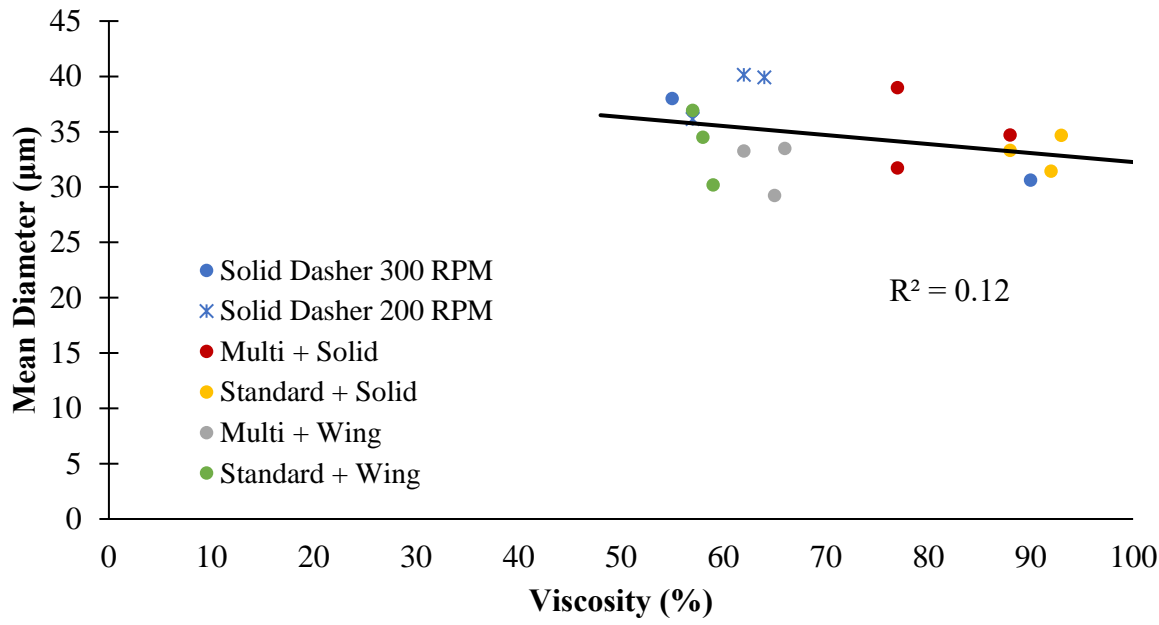


Figure 4.1.8. Correlation between viscosity, (measured as the torque on the dasher motor as a percentage of its total capacity), and ice crystal size distribution as a function of dasher assembly for hardened sorbet.

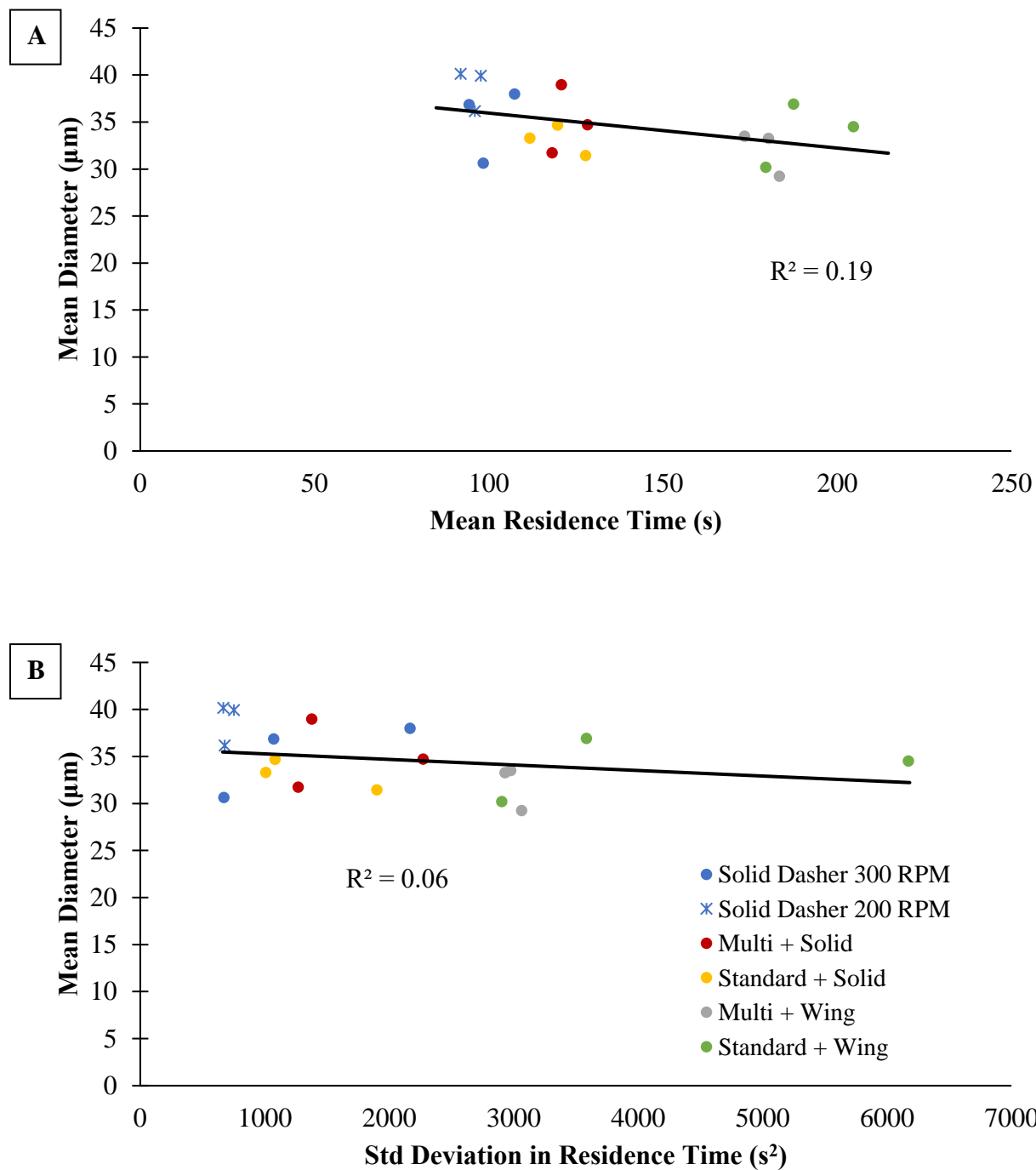


Figure 4.1.9. Correlation between ice crystal size distribution and A) mean residence time and B) standard deviation in residence time as a function of dasher assembly for hardened sorbet.

4.1.4 Summary

Russell et al. (1999) theorized that dasher design modulates ice crystal size by altering residence time. While this study found that dasher displacement is strongly correlated with residence time, the correlation between residence time and ice crystal size was weak. Differences in ice crystal size may only be observable above a certain threshold of difference in mean residence time. The largest difference in mean residence time, which was between the solid dasher and dasher assemblies containing a wing beater, was about 1.5 min. The largest difference in the average residence time in the Russell et al. (1999) study was greater than 3 min. Another consideration is that dasher displacement not only changes the average residence time but also the working volume of the freezing cylinder and the distance that heat must be conducted while the heat exchange area (i.e., the cylinder wall) remains the same. This will have effects on mass and heat transfer, important determinants of ice crystallization in an SSF.

4.2 RHEOLOGICAL CHARACTERIZATION OF A MODEL FOR THE FREEZE CONCENTRATED SERUM PHASE OF ICE CREAM

4.2.1 Freezing Curve, Moisture, and Freezing Point of Model Samples

The freezing point depression for the original ice cream mix was calculated as detailed in section 3.4.2. The freezing curve for the mix (Figure 4.2.1) was then generated by accounting for the water that would be removed from the serum phase as it is frozen to ice, a process known as freeze concentration (FC), and calculating the freezing point depression of the unfrozen serum phase at each FC. Models for the unfrozen phase of ice cream at different levels of FC were then produced by removing 0%, 10%, 20%, 30%, 40%, and 50% of water from the original ice cream mix. The moisture content and freezing points based on the freezing curve for each model FC are in Table 4.2.1. Moisture was within 1% of the target moisture content for each of the unfrozen phase models for FC.

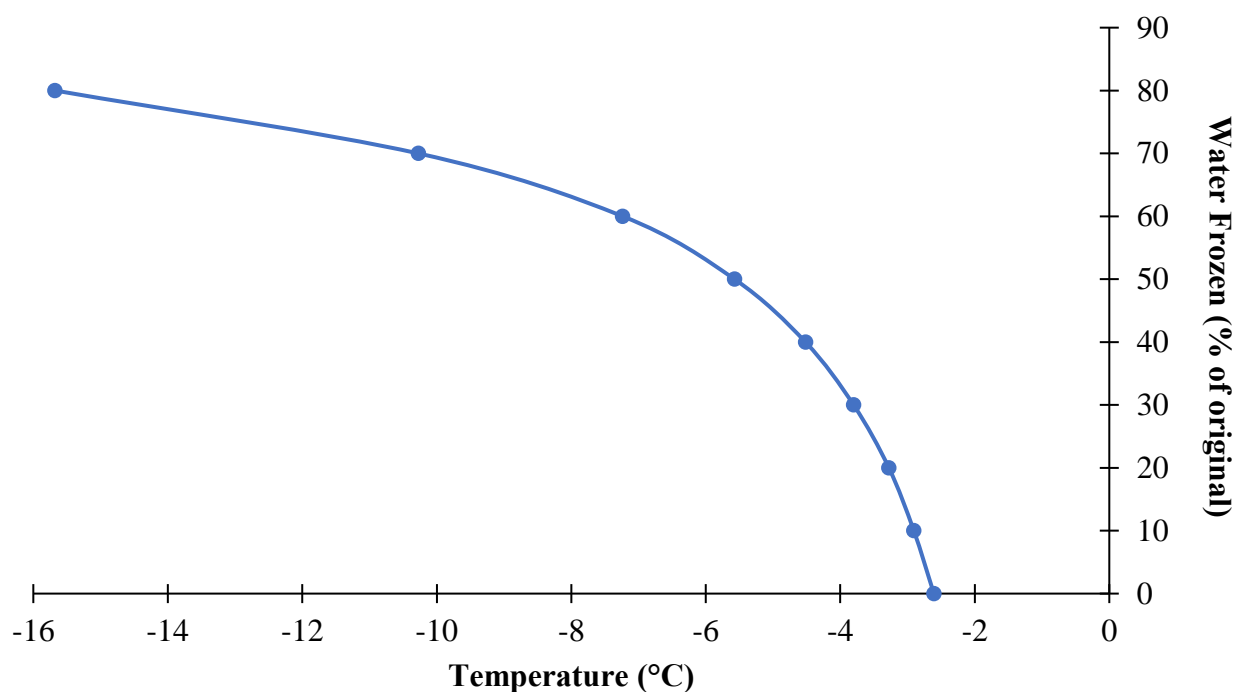


Figure 4.2.1. Freezing curve for ice cream mix calculated using method detailed by Goff and Hartel (2013).

Table 4.2.1. Moisture content and calculated freezing point for ice cream mix with water removed to create models of unfrozen phase as a result of freeze concentration.

% Water Removed	Moisture (%)	Freezing Point* (°C)
0% (Mix)	62.0 ± 0.1	-2.6
10%	56.7 ± 0.1	-2.9
20%	50.4 ± 0.2	-3.3
30%	44.1 ± 0.4	-3.8
40%	37.6 ± 0.4	-4.5
50%	31.1 ± 0.3	-5.6

* Calculated using method detailed by Goff and Hartel (2013).

4.2.2 Rheological Characteristics

The rheological characteristics of ice cream mix and the model unfrozen phase at different FCs and temperatures were tested by performing shear sweeps from 100 to 1 s⁻¹. Shear sweeps carried out at 5°C, 2.5°C, 0°C, and -2.5°C as a function of % water removed are depicted in Figures 4.2.2 – 4.2.5, respectively. These curves shifted up as % water removed was increased, indicating an increase in shear stress of the modeled unfrozen phase. In addition to the shear sweeps performed at the temperatures stated above, shear sweeps were also performed at the nearest 0.5°C and 1°C above the calculated freezing point to characterize the rheological properties across the range likely to be observed for the unfrozen phase in a continuous SSF (Appendix A). The apparent viscosity η was then plotted against shear rate as a function of FC and temperature (Figures 4.2.6 – 4.2.11). As expected, the apparent viscosity decreased with increasing shear rate across all treatments. Both shear stress and apparent viscosity increased dramatically with increasing FC. Decreasing the temperature within each FC model increased shear stress and apparent viscosity slightly, with larger differences observed for higher levels of FC.

To confirm these observations statistically, the apparent viscosity η at a shear rate of 50 s⁻¹ was compared as a function of % water removed and temperature (5°C, 2.5°C, 0°C, and -2.5°C only) (Figure 4.2.12). There was no significant increase in viscosity with decreasing temperature for samples modeling 30% FC or less. Samples modeling 40% and 50% FC were

more sensitive to temperature due to a significant interaction effect, with increasing apparent viscosity observed as temperature decreased. No significant differences in apparent viscosity were observed for samples modeling $\leq 20\%$ FC. There was a dramatic increase in viscosity between the 30%, 40%, and 50% FC models.

Goff et al. (1995) and Bolliger et al. (2000b) also modeled freeze concentration. Though the apparent viscosity was measured at the same shear rate and within the same temperature range as in this study, Goff et al. (1995) reported lower apparent viscosity values. Their study also found that a dramatic increase in apparent viscosity took place later in freeze concentration, around 60% FC. This difference is likely because the ice cream formulation used in Goff et al. (1995) only used guar gum as a stabilizer, whereas the system used in the present study also contained locust bean gum and carrageenan, which contributes to higher viscosity in ice cream mix (Cottrell et al., 1980). Bolliger et al. (2000b), who used carrageenan as well as guar gum, reported a dramatic increase in viscosity between 30 to 40% FC, which is more like the results of the present study.

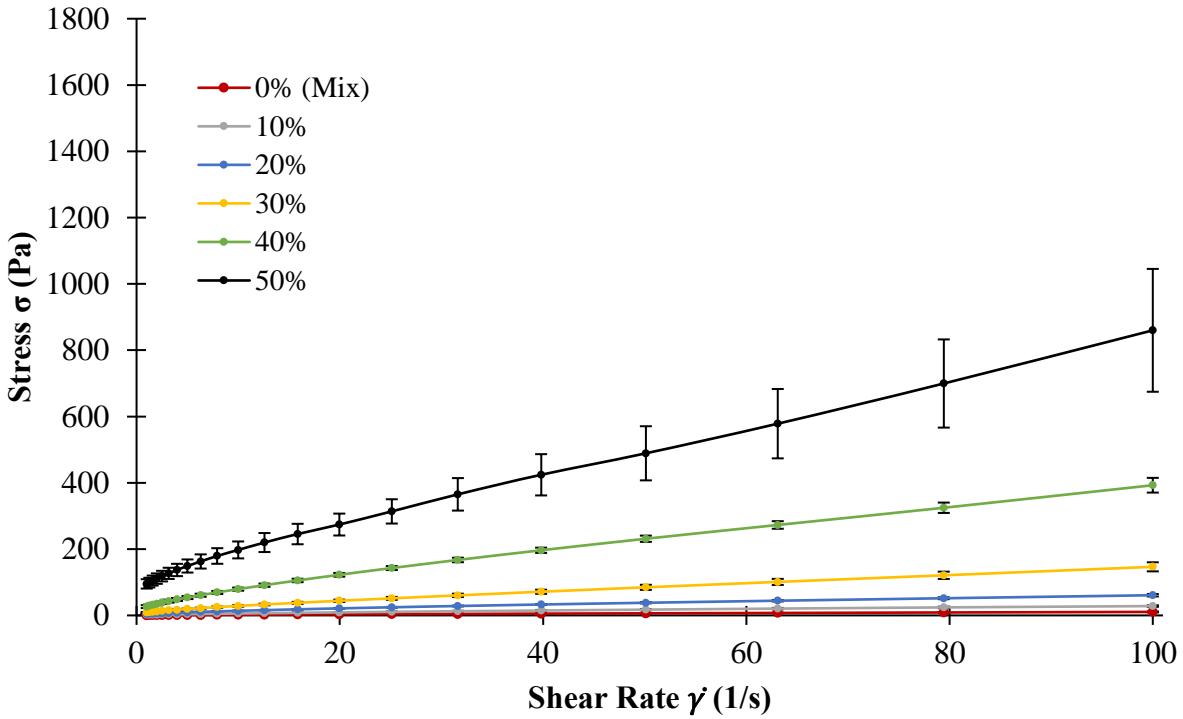


Figure 4.2.2. Shear sweep curves for model unfrozen phase of ice cream at 5°C as a function of % water removed. Error bars represent standard deviation for 3 replicates.

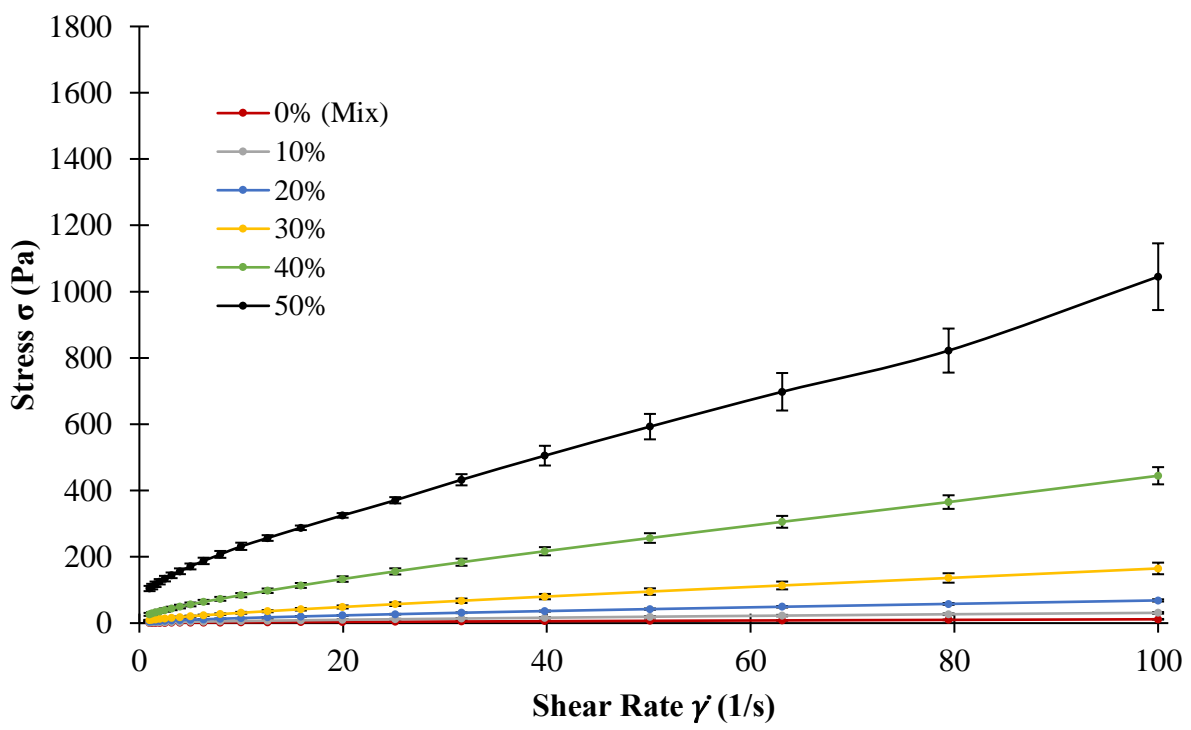


Figure 4.2.3. Shear sweep curves for model unfrozen phase of ice cream at 2.5°C as a function of % water removed. Error bars represent standard deviation for 3 replicates.

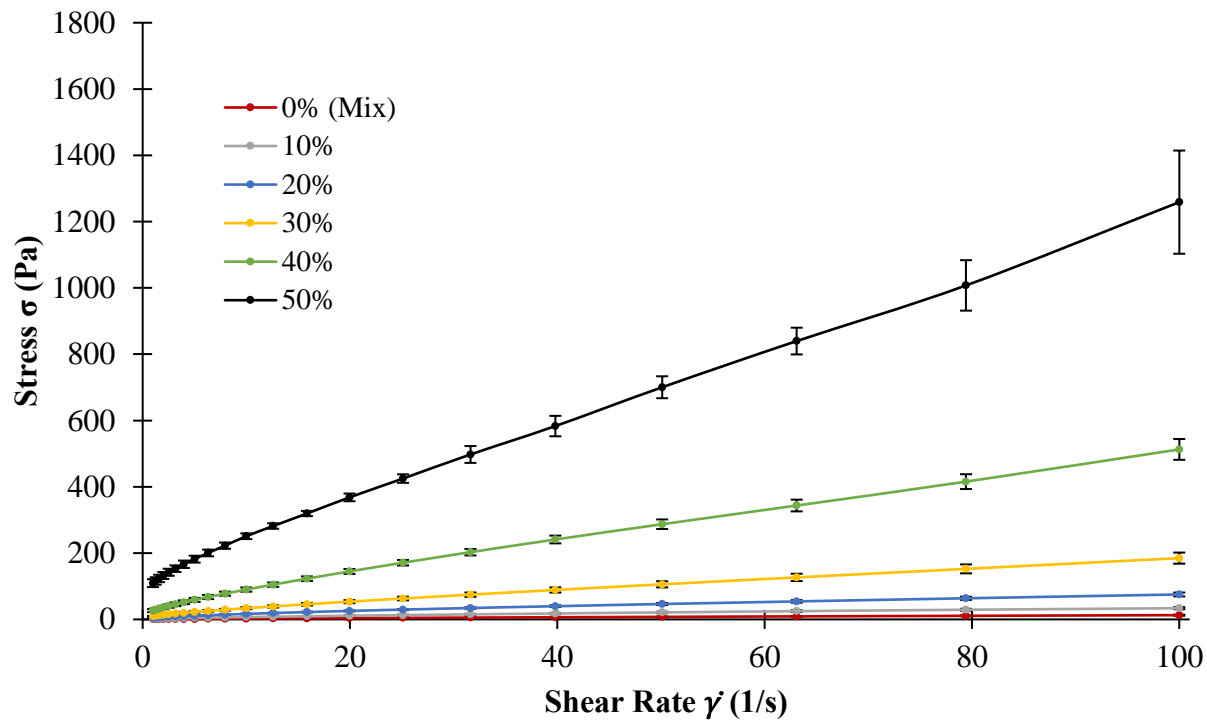


Figure 4.2.4. Shear sweep curves for model unfrozen phase of ice cream at 0°C as a function of % water removed. Error bars represent standard deviation for 3 replicates.

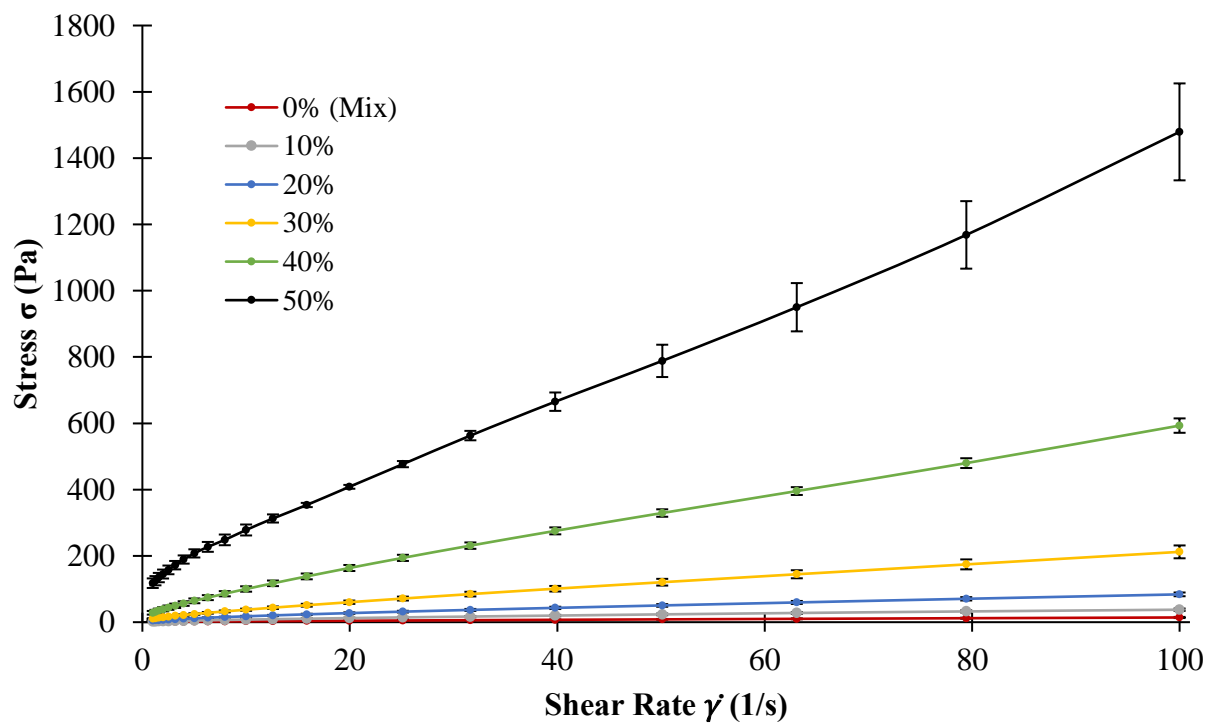


Figure 4.2.5. Shear sweep curves for model unfrozen phase of ice cream at -2.5°C as a function of % water removed. Error bars represent standard deviation for 3 replicates.

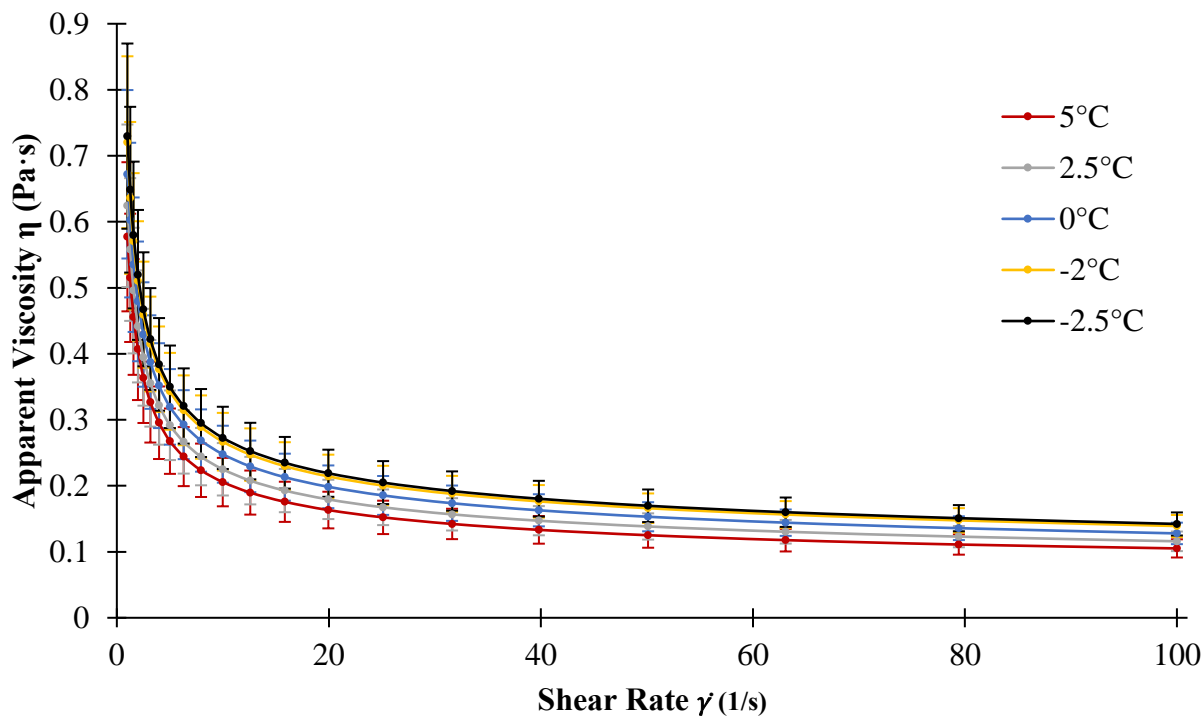


Figure 4.2.6. Viscosity as a function of shear rate and temperature for model unfrozen phase of ice cream mix (0% water removed). Error bars represent standard deviation for 3 replicates.

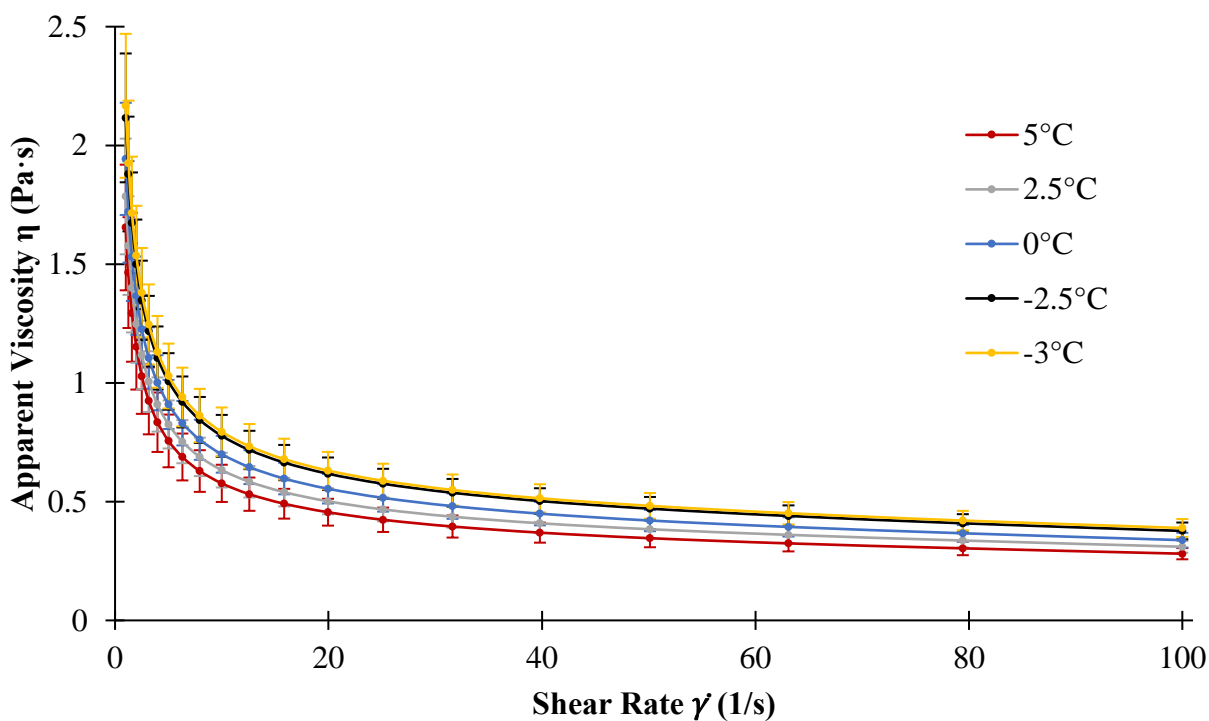


Figure 4.2.7. Viscosity as a function of shear rate and temperature for model unfrozen phase of ice cream at 10% freeze concentration (ice cream mix with 10% of water removed). Error bars represent standard deviation for 3 replicates.

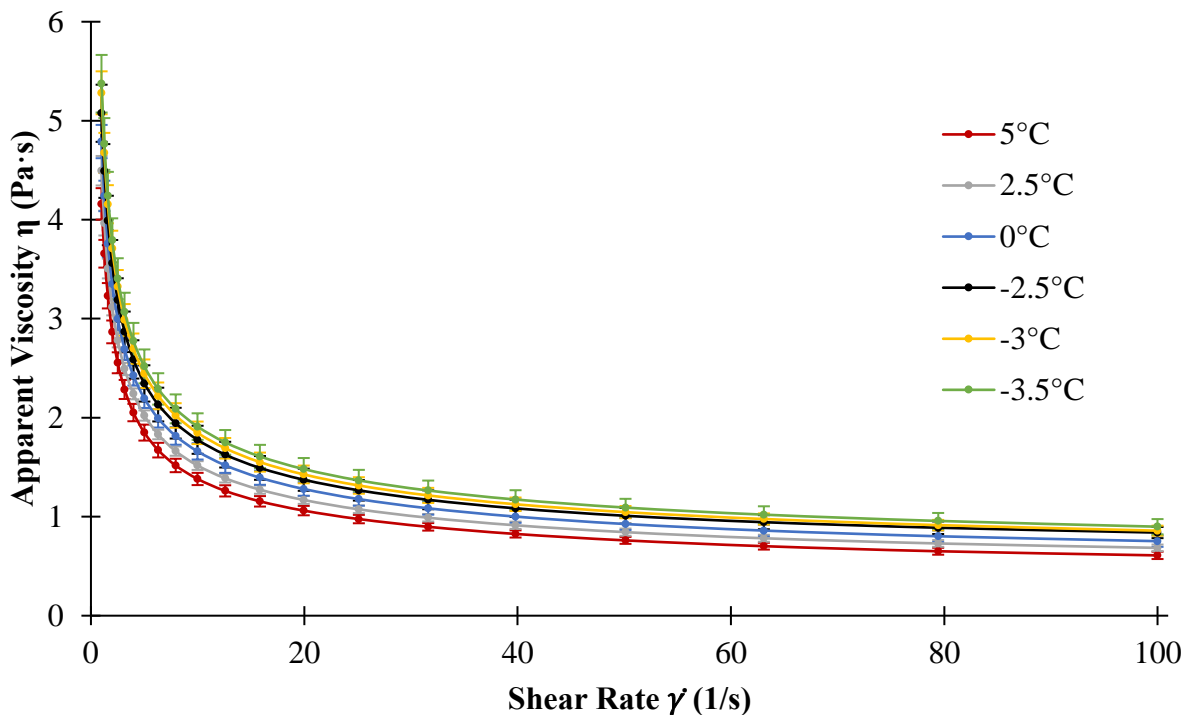


Figure 4.2.8. Viscosity as a function of shear rate and temperature for model unfrozen phase of ice cream at 20% freeze concentration (ice cream mix with 20% of water removed). Error bars represent standard deviation for 3 replicates.

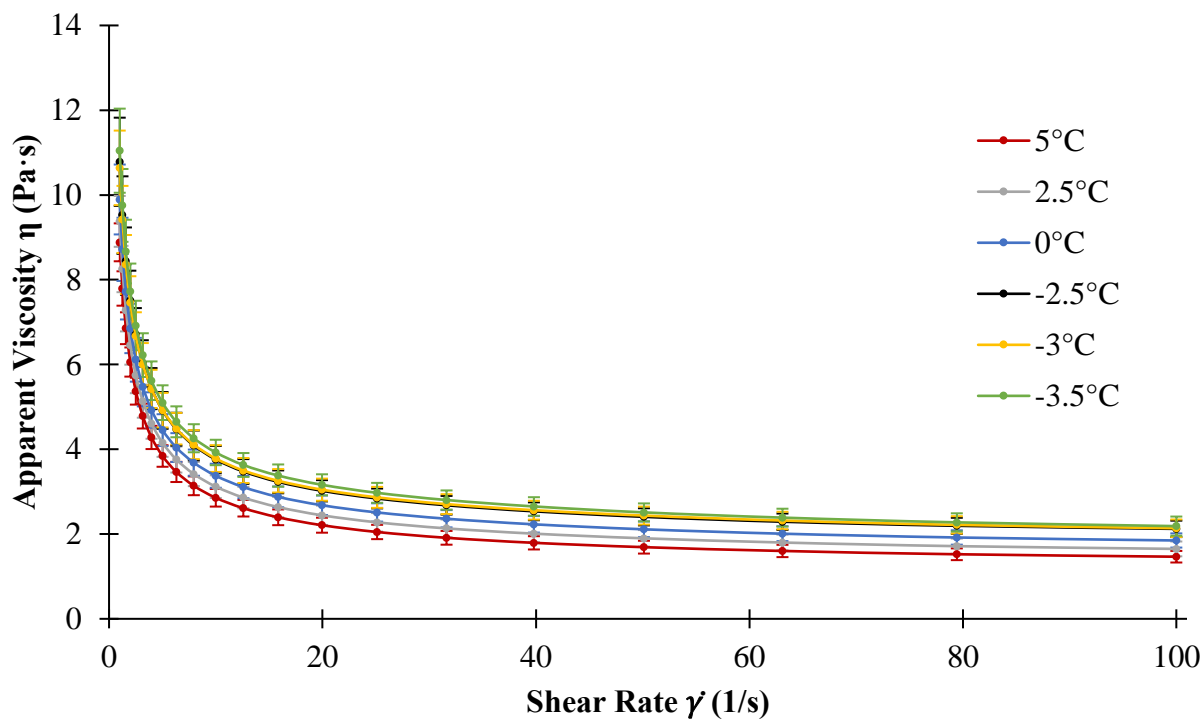


Figure 4.2.9. Viscosity as a function of shear rate and temperature for model unfrozen phase of ice cream at 30% freeze concentration (ice cream mix with 30% of water removed). Error bars represent standard deviation for 3 replicates.

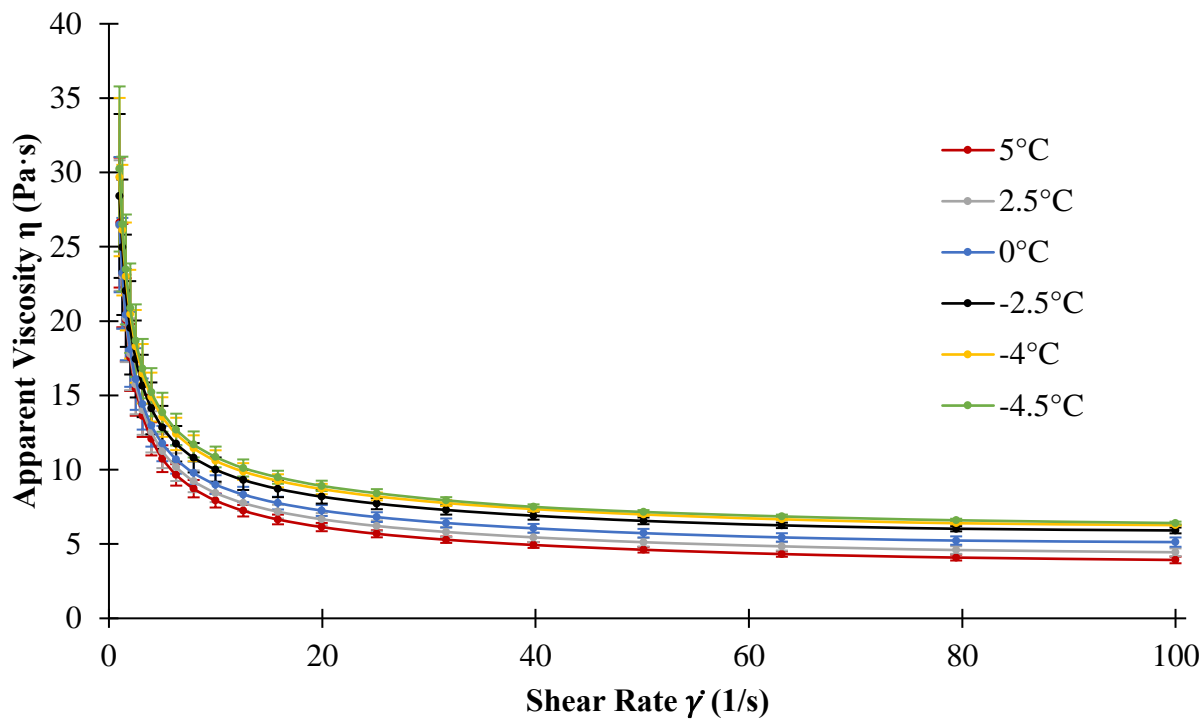


Figure 4.2.10. Viscosity as a function of shear rate and temperature for model unfrozen phase of ice cream at 40% freeze concentration (ice cream mix with 40% of water removed). Error bars represent standard deviation for 3 replicates.

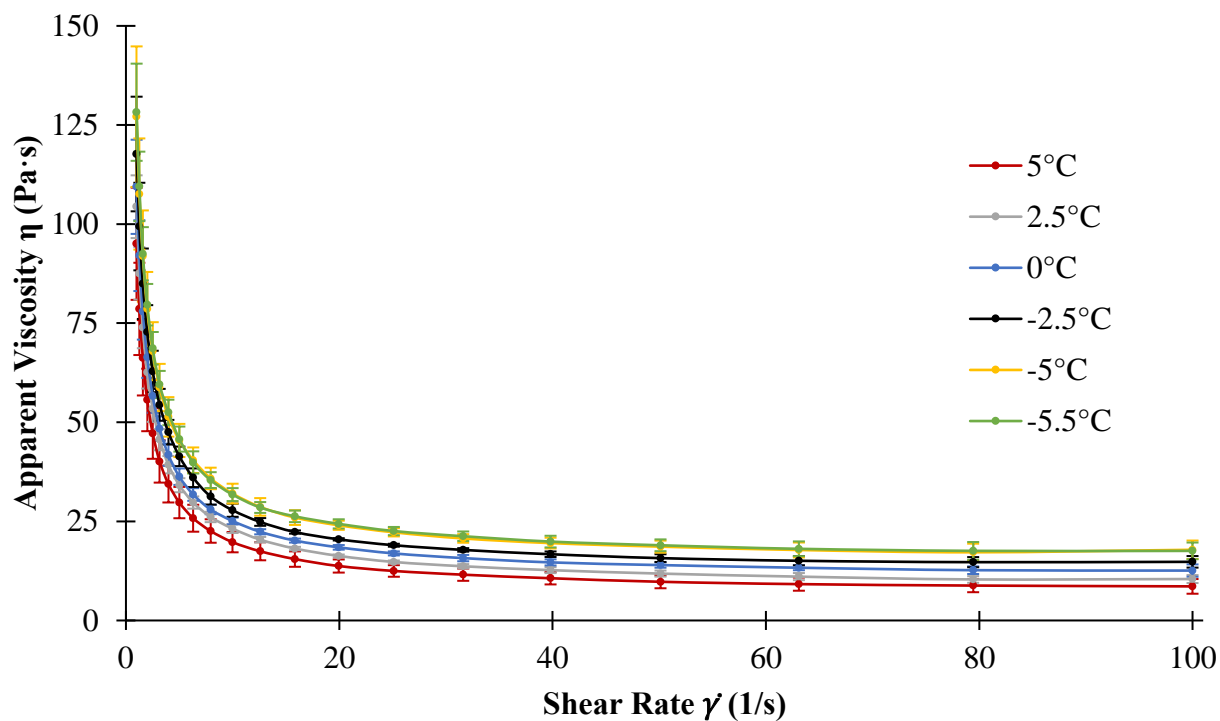


Figure 4.2.11. Viscosity as a function of shear rate and temperature for model unfrozen phase of ice cream at 50% freeze concentration (ice cream mix with 50% of water removed). Error bars represent standard deviation for 3 replicates.

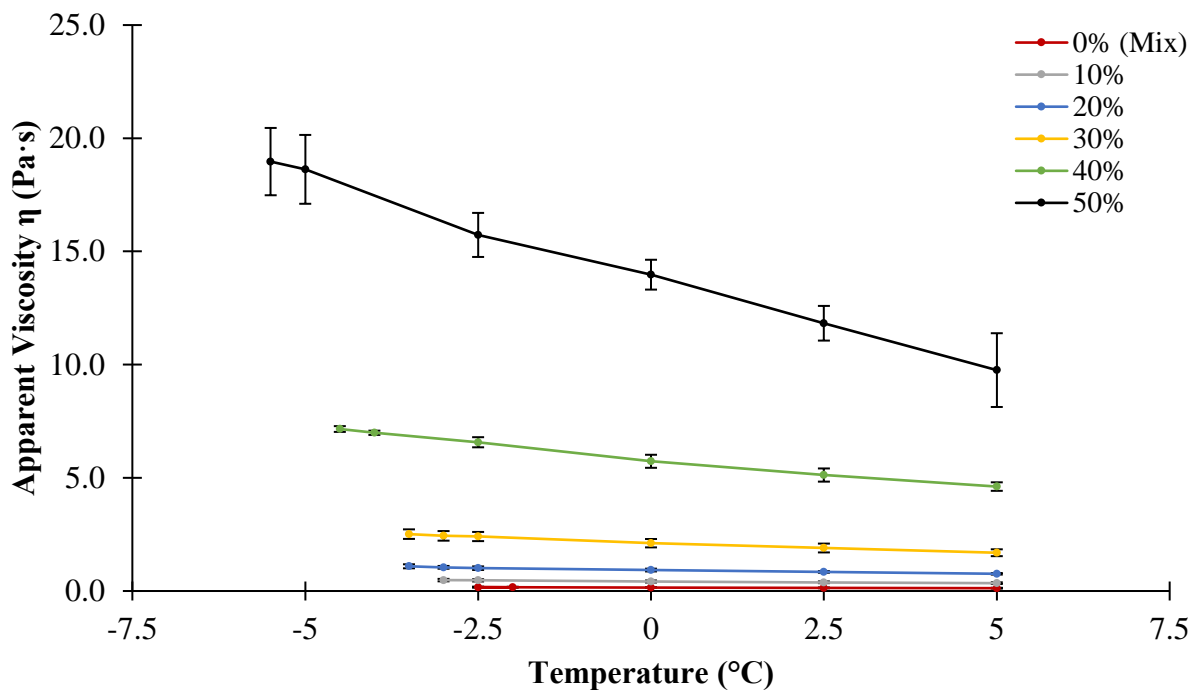


Figure 4.2.12. Apparent viscosity at shear rate of 50 s^{-1} for ice cream mix as a function of % water removed and temperature. Error bars represent standard deviation for 3 replicates.

4.2.3 Summary

The goal of this experiment was to model the serum phase as water is removed, which occurs when water frozen out of the unfrozen serum phase during continuous freezing. The rheological results could be used in computational fluid dynamics (CFD) modeling to calculate the shear forces that ice cream would experience throughout a scraped surface freezer under a given set of processing conditions. Determining the amount of shear a product undergoes may assist in predicting microstructural outcomes.

Unsurprisingly, this experiment found that FC models experienced an increase in apparent viscosity with increasing water removal. This increase in apparent viscosity was more rapid within the range of the typical freeze concentration that is expected at the outlet of a continuous freezer, which is about 40-50% (Cook and Hartel, 2010). Additionally, apparent viscosity was more sensitive to changes in temperature at 40% and 50% FC. There are several important limitations

to note about this study. While this contributes to our understanding of the serum phase of ice cream, it cannot be directly applied to ice cream as a whole as the presence and amount of air affect the rheological properties of ice cream (Goff et al., 1995; Freire et al., 2020). Interactions between fat, air, protein, and emulsifiers will also change the distributions of these components within the serum phase of ice cream. The lamellae of the unfrozen serum phase between air cells in ice cream are also significantly smaller than the gap in the concentric cylinders geometry used in this study (Goff et al., 1999; Liu et al., 2023), which will affect shear.

4.3 MICROSTRUCTURAL EVOLUTION OF ICE CREAM AFTER START-UP IN A CONTINUOUS SCRAPED SURFACE FREEZER

The purpose of this experiment was to evaluate the development in microstructure that occurs during start-up of a continuous scraped surface freezer. During start-up, mix is pumped continuously through the freezer as the refrigeration system, dasher motor, and air injection unit are all powered on. This allows for the nucleation and growth of ice crystals, incorporation of air cells, and destabilization of fat globules to begin. The changes in each of the microstructural elements were monitored to determine how long it takes for the overall microstructure to stabilize after freezer start-up. This data was intended to inform experiments conducted in section 4.4, specifically how long the freezer would need to be operated prior to collecting samples for microstructural analysis. As such, the freezer conditions that gave the longest theoretical residence time for these experiments were utilized. These conditions included the use of the standard dasher + wing beater configuration, throughput rate = 190 L/h, overrun = 75%, and dasher speed = 200 RPM. Assuming plug flow conditions, the theoretical residence time under these parameters would be 4.9 min. Time to steady state conditions is generally taken to be 10x the residence time, therefore giving a time to steady state conditions of 49 min, although steady state is often reached before this. To be conservative, the freezer conditions and microstructure were monitored for a total of 78 min.

4.3.1 Processing Conditions

Prior to freezer start-up, the freezer barrel was “charged”, or filled with mix which was at a temperature of approximately 5°C. The draw temperature (Figure 4.3.1) and viscosity (Figure 4.3.2), which is a function of the torque on dasher motor as percentage of its total capacity, were

then monitored over time. The viscosity is indirectly related to the amount of ice in the freezer barrel, and was manipulated to indirectly maintain the draw temperature at a target of -5.5°C . The temperature of the product at the outlet at the time of freezer start-up was approximately 14°C , likely because there was heat transfer from the freezer equipment (which starts at room temperature) to the product. Although there was little change in draw temperature 1 min after freezer start-up, the temperature of product at the outlet decreased rapidly from 14°C to -5°C over the first 5 min after freezer start-up and equilibrated at -5.5°C approximately 10 min after freezer start-up. Viscosity changed more rapidly than draw temperature during the first min of freezing, increasing from approximately 6% to 18%. It also appears there was a trend for the viscosity to take longer to equilibrate than the draw temperature. The overrun was also monitored over time (Figure 4.3.3), with a target of 75% for the final product. The overrun was controlled indirectly by setting mix flow and air flow rates at values that would theoretically achieve the target overrun. Overrun increased for the first 6 minutes of freezing, at which point it exceeded the target overrun by about 10%. The amount of overrun then decreased from ~ 6 to 12 min after start-up before equilibrating around 73%, slightly below the target overrun value.

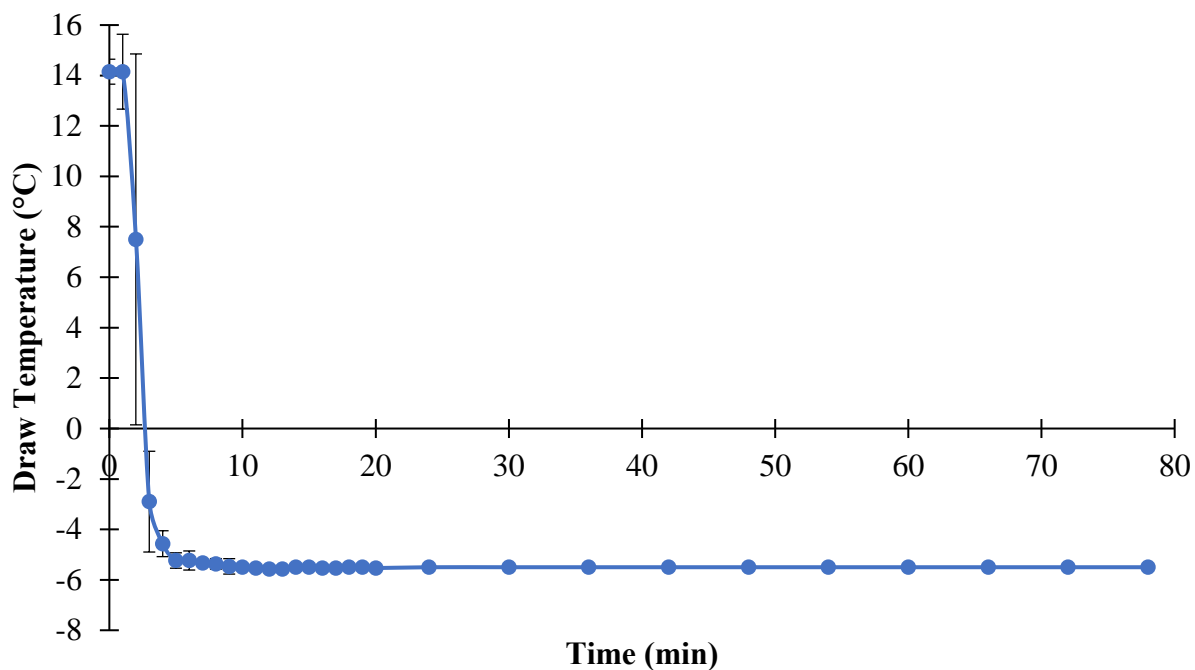


Figure 4.3.1. Draw temperature over time, where $t = 0$ min is freezer start-up. Target processing conditions were throughput rate = 200 L/h, draw temperature = -5.5°C , overrun = 75%, and dasher speed = 200 RPM.

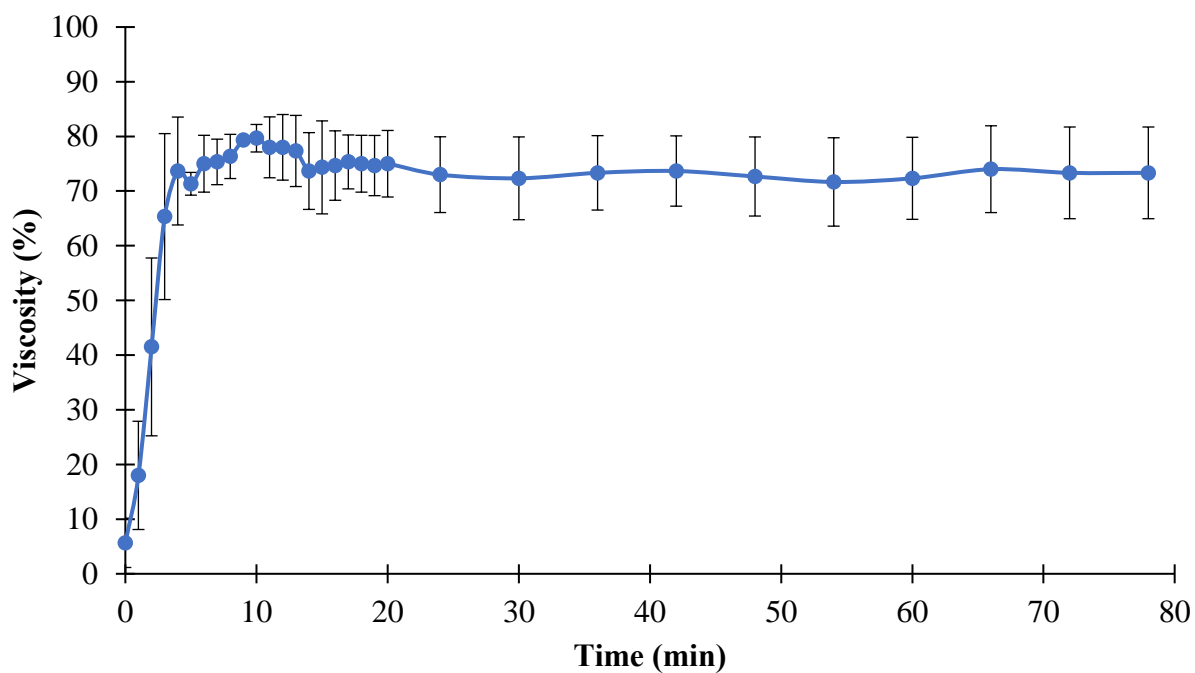


Figure 4.3.2. Viscosity, measured as torque on dasher motor as percentage of total capacity, over time where $t = 0$ is freezer start-up. Target processing conditions were throughput rate = 200 L/h, draw temperature = -5.5°C , overrun = 75%, and dasher speed = 200 RPM.

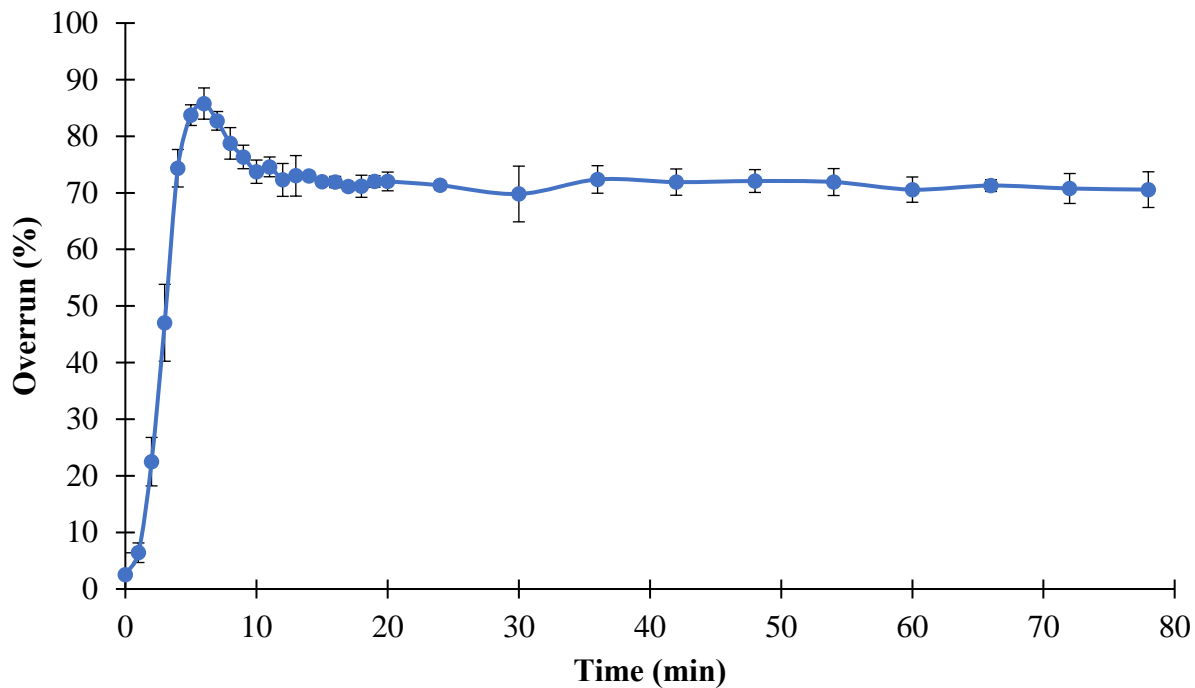


Figure 4.3.3. Overrun over time, where $t = 0$ is freezer start-up. Target processing conditions were throughput rate = 200 L/h, draw temperature = -5.5°C , overrun = 75%, and dasher speed = 200 RPM.

4.3.2 Microstructural Evolution Over Time

4.3.2.1 Ice Crystal Size

Ice crystal size at draw was monitored (Figure 4.3.4) by placing samples in a refrigerated glove box set at draw temperature (-5.5°C) immediately after being collected at draw. Samples were evaluated every 6 min after freezer start-up, which was the highest frequency of measurement that the method allowed. Statistically, there was not a change in the size over time after 6 min.

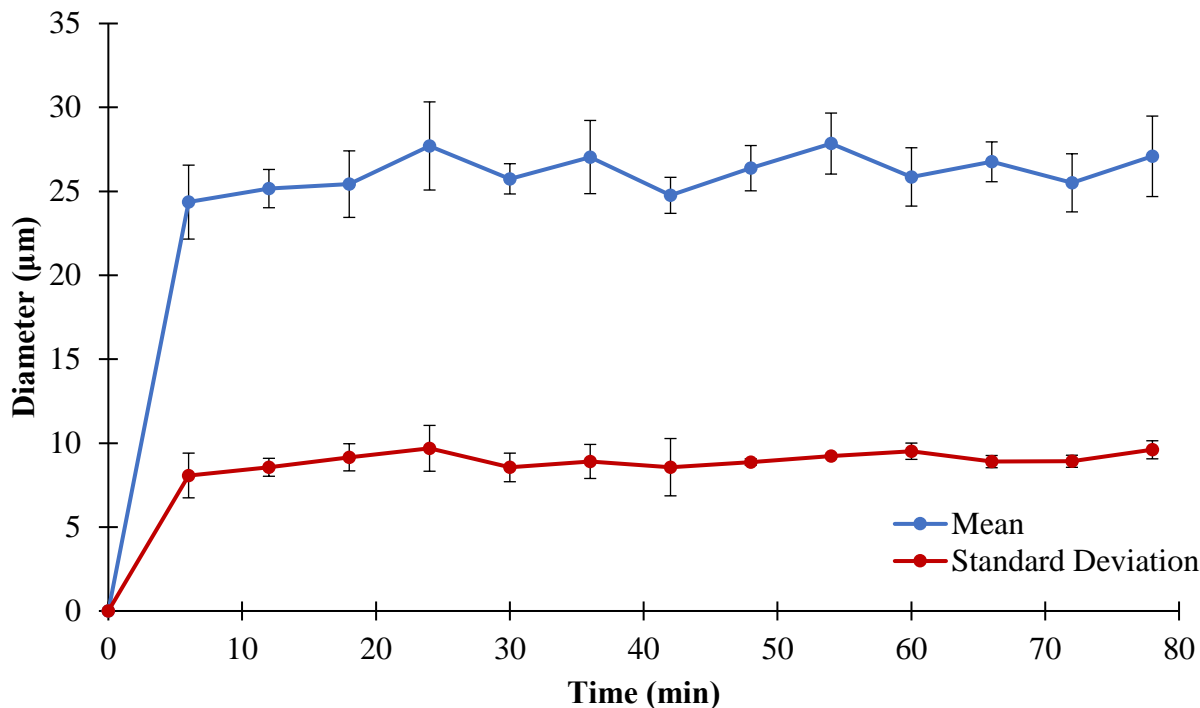


Figure 4.3.4. Evolution of ice crystal size in ice cream immediately after draw, where $t = 0$ min is freezer start-up. Target processing conditions were throughput rate = 200 L/h, draw temperature = -5.5°C , overrun = 75%, and dasher speed = 200 RPM. Draw ice crystal size analyzed at -5.5°C .

Ice crystal size was also evaluated in hardened ice cream samples. Samples were collected every minute for the first 20 min after freezer start-up (Figure 4.3.5) and every 6 min for 78 min (Figure 4.3.6). During the first 3 minutes after freezer start-up, ice crystals in hardened samples were large and irregular in shape. Their shape was comparable to what was observed by Caillet et al. (2003) in samples that had been drawn from a SSF at a temperature above the freezing point of the mix. Indeed, in this experiment the draw temperature during the first two min after freezer start-up was above the freezing point of the ice cream mix, which was calculated as -2.6°C using the method described by Goff and Hartel (2013). Even if ice crystals were being nucleated at the supercooled surface of the cylinder wall during this time frame, the bulk mix in the center of the would have melted any ice crystals before samples were collected at draw. Therefore, these large ice crystals are most likely a product of quiescent freezing during hardening.

Due to the size and shape of the ice crystals observed during the first 3 min after start-up, their size could not be measured quantitatively. Calliet et al. (2003) also found that optical microscopy was not a suitable method for evaluating ice crystals of this size. However, 4 min after freezer start-up, the ice crystals were smaller and became more disc-like in shape, suggesting that these ice crystals were initially formed by nucleation in the SSF. This is corroborated by the fact that the measured draw temperature was below the freezing point of the ice cream mix after 3 min. Ice crystal size could then be quantitatively evaluated over time (Figure 4.3.7). At 4 min after freezer start-up, the hardened ice crystal mean and standard deviation in size were still relatively large. At this point, the draw temperature had only reached -4.6°C , almost 1°C higher than the target draw temperature. This suggests that the ice content of the ice cream at draw was relatively low and likely contained fewer nuclei than samples that were collected at a draw temperature of -5.5°C . Therefore, when the samples collected at 4 min were hardened, the presence of fewer nuclei resulted in larger ice crystals. This was also observed by Amador et al. (2017) when evaluating the effect of draw temperature on hardened ice crystal size in ice cream. The mean and standard deviation in ice crystal size did not differ significantly after 5 min post freezer start-up.

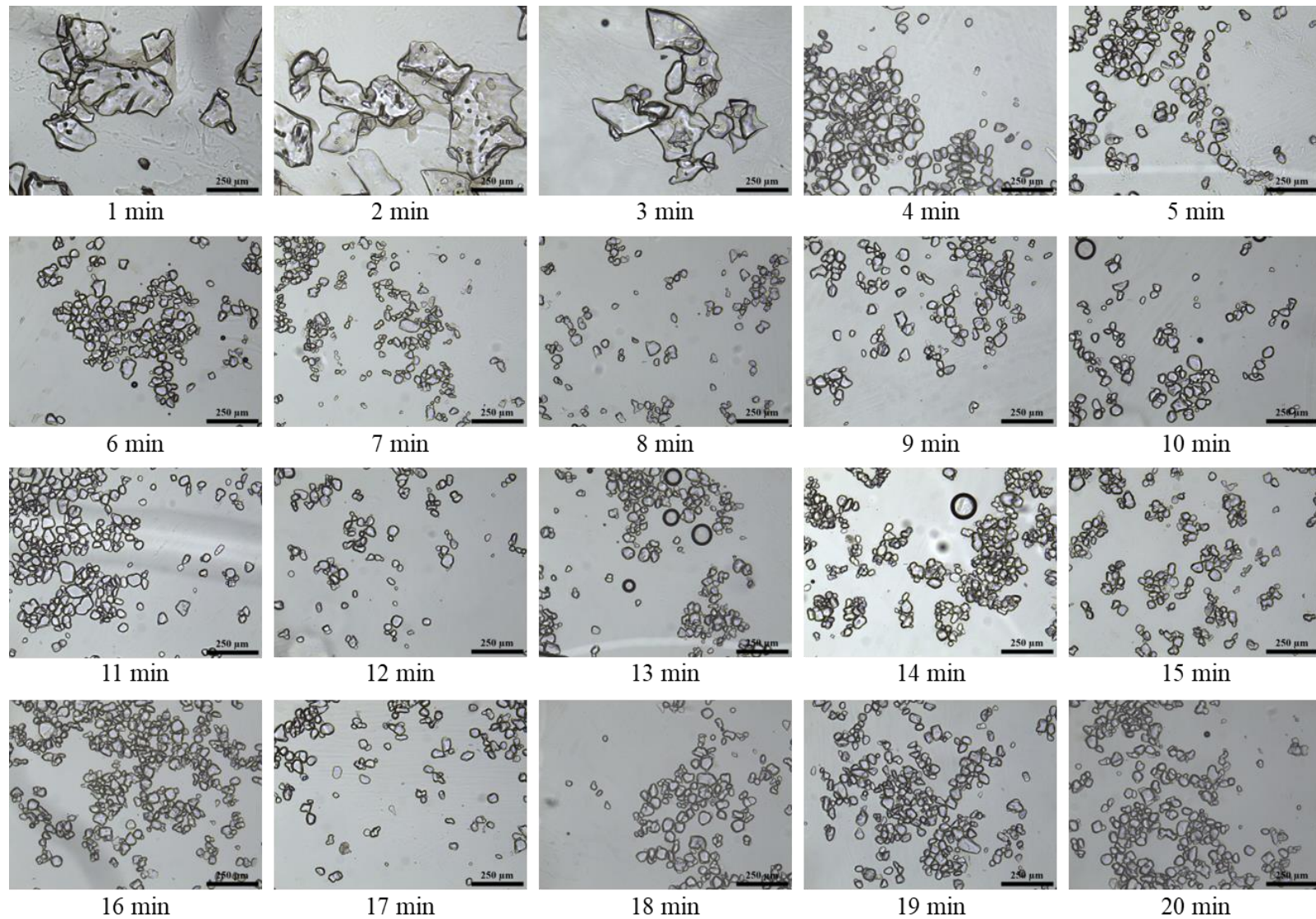


Figure 4.3.5. Optical microscopy images of ice crystals in hardened ice cream over time, where $t = 0$ min is freezer start-up. Samples collected every minute for the first 20 min of freezing. Target processing conditions were throughput rate = 200 L/h, draw temperature = -5.5°C , overrun = 75%, and dasher speed = 200 RPM. Hardened ice crystal size analyzed at -15°C .

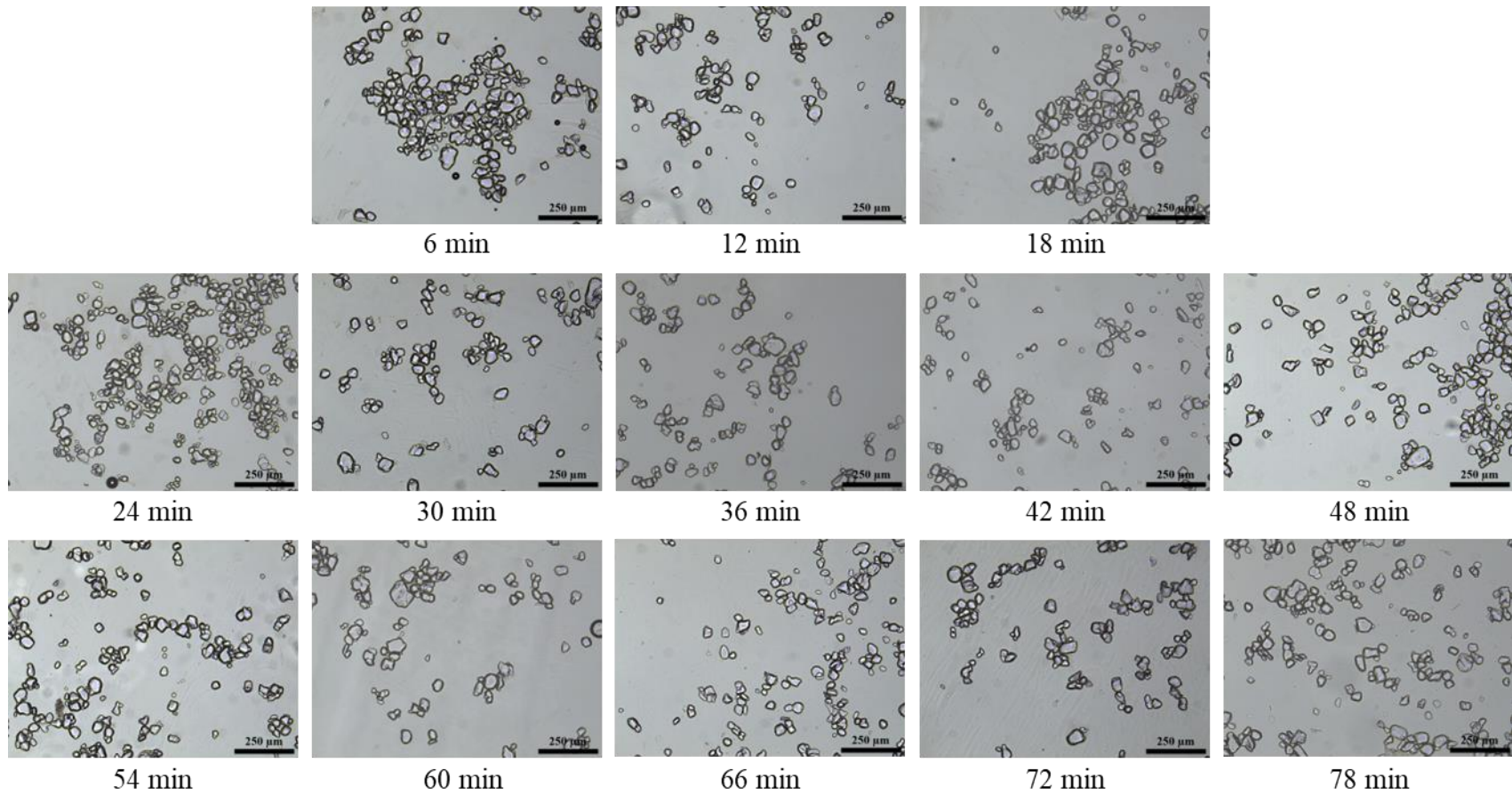


Figure 4.3.6. Optical microscopy images of ice crystals in hardened ice cream over time, where $t = 0$ min is freezer start-up. Samples collected every 6 min for 78 min. Target processing conditions were throughput rate = 200 L/h, draw temperature = -5.5°C , overrun = 75%, and dasher speed = 200 RPM. Hardened ice crystal size analyzed at -15°C .

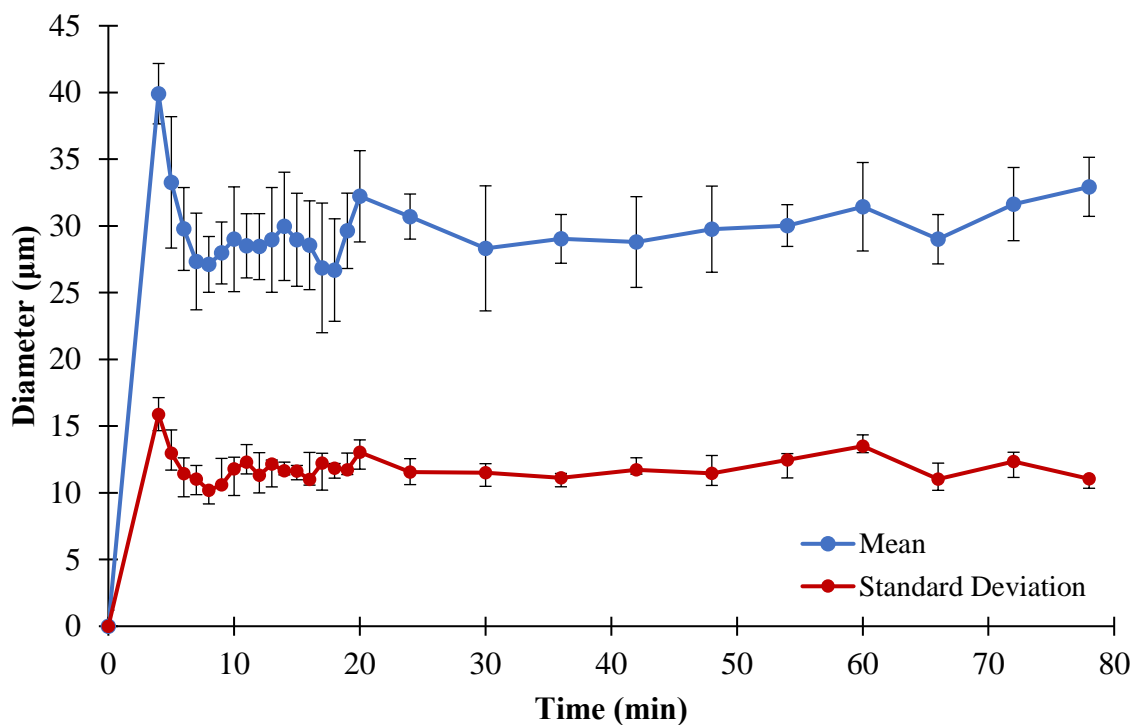


Figure 4.3.7. Evolution of ice crystal size of hardened ice cream, where $t = 0$ min is freezer start-up. Target processing conditions were throughput rate = 200 L/h, draw temperature = -5.5°C , overrun = 75%, and dasher speed = 200 RPM. Hardened ice crystal size analyzed at -15°C .

4.3.2.2 Air Cell Size

Air cell size was evaluated for hardened samples only. Samples were collected every minute for the first 20 min after freezer start-up (Figure 4.3.8) and every 6 min for 78 min (Figure 4.3.9). During the first 3 min after freezer start-up, the air cell size was not measured. This was because very few air cells were present, and the shape of air cells that were present was relatively irregular. There were no statistical differences in air cell size from 4 min to 78 min (Figure 4.3.10). Chang and Hartel (2002) observed that even in a batch freezer where the product is subject to longer periods of shear, the air cell size did not change after ~ 10 min of freezing. Air cell evolution likely occurred more slowly in the batch freezer as air was incorporated from the environment rather than being metered in through injection as it was in the continuous SSF in this experiment.

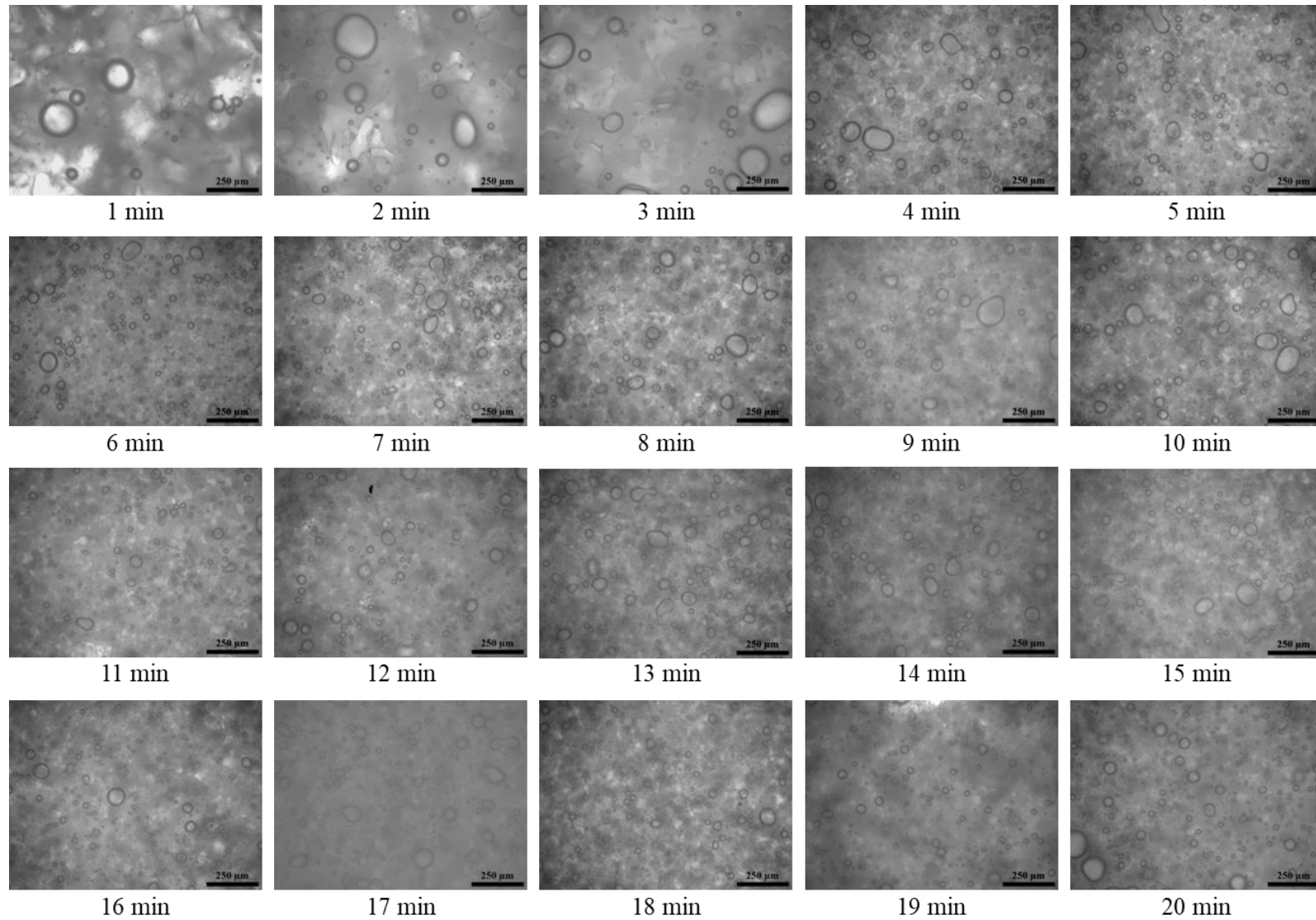


Figure 4.3.8. Optical microscopy images of air cells in hardened ice cream over time, where $t = 0$ min is freezer start-up. Samples collected every minute for the first 20 min of freezing. Target processing conditions were throughput rate = 200 L/h, draw temperature = -5.5°C , overrun = 75%, and dasher speed = 200 RPM. Hardened air cell size analyzed at -6°C .

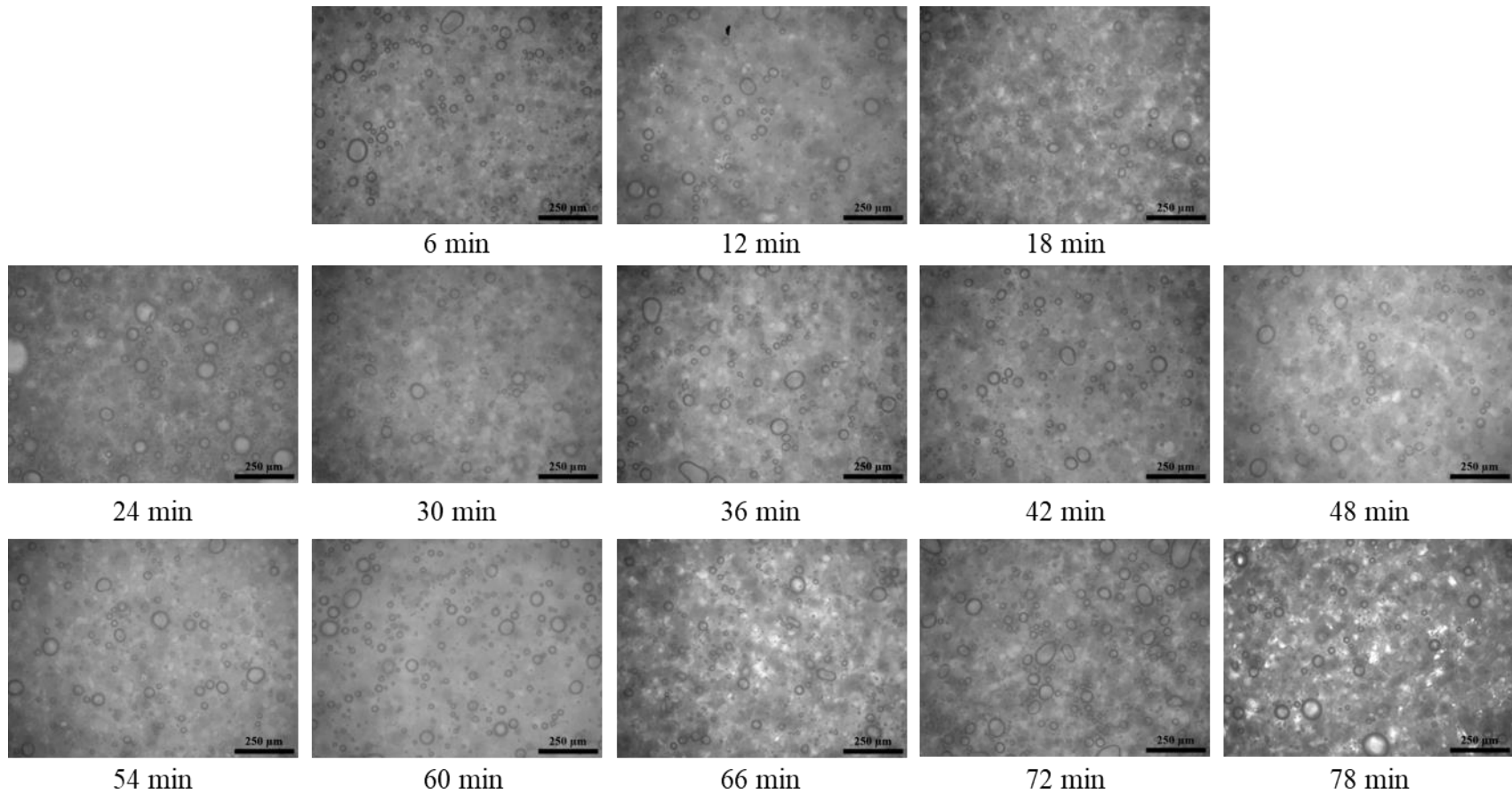


Figure 4.3.9. Optical microscopy images of air cells in hardened ice cream over time, where $t = 0$ min is freezer start-up. Samples collected every 6 min for 78 min. Target processing conditions were throughput rate = 200 L/h, draw temperature = -5.5°C , overrun = 75%, and dasher speed = 200 RPM. Hardened air cell size analyzed at -6°C .

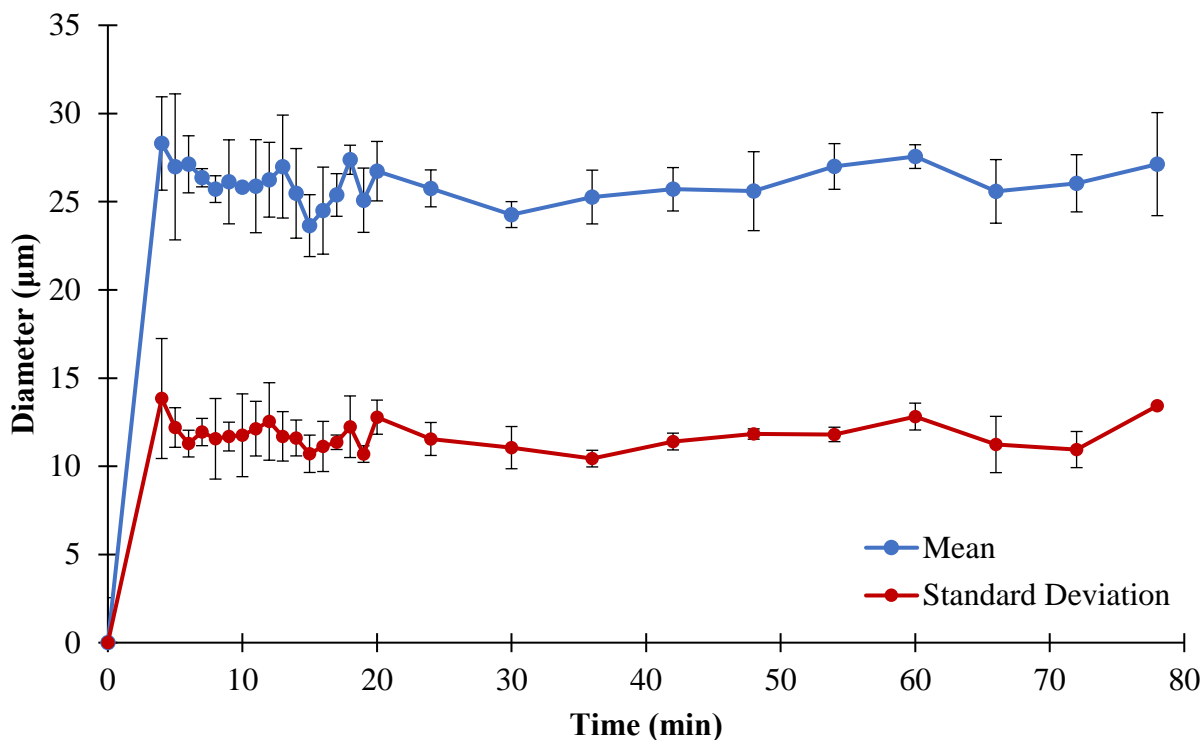


Figure 4.3.10. Evolution of air cell size of hardened ice cream, where $t = 0$ min is freezer start-up. Target processing conditions were throughput rate = 200 L/h, draw temperature = -5.5°C , overrun = 75%, and dasher speed = 200 RPM. Hardened air cell size analyzed at -6°C .

4.3.2.3 Fat Destabilization

Fat destabilization was analyzed every minute for the first 20 min (Figure 4.3.11) and every 6 min for 78 min (Figure 4.3.12) after freezer start-up. There were no significant differences in fat destabilization from 0 min to 4 min after freezer start-up (Figure 4.3.13), with fat destabilization remaining relatively low at $< 8\%$. After between 4 to 5 min after freezer start-up, fat destabilization increased dramatically to nearly 70%, likely due to the shear forces associated with increasing ice content and viscosity, and therefore the shear applied to the fat globules. After 5 min, there were no significant differences in fat destabilization. However, the standard deviation between replicates was large ($\sim 4 - 12\%$) from 5 min to 24 min. After 30 min, the standard deviation between replicates was $< 3\%$ with a fat destabilization value of $\sim 68\%$.

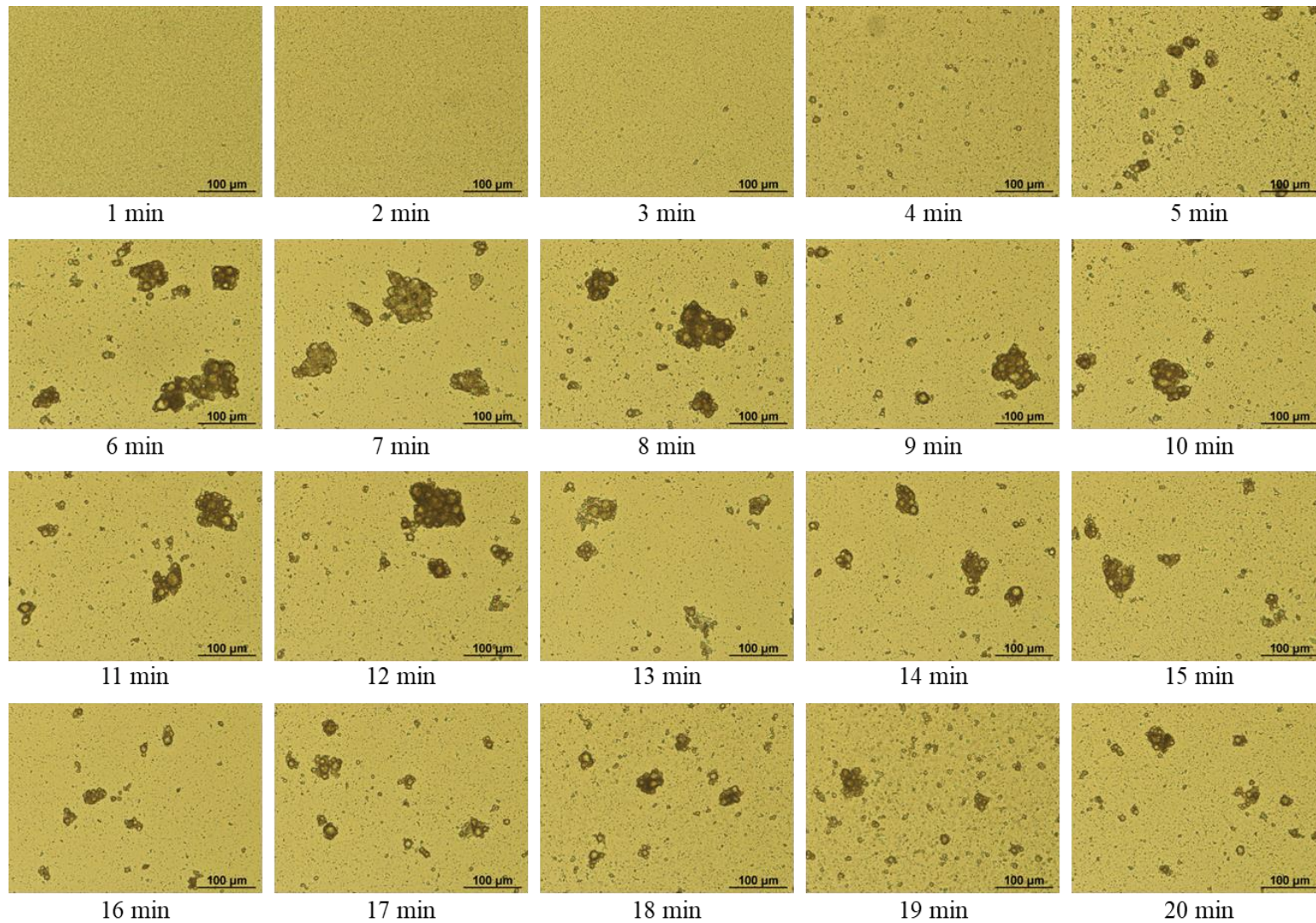


Figure 4.3.11. Optical microscopy images of fat destabilization over time, where $t = 0$ min is freezer start-up. Samples collected every minute for the first 20 min of freezing. Target processing conditions were throughput rate = 200 L/h, draw temperature = -5.5°C , overrun = 75%, and dasher speed = 200 RPM. Melted ice cream samples diluted 1:20 in deionized water for imaging.

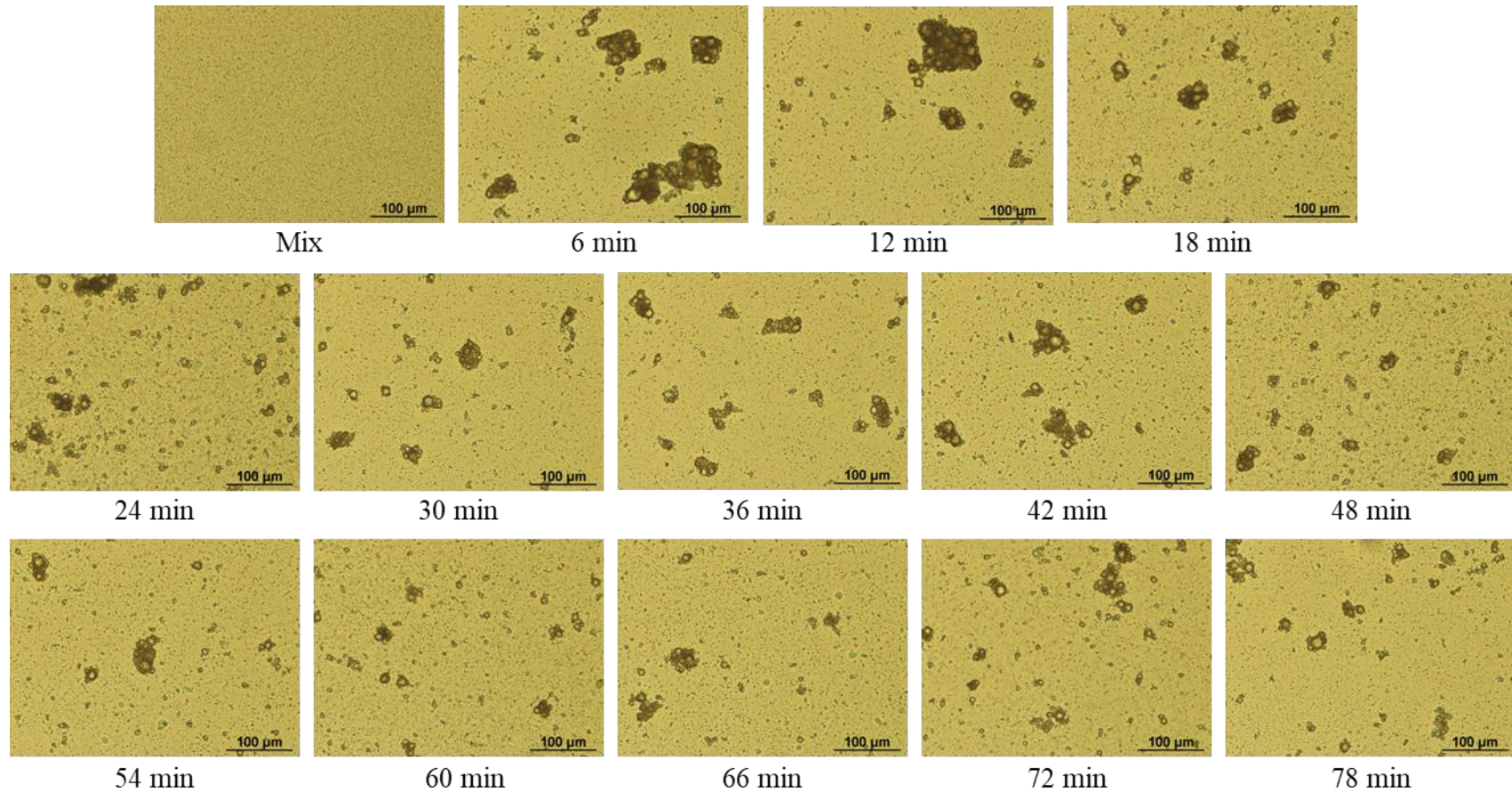


Figure 4.3.12. Optical microscopy images of fat destabilization over time, where $t = 0$ min is freezer start-up. Samples collected every 6 min for 78 min. Target processing conditions were throughput rate = 200 L/h, draw temperature = -5.5°C , overrun = 75%, and dasher speed = 200 RPM. Melted ice cream samples diluted 1:20 in deionized water for imaging.

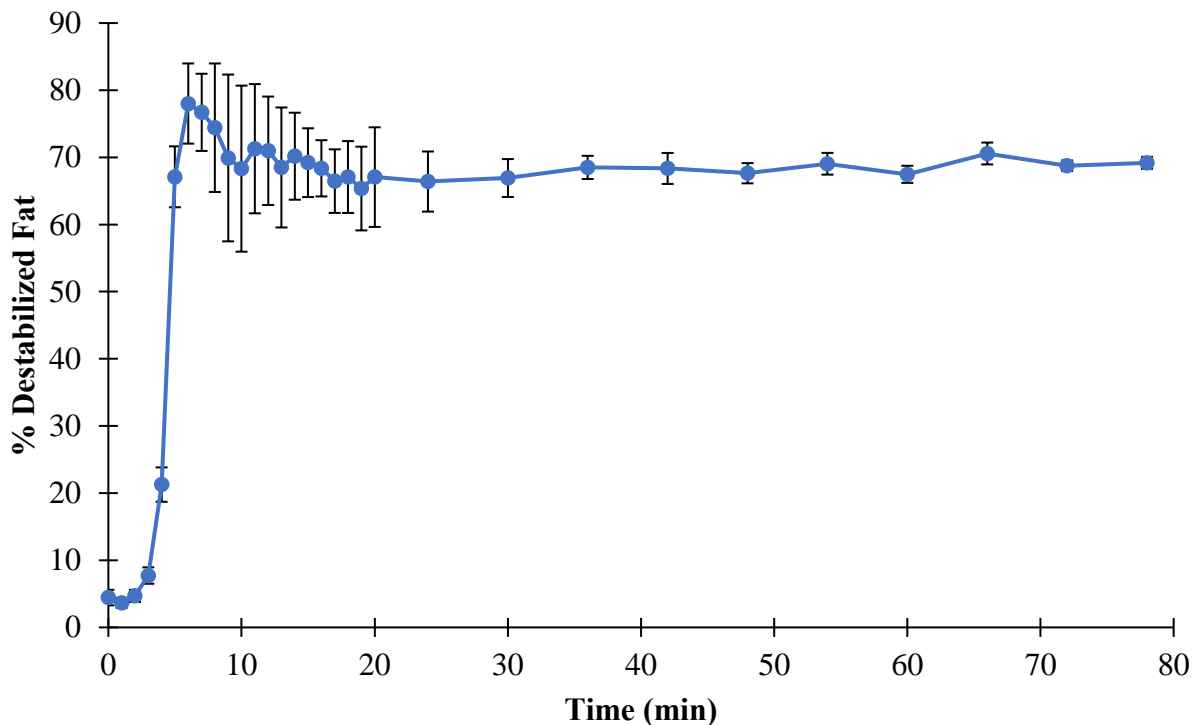


Figure 4.3.13. Evolution of fat destabilization in ice cream, where $t = 0$ min is freezer start-up. Target processing conditions were throughput rate = 200 L/h, draw temperature = -5.5°C , overrun = 75%, and dasher speed = 200 RPM.

4.3.2.4 Practical Considerations

These results contribute to our understanding of microstructure development in continuous SSFs. Processing conditions like draw temperature, viscosity (as a percentage of the total torque capacity on the dasher motor) and overrun took ~ 10 min to stabilize. For the Tetra Pak CF700, it appears that the first 5 min after freezer start-up are the most crucial in microstructure formation. The mean ice crystal, air cell, and fat destabilization values did not differ significantly 6 min after freezer start-up. However, standard deviations between replicates for microstructural properties were relatively large until ~ 30 min. Therefore, the time to achieve consistent microstructure was $\sim 60\%$ of the calculated time to steady state assuming plug flow conditions, which was 49 min. It is fair to assume that 10x the theoretical residence time assuming plug flow conditions is an

adequate, conservative estimate to ensure steady state conditions are reached. These results were employed for achieving steady state conditions for experiments conducted in section 4.4.

4.4 EFFECT OF DASHER DESIGN AND PROCESSING PARAMETERS ON RESIDENCE TIME DISTRIBUTION AND MICROSTRUCTURAL CHARACTERISTICS OF ICE CREAM MADE WITH A CONTINUOUS SCRAPED SURFACE FREEZER

4.4.1 Dasher Speed Experiment

The purpose of the dasher speed experiment was to evaluate the effects of dasher assembly and dasher speed on the processing conditions, residence time distribution (RTD) parameters, and microstructural attributes of ice cream made using a continuous SSF. Additionally, potential interactions between dasher assembly and dasher speed were evaluated. Initial results found that when dasher speed was set to 100 RPM, there was a large amount of blow-by, (that is, pockets of air escaping from the outlet of the freezer without being incorporated into the product), resulting in an overrun that was well below the target. It is likely that due to the lower shear placed on the product, there was inadequate partial coalescence of fat and therefore air could not be stabilized within the ice cream matrix. Therefore, each of the 5 dasher designs was tested at only 2 dasher speeds (200 and 300 RPM) in a 5x2 factorial.

4.4.1.1 Processing Conditions

Processing conditions as a function of dasher rotational speed and dasher assembly are detailed in Table 4.4.1. There was a significant effect of dasher assembly on viscosity (measured as the torque placed on the dasher motor as a percentage of its total capacity), with significant differences between all assemblies except the solid dasher and multi + solid configurations when dasher speed was set to 200 RPM. Generally, increasing dasher displacement (Table 3.1) and dasher speed resulted in a higher viscosity setting necessary to achieve the target draw temperature. However, at 300 RPM dasher speed, the maximum practical viscosity value (98%) was reached

for the solid dasher, multi + solid, and standard + solid configurations. This resulted in a draw temperature that was higher than the target draw temperature of -5.5°C , which must be acknowledged when considering microstructural results for these configurations as they are temperature dependent. The inability of the freezer to reach the desired draw temperature despite operating at the maximum cooling power is likely due to heat generation from friction of scraper blades. The higher displacement dashers also have a lower working volume, resulting in less of a ‘heat sink’ for dissipation of this heat into the product. The overrun itself was not controlled, but a constant mass airflow rate was maintained to theoretically achieve an overrun of 75% overrun. A measured overrun of $75\pm 5\%$ was achieved for all samples.

Table 4.4.1. Effects of dasher assembly and dasher speed on processing conditions for ice cream made at a throughput rate = 300 L/h, overrun = 75%, and target draw temperature = -5.5°C .

Condition	Dasher Assembly	Dasher Speed	
		200 RPM	300 RPM
Viscosity (%)	Solid	83 ± 3 ^{A,b}	98 ± 1 ^{A,a}
	Multi + Solid	80 ± 2 ^{A,b}	98 ± 1 ^{A,a}
	Standard + Solid	74 ± 2 ^{B,b}	98 ± 0 ^{A,a}
	Multi + Wing	67 ± 3 ^{C,b}	97 ± 2 ^{A,a}
	Standard + Wing	54 ± 2 ^{D,b}	77 ± 2 ^{B,a}
Overrun (%)	Solid	76.6 ± 2.3 ^{A,a}	72.3 ± 1.1 ^{A,a}
	Multi + Solid	79.4 ± 4.1 ^{A,a}	72.1 ± 1.0 ^{A,b}
	Standard + Solid	75.1 ± 3.5 ^{A,a}	71.6 ± 3.0 ^{A,a}
	Multi + Wing	77.7 ± 1.0 ^{A,a}	75.8 ± 3.1 ^{A,a}
	Standard + Wing	76.6 ± 1.3 ^{A,a}	74.2 ± 2.1 ^{A,a}
Measured Draw Temperature ($^{\circ}\text{C}$)	Solid	-5.5 ± 0.0 ^{A,b}	-4.9 ± 0.0 ^{A,a}
	Multi + Solid	-5.5 ± 0.0 ^{A,b}	-5.1 ± 0.1 ^{B,a}
	Standard + Solid	-5.5 ± 0.0 ^{A,b}	-5.1 ± 0.1 ^{B,a}
	Multi + Wing	-5.5 ± 0.0 ^{A,a}	-5.5 ± 0.1 ^{C,a}
	Standard + Wing	-5.5 ± 0.0 ^{A,a}	-5.5 ± 0.0 ^{C,a}

^{A-D} Within a condition and column, means without a common uppercase superscript differ ($P < 0.05$) due to dasher.

^{a-b} Within a row, means without a common lowercase superscript differ ($P < 0.05$) due to dasher speed.

\pm Values indicate standard deviation for 3 replicates.

4.4.1.2 Residence Time Distribution

Cumulative RTD curves as a function of dasher assembly and dasher speed are depicted in Figure 4.4.1. The first three moments of the distribution (defined in Eqns. 3.7-3.9) are given in Table 4.4.2 with the ANOVA results in table 4.4.3. Dashers with similar displacements exhibited similar RTD curves (Figures 4.4.2 – 3) and mean residence times (Table 4.4.2). RTD curves were shifted left as dasher displacement increased, indicating a decrease in the mean residence time. Within each dasher assembly, there was no significant difference in mean residence time for ice cream made at dasher speeds of 200RPM and 300RPM. This is consistent with the findings of Arellano et al. (2013a) who found that dasher rotational speed had no effect on RTD of sorbet made in a continuous SSF. There were no differences in the variance of residence times as a function of dasher assembly, except for the standard + wing configuration. This configuration had higher variance than other assemblies at 200 RPM and displayed a significant decrease in variance as dasher speed was increased, likely due to improved mixing. All treatments had a positive skew as can be seen in the right tailing of the $E(t)$ curves (Figures 4.4.2a – 3a). However, there were no significant differences in the degree of skew. Tailing can also be seen when qualitatively considering the intensity of color of ice cream samples collected during the pulse injection study (Figure 4.4.4). Considering the normalized RTD curves (i.e., $E(\theta)$ curves) is also important as the working volume of the freezer depends on the dasher assembly employed (Table 3.1). This allows for direct comparison of the flow performance of assemblies with different displacements. $E(\theta)$ curves (Figures 4.4.2b – 3b for configurations with the wing beater appear to be slightly narrower, which would indicate a reduction in axial dispersion. This may be a result of the reduced viscosity observed with wing beater configurations (Table 4.4.1). While the viscosity measurement in this study is not directly equivalent to product viscosity, Arellano et al. (2013) observed that a reduction

in viscosity of sorbet in a continuous SSF resulted in reduced axial dispersion due to more efficient radial mixing. This suggests that the wing beater did cause a reduction in viscosity in the freezer.

Table 4.4.2. Effects of dasher assembly and dasher speed on residence time distribution parameters for ice cream made at a throughput rate = 300 L/h, overrun = 75%, and target draw temperature = -5.5°C as determined by pulse injection study.

Residence Time Parameter	Dasher Assembly	Dasher Speed	
		200 RPM	300 RPM
Mean Residence Time, t_s (s)	Solid	95±4 ^{C,a}	93±4 ^{C,a}
	Multi + Solid	116±3 ^{BC,a}	114±2 ^{BC,a}
	Standard + Solid	117±4 ^{B,a}	123±5 ^{B,a}
	Multi + Wing	174±3 ^{A,a}	175±3 ^{A,a}
	Standard + Wing	171±21 ^{A,a}	178±0 ^{A,a}
Variance, σ^2 (s ²)	Solid	816±120 ^{B,a}	863±56 ^{A,a}
	Multi + Solid	1340±317 ^{B,a}	1250±173 ^{A,a}
	Standard + Solid	1430±233 ^{B,a}	1450±213 ^{A,a}
	Multi + Wing	1930±102 ^{B,a}	1700±383 ^{A,a}
	Standard + Wing	3250±1000 ^{A,a}	1870±304 ^{A,b}
Skewness, s^3	Solid	0.76±0.04 ^{A,a}	0.87±0.12 ^{A,a}
	Multi + Solid	0.85±0.07 ^{A,a}	0.94±0.08 ^{A,a}
	Standard + Solid	0.87±0.07 ^{A,a}	0.87±0.14 ^{A,a}
	Multi + Wing	0.60±0.05 ^{A,a}	0.52±0.08 ^{A,a}
	Standard + Wing	1.06±0.60 ^{A,a}	0.66±0.15 ^{A,a}

^{A-C} Within a parameter and column, means without a common uppercase superscript differ ($P < 0.05$) due to dasher.

^{a-b} Within a row, means without a common lowercase superscript differ ($P < 0.05$) due to dasher speed.

± Values indicate standard deviation for 3 replicates.

Table 4.4.3. ANOVA table assessing factors affecting residence time distribution parameters.

Parameter	Factor	F-value	P-value
Mean	Dasher Speed	0.43	0.52
	Dasher Assembly	147	<0.001*
	Dasher Speed : Dasher Assembly	0.54	0.71
Variance	Dasher Speed	5.22	0.03*
	Dasher Assembly	16.7	<0.001*
	Dasher Speed : Dasher Assembly	3.57	0.02*
Skewness	Dasher Speed	0.54	0.47
	Dasher Assembly	2.55	0.07
	Dasher Speed : Dasher Assembly	1.43	0.26

* Denotes factors that are significant at $p < 0.05$.

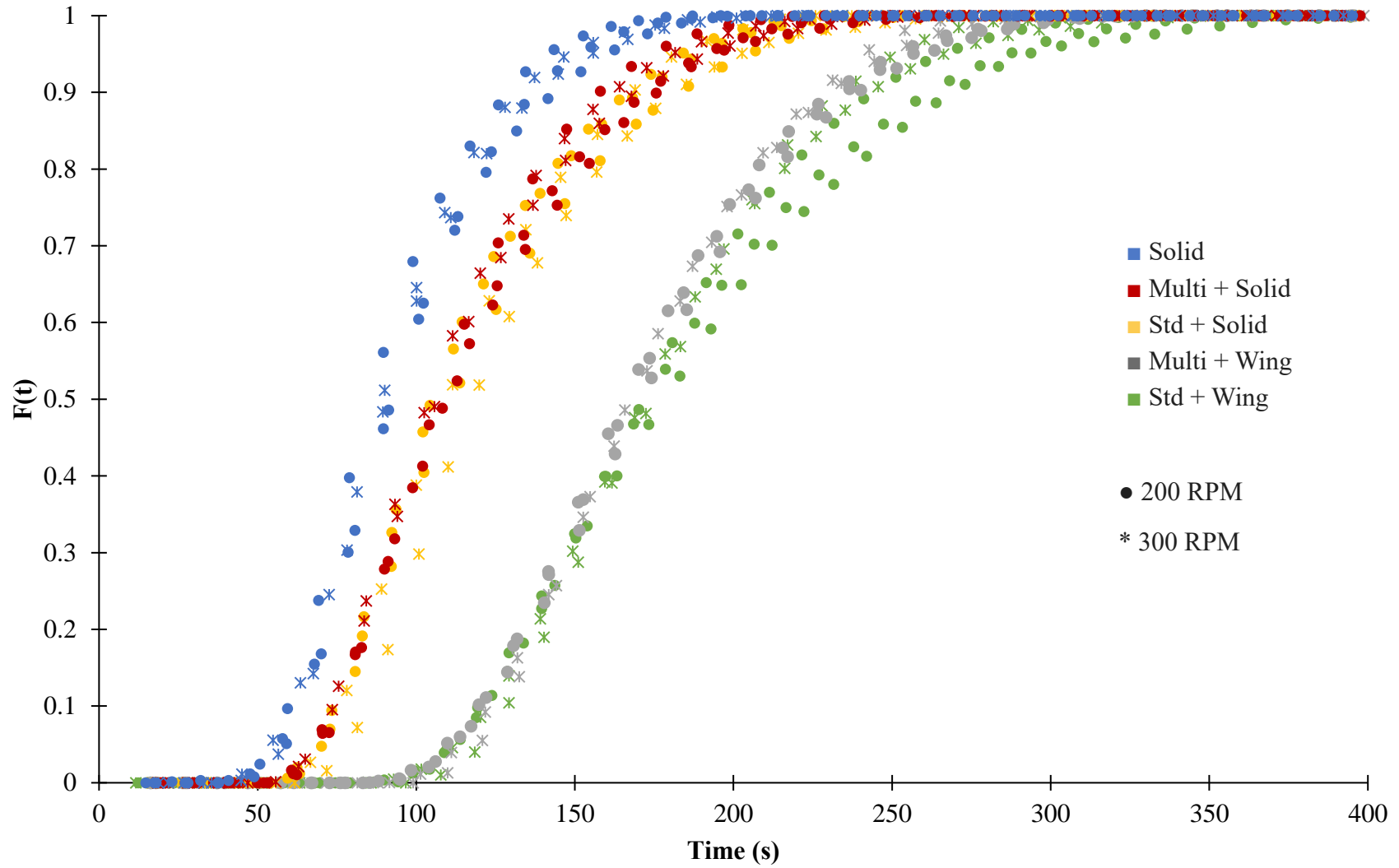


Figure 4.4.1. Cumulative residence time distribution $F(t)$ curves as a function of dasher assembly and dasher speed for ice cream made at 300 L/h throughput rate, 75% overrun, and -5.5°C target draw temperature ($n=3$).

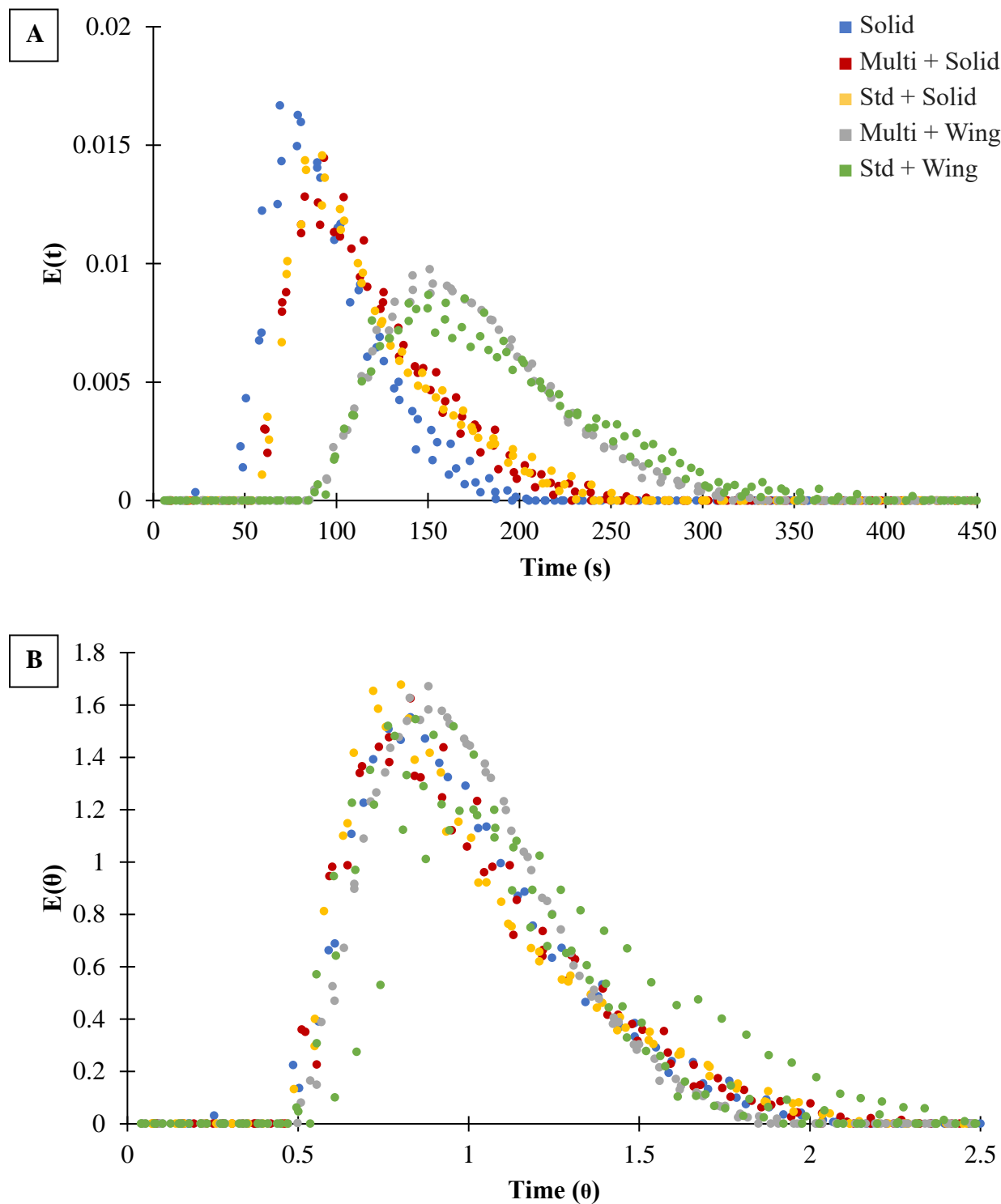


Figure 4.4.2. A) $E(t)$ curves and B) $E(\theta)$ curves as a function of dasher assembly for ice cream made at 200 RPM dasher speed. Throughput rate = 300 L/h, overrun = 75%, target draw temperature = -5.5°C ($n=3$).

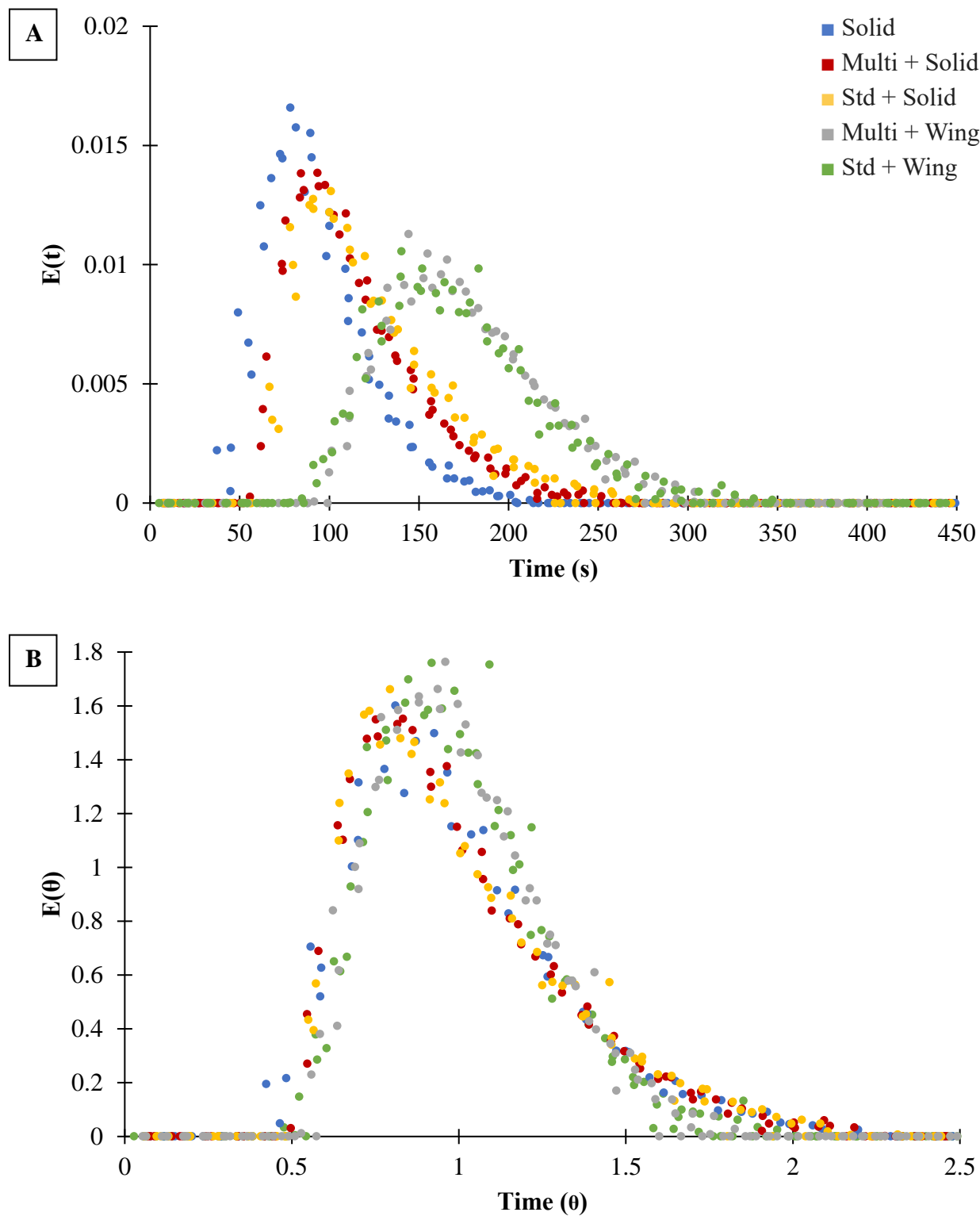


Figure 4.4.3. A) $E(t)$ curves and B) $E(\theta)$ curves as a function of dasher assembly for ice cream made at 300 RPM dasher speed. Throughput rate = 300 L/h, overrun = 75%, target draw temperature = -5.5°C ($n=3$).

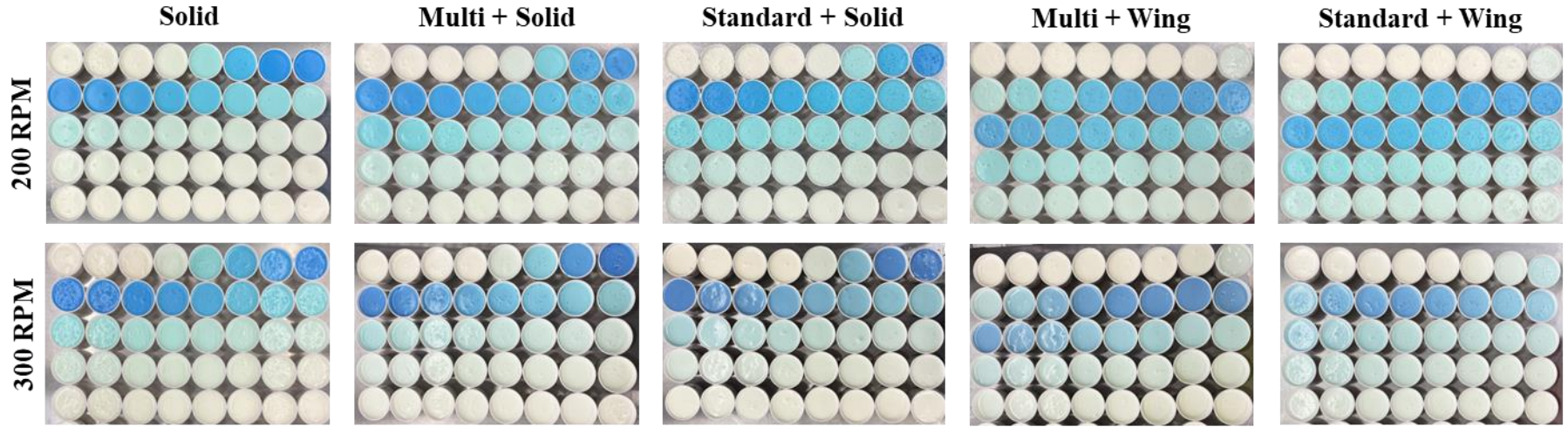


Figure 4.4.4. Images of samples collected during pulse injection experiment for evaluating residence time distribution of ice cream as a function of dasher assembly and dasher speed. Throughput rate = 300 L/h, overrun = 75%, target draw temperature = -5.5°C . Top left cup in each image was collected at $t = 0\text{s}$ when 20 mL of tracer (1% methylene blue in ice cream mix) was injected into freezer.

4.4.1.3 Microstructure

Microstructural attributes as a function of dasher rotational speed and dasher assembly are summarized in Table 4.4.4.

4.4.1.3.1 Ice Crystal Size – Draw

Mean ice crystal size at draw ranged from 17.4 – 25.7 μm . Cumulative ice crystal size distributions at draw are presented in Figure 4.4.5. While it appears that the ice crystal size distribution of the standard + wing configuration is shifted to the right (Figure 4.4.5a), indicating larger ice crystals, there were no statistically significant differences in the mean ice crystal diameter at draw. When data from all dasher assemblies were modeled together, there was a main effect of dasher rotational speed on mean ice crystal diameter, with increased dasher speed resulting in smaller ice crystals (Table 4.4.5). This agrees with the findings of Inoue et al. (2008), Haddad Amamou et al. (2010), and Arellano et al. (2012). Smaller ice crystal size with increasing dasher speed could be attributed to increased frequency of scrapes, which allows ice crystals less time to grow at the wall of the freezing cylinder. It is also possible that attrition contributed to smaller ice crystal size as the torque on the dasher motor, or ‘viscosity’, was increased as dasher speed increased. However, it is also necessary to consider that the measured draw temperature for the solid dasher and solid beater configurations was higher than the target draw temperature at a dasher rotational speed of 300 RPM. At draw, this higher temperature would result in smaller ice crystal sizes, which likely confounds the results of dasher speed on ice crystal size. Previous studies have suggested that the increased frictional heat generated by increasing dasher rotational speed would increase the temperature, and therefore increase recrystallization rates (Russell et al., 1999). An effect of frictional heat energy seems likely as the target draw temperature could not be reached.

Table 4.4.4. Effects of dasher assembly and dasher speed on microstructural attributes of ice cream made at a throughput rate = 300 L/h, overrun = 75%, and target draw temperature = -5.5°C.

Microstructural Attribute	Dasher Assembly	Dasher Speed	
		200 RPM	300 RPM
Draw Ice Crystal Diameter [†]	Solid	19.1±1.0 ^{A,a}	18.3±1.7 ^{A,a}
		5.4±0.3 ^{A,a}	5.7±0.3 ^{A,a}
	Multi + Solid	20.8±0.7 ^{A,a}	20.0±3.0 ^{A,a}
		6.3±0.5 ^{A,a}	6.7±0.9 ^{A,a}
	Standard + Solid	22.0±2.6 ^{A,a}	17.4±0.9 ^{A,a}
		6.1±0.4 ^{A,a}	5.8±0.2 ^{A,a}
	Multi + Wing	21.3±1.7 ^{A,a}	20.0±4.4 ^{A,a}
		6.3±0.3 ^{A,a}	7.1±1.1 ^{A,a}
	Standard + Wing	25.7±6.6 ^{A,a}	20.4±1.6 ^{A,a}
		8.4±2.8 ^{A,a}	7.8±0.6 ^{A,a}
Hardened Ice Crystal Diameter [‡]	Solid	30.7±0.7 ^{A,a}	30.3±0.8 ^{A,a}
		9.4±0.3 ^{A,b}	12.1±0.7 ^{A,a}
	Multi + Solid	30.5±1.2 ^{A,a}	29.4±3.7 ^{A,a}
		9.9±0.9 ^{A,a}	11.6±1.5 ^{A,a}
	Standard + Solid	30.2±0.7 ^{A,a}	27.6±2.8 ^{A,a}
		10.1±0.2 ^{A,a}	11.5±0.7 ^{A,a}
	Multi + Wing	31.8±1.2 ^{A,a}	29.0±2.9 ^{A,a}
		11.0±0.4 ^{A,a}	12.1±1.3 ^{A,a}
	Standard + Wing	32.2±0.8 ^{A,a}	28.7±2.8 ^{A,a}
		11.3±0.2 ^{A,a}	11.9±1.5 ^{A,a}
Air Cell Diameter [‡]	Solid	27.0±2.2 ^{A,a}	23.1±1.1 ^{A,a}
		15.8±1.4 ^{A,a}	10.9±0.6 ^{A,a}
	Multi + Solid	23.1±1.4 ^{A,a}	23.2±1.6 ^{A,a}
		9.9±0.8 ^{A,a}	10.9±2.3 ^{A,a}
	Standard + Solid	25.1±4.9 ^{A,a}	23.6±1.2 ^{A,a}
		12.8±4.5 ^{A,a}	11.4±1.8 ^{A,a}
	Multi + Wing	26.6±2.0 ^{A,a}	22.1±2.6 ^{A,a}
		13.4±2.3 ^{A,a}	10.4±3.0 ^{A,a}
	Standard + Wing	24.9±2.1 ^{A,a}	23.8±2.8 ^{A,a}
		11.8±0.5 ^{A,a}	11.6±3.6 ^{A,a}
Fat	Solid	57.0±7.4 ^{A,a}	59.1±5.5 ^{B,a}
	Multi + Solid	57.3±3.7 ^{A,b}	73.1±4.4 ^{AB,a}
	Standard + Solid	50.6±6.5 ^{AB,b}	72.0±4.3 ^{AB,a}
	Multi + Wing	41.8±8.0 ^{AB,b}	76.8±1.6 ^{A,a}
	Standard + Wing	37.0±6.9 ^{B,b}	67.0±1.6 ^{AB,a}
	% Destabilization		

^{A-D} Within an attribute and column, means without a common uppercase superscript differ ($P < 0.05$) due to dasher.

^{a-b} Within a row, means without a common lowercase superscript differ ($P < 0.05$) due to dasher speed.

[†] Draw ice crystal diameter mean and variance evaluated at -5.5°C.

[‡] Hardened ice crystal/air cell diameter mean and variance evaluated at -15°C.

± Values indicate standard deviation for 3 replicates.

There was not an effect of dasher rotational speed on standard deviation in ice crystal size. However, the standard deviation in ice crystal size was trending towards being significantly larger ($P = 0.052$) when comparing standard + wing configuration to the solid dasher at 200 RPM (Figure 4.4.6b). There was also a main effect of dasher assembly on standard deviation in ice crystal size, with the standard + wing configuration having a larger standard deviation than the solid dasher and standard + solid configurations (Table 4.4.5). There was not an interaction effect between dasher speed and dasher assembly on the mean or standard deviation of draw ice crystal size.

Table 4.4.5. ANOVA table assessing factors affecting ice crystal size at draw (target = -5.5°C).

Attribute	Factor	F-value	P-value
Mean	Dasher Speed	5.41	0.03*
	Dasher Assembly	1.73	0.18
	Dasher Speed : Dasher Assembly	0.82	0.53
Standard Deviation	Dasher Speed	0.13	0.72
	Dasher Assembly	5.07	0.005*
	Dasher Speed : Dasher Assembly	0.44	0.78

* Denotes factors that are significant at $p < 0.05$.

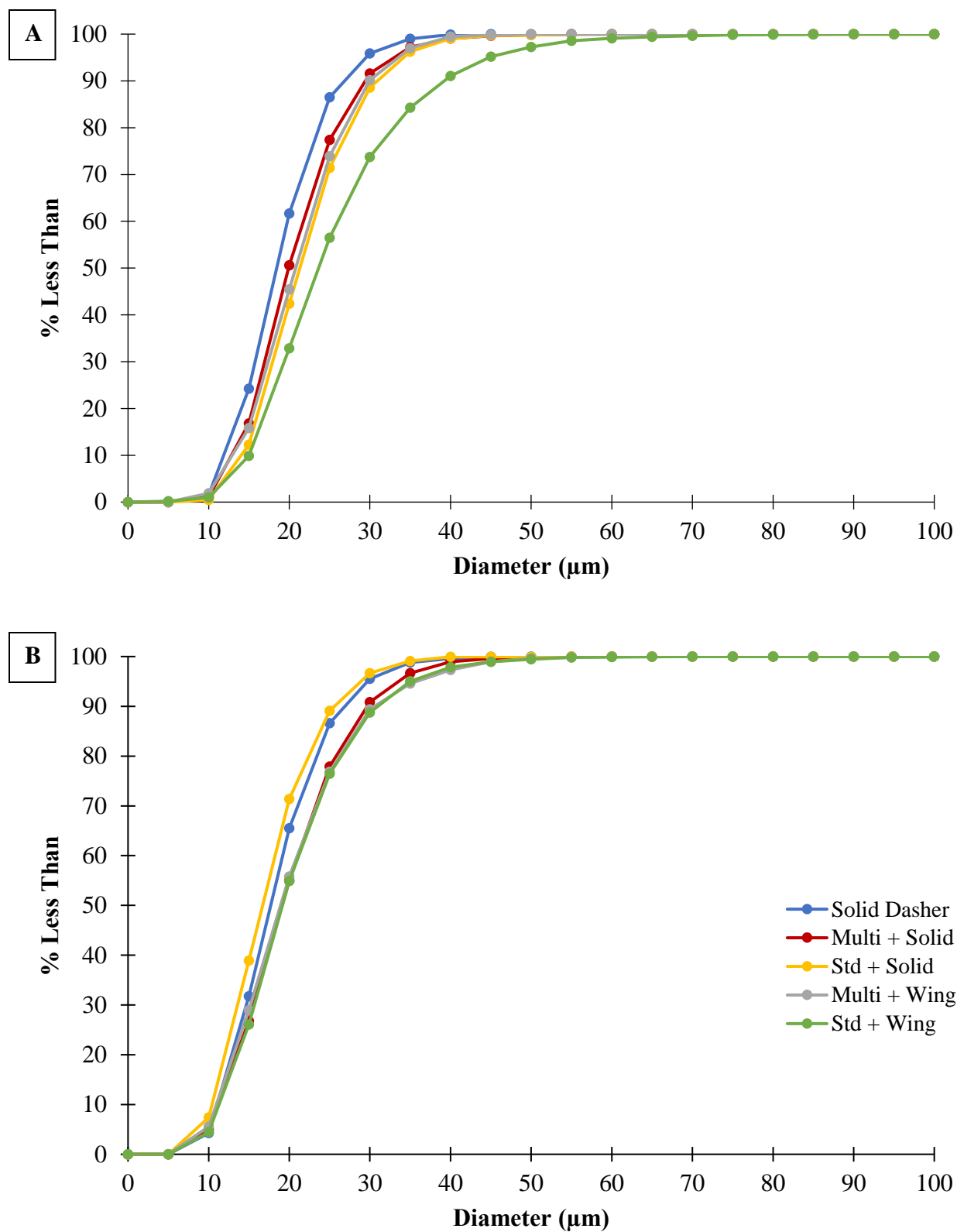
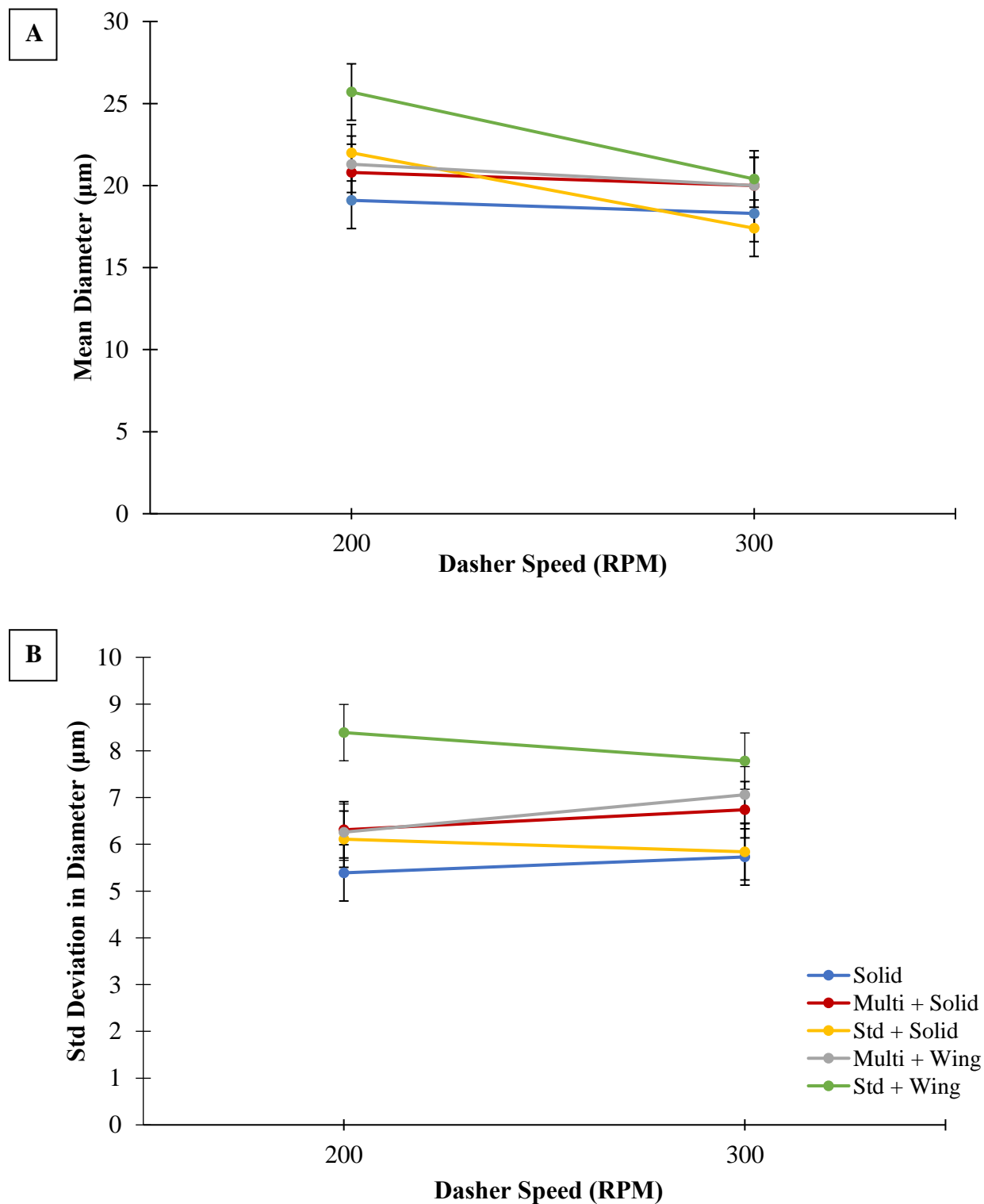


Figure 4.4.5. Cumulative ice crystal size distributions immediately after draw (-5.5°C) as a function of dasher assembly for ice cream made at a dasher speed of A) 200 RPM and B) 300 RPM. Throughput rate = 300 L/h, overrun = 75%, target draw temperature = -5.5°C .



4.4.1.3.2 Ice Crystal Size – Hardened

The mean ice crystal diameter for hardened samples ranged from 27.6 – 32.2 μm . Cumulative size distributions of ice crystals in hardened ice cream are depicted in Figure 4.4.7. While there were not significant differences between individual treatments (Table 4.4.4), there was a significant main effect of dasher speed when combining data from all dasher assemblies in the model (Table 4.4.6). Increasing dasher speed from 200 RPM to 300 RPM decreased the mean diameter of hardened ice crystals slightly from 25.3 to 23.2 μm and increased the standard deviation in hardened ice crystal size from 10.3 to 11.8 μm . There was not a significant effect of dasher assembly on hardened ice crystal size. This differs from draw ice crystal results, where there was an effect of dasher assembly but not dasher rotational speed on the standard deviation in ice crystal size. There was not an interaction effect between dasher speed and dasher assembly on the mean and standard deviation of hardened ice crystal size. It is necessary to consider that the actual draw temperature for the solid dasher and solid beater configurations was higher than the target draw temperature. Increased draw temperature has been shown to result in larger ice crystal size in hardened ice cream once the ice phase volume has equilibrated, so this may confound the results of both dasher speed and dasher assembly on results on ice crystal size (Koxholt et al., 2000; Drewett and Hartel, 2007; Inoue et al., 2008, Amador et al., 2017).

Table 4.4.6. ANOVA table assessing factors affecting ice crystal size in hardened ice cream.

Attribute	Factor	F-value	P-value
Mean	Dasher Speed	7.53	0.01*
	Dasher Assembly	0.62	0.65
	Dasher Speed : Dasher Assembly	0.58	0.68
Standard Deviation	Dasher Speed	20.7	<0.001*
	Dasher Assembly	1.48	0.25
	Dasher Speed : Dasher Assembly	1.03	0.42

* Denotes factors that are significant at $p < 0.05$.

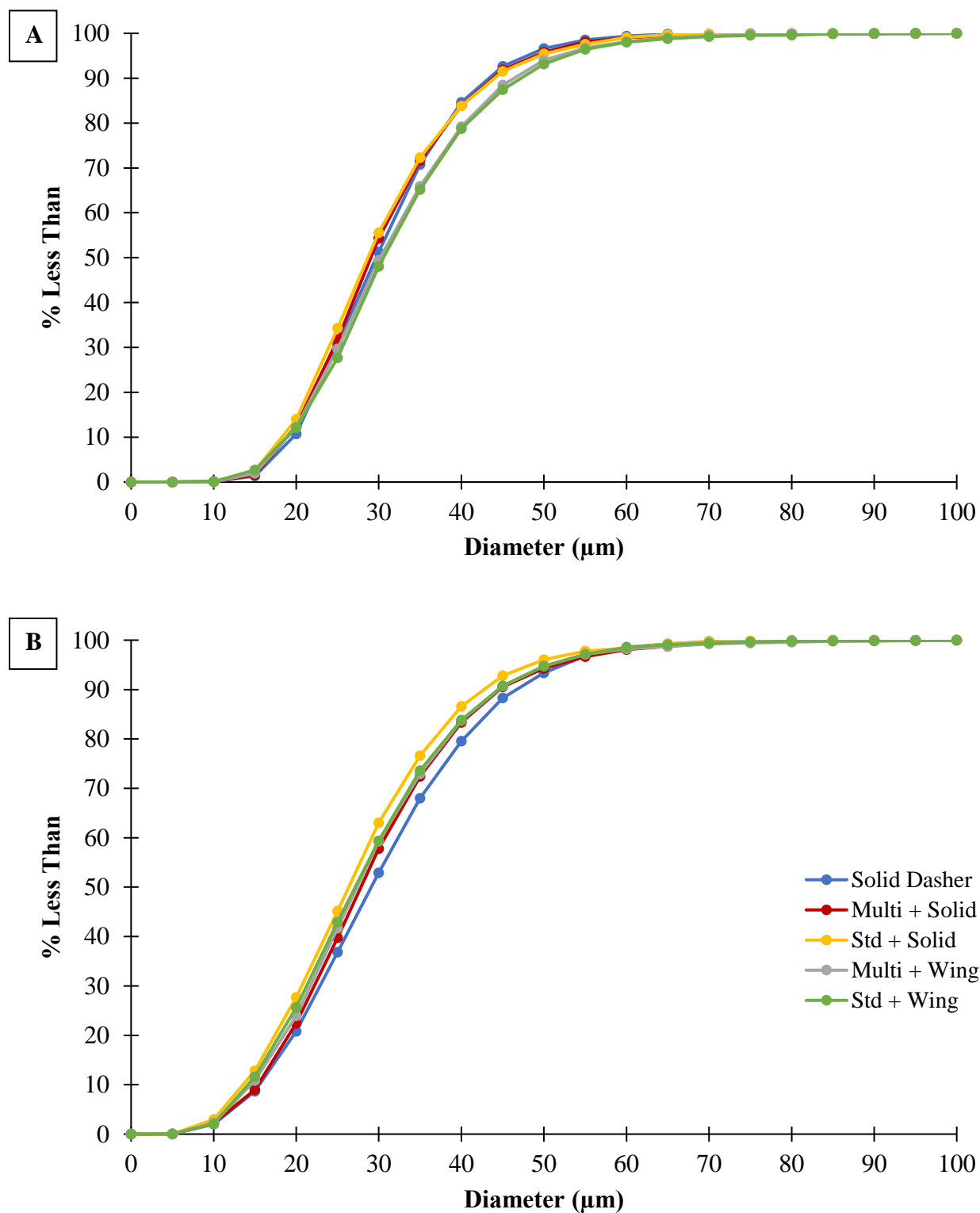


Figure 4.4.7. Cumulative ice crystal size distributions as a function of dasher assembly for hardened ice cream samples made at a dasher speed of A) 200 RPM and B) 300 RPM. Throughput rate = 300 L/h, overrun = 75%, target draw temperature = -5.5°C . Samples were evaluated at -15°C .

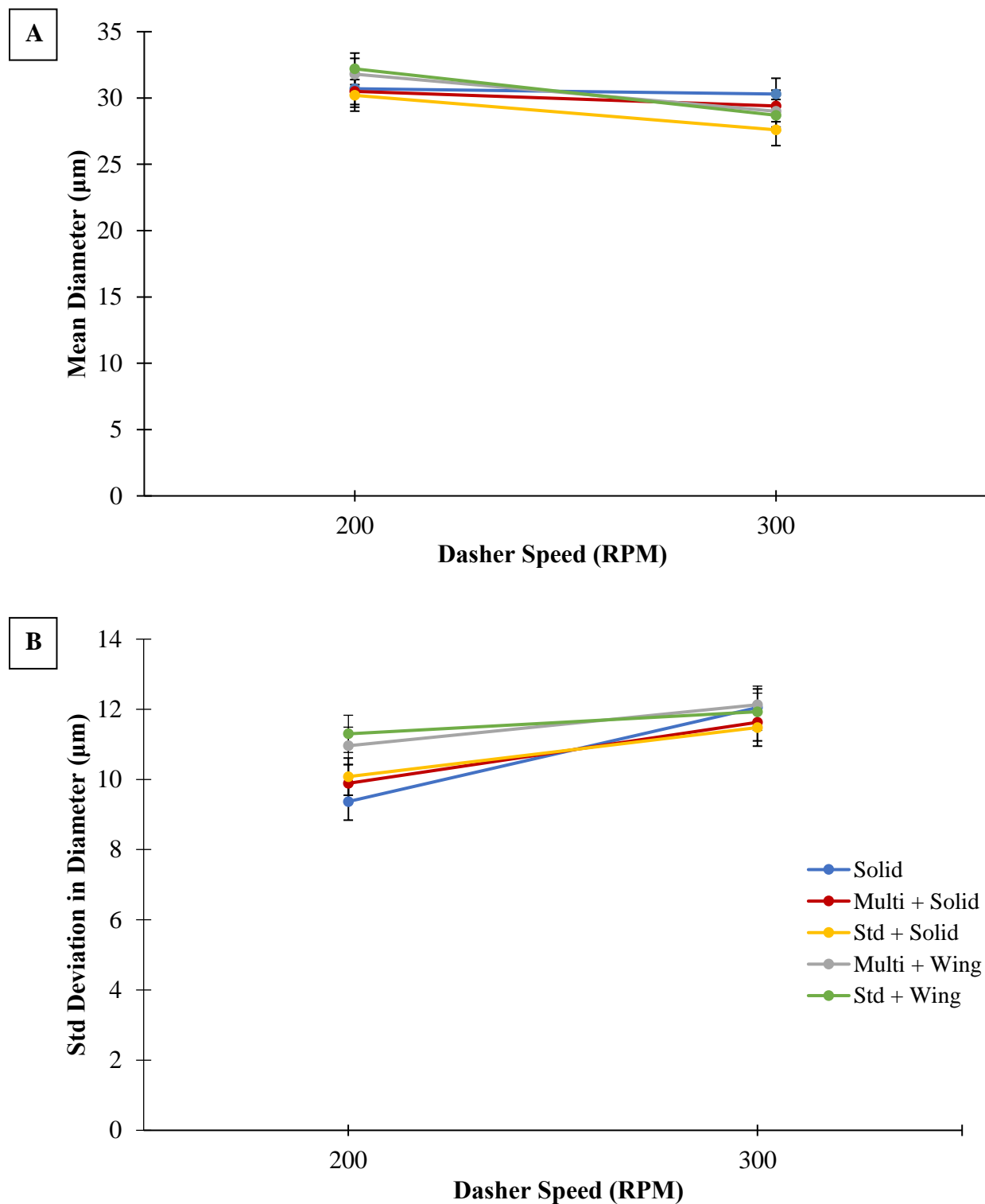


Figure 4.4.8. A) Mean ice crystal size and B) standard deviation in ice crystal size of hardened ice cream samples as a function of dasher assembly and dasher speed. Throughput rate = 300 L/h, overrun = 75%, target draw temperature = -5.5°C . Samples were evaluated at -15°C . Values represent the modeled averages for three replicates.

4.4.1.3.3 *Air Cell Size*

The mean air cell size of hardened samples ranged from 22.1 – 27.0 μm . Cumulative air cell size distributions are shown in Figure 4.4.9, and the mean and standard deviation in air cell size as a function of dasher speed and dasher assembly are depicted in Figure 4.4.10. There were no significant differences between individual treatments (Table 4.4.4). However, when considering the modeled averages when including all dasher assemblies, there was a main effect of dasher speed on average air cell size (Table 4.4.7). When dasher speed was increased from 200 RPM to 300 RPM, mean air cell size decreased from 25.3 to 23.2 μm . This is consistent with previous studies (Rohenkohl and Kohlus, 1999; Inoue et al., 2008; Warren and Hartel, 2018; Masuda et al., 2020). Increasing dasher speed also increases the amount of shear placed on the product, causing more air bubble breakup. There was not a main effect of dasher assembly, and there was no interaction effect between dasher speed and dasher assembly on mean and standard deviation of air cell size.

It is interesting that the air cell size decreased with increasing dasher speed even though the draw temperature was higher than the target draw temperature for 3 of the 5 dasher assemblies tested. Several studies have concluded that increased draw temperature results in increased air cell size (Chang and Hartel, 2002b; Caillet et al., 2003; Eisner et al., 2005; Hernández-Parra et al., 2018a). In a study by Inoue et al. (2008), it was determined that draw temperature had a larger effect on air cell size than dasher speed. It is difficult to surmise exactly why an effect of dasher speed was still discernable, even though the target draw temperature could not be achieved. A more complete understanding of the shear conditions in the freezer would be necessary for further assessment.

Table 4.4.7. ANOVA table assessing factors affecting air cell size in hardened ice cream.

Attribute	Factor	F-value	P-value
Mean	Dasher Speed	5.86	0.03*
	Dasher Assembly	0.47	0.76
	Dasher Speed : Dasher Assembly	0.92	0.47
Standard Deviation	Dasher Speed	3.53	0.07
	Dasher Assembly	1.12	0.37
	Dasher Speed : Dasher Assembly	1.34	0.29

* Denotes factors that are significant at $p < 0.05$.

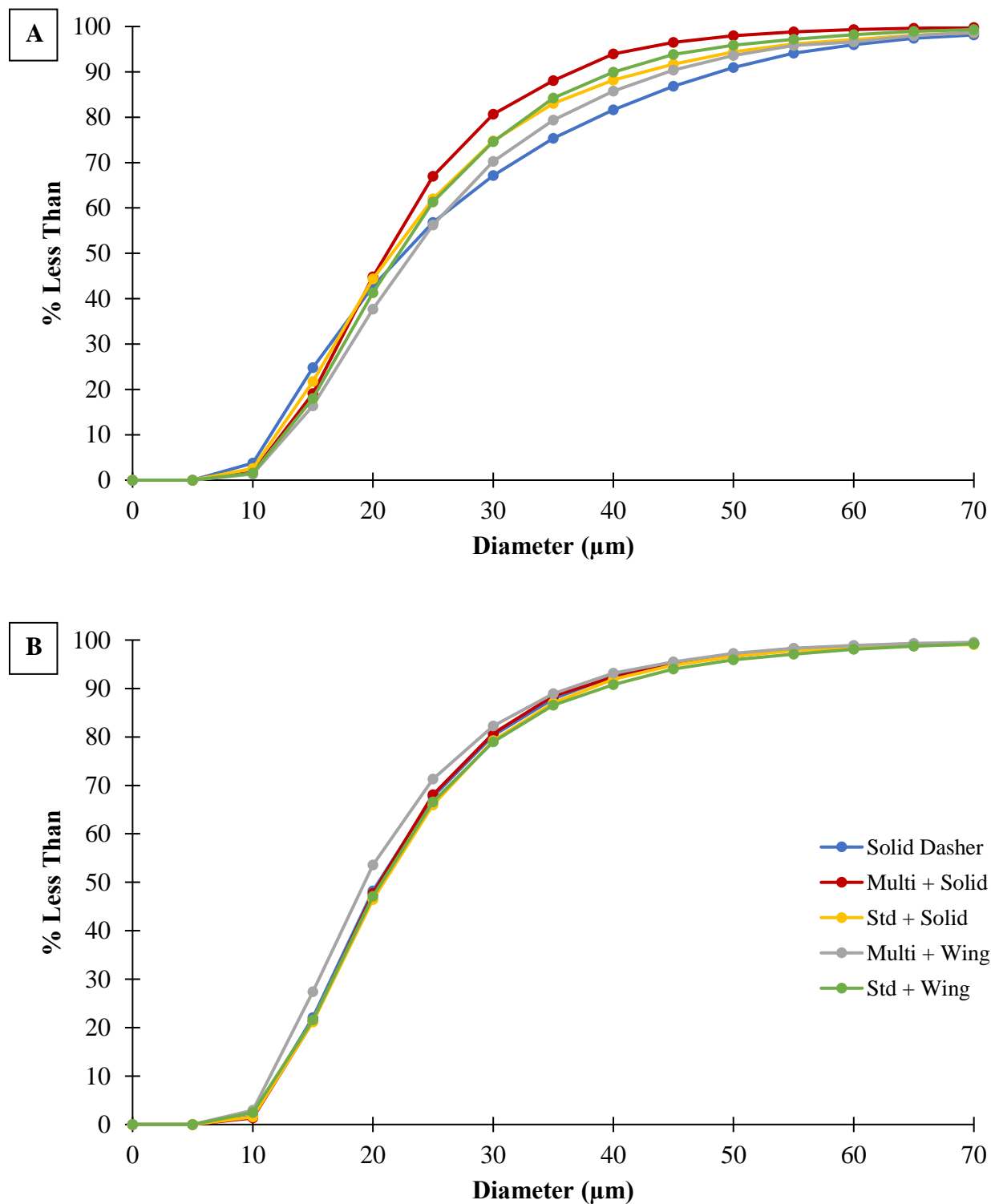


Figure 4.4.9. Cumulative air cell size distributions as a function of dasher assembly for hardened ice cream samples made at a dasher speed of A) 200 RPM and B) 300 RPM. Samples were evaluated at -6°C . Throughput rate = 300 L/h, overrun = 75%, target draw temperature = -5.5°C .

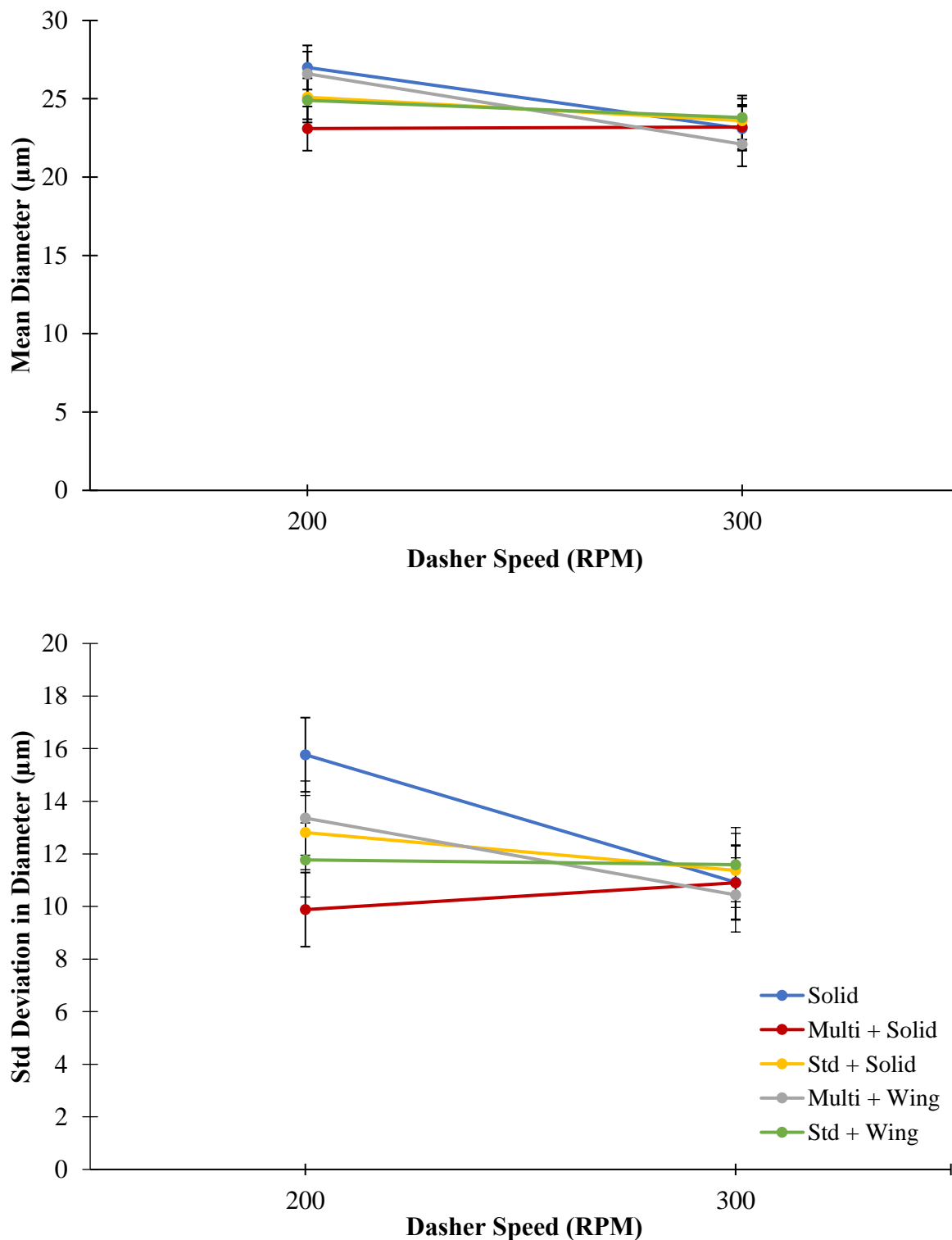


Figure 4.4.10. A) Mean air cell size and B) standard deviation in air cell size of hardened ice cream samples as a function of dasher assembly and dasher speed. Throughput rate = 300 L/h, overrun = 75%, target draw temperature = -5.5°C . Samples were evaluated at -6°C . Values represent the modeled averages for three replicates.

4.4.1.3.4 *Fat Destabilization*

The level of fat destabilization in ice cream ranged from 37.0 – 76.8%. The size distributions of fat globules are given in Figure 4.4.11, with the second peak for each sample representing destabilized fat. Differences in fat destabilization can also be seen qualitatively in Figure 4.4.12. There were significant effects of both dasher speed and dasher assembly on fat destabilization, as well as an interaction effect between dasher speed and dasher assembly (Table 4.4.8). As dasher speed increased, there was an increase in fat destabilization for all open dasher assemblies (Figure 4.4.13). This is consistent with the findings of previous studies (Kokubo et al., 1996; Rohenkohl and Kohlus, 1999; Inoue et al., 2008; Warren and Hartel, 2018). However, there was no significant difference in fat destabilization between 200 and 300 RPM for the solid dasher. This might suggest that increasing the rotational speed increases shear forces to a greater degree in open dasher configurations than solid dashers. However, it should be considered that the draw temperature for the solid dasher was also significantly higher at 0.6°C above the -5.5°C target draw temperature. Most evidence suggests that increased draw temperature results in decreased fat globule destabilization (Kokubo et al., 1996; Rohenkohl and Kohlus, 1999; Eisner et al., 2005; Inoue et al., 2008), which could confound the effect of dasher speed on fat destabilization for the solid dasher configuration.

At 200 RPM, the solid dasher and multi + solid configurations had significantly higher levels of fat destabilization than the standard + wing configuration. Additionally, the solid dasher and multi + solid configurations were approaching statistical significance with $P = 0.065$ and $P = 0.056$, respectively, when compared to the multi + wing configuration at 200 RPM. At 300 RPM, the only dasher configurations that differed significantly in fat destabilization were the solid dasher and multi + wing, the latter of which had significantly higher fat destabilization. The results at 200

RPM reflect those of Kokubo et al. (1996) in which increased dasher displacement resulted in more fat destabilization. This is likely a result of increased agitation and shear, which will increase the likelihood of fat globule collisions. However, the differences caused by dasher assembly seemingly lessened at 300 RPM. This, in addition to the fact that the statistical F -value is over 23 times larger for the effect of dasher speed than for dasher assembly (Table 4.4.8), strongly suggests that dasher speed is a more efficient way of controlling fat destabilization than dasher assembly for open dashers.

Table 4.4.8. ANOVA table assessing factors affecting fat destabilization.

Factor	F-value	P-value
Dasher Speed	110	<0.001*
Dasher Assembly	4.73	0.008*
Dasher Speed : Dasher Assembly	8.39	<0.001*

* Denotes factors that are significant at $p < 0.05$.

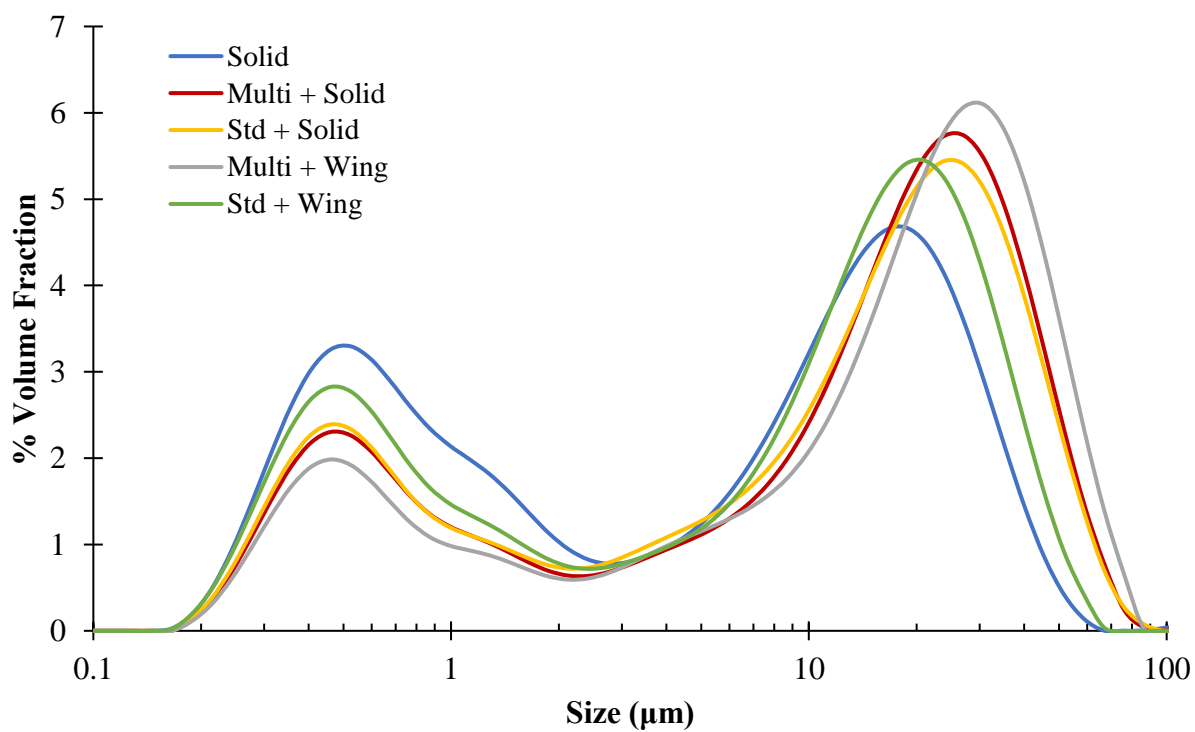
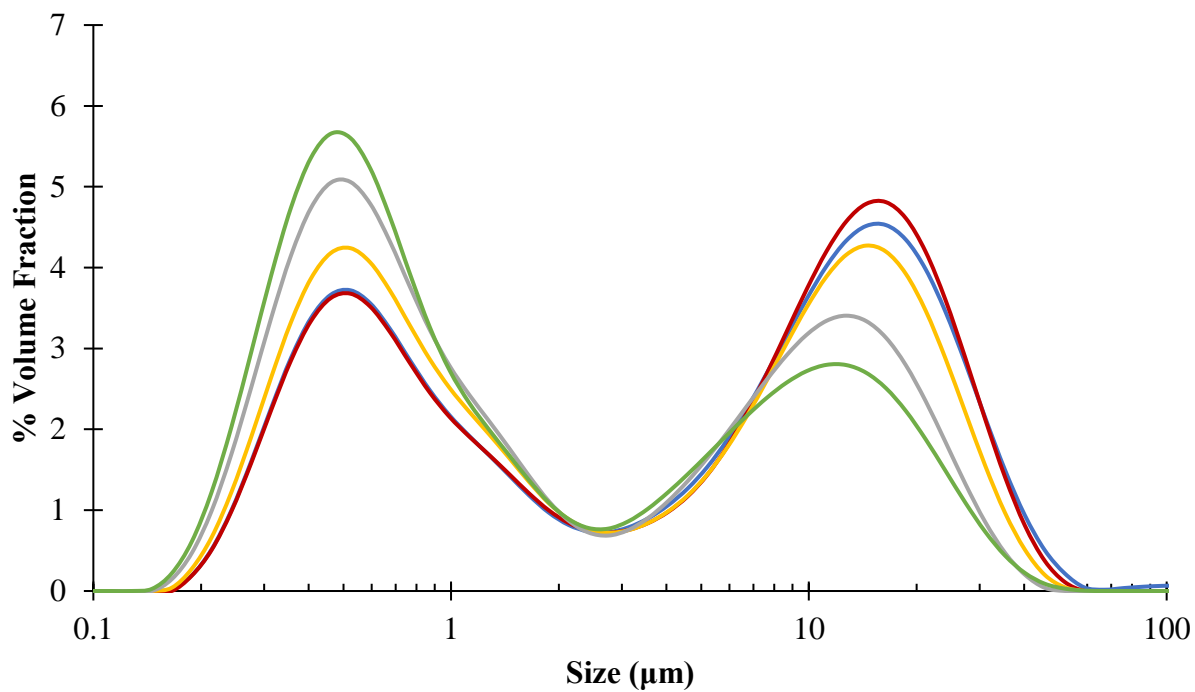


Figure 4.4.11. Fat globule size distributions as a function of dasher assembly for ice cream samples made at a dasher speed of A) 200 RPM and B) 300 RPM. Throughput rate = 300 L/h, overrun = 75%, target draw temperature = -5.5°C . Curves represent the averages for three replicates.

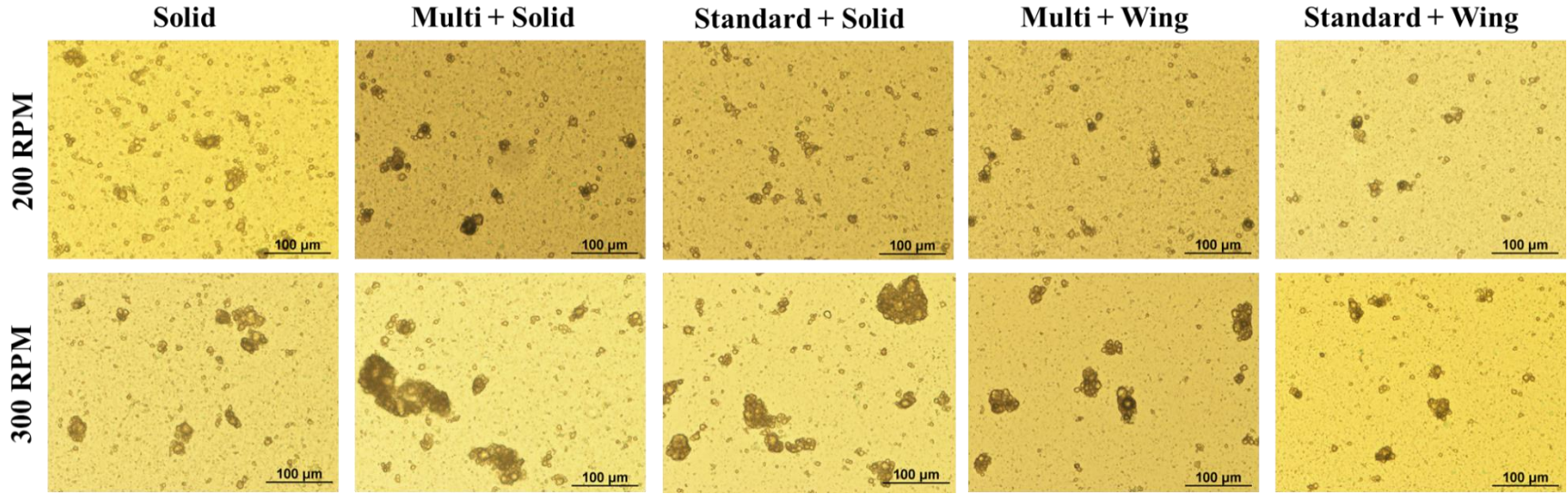


Figure 4.4.12. Optical microscopy images (20x magnification) of destabilized fat clusters as a function of dasher speed and dasher assembly.

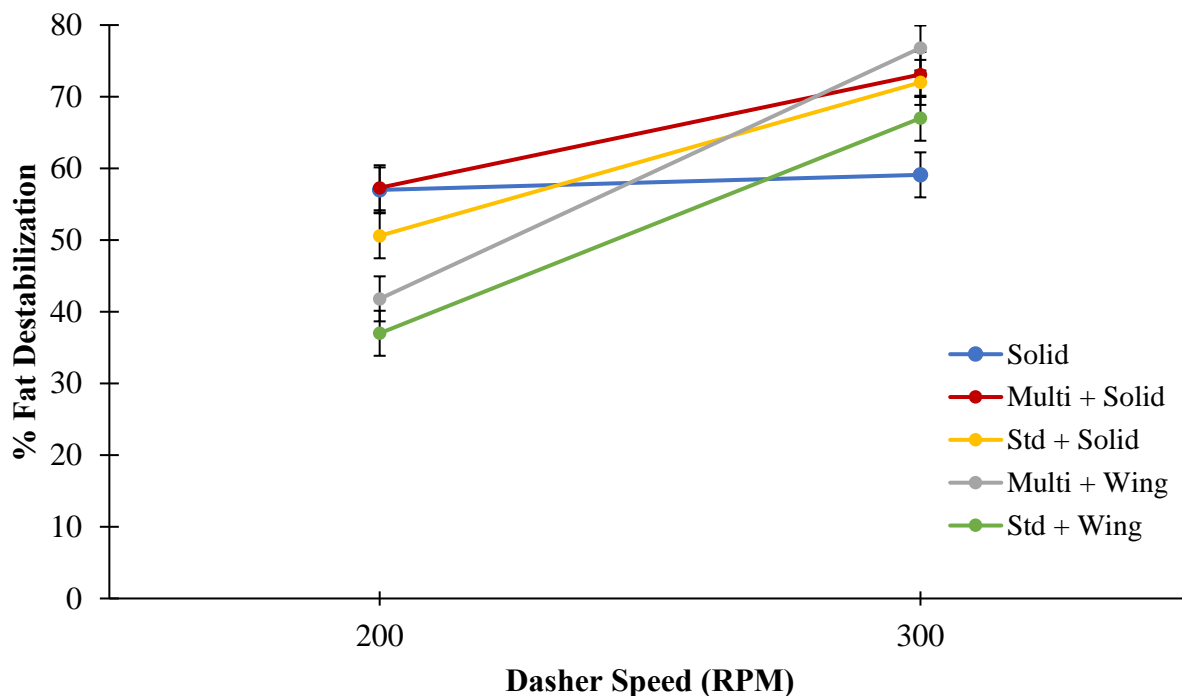


Figure 4.4.13. Mean % fat destabilization values for ice cream samples as a function of dasher assembly and dasher speed. Throughput rate = 300 L/h, overrun = 75%, target draw temperature = -5.5°C . Values represent the modeled averages for three replicates.

4.4.1.4 Correlations

The dasher displacement (Table 3.1) was plotted against microstructural attributes to investigate whether there was a correlation between working volume (i.e., the volume available to the product in the freezing cylinder) and microstructure (Table 4.4.9). Correlations between dasher displacement and all microstructural attributes were low ($R^2 \leq 0.34$). Viscosity and residence time (both mean and standard deviation) were also plotted against microstructural attributes to investigate if correlations existed for processing conditions (Table 4.4.9). Viscosity tended to be negatively correlated with ice crystal size, while residence time was positively correlated with ice crystal size. The standard deviation in residence time had the highest correlation with ice crystal size at draw ($R^2 = 0.43 - 0.52$), though this correlation decreases significantly after hardening. While there was a negative correlation of viscosity and a positive correlation of residence time on

average air cell size, these correlations were very weak ($R^2 \leq 0.14$). There was a relatively strong positive correlation between viscosity and fat destabilization ($R^2 = 0.68$). This supports the theory that increased fat destabilization with increasing dasher displacement was related to an increase of shear in the freezer. The correlations between residence time and fat destabilization were negative, although these correlations were relatively small ($R^2 \leq 0.16$).

Correlations were also tested for individual dasher assemblies to evaluate whether their behavior differed. Correlation coefficients between viscosity and microstructural attributes for individual dashers are given in Table 4.4.10. However, these correlation values may be misleading because the viscosity parameter, or the % of total torque capacity on the dasher motor, was set at the maximum for the solid dasher and configurations containing a solid beater when dasher speed was at 300 RPM. Correlations may have been weaker had the viscosity not been limiting. There were no obvious trends in correlations between viscosity and mean ice crystal size. Though the standard deviation in ice crystal size at draw had low correlations with viscosity ($R^2 \leq 0.23$), the standard deviation in ice crystal size of hardened ice cream samples was more highly correlated with viscosity. This was particularly true for the solid dasher and configurations with the solid beater. This is likely related to the maximization of the viscosity setting on the freezer rather than a physical phenomenon. Air cell size was most highly correlated with viscosity for the solid dasher ($R^2 = 0.80$). Again, however, this is likely due to the maximization of the viscosity parameter.

Finally, there was a strong correlation between viscosity and fat destabilization for open dasher assemblies ($R^2 \geq 0.83$) compared to the solid dasher assembly ($R^2 = 0.06$). The open dasher assemblies were less limited by the viscosity parameter, and therefore the change in % viscosity tended to be greater for open dashers. This would be related to a larger change in the shear forces placed on the product in the freezer, which would increase fat destabilization.

Table 4.4.9. Overall correlation coefficient R^2 between processing conditions and microstructural attributes.

Microstructural Attribute	Dasher Displacement	Viscosity	Average Residence Time	Std Dev in Residence Time
Draw Mean Ice Crystal Size	0.14 ⁽⁻⁾	0.33 ⁽⁻⁾	0.13 ⁽⁺⁾	0.43 ⁽⁺⁾
Draw Std Dev in Ice Crystal Size	0.34 ⁽⁻⁾	0.13 ⁽⁻⁾	0.33 ⁽⁺⁾	0.52 ⁽⁺⁾
Hardened Mean Ice Crystal Size	0.01 ⁽⁻⁾	0.21 ⁽⁻⁾	0.00 ⁽⁺⁾	0.04 ⁽⁺⁾
Hardened Std Dev in Ice Crystal Size	0.11 ⁽⁻⁾	0.06 ⁽⁺⁾	0.11 ⁽⁺⁾	0.02 ⁽⁺⁾
Mean Air Cell Size	0.00 ⁽⁺⁾	0.14 ⁽⁻⁾	0.00 ⁽⁺⁾	0.02 ⁽⁺⁾
Std Dev in Air Cell Size	0.01 ⁽⁺⁾	0.05 ⁽⁻⁾	0.01 ⁽⁻⁾	0.00 ⁽⁻⁾
% Fat Destabilization	0.03 ⁽⁺⁾	0.68 ⁽⁺⁾	0.01 ⁽⁻⁾	0.16 ⁽⁻⁾

* The symbol in parenthesis indicates the whether the correlation is positive⁽⁺⁾ or negative⁽⁻⁾.

Table 4.4.10. Correlation coefficient R^2 between viscosity and microstructural attributes as a function of dasher assembly.

Microstructural Attribute	Dasher Assembly				
	Solid Dasher	Multi + Solid	Standard + Solid	Multi + Wing	Standard + Wing
Draw Mean Ice Crystal Size	0.15 ⁽⁻⁾	0.04 ⁽⁻⁾	0.66 ⁽⁻⁾	0.09 ⁽⁻⁾	0.27 ⁽⁻⁾
Draw Std Dev in Ice Crystal Size	0.23 ⁽⁺⁾	0.14 ⁽⁺⁾	0.18 ⁽⁻⁾	0.19 ⁽⁺⁾	0.02 ⁽⁻⁾
Hardened Mean Ice Crystal Size	0.13 ⁽⁻⁾	0.06 ⁽⁻⁾	0.38 ⁽⁻⁾	0.43 ⁽⁻⁾	0.44 ⁽⁻⁾
Hardened Std Dev in Ice Crystal Size	0.81 ⁽⁺⁾	0.41 ⁽⁺⁾	0.73 ⁽⁺⁾	0.31 ⁽⁺⁾	0.10 ⁽⁺⁾
Mean Air Cell Size	0.80 ⁽⁻⁾	0.01 ⁽⁺⁾	0.05 ⁽⁻⁾	0.70 ⁽⁻⁾	0.09 ⁽⁻⁾
Std Dev in Air Cell Size	0.80 ⁽⁻⁾	0.14 ⁽⁺⁾	0.05 ⁽⁻⁾	0.42 ⁽⁻⁾	0.02 ⁽⁻⁾
% Fat Destabilization	0.06 ⁽⁺⁾	0.83 ⁽⁺⁾	0.83 ⁽⁺⁾	0.95 ⁽⁺⁾	0.96 ⁽⁺⁾

* The symbol in parenthesis indicates the whether the correlation is positive⁽⁺⁾ or negative⁽⁻⁾.

Correlation coefficients between microstructural attributes and the mean residence time and standard deviation in residence time are given in Tables 4.4.11 and 4.4.12, respectively. Correlations between residence time and ice crystal size were generally very low, though the standard + solid configuration had higher correlation values than other dasher assemblies. The correlation between mean residence time and air cell size were weak for all dasher assemblies ($R^2 \leq 0.22$). Correlations between standard deviation in residence time and air cell size were slightly higher ($R^2 \leq 0.46$), particularly for dasher configurations containing a wing beater. The correlations between mean residence time and fat destabilization were highest for dasher configurations containing a solid beater ($R^2 \approx 0.33$), but otherwise were very weak. The solid dasher and configurations containing a wing beater were more highly correlated with standard deviation in residence time ($R^2 = 0.28 - 0.66$) than mean residence time.

Table 4.4.11. Correlation coefficient R^2 between mean residence time and microstructural attributes as a function of dasher assembly.

Microstructural Attribute	Dasher Assembly				
	Solid Dasher	Multi + Solid	Standard + Solid	Multi + Wing	Standard + Wing
Draw Mean Ice Crystal Size	0.03 (+)	0.00 (-)	0.50 (-)	0.11 (-)	0.07 (+)
Draw Std Dev in Ice Crystal Size	0.15 (-)	0.04 (+)	0.64 (-)	0.16 (-)	0.08 (+)
Hardened Mean Ice Crystal Size	0.27 (+)	0.27 (+)	0.50 (-)	0.63 (-)	0.00 (-)
Hardened Std Dev in Ice Crystal Size	0.04 (-)	0.01 (-)	0.08 (+)	0.24 (-)	0.03 (+)
Mean Air Cell Size	0.01 (-)	0.01 (+)	0.22 (+)	0.01 (-)	0.08 (+)
Std Dev in Air Cell Size	0.08 (+)	0.02 (-)	0.21 (+)	0.06 (-)	0.00 (+)
% Fat Destabilization	0.03 (+)	0.32 (-)	0.33 (+)	0.04 (+)	0.16 (+)

* The symbol in parenthesis indicates the whether the correlation is positive (+) or negative (-).

Table 4.4.12. Correlation coefficient R^2 between standard deviation in residence time and microstructural attributes as a function of dasher assembly.

Microstructural Attribute	Dasher Assembly				
	Solid Dasher	Multi + Solid	Standard + Solid	Multi + Wing	Standard + Wing
Draw Mean Ice Crystal Size	0.10 ⁽⁻⁾	0.07 ⁽⁺⁾	0.05 ⁽⁻⁾	0.04 ⁽⁻⁾	0.85 ⁽⁺⁾
Draw Std Dev in Ice Crystal Size	0.02 ⁽⁻⁾	0.11 ⁽⁺⁾	0.35 ⁽⁻⁾	0.22 ⁽⁻⁾	0.42 ⁽⁺⁾
Hardened Mean Ice Crystal Size	0.05 ⁽⁺⁾	0.21 ⁽⁺⁾	0.17 ⁽⁻⁾	0.06 ⁽⁻⁾	0.32 ⁽⁺⁾
Hardened Std Dev in Ice Crystal Size	0.05 ⁽⁺⁾	0.00 ⁽⁺⁾	0.03 ⁽⁻⁾	0.72 ⁽⁻⁾	0.04 ⁽⁻⁾
Mean Air Cell Size	0.04 ⁽⁻⁾	0.00 ⁽⁻⁾	0.00 ⁽⁻⁾	0.31 ⁽⁺⁾	0.46 ⁽⁺⁾
Std Dev in Air Cell Size	0.36 ⁽⁻⁾	0.00 ⁽⁺⁾	0.03 ⁽⁻⁾	0.14 ⁽⁺⁾	0.05 ⁽⁺⁾
% Fat Destabilization	0.66 ⁽⁻⁾	0.10 ⁽⁻⁾	0.00 ⁽⁺⁾	0.28 ⁽⁻⁾	0.34 ⁽⁻⁾

* The symbol in parenthesis indicates the whether the correlation is positive⁽⁺⁾ or negative⁽⁻⁾.

4.4.2 Overrun Experiment

The purpose of the overrun experiment was to evaluate the effects of dasher assembly and overrun on the processing conditions, RTD parameters, and microstructural attributes of ice cream made using a continuous SSF. Additionally, potential interactions between dasher assembly and overrun were evaluated.

4.4.2.1 Processing Conditions

The draw temperature was $-5.5 \pm 0.1^\circ\text{C}$ for all treatments. Viscosity and measured overrun are detailed in Table 4.4.13. The viscosity, or torque on the motor of the dasher, tended to increase with increasing dasher displacement. It is uncertain exactly what might cause this effect. Dasher assemblies with higher displacements weigh more, due to the increased amount of stainless steel required to make the assembly components. They also tend to have a higher surface area (Table 3.1) with which the product can come into contact, which would increase friction on the dasher. Both of these would necessitate more torque to turn the dasher. Additionally, the ‘viscosity’ is a method of cooling control on the CF700 freezer, as higher viscosities tend to be correlated with a higher proportion of ice. Increasing the viscosity would be related to a decrease in the refrigerant temperature, which would increase the rate of cooling at the wall of the freezing cylinder. Since the higher displacement dashers had shorter residence times, a higher rate of cooling (and thus viscosity) was necessary to achieve the target draw temperature.

The measured overrun was $75\% \pm 5\%$, with no differences measured between dasher assemblies within each overrun treatment. Increasing the overrun reduces the proportion of ice cream mix that is introduced to the freezing cylinder. This reduces the friction on the dasher assembly and therefore less torque (i.e., lower viscosity) is required to turn the dasher.

Additionally, since the draw temperature is related to the ice *fraction* relative to total moisture content (Figure 2.7), less total water needs to be frozen in a product with higher overrun to achieve the same draw temperature. As previously discussed, this would reduce the cooling requirements and thus ‘viscosity’ for higher overrun ice cream. This is an interesting finding as it contradicts previous research (Chang and Hartel, 2002a). However, the study by Chang and Hartel (2002a) measured the change in viscosity over time in a batch freezer. Although the overrun was increased, the change in viscosity would presumably be related to increasing ice content.

Table 4.4.13. Effects of dasher assembly and overrun on viscosity (measured as the torque placed on the dasher motor as a percentage of its total capacity) for ice cream made at a throughput rate = 300 L/h, dasher speed = 200 RPM, and draw temperature = -5.5 ± 0.1 °C.

Condition	Dasher Assembly	Overrun		
		50%	75%	100%
Viscosity (%)	Solid	97±2 ^{A,a}	83±3 ^{A,b}	77±0 ^{A,b}
	Multi + Solid	93±5 ^{A,a}	80±2 ^{AB,b}	70±1 ^{AB,c}
	Standard + Solid	94±3 ^{A,a}	74±2 ^{B,b}	66±1 ^{BC,c}
	Multi + Wing	75±3 ^{B,a}	67±3 ^{C,b}	59±2 ^{C,c}
	Standard + Wing	64±1 ^{C,a}	54±2 ^{D,b}	49±2 ^{D,b}

^{A-D} Within a column, means without a common uppercase superscript differ ($P < 0.05$) due to dasher.

^{a-c} Within a row, means without a common lowercase superscript differ ($P < 0.05$) due to overrun.

± Values indicate standard deviation for 3 replicates.

4.4.2.2 Residence Time Distribution

Cumulative RTD curves are presented in Figure 4.4.14. The first three moments of the distribution (defined in Eqns. 3.7-3.9) are given in Table 4.4.14. As overrun increased, these curves were shifted right, indicating a longer residence time for ice cream. Ndoye et al. (2018) found that an increased airflow rate resulted in a shorter mean residence time. However, the working fluid in their study was sorbet, which lacks fat and protein. Sorbet therefore cannot entrain as much air as ice cream. Additionally, their mix flow rate was kept constant. The study suggested that for sorbet,

a pocket of stagnant air was present in their SSF. As airflow rate increased, the volume of the pocket increased, theoretically creating a smaller volume through which the liquid phase could flow. This, they concluded, was the reason for the decreased residence time with increasing airflow rates. In the present study, the ratio of mix to airflow rate was adjusted to achieve a desired overrun, rather than only adjusting airflow. This meant that the mix flow rate was increased with decreasing airflow rate, which explains why a shorter residence time was observed for lower overrun treatments.

Dasher assemblies with a common beater tended to have similar RTD curves. $E(t)$ and $E(\theta)$ curves are presented in Figures 4.4.15 – 17, with a visual depiction of RTD samples collected given in Figure 4.4.18. The $E(\theta)$ curves tended to be similar overall; however, it appears that as overrun decreased, the curves for dasher assemblies containing a wing beater became narrower relative to the other dasher assemblies. This would indicate a decrease in axial dispersion with decreasing overrun for dasher assemblies with wing beaters. This could be related to higher radial temperature gradients, which would be more pronounced in higher overrun products since air would decrease the overall thermal conductivity of the ice cream. An increase in the radial temperature gradient causes product near the freezer wall, which is colder and therefore has a higher viscosity, to have a slower fluid flow relative to ice cream further from the cylinder wall. This effectively causes differences in axial velocities, thereby increasing axial dispersion (Arellano et al., 2013a). This was likely only observed in configurations containing the wing beater because it allows a larger working volume and for mix to flow more proximally relative to the freezing cylinder, both of which would enhance radial temperature gradients.

The mean residence time ranged from 82 – 205 s. There was a significant effect of dasher assembly on mean residence time, with average residence time tending to decrease as the dasher

displacement increased (Table 3.1) due to the lower volume available for the working fluid to flow. As overrun increased, mean residence time also significantly increased for all dasher assemblies (Figure 4.4.19). However, there was also an interaction effect of dasher assembly and overrun on mean residence time (Table 4.4.15). Increasing the overrun seemingly had a larger effect on dasher assemblies containing a wing beater. At 50% and 75% overrun, there were no significant differences in mean residence time between open dasher assemblies with a common beater. At 100% overrun, the mean residence time for the standard + wing configuration was significantly longer than for the multi + wing configuration. However, there was still no difference between configurations with the solid beater.

There was a significant effect of dasher assembly on the variance in residence time. The solid dasher and multi + solid configuration consistently had lower variance than the standard + wing configuration. A significant effect of overrun on variance in residence time was observed (Table 4.4.15). While there were not significant differences among individual treatments, it seems there was a trend of increased variance with increasing overrun (Table 4.4.14). Overrun did not have a significant effect on skewness. While a significant effect of dasher assembly was attained, there were no significant differences between individual treatments and no meaningful trends were observed.

Table 4.4.14. Effects of dasher assembly and overrun on residence time distribution parameters for ice cream made at a throughput rate = 300 L/h, dasher speed = 200 RPM, and draw temperature = -5.5 ± 0.1 °C as determined by pulse injection study.

Residence Time Parameter	Dasher Assembly	Overrun		
		50%	75%	100%
Mean Residence Time, t_s (s)	Solid	82±1 ^{C,b}	95±4 ^{C,ab}	106±6 ^{D,a}
	Multi + Solid	106±3 ^{B,b}	116±3 ^{B,ab}	125±2 ^{C,a}
	Standard + Solid	105±2 ^{B,b}	117±4 ^{B,ab}	129±4 ^{C,a}
	Multi + Wing	152±3 ^{A,c}	174±3 ^{A,b}	189±3 ^{B,a}
	Standard + Wing	155±8 ^{A,c}	187±9 ^{A,b}	205±6 ^{A,a}
Variance, σ^2 (s ²)	Solid	679±73 ^{B,a}	817±120 ^{B,a}	1110±314 ^{C,a}
	Multi + Solid	1240±105 ^{B,a}	1340±317 ^{B,a}	1440±134 ^{BC,a}
	Standard + Solid	1300±29 ^{AB,a}	1430±233 ^{B,a}	1660±481 ^{BC,a}
	Multi + Wing	1460±80 ^{AB,a}	1930±102 ^{B,a}	2250±146 ^{AB,a}
	Standard + Wing	2390±725 ^{A,a}	3250±1000 ^{A,a}	3110±275 ^{A,a}
Skewness, s^3	Solid	0.76±0.15 ^{A,a}	0.76±0.04 ^{A,a}	1.06±0.38 ^{A,a}
	Multi + Solid	0.81±0.14 ^{A,a}	0.85±0.07 ^{A,a}	0.87±0.06 ^{A,a}
	Standard + Solid	1.05±0.08 ^{A,a}	0.87±0.08 ^{A,a}	0.96±0.15 ^{A,a}
	Multi + Wing	0.63±0.10 ^{A,a}	0.60±0.05 ^{A,a}	0.55±0.16 ^{A,a}
	Standard + Wing	1.05±0.08 ^{A,a}	1.06±0.60 ^{A,a}	0.60±0.15 ^{A,a}

^{A-D} Within a parameter and column, means without a common uppercase superscript differ ($P < 0.05$) due to dasher.

^{a-c} Within a row, means without a common lowercase superscript differ ($P < 0.05$) due to overrun.

± Values indicate standard deviation for 3 replicates.

Table 4.4.15. ANOVA table assessing factors residence time distribution parameters.

Parameter	Factor	F-value	P-value
Mean	Overrun	173	<0.001*
	Dasher Assembly	640	<0.001*
	Overrun : Dasher Assembly	6.27	<0.001*
Variance	Overrun	6.77	0.004*
	Dasher Assembly	37.1	<0.001*
	Overrun : Dasher Assembly	0.07	0.68
Skewness	Overrun	0.22	0.80
	Dasher Assembly	4.10	0.009*
	Overrun : Dasher Assembly	1.80	0.12

* Denotes factors that are significant at $p < 0.05$.

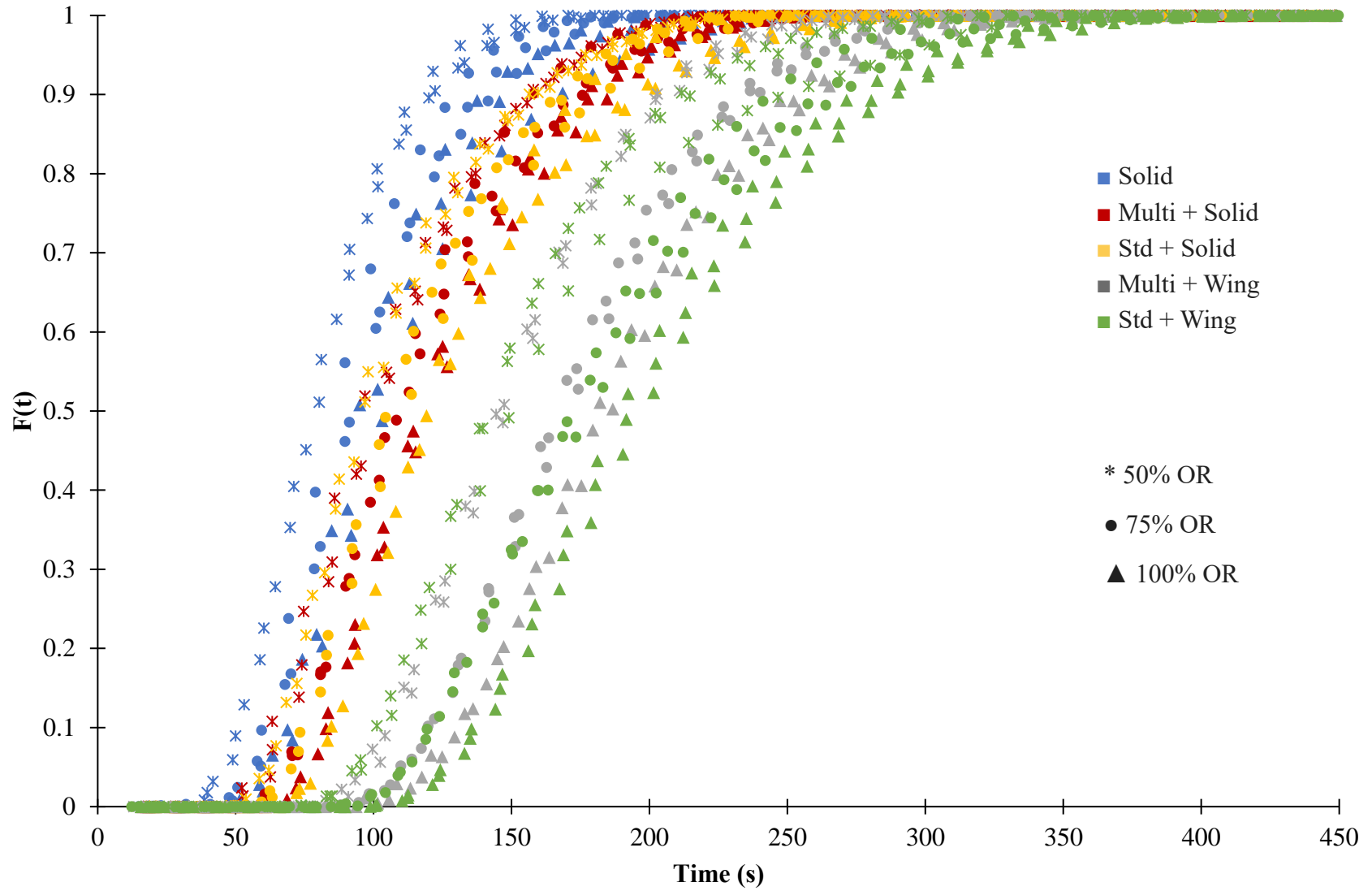


Figure 4.4.14. Cumulative residence time distribution $F(t)$ curves as a function of dasher assembly and overrun for ice cream made at 300 L/h throughput, 200 RPM dasher speed, and -5.5°C draw temperature ($n=3$).

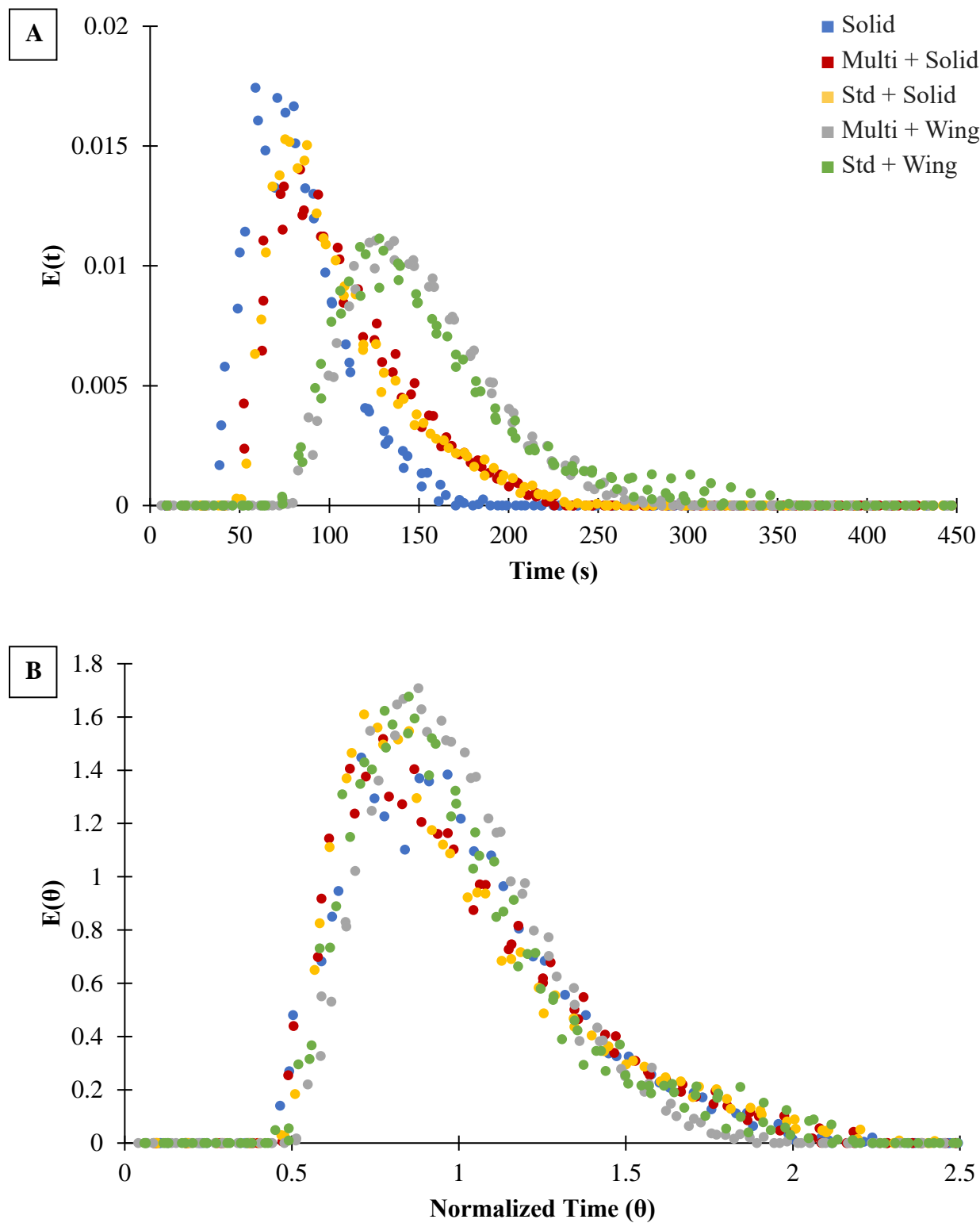


Figure 4.4.15. A) $E(t)$ curves and B) $E(\theta)$ curves as a function of dasher assembly for ice cream made at 50% overrun. Throughput = 300 L/h, dasher speed = 200 RPM, draw temperature = $-5.5 \pm 0.1^\circ\text{C}$ ($n=3$).

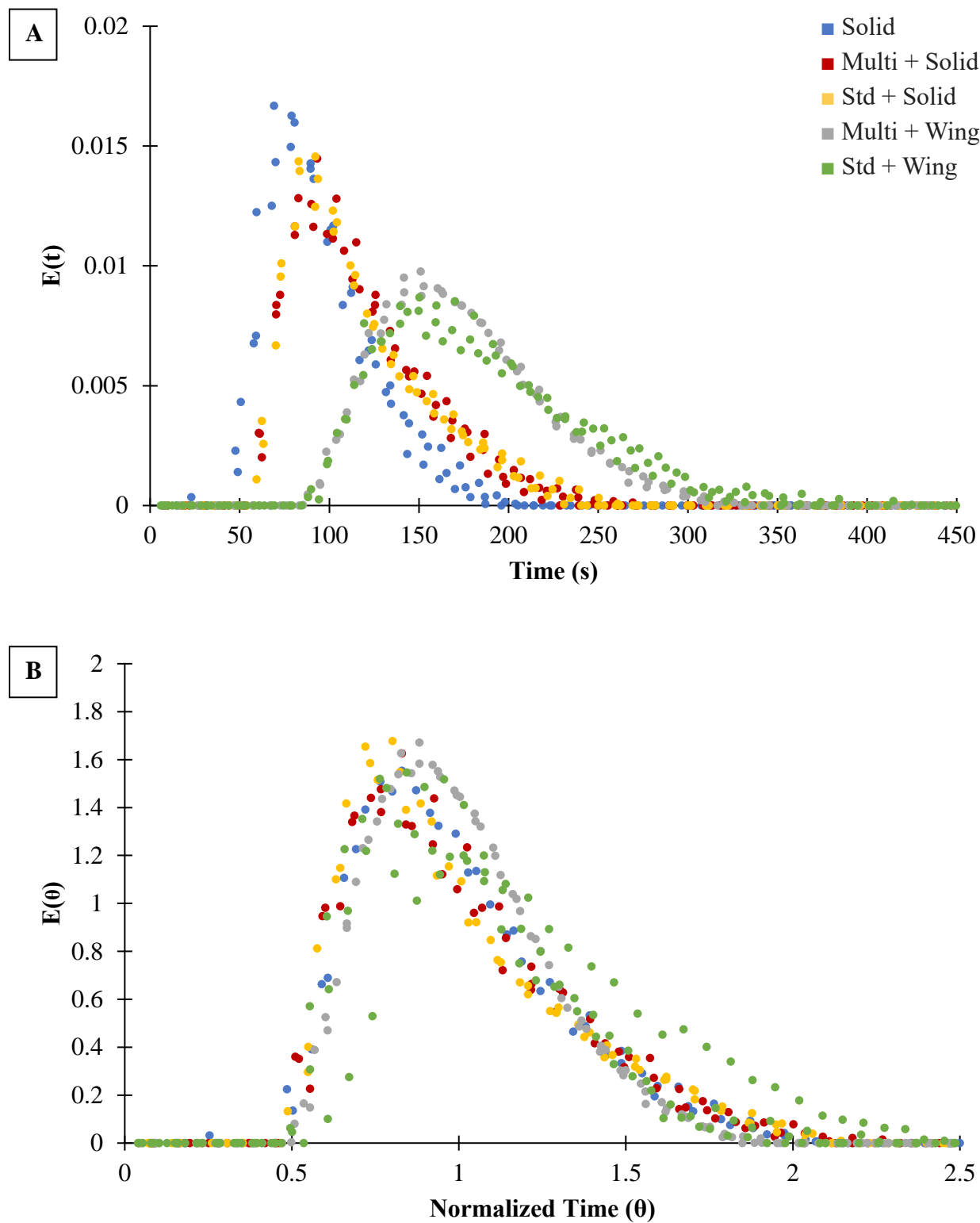


Figure 4.4.16. A) $E(t)$ curves and B) $E(\theta)$ curves as a function of dasher assembly for ice cream made at 75% overrun. Throughput = 300 L/h, dasher speed = 200 RPM, draw temperature = $-5.5 \pm 0.1^\circ\text{C}$ ($n=3$).

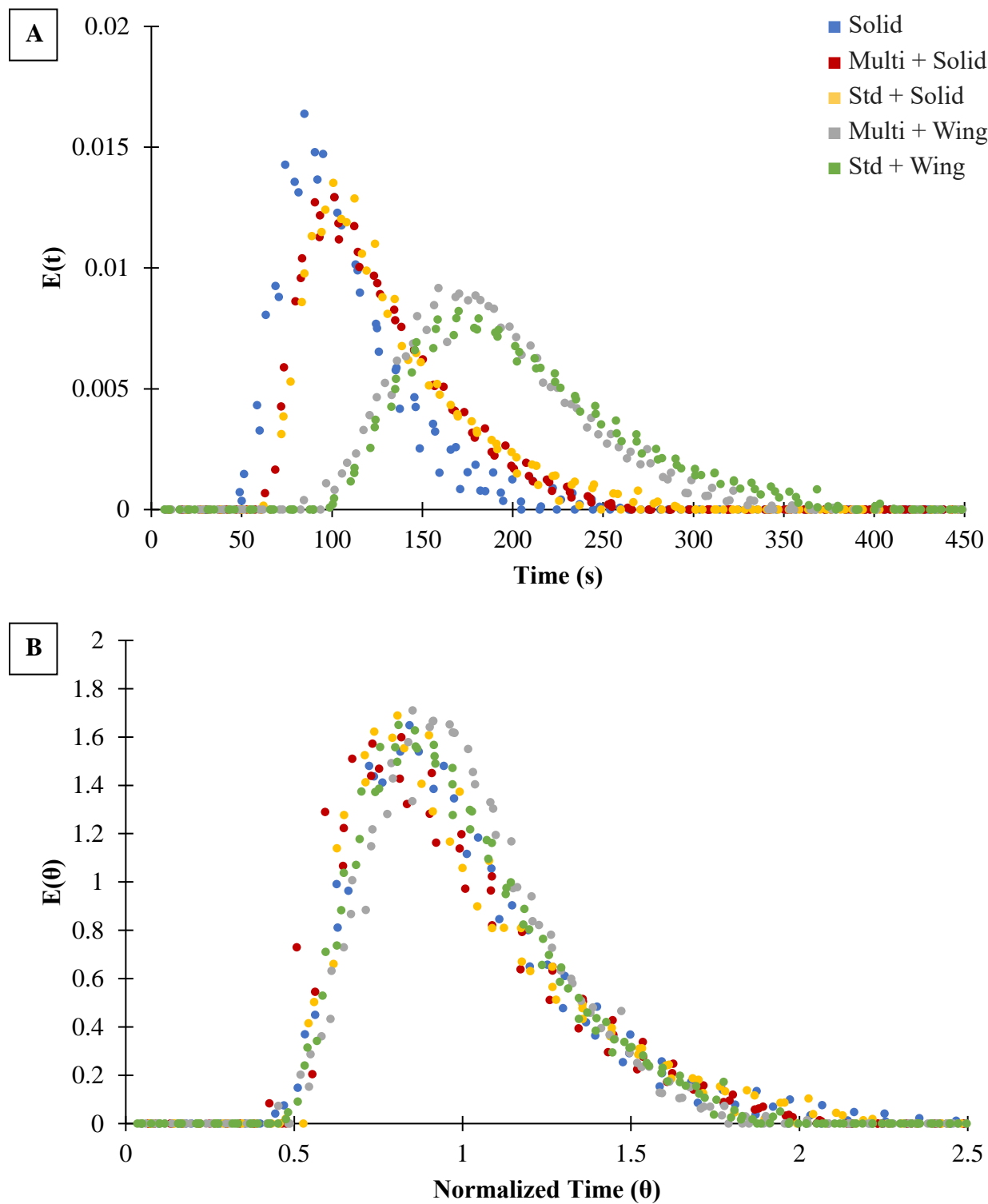


Figure 4.4.17. A) $E(t)$ curves and B) $E(\theta)$ curves as a function of dasher assembly for ice cream made at 100% overrun. Throughput = 300 L/h, dasher speed = 200 RPM, draw temperature = $-5.5 \pm 0.1^\circ\text{C}$ ($n=3$).

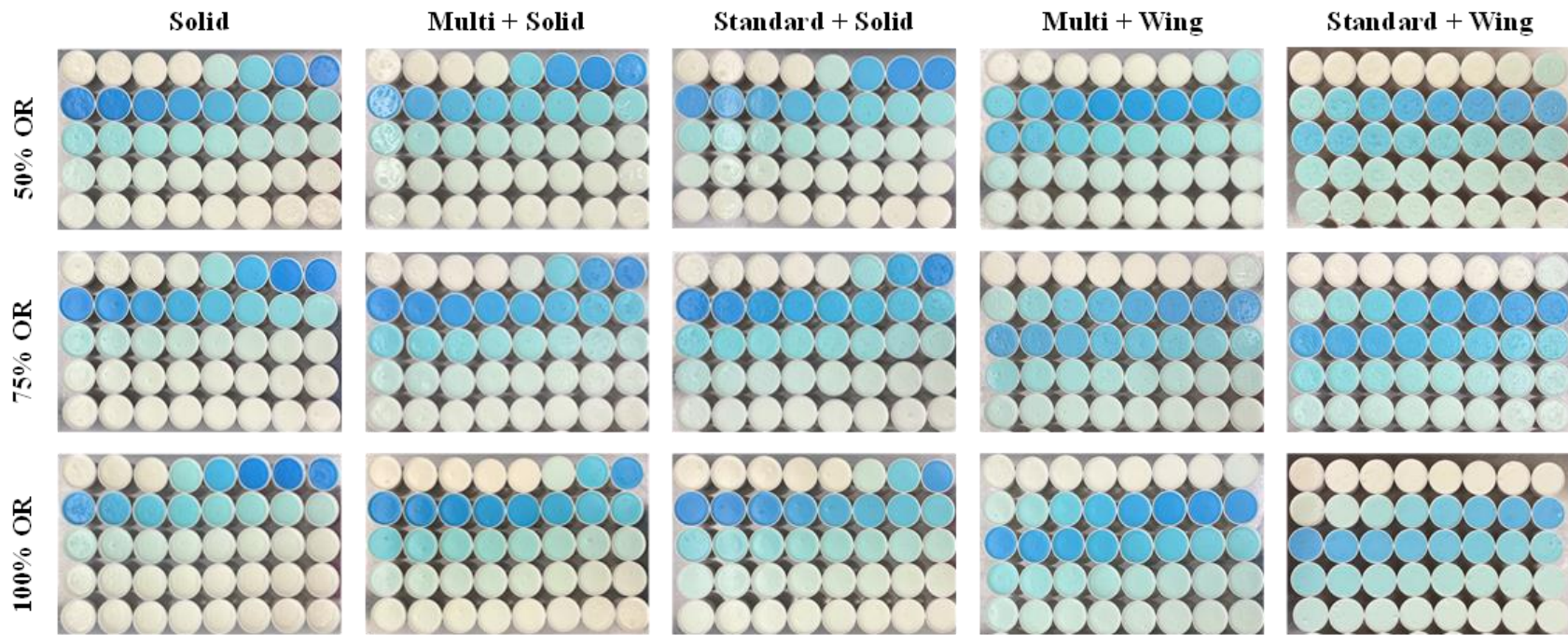


Figure 4.4.18. Images of samples collected during pulse injection experiment for evaluating residence time distribution of ice cream as a function of dasher assembly and overrun. Throughput = 300 L/h, dasher speed = 200 RPM, draw temperature = -5.5 ± 0.1 °C. Top left cup in each image was collected at $t = 0$ s when 20 mL of tracer (1% methylene blue in ice cream mix) was injected into freezer.

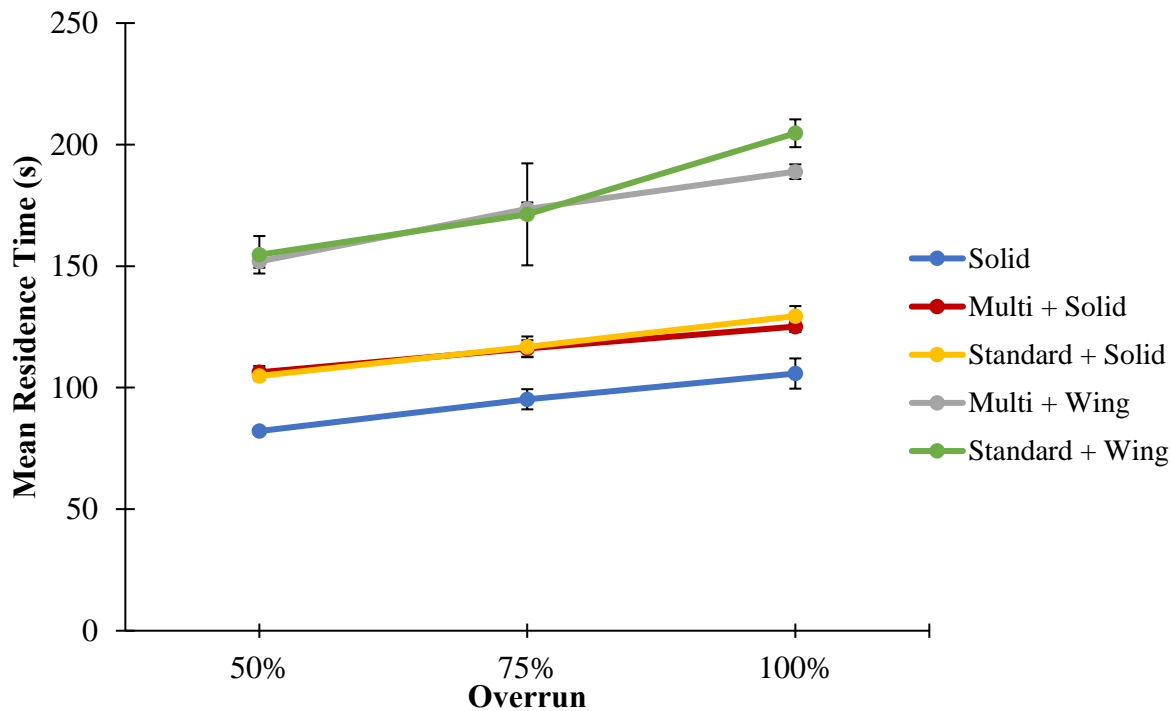


Figure 4.4.19. Mean residence time t_s as a function of dasher assembly and overrun. Throughput = 300 L/h, dasher speed = 200 RPM, draw temperature = $-5.5 \pm 0.1^\circ\text{C}$. Values represent averages for three replicates.

4.4.2.3 Microstructure

Microstructural parameters as a function of overrun and dasher assembly are summarized in Table 4.4.16.

4.4.2.3.1 Ice Crystal Size – Draw

The average ice crystal size at draw ranged from 19.0 – 25.7 μm . The cumulative ice crystal size distribution curves are presented in Figure 4.4.20. There were no statistically significant differences among individual treatments on ice crystal size (Table 4.4.16). While there was not a significant effect of overrun on ice crystal size, when results from all modeled overruns were averaged, there was a significant effect of dasher assembly (Table 4.4.17) where the standard + wing assembly had significantly larger mean size than the solid dasher. Similarly, the standard +

Table 4.4.16. Effects of dasher assembly and overrun on microstructural attributes of ice cream made at a throughput rate = 300 L/h, dasher speed = 200 RPM, and draw temperature = $-5.5 \pm 0.1^\circ\text{C}$.

Microstructural Attribute	Dasher Assembly	Overrun			
		50%	75%	100%	
Draw Ice Crystal Diameter [†]	Mean (μm) Variance (μm)	Solid	19.5 \pm 4.1 ^{A,a} 6.0 \pm 0.0 ^{A,a}	19.1 \pm 1.0 ^{A,a} 5.4 \pm 0.3 ^{A,a}	19.0 \pm 4.2 ^{A,a} 5.9 \pm 0.4 ^{A,a}
		Multi + Solid	22.5 \pm 2.0 ^{A,a} 7.4 \pm 1.4 ^{A,a}	20.8 \pm 0.7 ^{A,a} 6.3 \pm 0.5 ^{A,ab}	21.2 \pm 0.3 ^{A,a} 7.2 \pm 0.8 ^{A,a}
		Standard + Solid	20.9 \pm 2.7 ^{A,a} 7.3 \pm 0.6 ^{A,a}	22.0 \pm 2.6 ^{A,a} 6.1 \pm 0.4 ^{A,ab}	20.3 \pm 2.4 ^{A,a} 6.1 \pm 0.9 ^{A,a}
		Multi + Wing	21.0 \pm 1.7 ^{A,a} 7.5 \pm 0.6 ^{A,a}	21.3 \pm 1.7 ^{A,a} 6.3 \pm 0.3 ^{A,ab}	21.1 \pm 1.3 ^{A,a} 7.3 \pm 0.6 ^{A,a}
		Standard + Wing	22.4 \pm 3.7 ^{A,a} 8.2 \pm 0.5 ^{A,a}	25.7 \pm 6.6 ^{A,a} 8.4 \pm 2.8 ^{A,b}	23.4 \pm 2.9 ^{A,a} 8.5 \pm 0.2 ^{A,a}
Hardened Ice Crystal Diameter [‡]	Mean (μm) Variance (μm)	Solid	29.7 \pm 2.9 ^{A,a} 10.2 \pm 0.8 ^{A,a}	30.6 \pm 0.7 ^{A,a} 9.7 \pm 0.8 ^{A,a}	28.9 \pm 2.4 ^{A,a} 10.1 \pm 0.8 ^{A,a}
		Multi + Solid	30.3 \pm 0.5 ^{A,a} 10.2 \pm 1.4 ^{A,a}	30.5 \pm 1.2 ^{A,a} 9.9 \pm 0.9 ^{A,a}	30.8 \pm 0.2 ^{A,a} 10.3 \pm 1.7 ^{A,a}
		Standard + Solid	29.0 \pm 3.8 ^{A,a} 10.6 \pm 0.8 ^{A,a}	30.2 \pm 0.7 ^{A,a} 10.1 \pm 0.2 ^{A,a}	29.2 \pm 3.7 ^{A,a} 10.7 \pm 0.6 ^{A,a}
		Multi + Wing	31.1 \pm 1.7 ^{A,a} 11.3 \pm 1.5 ^{A,a}	31.8 \pm 1.2 ^{A,a} 11.0 \pm 0.4 ^{A,a}	30.4 \pm 5.4 ^{A,a} 10.9 \pm 1.2 ^{A,a}
		Standard + Wing	31.3 \pm 0.7 ^{A,a} 10.9 \pm 1.8 ^{A,a}	32.2 \pm 0.8 ^{A,a} 11.3 \pm 0.2 ^{A,a}	31.1 \pm 1.5 ^{A,a} 10.9 \pm 1.5 ^{A,a}
Air Cell Diameter [‡]	Mean (μm) Variance (μm)	Solid	25.7 \pm 2.1 ^{A,a} 12.5 \pm 2.7 ^{AB,a}	27.0 \pm 2.2 ^{A,a} 15.8 \pm 1.4 ^{B,a}	24.3 \pm 2.9 ^{A,a} 11.3 \pm 2.1 ^{A,a}
		Multi + Solid	25.9 \pm 0.8 ^{A,a} 12.4 \pm 1.3 ^{AB,a}	23.1 \pm 1.4 ^{A,a} 9.9 \pm 0.8 ^{A,a}	25.0 \pm 0.9 ^{A,a} 11.6 \pm 0.4 ^{A,a}
		Standard + Solid	29.1 \pm 2.1 ^{A,a} 15.7 \pm 0.8 ^{B,a}	25.1 \pm 4.9 ^{A,a} 12.8 \pm 4.5 ^{AB,a}	26.1 \pm 1.0 ^{A,a} 14.3 \pm 2.5 ^{A,a}
		Multi + Wing	26.0 \pm 1.1 ^{A,a} 8.4 \pm 0.4 ^{A,a}	26.6 \pm 2.0 ^{A,a} 13.4 \pm 2.3 ^{AB,a}	24.1 \pm 1.3 ^{A,a} 12.0 \pm 1.6 ^{A,a}
		Standard + Wing	26.8 \pm 3.0 ^{A,a} 13.0 \pm 1.7 ^{AB,a}	24.9 \pm 2.1 ^{A,a} 11.8 \pm 0.5 ^{AB,a}	23.5 \pm 1.8 ^{A,a} 11.3 \pm 1.7 ^{A,a}
Fat	% Destabilization	Solid	44.2 \pm 3.0 ^{A,b}	57.0 \pm 7.4 ^{A,ab}	61.1 \pm 2.8 ^{A,a}
		Multi + Solid	40.0 \pm 3.0 ^{ABC,b}	57.3 \pm 3.7 ^{A,a}	58.7 \pm 3.0 ^{AB,a}
		Standard + Solid	45.2 \pm 8.7 ^{A,a}	50.6 \pm 6.5 ^{AB,a}	53.9 \pm 3.1 ^{AB,a}
		Multi + Wing	27.0 \pm 7.1 ^{BC,b}	41.8 \pm 8.0 ^{AB,ab}	49.7 \pm 6.9 ^{AB,a}
		Standard + Wing	25.6 \pm 2.0 ^{C,b}	37.0 \pm 6.9 ^{B,ab}	43.9 \pm 3.7 ^{B,a}

^{A-B} Within an attribute and column, means without a common uppercase superscript differ ($P < 0.05$) due to dasher.

^{a-b} Within a row, means without a common lowercase superscript differ ($P < 0.05$) due to overrun.

[†] Draw ice crystal diameter mean and variance evaluated at -5.5°C .

[‡] Hardened ice crystal/air cell diameter mean and variance evaluated at -15°C .

\pm Values indicate standard deviation for 3 replicates.

wing assembly had a significantly higher standard deviation in ice crystal size than all other dasher assemblies when results from all modeled overruns were averaged (Figure 4.4.21b).

Warren and Hartel (2018) and Hernández-Parra et al. (2018a) also found that overrun did not influence ice crystal size. However, other studies have found that increasing overrun decreases the ice crystal size, likely due to the insulating effect of air which limits heat transfer and therefore recrystallization (Flores and Goff, 1999b; Caillet et al., 2003; Sofjan and Hartel, 2004; Inoue et al., 2008). Perhaps this insulating effect is offset by the increased residence time associated with increasing overrun, and this is why a difference in ice crystal size due to overrun was not observed.

Table 4.4.17. ANOVA table assessing factors affecting ice crystal size at draw ($-5.5 \pm 0.1^\circ\text{C}$).

Attribute	Factor	F-value	P-value
Mean	Overrun	0.27	0.77
	Dasher Assembly	2.79	0.04*
	Overrun : Dasher Assembly	0.30	0.96
Standard Deviation	Overrun	2.66	0.09
	Dasher Assembly	9.08	<0.001*
	Overrun : Dasher Assembly	0.46	0.88

* Denotes factors that are significant at $p < 0.05$.

4.4.2.3.2 *Ice Crystal Size – Hardened*

The average size of ice crystals in hardened ice cream ranged from 29.0 – 32.2 μm . Cumulative ice crystal size distributions for hardened ice cream are presented in Figure 4.4.22. No differences were observed among treatments (Table 4.4.16; Figure 4.4.23) and no effect of dasher assembly or overrun was detected (Table 4.4.18). Differences that were detected in ice crystal size distributions at draw were perhaps not large enough to have a significant impact after ice crystal growth during hardening.

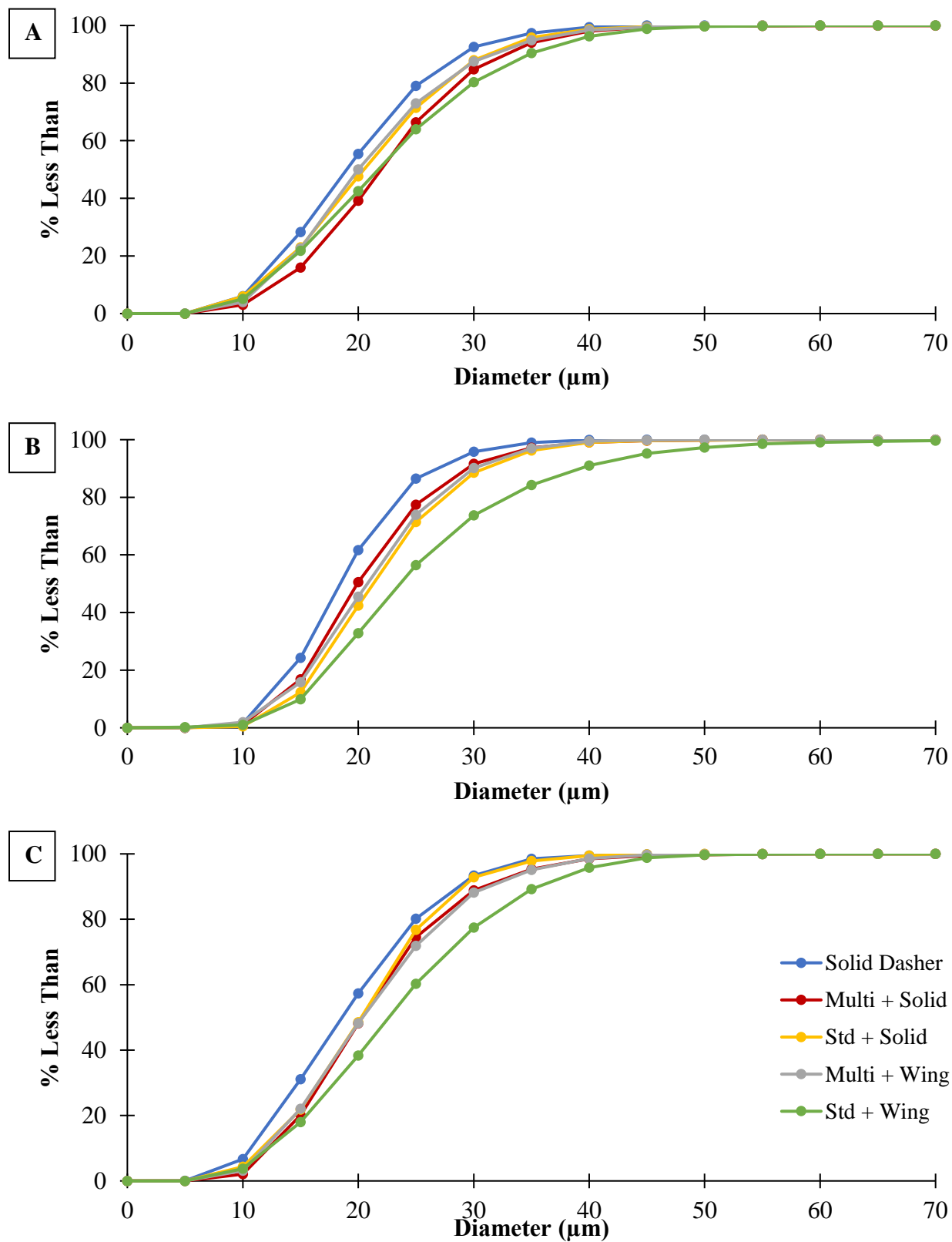


Figure 4.4.20. Cumulative ice crystal size distributions immediately after draw (-5.5°C) as a function of dasher assembly for ice cream made at an overrun of A) 50%, B) 75% and C) 100%. Throughput = 300 L/h, dasher speed = 200 RPM, draw temperature = $-5.5 \pm 0.1^{\circ}\text{C}$.

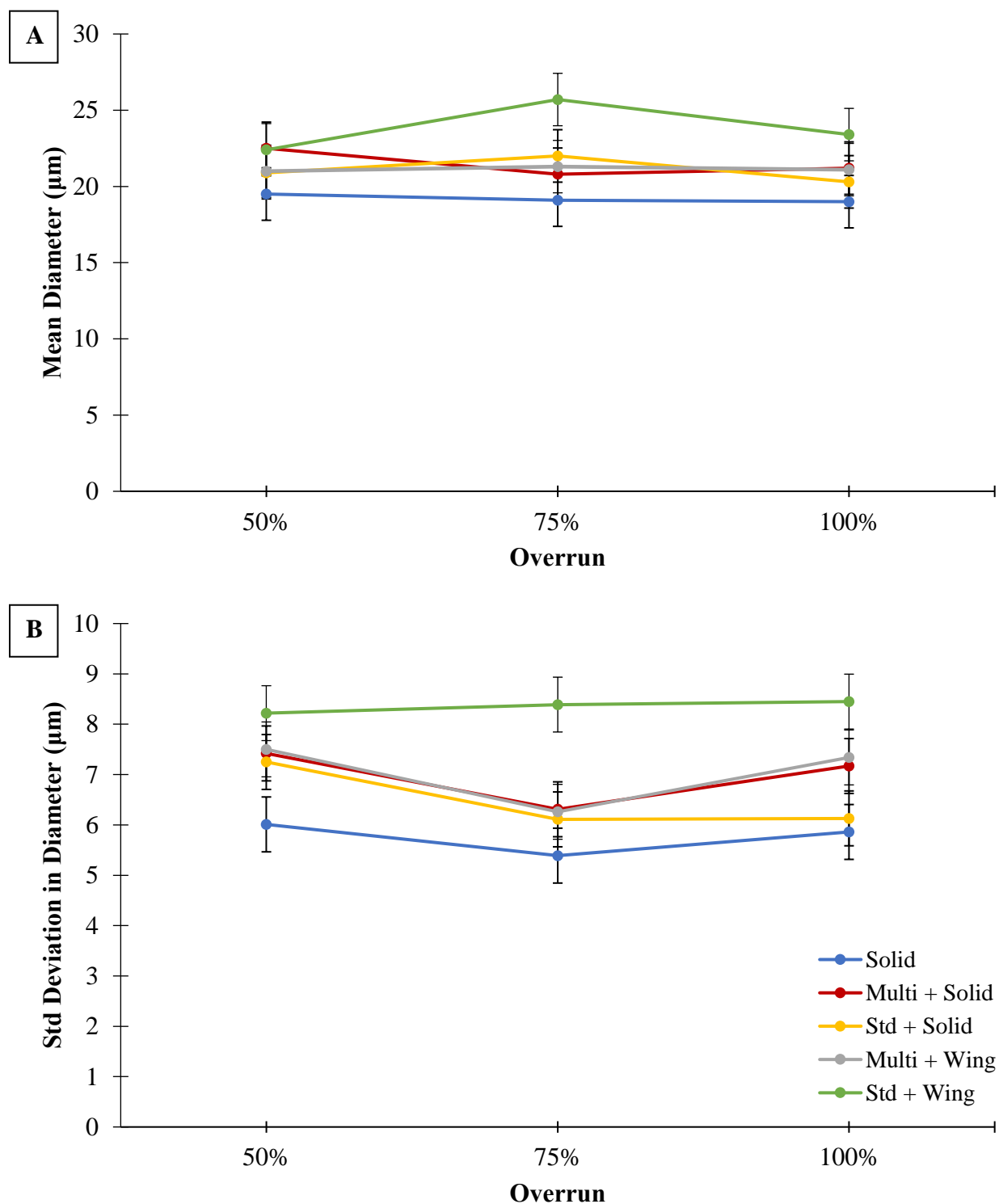


Figure 4.4.21. A) Mean ice crystal size and B) standard deviation in ice crystal size of ice cream immediately after draw (-5.5°C) as a function of dasher assembly and overrun. Throughput = 300 L/h, dasher speed = 200 RPM, draw temperature = $-5.5 \pm 0.1^{\circ}\text{C}$. Values represent the modeled averages for three replicates.

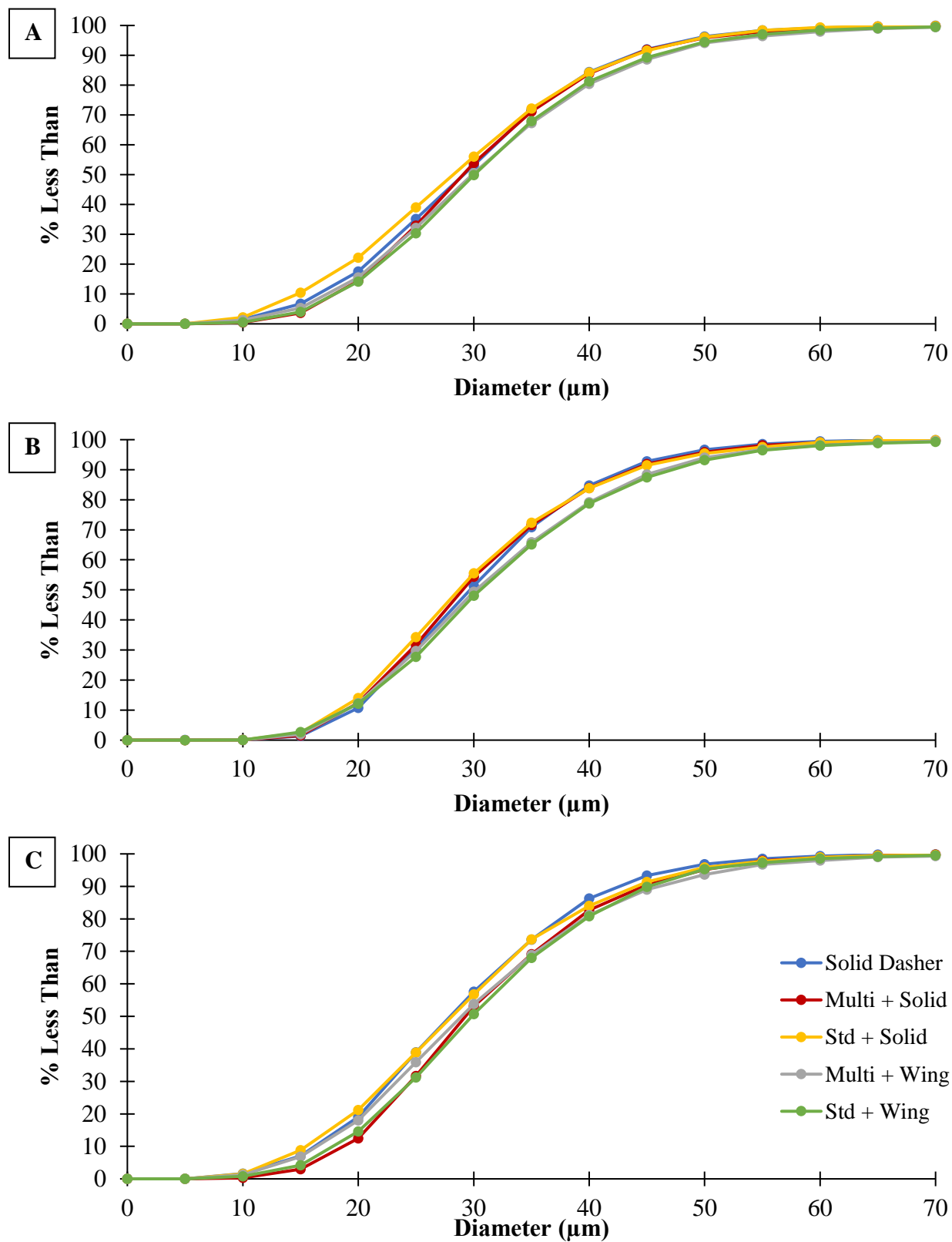


Figure 4.4.22. Cumulative ice crystal size distributions as a function of dasher assembly for hardened ice cream samples made at an overrun of A) 50%, B) 75% and C) 100%. Throughput = 300 L/h, dasher speed = 200 RPM, draw temperature = $-5.5 \pm 0.1^\circ\text{C}$.

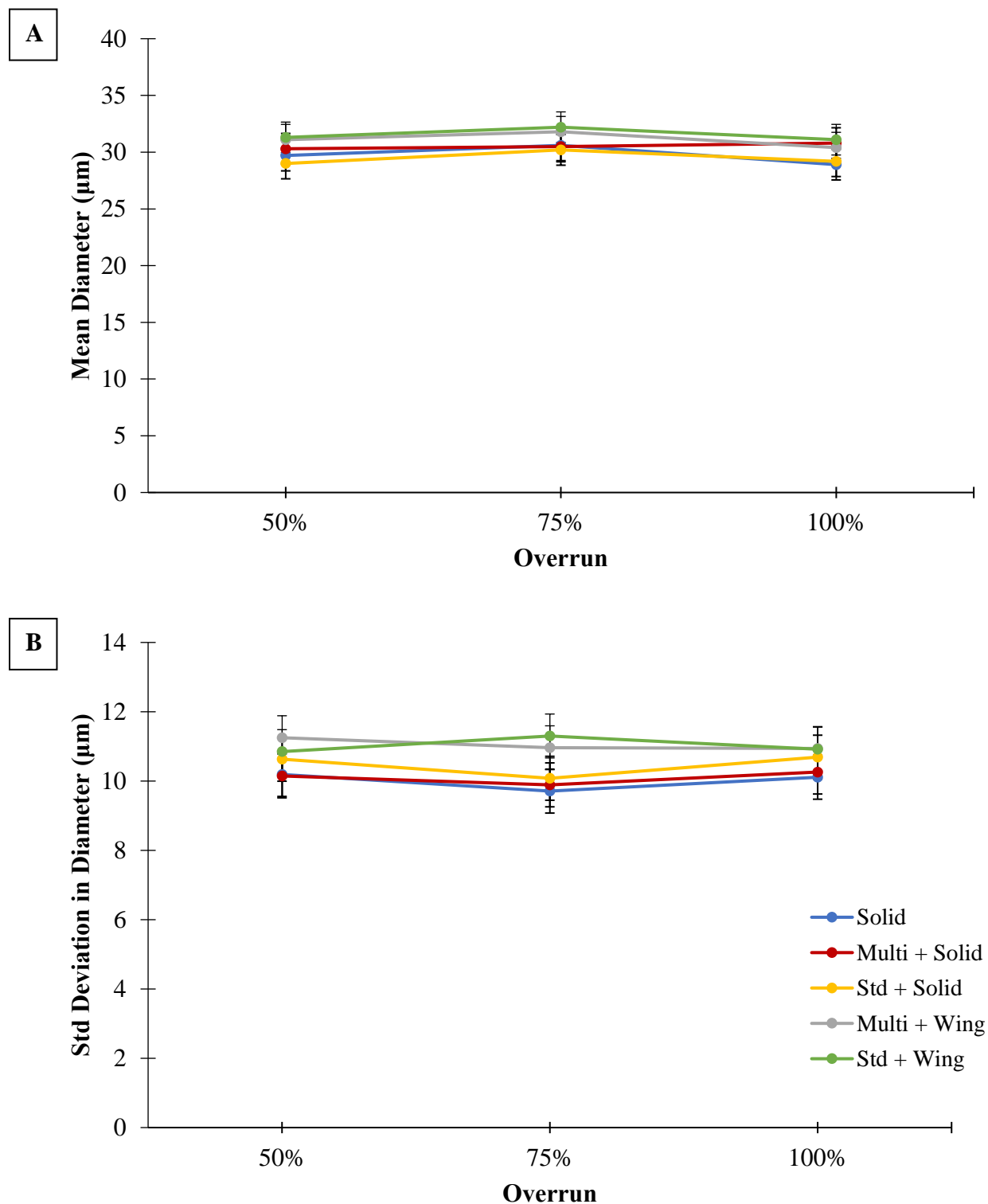


Figure 4.4.23. A) Mean ice crystal size and B) standard deviation in ice crystal size of hardened ice cream samples as a function of dasher assembly and overrun. Throughput = 300 L/h, dasher speed = 200 RPM, draw temperature = $-5.5 \pm 0.1^\circ\text{C}$. Samples were evaluated at -15°C . Values represent the modeled averages for three replicates.

Table 4.4.18. ANOVA table assessing factors affecting ice crystal size in hardened ice cream.

Attribute	Factor	F-value	P-value
Mean	Overrun	0.75	0.48
	Dasher Assembly	1.27	0.30
	Overrun : Dasher Assembly	0.09	0.99
Standard Deviation	Overrun	0.19	0.83
	Dasher Assembly	1.83	0.15
	Overrun : Dasher Assembly	0.14	0.99

* Denotes factors that are significant at $p < 0.05$.

4.4.2.3.3 *Air Cell Size*

The air cell size of hardened ice cream samples ranged from 23.1 – 29.1 μm . The cumulative air cell size distributions are presented in Figure 4.4.24. There were no significant differences among individual treatments (Table 4.4.16). There was not a significant effect of dasher assembly on mean air cell size. However, when data from all dasher assemblies was modeled together, mean air cell size decreased as overrun increased (Table 4.4.19). Specifically, there was a significant difference in air cell size between samples made at 50% versus 100% overrun (Figure 4.4.25a). This is consistent with the findings of Sofjan and Hartel (2004), Hernández-Parra et al. (2018a), and Warren and Hartel (2018), and may be related to the increasing viscosity (torque on dasher motor) that was observed, which would suggest that shear forces inside the freezer were increased and promoting air cell breakup during freezing.

There was not a significant effect of overrun on the standard deviation in air cell size; however, there was a significant effect of dasher assembly as well as an interaction effect between dasher assembly and overrun. The standard + solid assembly had significantly higher standard deviation in air cell size than the multi + wing configuration at 50% OR, and the solid dasher had significantly higher standard deviation in air cell size than the multi + solid configuration at 75% OR (Figure 4.4.25b). However, these differences do not appear to follow any trends. The same can be said for potential interactions.

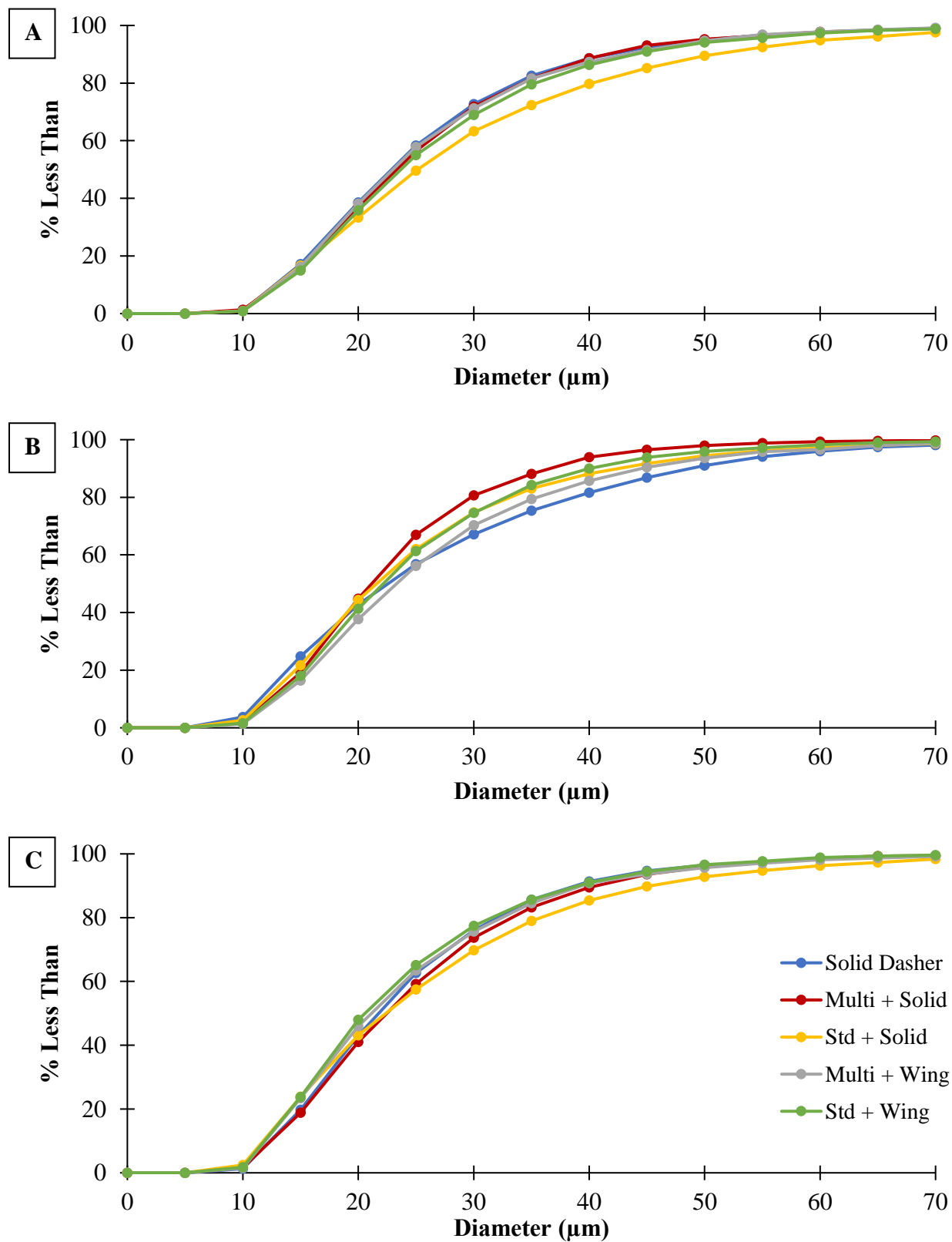


Figure 4.4.24. Cumulative air cell size distributions as a function of dasher assembly for hardened ice cream samples made at an overrun of A) 50%, B) 75% and C) 100%. Throughput = 300 L/h, dasher speed = 200 RPM, draw temperature = $-5.5 \pm 0.1^\circ\text{C}$. Samples were evaluated at -6°C .

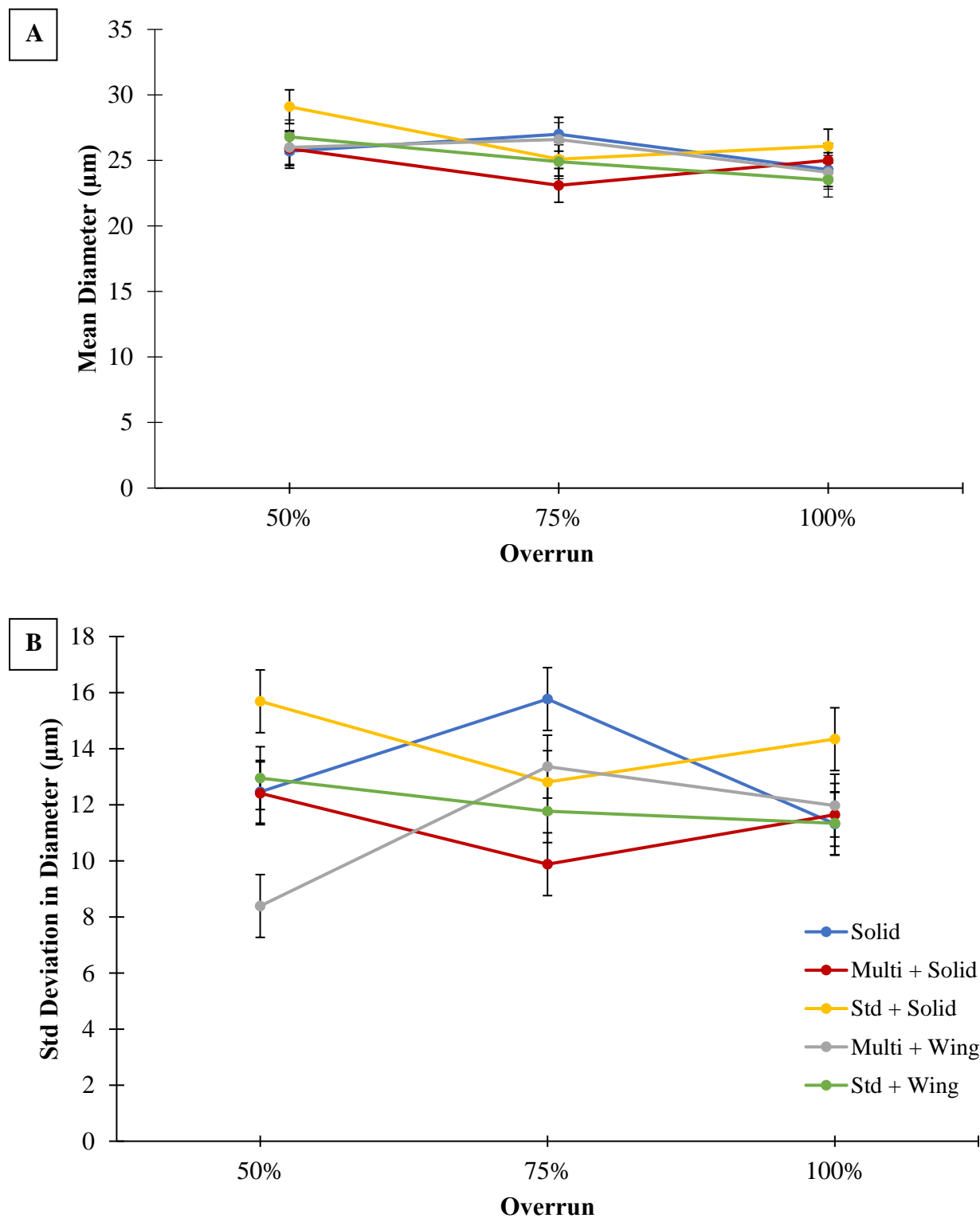


Figure 4.4.25. A) Mean air cell size and B) standard deviation in air cell size of hardened ice cream samples as a function of dasher assembly and overrun. Throughput = 300 L/h, dasher speed = 200 RPM, draw temperature = $-5.5 \pm 0.1^\circ\text{C}$. Samples were evaluated at -6°C . Values represent the modeled averages for three replicates.

Table 4.4.19. ANOVA table assessing factors affecting air cell size in hardened ice cream.

Attribute	Factor	F-value	P-value
Mean	Overrun	3.32	0.049*
	Dasher Assembly	1.09	0.38
	Overrun : Dasher Assembly	1.04	0.43
Standard Deviation	Overrun	0.35	0.71
	Dasher Assembly	4.05	0.01*
	Overrun : Dasher Assembly	3.15	0.01*

* Denotes factors that are significant at $p < 0.05$.

4.4.2.3.4 Fat Destabilization

The level of fat destabilization ranged from 25.6 – 61.1%. There was a significant effect of overrun on fat destabilization (Figure 4.4.26; Table 4.4.20). The size distributions of fat globules/clusters are shown in Figure 4.4.27. The second peak, which indicates destabilized fat, became larger with increasing overrun. This can also be seen in the microscopy images in Figure 4.4.28, in which fat clusters appear to become larger as overrun increases. This agrees with previous studies (Kokubo et al., 1996; Kokubo et al., 1998; Inoue et al., 2008; Warren and Hartel, 2018). As overrun increases, the ratio of mix to air in the freezer decreases. At a given ice cream throughput rate, this increases the average residence time of the mix portion in the freezer. This increases the likelihood that a fat globule collision will occur. Additionally, shear in the serum phase is increased as overrun increases due to narrowing of the lamellae between air cells, which also promotes fat destabilization.

There was also a significant effect of dasher assembly on fat destabilization (Figure 4.4.26; Table 4.4.20). Generally, higher displacement dashers exhibited higher levels of fat destabilization. The solid dasher consistently had higher levels of fat destabilization than the standard + wing configuration. At 50% OR, the solid dasher and standard + solid dasher also had significantly higher fat destabilization than the multi + wing configuration. At 75% OR, the multi + solid had higher fat destabilization than the standard + wing. This is consistent with the results

of Kokubo et al. (1996) who found that increased dasher displacement resulted in higher levels of fat destabilization. While it was believed increasing the residence time would increase the likelihood of fat globule collisions and therefore increase fat destabilization, the dasher with the shortest residence time had the highest level of fat destabilization. Fat destabilization is therefore likely related to the increase in viscosity of the product in the freezer that is observed with higher displacement dashers, which would impart more shear on the product. However, it does not appear that the relationship between displacement and destabilization is sensitive, as only the dashers with the largest differences in displacement exhibited differences in fat destabilization.

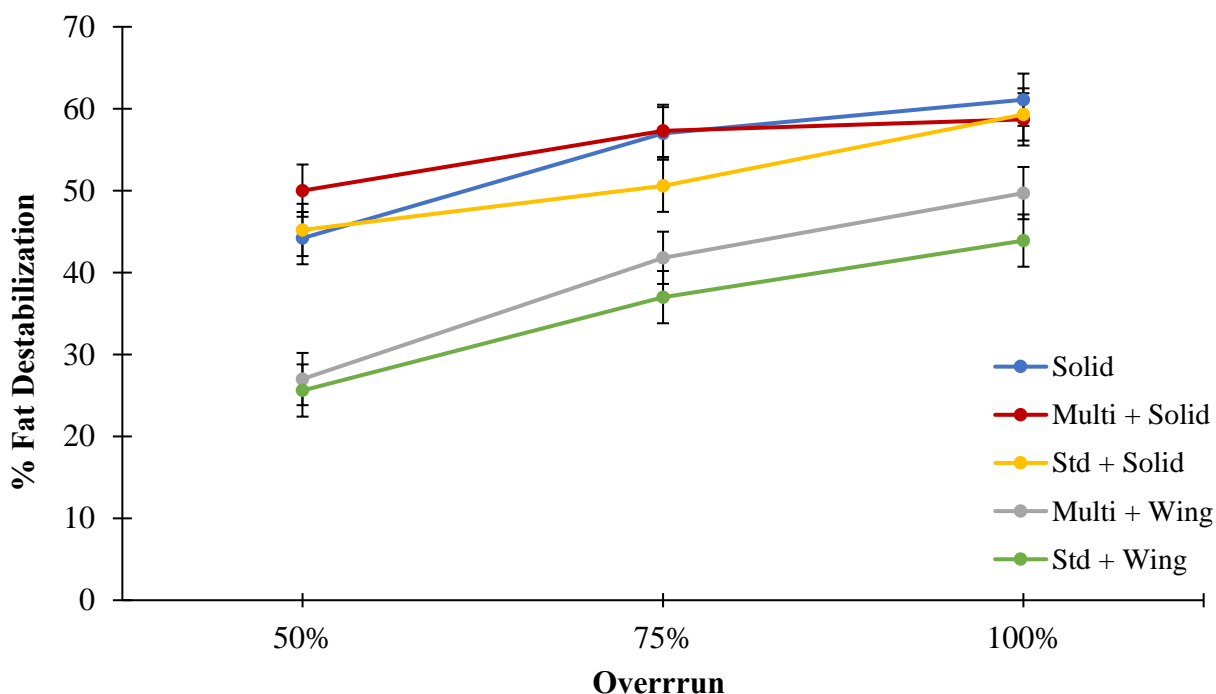


Figure 4.4.26. Mean fat destabilization (%) for ice cream samples as a function of dasher assembly and overrun. Throughput = 300 L/h, dasher speed = 200 RPM, draw temperature = -5.5°C. Values represent the modeled averages for three replicates.

Table 4.4.20. ANOVA table assessing factors affecting fat destabilization.

Factor	F-value	P-value
Overrun	38.0	<0.001*
Dasher Assembly	19.8	<0.001*
Overrun : Dasher Assembly	0.88	0.55

* Denotes factors that are significant at $p < 0.05$.

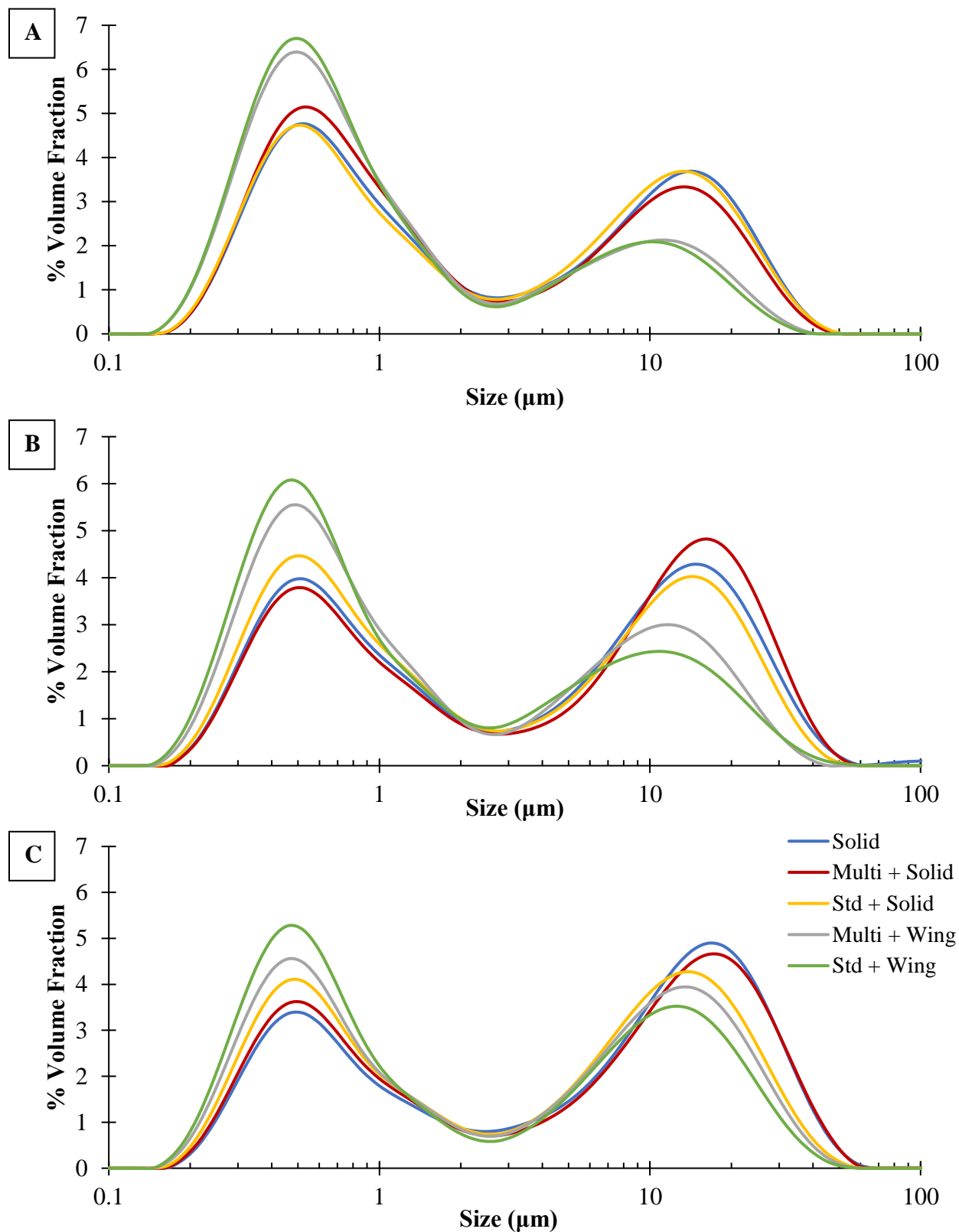


Figure 4.4.27. Fat globule size distributions as a function of dasher assembly for ice cream samples made at an overrun of A) 50%, B) 75%, and C) 100%. Throughput = 300 L/h, dasher speed = 200 RPM, draw temperature = $-5.5 \pm 0.1^\circ\text{C}$. Curves represent averages for three replicates.

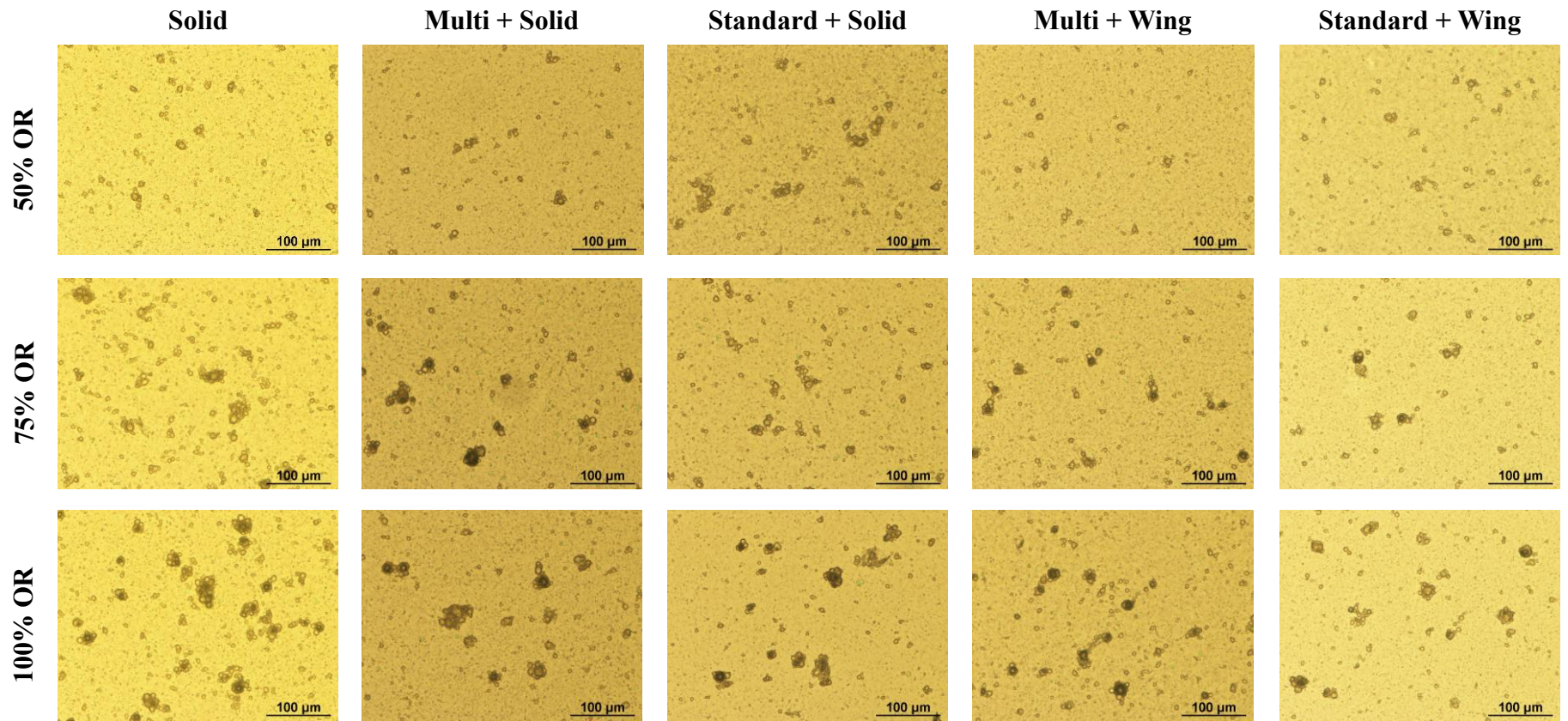


Figure 4.4.28. Optical microscopy images (20x magnification) of destabilized fat clusters as a function of overrun and dasher assembly.

4.4.2.4 Correlations

The dasher displacement (Table 3.1) was plotted against microstructural attributes to investigate whether there was a correlation between working volume (i.e., the volume available to the product in the freezing cylinder) and microstructure (Table 4.4.21). Overall, correlations were weak. Of the microstructural attributes, fat destabilization had the highest correlation with dasher displacement ($R^2 = 0.40$). Viscosity and residence time (both mean and standard deviation) were also plotted against microstructural attributes (Table 4.4.21). Ice crystal size was negatively correlated with viscosity and positively correlated with residence time. While correlations were weak ($R^2 \leq 0.25$), ice crystal size tended to be most highly correlated with mean residence time. Air cell size was positively correlated with viscosity and negatively correlated with residence time; however, correlations were very weak ($R^2 \leq 0.08$). Fat destabilization was positively correlated with viscosity and negatively correlated with residence time, but again, correlations were very weak ($R^2 \leq 0.14$).

Table 4.4.21. Overall correlation coefficient R^2 between processing conditions and microstructural attributes.

Microstructural Attribute	Dasher Displacement	Viscosity	Average Residence Time	Std Dev in Residence Time
Draw Mean Ice Crystal Size	0.15 ⁽⁻⁾	0.10 ⁽⁻⁾	0.13 ⁽⁺⁾	0.13 ⁽⁺⁾
Draw Std Dev in Ice Crystal Size	0.35 ⁽⁻⁾	0.13 ⁽⁻⁾	0.25 ⁽⁺⁾	0.18 ⁽⁺⁾
Hardened Mean Ice Crystal Size	0.10 ⁽⁻⁾	0.08 ⁽⁻⁾	0.09 ⁽⁺⁾	0.08 ⁽⁺⁾
Hardened Std Dev in Ice Crystal Size	0.18 ⁽⁻⁾	0.06 ⁽⁻⁾	0.14 ⁽⁺⁾	0.09 ⁽⁺⁾
Mean Air Cell Size	0.00 ⁽⁺⁾	0.08 ⁽⁺⁾	0.05 ⁽⁻⁾	0.04 ⁽⁻⁾
Std Dev in Air Cell Size	0.05 ⁽⁺⁾	0.03 ⁽⁺⁾	0.05 ⁽⁻⁾	0.02 ⁽⁻⁾
% Fat Destabilization	0.40 ⁽⁺⁾	0.10 ⁽⁻⁾	0.13 ⁽⁺⁾	0.13 ⁽⁺⁾

* The symbol in parenthesis indicates the whether the correlation is positive⁽⁺⁾ or negative⁽⁻⁾.

Correlations were also tested for individual dasher assemblies to evaluate whether their behavior differed. Correlation coefficients between viscosity and microstructural attributes for individual dashers are given in Table 4.4.22. Correlations between viscosity and ice crystal size tended to be weak regardless of dasher and no obvious trends were identified. Correlations between air cell size and viscosity were stronger for open dasher configurations than for the solid dasher, but were still weak ($R^2 \leq 0.44$). Correlations between viscosity and fat destabilization were negative and strong ($R^2 = 0.20 - 0.78$) relative to the overall correlation for viscosity and fat destabilization. Interestingly, the correlation between viscosity and fat destabilization was positive when all dashers were considered, but negative when results were broken out by dasher (Figure 4.4.29). For all dasher assemblies except the standard + solid, the slope of the correlation between viscosity and fat destabilization was similar.

Table 4.4.22. Correlation coefficient R^2 between viscosity and microstructural attributes as a function of dasher assembly.

Microstructural Attribute	Dasher Assembly				
	Solid Dasher	Multi + Solid	Standard + Solid	Multi + Wing	Standard + Wing
Draw Mean Ice Crystal Size	0.01 (+)	0.29 (+)	0.00 (-)	0.03 (-)	0.01 (-)
Draw Std Dev in Ice Crystal Size	0.06 (+)	0.10 (+)	0.48 (+)	0.01 (+)	0.00 (+)
Hardened Mean Ice Crystal Size	0.02 (+)	0.10 (-)	0.02 (-)	0.00 (-)	0.00 (-)
Hardened Std Dev in Ice Crystal Size	0.00 (-)	0.02 (+)	0.01 (+)	0.06 (+)	0.00 (+)
Mean Air Cell Size	0.00 (+)	0.12 (+)	0.22 (+)	0.13 (+)	0.44 (+)
Std Dev in Air Cell Size	0.00 (-)	0.04 (+)	0.08 (+)	0.41 (-)	0.38 (+)
% Fat Destabilization	0.60 (-)	0.78 (-)	0.20 (-)	0.43 (-)	0.69 (-)

* The symbol in parenthesis indicates the whether the correlation is positive (+) or negative (-).

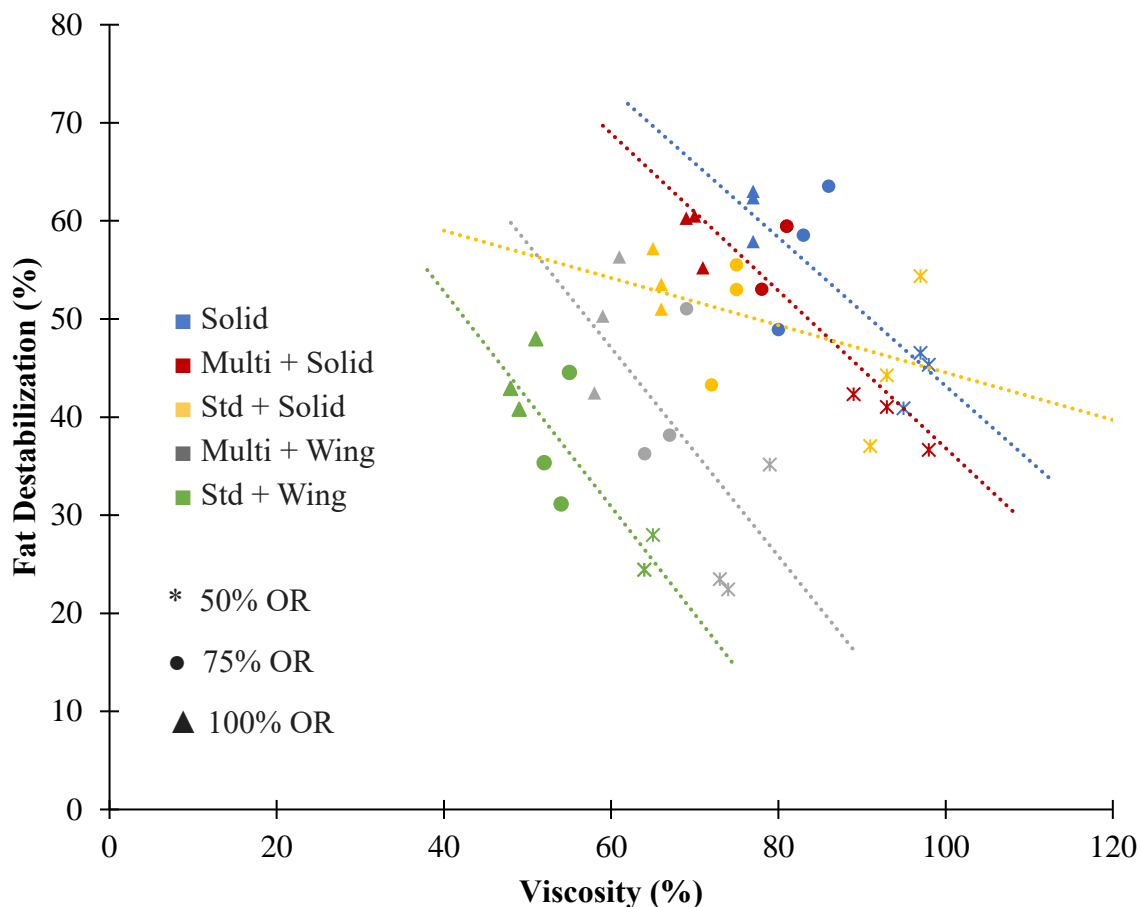


Figure 4.4.29. Correlation between fat destabilization and viscosity (i.e., torque on dasher motor as % of total capacity) as a function of dasher. Dotted lines indicate correlation for individual dashers.

Table 4.4.23 provides correlations between mean residence time and microstructural attributes and Table 4.4.24 provides correlations between the standard deviation in residence time and microstructural attributes as a function of dasher assembly. Overall, no trends could be identified in the correlations between ice crystal size and residence time as a function of dasher. With regards to air cell size, there appeared to be a higher correlation with residence time for the configurations containing a wing beater, suggesting that air cell size might be affected differentially by residence time depending on the dasher configuration. The correlation between

fat destabilization and mean residence time was relatively consistent for most dasher assemblies, though the standard + solid configuration had a slightly lower correlation value. It is interesting to note that while the overall correlation coefficient between residence time and fat destabilization is negative, the coefficients for all individual dashers were positive (Figure 4.4.30).

Table 4.4.23. Correlation coefficient R^2 between mean residence time and microstructural attributes as a function of dasher assembly.

Microstructural Attribute	Dasher Assembly				
	Solid Dasher	Multi + Solid	Standard + Solid	Multi + Wing	Standard + Wing
Draw Mean Ice Crystal Size	0.01 (+)	0.20 (-)	0.03 (-)	0.03 (+)	0.00 (+)
Draw Std Dev in Ice Crystal Size	0.10 (-)	0.00 (-)	0.40 (-)	0.05 (-)	0.01 (-)
Hardened Mean Ice Crystal Size	0.00 (+)	0.10 (+)	0.02 (+)	0.00 (-)	0.01 (-)
Hardened Std Dev in Ice Crystal Size	0.09 (-)	0.00 (+)	0.00 (+)	0.04 (-)	0.00 (+)
Mean Air Cell Size	0.15 (-)	0.04 (-)	0.05 (-)	0.12 (-)	0.45 (-)
Std Dev in Air Cell Size	0.05 (-)	0.07 (-)	0.00 (-)	0.45 (+)	0.33 (-)
% Fat Destabilization	0.68 (+)	0.75 (+)	0.34 (+)	0.67 (+)	0.66(+)

* The symbol in parenthesis indicates the whether the correlation is positive (+) or negative (-).

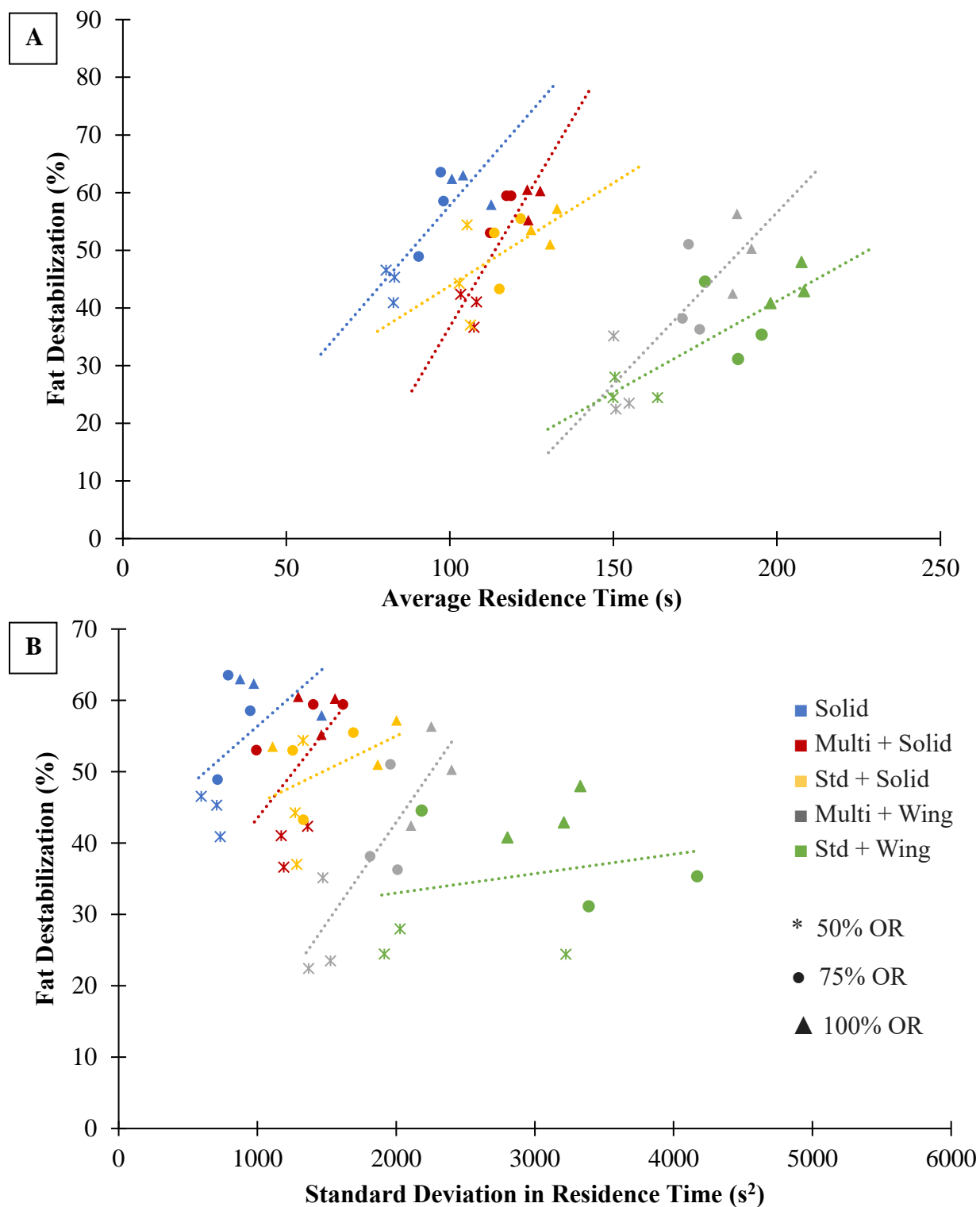


Figure 4.4.30. Correlation between fat destabilization and A) mean residence time and B) standard deviation in residence time as a function of dasher. Solid black line denotes the overall correlation and dotted lines indicate correlation for individual dashers.

Table 4.4.24. Correlation coefficient R^2 between standard deviation in residence time and microstructural attributes as a function of dasher assembly.

Microstructural Attribute	Dasher Assembly				
	Solid Dasher	Multi + Solid	Standard + Solid	Multi + Wing	Standard + Wing
Draw Mean Ice Crystal Size	0.15 (+)	0.05 (-)	0.10 (-)	0.05 (+)	0.05 (-)
Draw Std Dev in Ice Crystal Size	0.00 (-)	0.01 (-)	0.17 (-)	0.10 (-)	0.34 (-)
Hardened Mean Ice Crystal Size	0.03 (+)	0.31 (+)	0.16 (+)	0.01 (-)	0.03 (-)
Hardened Std Dev in Ice Crystal Size	0.18 (-)	0.00 (+)	0.00 (+)	0.05 (-)	0.00 (+)
Mean Air Cell Size	0.13 (-)	0.02 (+)	0.04 (+)	0.08 (-)	0.39 (-)
Std Dev in Air Cell Size	0.12 (-)	0.05 (+)	0.02 (+)	0.45 (+)	0.21 (-)
% Fat Destabilization	0.25 (+)	0.28 (+)	0.19 (+)	0.74 (+)	0.05 (+)

* The symbol in parenthesis indicates the whether the correlation is positive (+) or negative (-).

4.4.3 Throughput Experiment

The purpose of the throughput experiment was to evaluate the effects of dasher assembly and throughput rate on the processing conditions, RTD parameters, and microstructural attributes of ice cream made using a continuous SSF. Additionally, potential interactions between dasher assembly and throughput were evaluated.

4.4.3.1 Processing Conditions

Processing conditions are summarized in Table 4.4.25. The average draw temperature was $-5.5 \pm 0.1^\circ\text{C}$ for all treatments. There was a significant effect of throughput rate on viscosity, or the torque on the dasher motor as a percentage of its total capacity. The viscosity increased when throughput rate was increased from 300 to 400 L/h for all dasher assemblies except for the solid dasher (Figure 4.4.31). There was not a consistent pattern for the solid dasher, which exhibited a lower viscosity at the midpoint throughput rate of 300 L/h than at 200 L/h or 400 L/h. There was also a significant effect of dasher assembly on viscosity. Generally, as dasher displacement increased (Table 3.1), viscosity also increased. At a throughput rate of 200 L/h, there were significant differences between all dasher assemblies, except for the two dasher configurations with the solid beater. As throughput rate increased to 300 L/h, the significant difference between the solid dasher and the multi + solid assembly was eliminated. Similarly, as throughput rate increased to 400 L/h, there were no longer significant differences between the solid dasher, multi + solid, or standard + solid configurations. Significant differences in viscosity were maintained between the dasher assemblies containing a wing beater at approximately the same magnitude across all throughput rates (Figure 4.4.31). This increase in viscosity with increasing dasher displacement can be attributed to the weight of the dasher, the contact area of the dasher with the

product, or the higher rate of cooling required to achieve the target draw temperature (see section 4.4.2.1 for elaboration).

There was a significant effect of dasher and throughput rate on overrun. Specifically, the two dasher assemblies with the solid beater tended to have lower overruns than the other dasher configurations at the 400 L/h throughput rate. The reason for this difference is unclear. There do not appear to be any significant differences in processing conditions or microstructural attributes that would be indicative of an inability for ice cream to hold air. However, qualitative notes were made during processing that a small but persistent amount of blow-by (that is, pockets of air escaping the draw of the freezer without being incorporated into the product) was observed not only for the solid beater configurations, but also for the solid dasher. This might be related to the fact that the viscosity (torque on the dasher motor) was approaching its maximum capacity (100%).

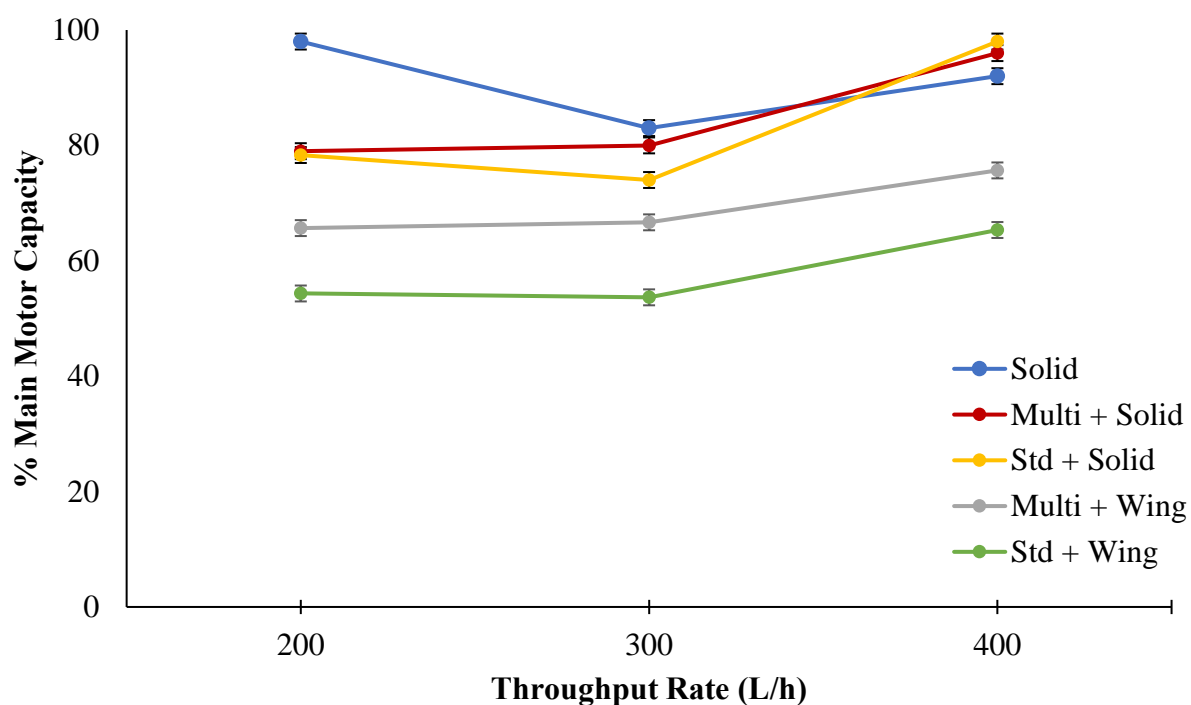


Figure 4.4.31. Viscosity as a function of dasher assembly and throughput rate. Viscosity was measured as a percentage of the total torque capacity on the motor turning the dasher (n=3).

Table 4.4.25. Effects of dasher assembly and throughput rate on processing conditions for ice cream made at a dasher speed = 200 RPM, target overrun = 75%, and draw temperature = $-5.5 \pm 0.1^\circ\text{C}$.

Condition	Dasher Assembly	Throughput Rate		
		200 L/h	300 L/h	400 L/h
Viscosity (%)	Solid	98 \pm 0 ^{A,a}	83 \pm 3 ^{A,b}	92 \pm 5 ^{A,a}
	Multi + Solid	79 \pm 4 ^{B,b}	80 \pm 2 ^{AB,b}	96 \pm 3 ^{A,a}
	Standard + Solid	78 \pm 1 ^{B,b}	74 \pm 2 ^{B,b}	98 \pm 0 ^{A,a}
	Multi + Wing	66 \pm 2 ^{C,b}	67 \pm 3 ^{C,b}	76 \pm 2 ^{B,a}
	Standard + Wing	54 \pm 1 ^{D,b}	54 \pm 2 ^{D,b}	65 \pm 2 ^{C,a}
Overrun (%)	Solid	72.9 \pm 2.1 ^{A,a}	76.6 \pm 2.3 ^{A,a}	73.3 \pm 1.4 ^{ABC,a}
	Multi + Solid	75.0 \pm 2.8 ^{A,a}	79.4 \pm 4.1 ^{A,a}	64.2 \pm 1.5 ^{D,b}
	Standard + Solid	73.0 \pm 1.3 ^{A,a}	75.1 \pm 3.5 ^{A,a}	68.6 \pm 1.6 ^{CD,a}
	Multi + Wing	74.0 \pm 1.0 ^{A,a}	77.7 \pm 1.0 ^{A,a}	75.9 \pm 3.3 ^{A,a}
	Standard + Wing	73.7 \pm 0.7 ^{A,a}	76.6 \pm 1.3 ^{A,a}	75.7 \pm 3.1 ^{AB,a}

^{A-D} Within a condition and column, means without a common uppercase superscript differ ($P < 0.05$) due to dasher.

^{a-b} Within a row, means without a common lowercase superscript differ ($P < 0.05$) due to throughput rate.

\pm Values indicate standard deviation for 3 replicates.

4.4.3.2 Residence Time Distribution

Cumulative RTD curves as a function of throughput rate and dasher assembly are shown in Figure 4.4.32, with images of the samples collected during the pulse injection trial depicted in Figure 4.4.33. The first three moments of the RTD curves (defined in Eqns. 3.7-3.9) are given in Table 4.4.26. As throughput rate increased, the $F(t)$ curves and $E(t)$ curves (Figures 4.4.34a – 36a) were shifted left to shorter residence times. Additionally, as dasher displacement increased, these curves were also shifted left, although configurations with a common beater had similar curves. Generally, $E(\theta)$ curves (Figures 4.4.34 – 36b) were similar for each dasher, but the curves appear to broaden as throughput rate was increased. This would indicate increased axial dispersion at higher throughput rates when there is a control of average residence time. Increasing the throughput rate would also increase the Reynold's number Re . This suggests that the flow would

become more turbulent at higher throughput rates, resulting in eddies that could contribute to increased axial dispersion.

Mean residence time varied from 68 – 286s. There was a significant effect of throughput rate on average residence time and standard deviation in residence time (Table 4.4.26). Increasing throughput rate decreased the mean residence time across all dasher assemblies (Figure 4.4.27). This is intuitive and consistent with previous studies on frozen desserts made in SSFs (Arellano et al., 2013a; Fayolle et al., 2013; Ndoye et al., 2018). There was also a significant effect of dasher assembly on mean residence time, with dasher assemblies containing a common beater having similar mean residence times (Figure 4.4.37). At a throughput rate of 200 L/h, the solid dasher had a lower mean residence time than all other assemblies. At 300 L/h and 400 L/h, the solid dasher had a similar mean residence time to the two dasher assemblies containing a solid beater. An interaction effect between throughput rate and dasher assembly was observed (Table 4.4.27). Increasing the throughput rate had a larger impact on decreasing the average residence time for dashers with lower displacements (Table 3.1).

Standard deviation in residence time increased as throughput rate decreased across all dasher assemblies. There was also a significant effect of dasher assembly on the variance in residence time, with the most differences observed at 200 L/h. The standard + wing configuration had a significantly larger variance in residence time than all other dasher designs, and the multi + wing configuration had a significantly larger variance than the solid dasher. At a throughput rate of 300 L/h, the standard + wing configuration only had a significantly larger variance than the solid dasher. At a throughput rate of 400 L/h, all dasher assemblies had similar standard deviations in residence time. Similar to mean residence time, an interaction effect was observed (Table 4.4.27)

where increasing the throughput rate had a larger impact on decreasing the average residence time for dashers with lower displacements (Table 3.1).

Table 4.4.26. Effects of dasher assembly and throughput rate on residence time distribution parameters for ice cream made at a dasher speed = 200 RPM, target overrun = 75%, and draw temperature = -5.5 ± 0.1 °C as determined by pulse injection study.

Residence Time Parameter	Dasher Assembly	Throughput Rate		
		200 L/h	300 L/h	400 L/h
Mean Residence Time, t_s (s)	Solid	143±4 ^{C,a}	95±4 ^{B,b}	68±1 ^{B,c}
	Multi + Solid	177±3 ^{B,a}	116±3 ^{B,b}	80±3 ^{B,c}
	Standard + Solid	191±2 ^{B,a}	117±4 ^{B,b}	82±2 ^{B,c}
	Multi + Wing	268±8 ^{A,a}	174±3 ^{A,b}	125±6 ^{A,c}
	Standard + Wing	286±11 ^{A,a}	171±21 ^{A,b}	126±4 ^{A,c}
Variance, σ^2 (s ²)	Solid	1480±256 ^{C,a}	816±120 ^{B,a}	457±45 ^{A,a}
	Multi + Solid	2350±271 ^{BC,a}	1340±317 ^{AB,a}	798±172 ^{A,a}
	Standard + Solid	2970±145 ^{BC,a}	1430±233 ^{AB,a}	1080±16 ^{A,a}
	Multi + Wing	4140±553 ^{B,a}	1930±102 ^{AB,b}	1170±283 ^{A,b}
	Standard + Wing	6670±2420 ^{A,a}	3250±1000 ^{A,b}	2040±417 ^{A,b}
Skewness, s^3	Solid	0.66±0.15 ^{A,a}	0.76±0.04 ^{A,a}	0.88±0.01 ^{A,a}
	Multi + Solid	0.76±0.19 ^{A,a}	0.85±0.07 ^{A,a}	0.83±0.08 ^{A,a}
	Standard + Solid	0.82±0.03 ^{A,a}	0.87±0.07 ^{A,a}	0.94±0.03 ^{A,a}
	Multi + Wing	0.78±0.47 ^{A,a}	0.60±0.05 ^{A,a}	0.57±0.03 ^{A,a}
	Standard + Wing	0.99±0.50 ^{A,a}	1.06±0.60 ^{A,a}	1.15±0.18 ^{A,a}

^{A-C} Within a parameter and column, means without a common uppercase superscript differ ($P < 0.05$) due to dasher.

^{a-c} Within a row, means without a common lowercase superscript differ ($P < 0.05$) due to throughput rate.

± Values indicate standard deviation for 3 replicates.

Table 4.4.27. ANOVA table assessing factors residence time distribution parameters.

Parameter	Factor	F-value	P-value
Mean	Throughput Rate	1020	<0.001*
	Dasher Assembly	295	<0.001*
	Throughput Rate : Dasher Assembly	19.0	<0.001*
Variance	Throughput Rate	45.1	<0.001*
	Dasher Assembly	23.8	<0.001*
	Throughput Rate : Dasher Assembly	3.26	0.009*
Skewness	Throughput Rate	0.32	0.73
	Dasher Assembly	3.35	0.02*
	Throughput Rate : Dasher Assembly	0.37	0.93

* Denotes factors that are significant at $p < 0.05$.

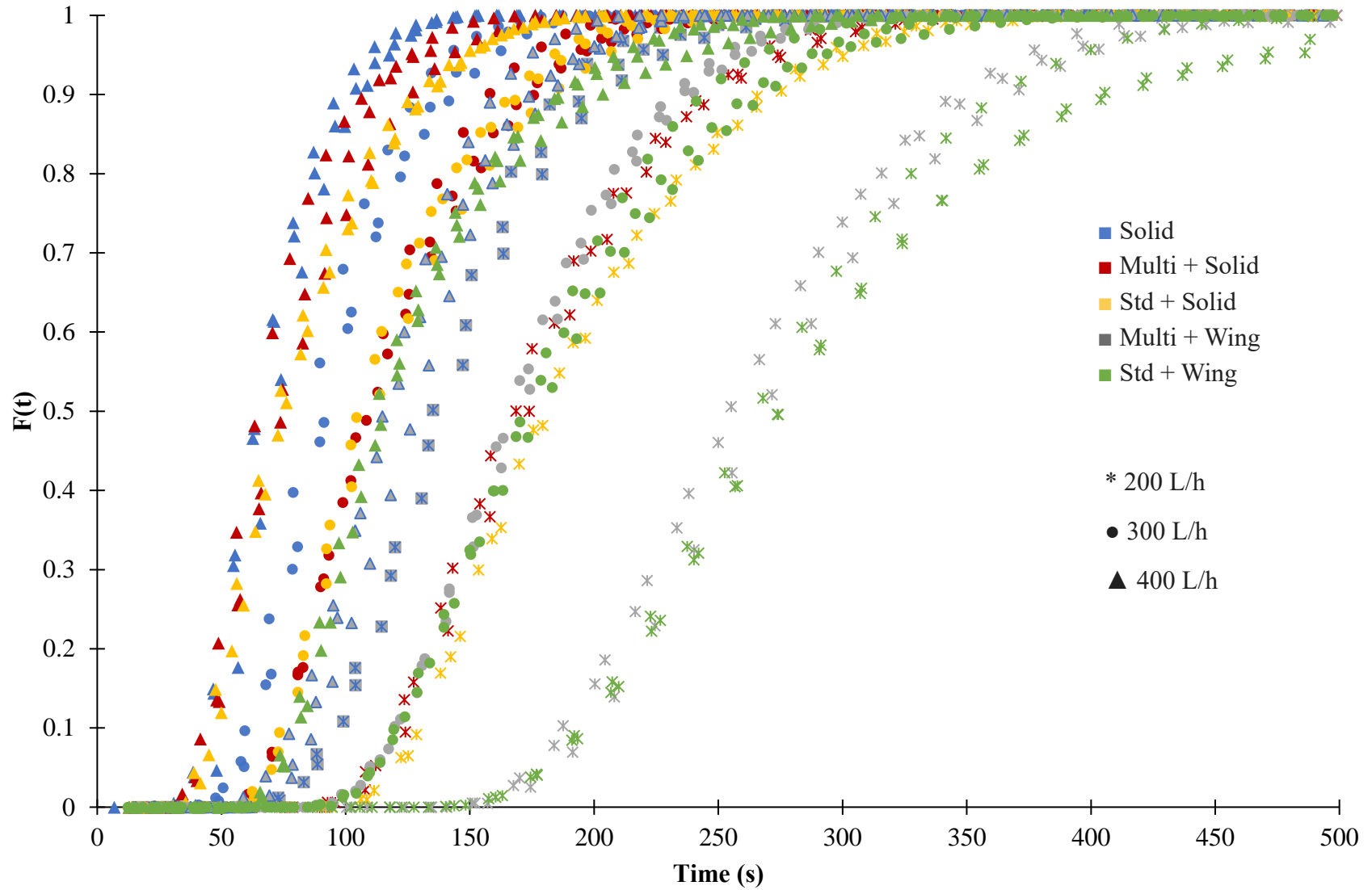


Figure 4.4.32. Cumulative residence time distribution $F(t)$ curves as a function of dasher assembly and throughput rate for ice cream made at 200 RPM dasher speed, 75% target overrun, and $-5.5 \pm 0.1^\circ\text{C}$ draw temperature ($n=3$).

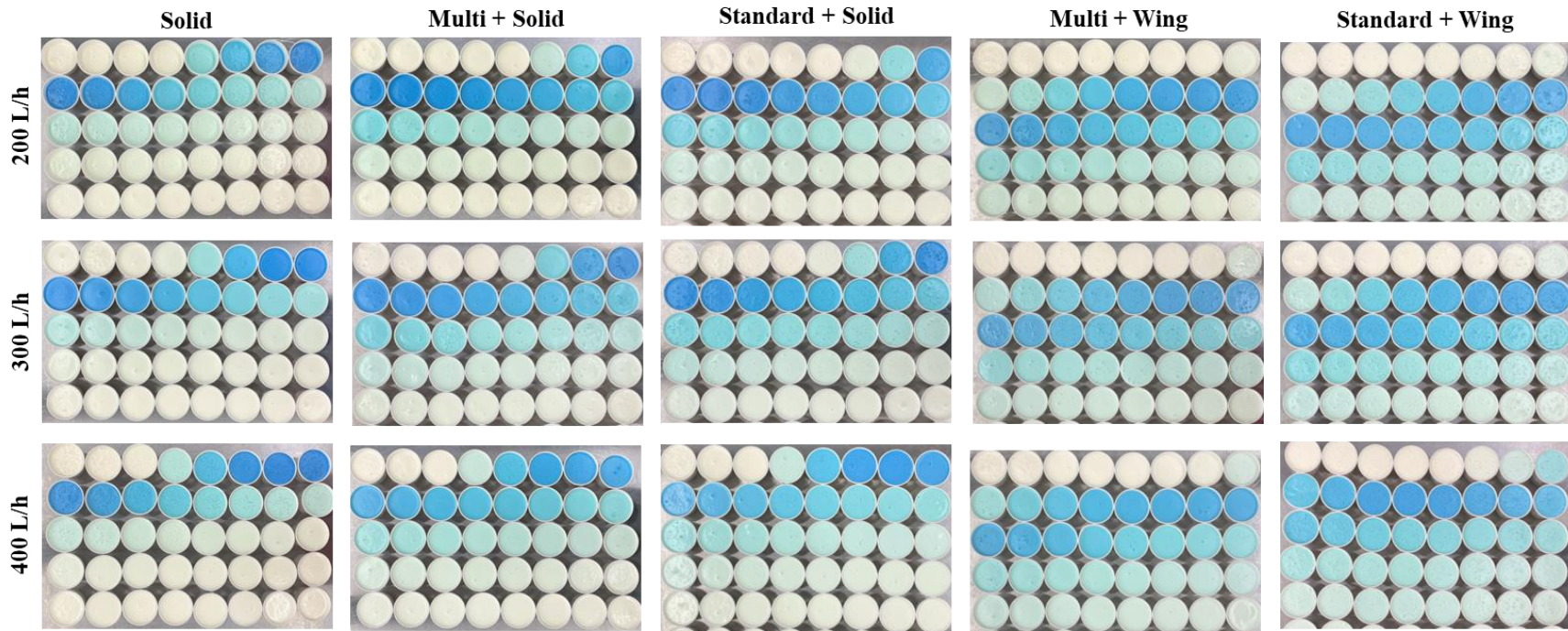


Figure 4.4.33. Images of samples collected during pulse injection experiment for evaluating residence time distribution of ice cream as a function of dasher assembly and throughput rate. Average time of cup collection at 200 L/h = 16s, 300 L/h = 10s, and 400 L/h = 8s. Dasher speed = 200 RPM, target overrun = 75%, draw temperature = $-5.5 \pm 0.1^\circ\text{C}$. Top left cup in each image was collected at $t = 0\text{s}$ when 20 mL of tracer (1% methylene blue in ice cream mix) was injected into freezer.

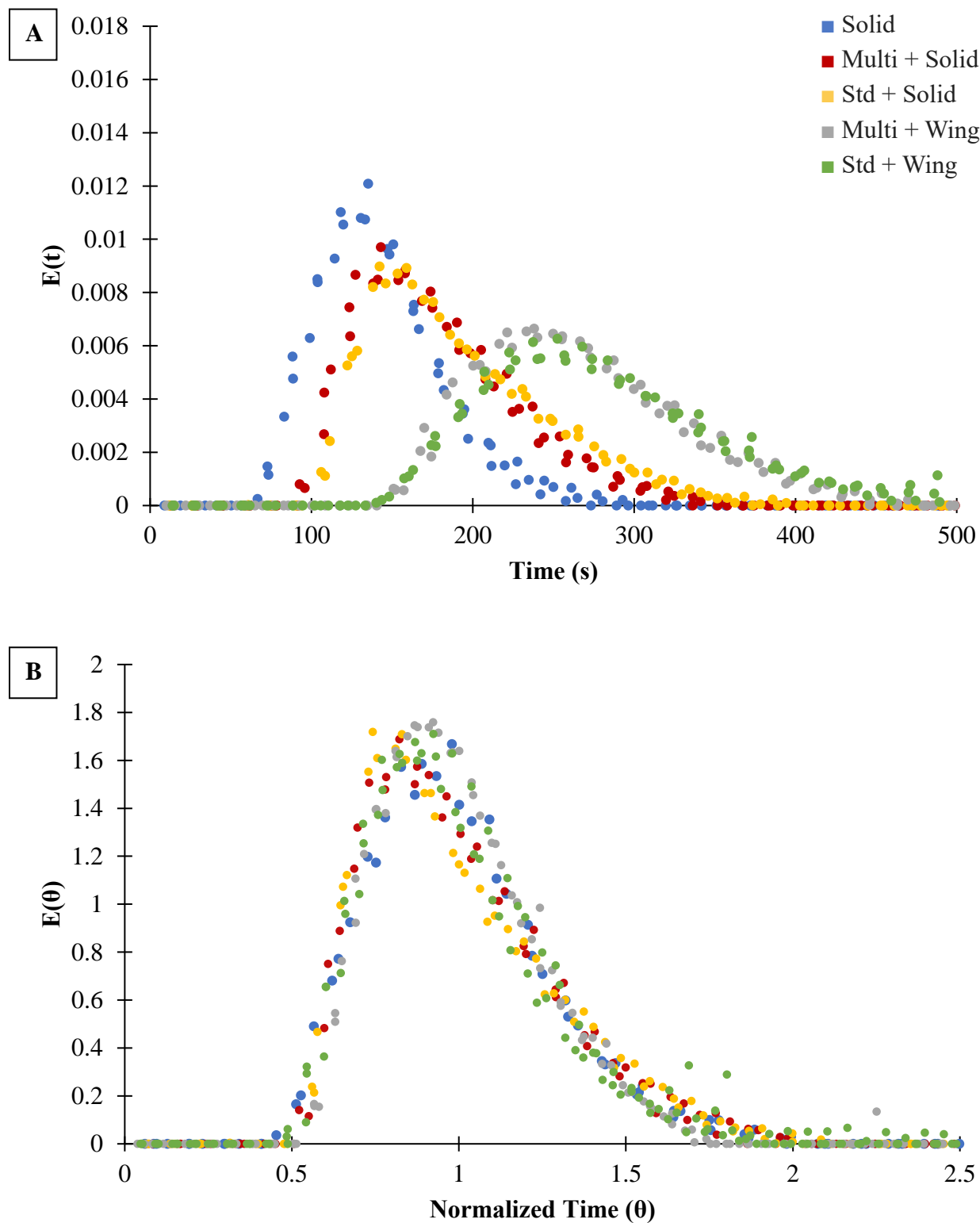


Figure 4.4.34. A) $E(t)$ curves and B) $E(\theta)$ curves as a function of dasher assembly for ice cream made at a throughput rate of 200 L/h. Dasher speed = 200 RPM, target overrun = 75%, draw temperature = $-5.5 \pm 0.1^\circ\text{C}$ ($n=3$).

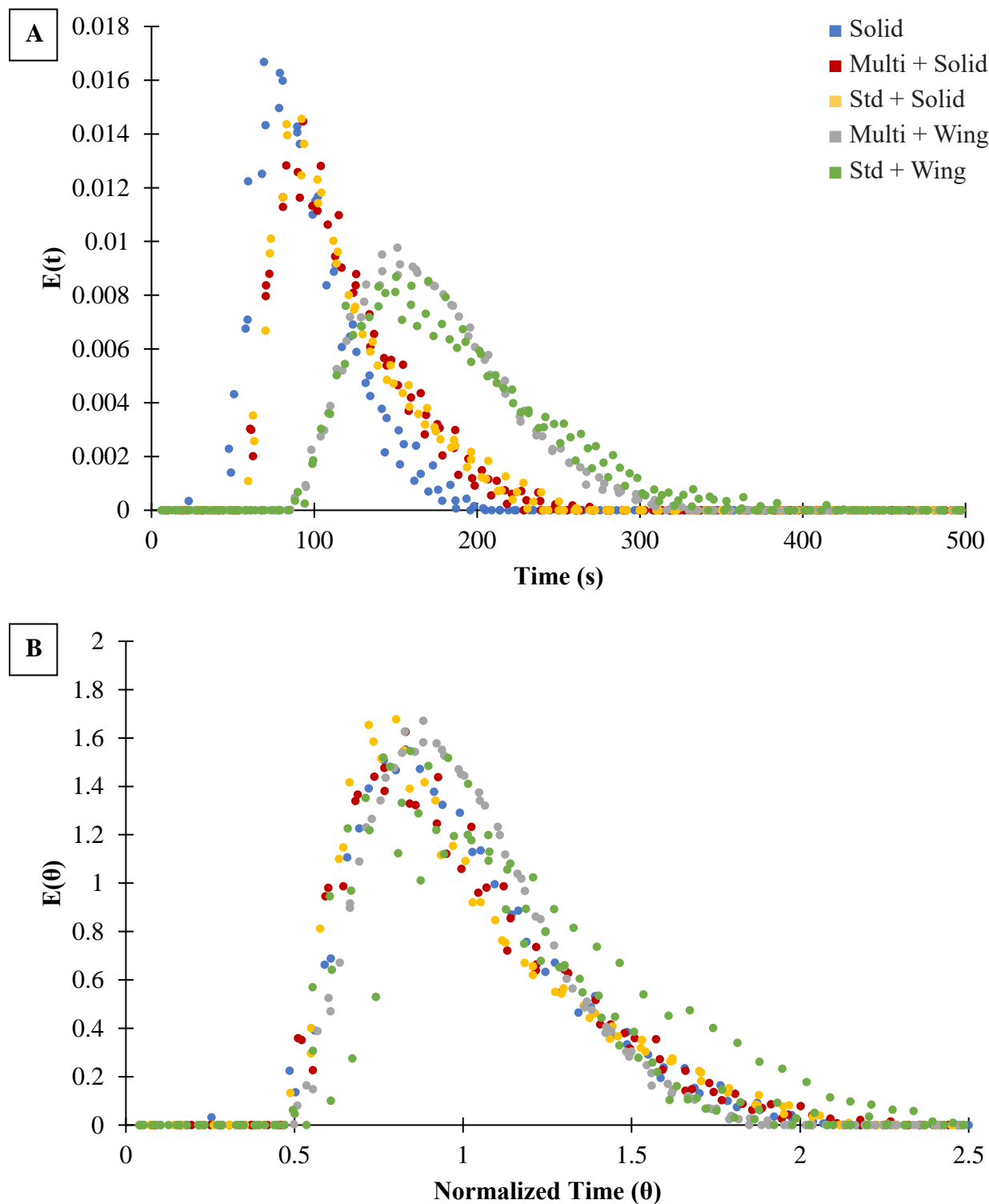


Figure 4.4.35. A) $E(t)$ curves and B) $E(\theta)$ curves as a function of dasher assembly for ice cream made at a throughput rate of 300 L/h. Dasher speed = 200 RPM, target overrun = 75%, draw temperature = $-5.5 \pm 0.1^\circ\text{C}$ ($n=3$).

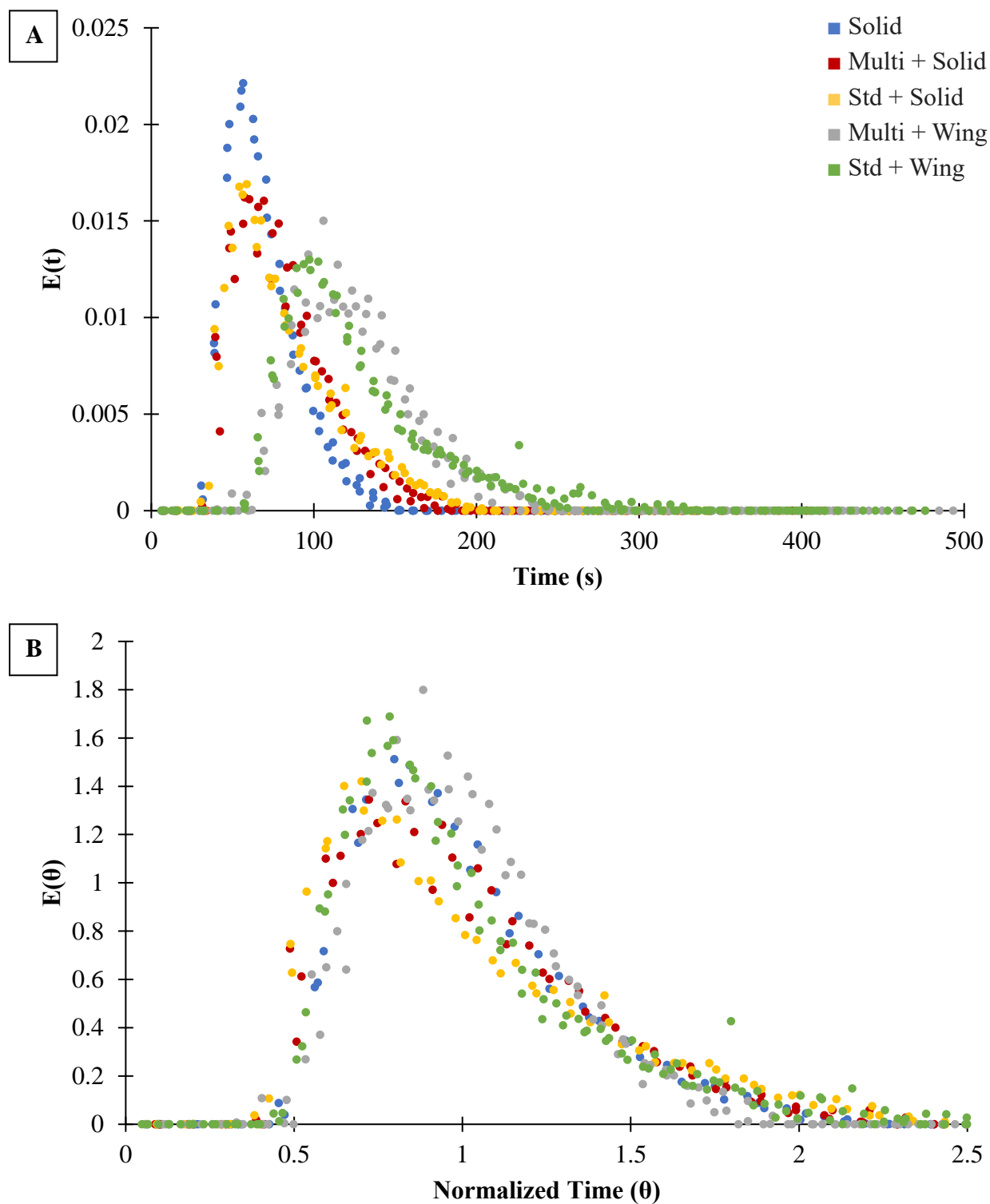


Figure 4.4.36. A) $E(t)$ curves and B) $E(\theta)$ curves as a function of dasher assembly for ice cream made at a throughput rate of 400 L/h. Dasher speed = 200 RPM, target overrun = 75%, draw temperature = $-5.5 \pm 0.1^\circ\text{C}$ ($n=3$).

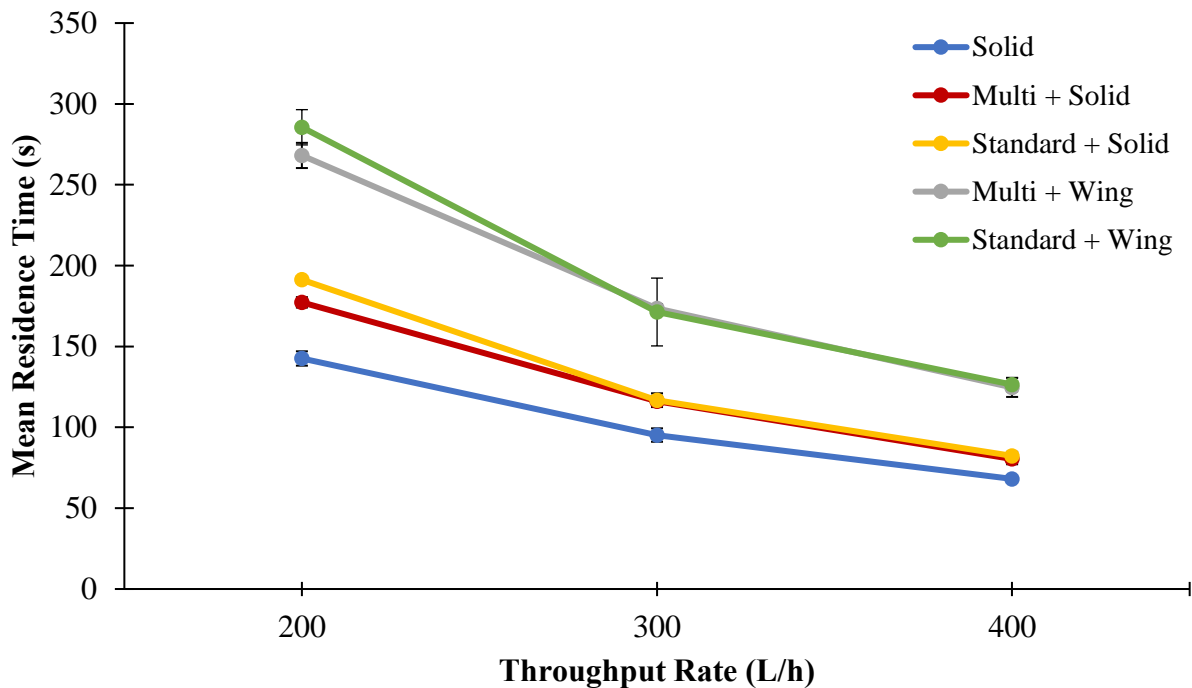


Figure 4.4.37. Mean residence time t_s as a function of dasher assembly and throughput rate. Dasher speed = 200 RPM, target overrun = 75%, draw temperature = $-5.5 \pm 0.1^\circ\text{C}$. Values represent averages for three replicates.

4.4.3.3 Microstructure

Microstructural attributes as a function of dasher assembly and throughput rate are detailed in Table 4.4.28.

4.4.3.3.1 Ice Crystal Size – Draw

The average ice crystal size at draw ranged from $17.1 - 26.4\mu\text{m}$. Cumulative size distributions are given Figure 4.4.38, and mean and standard deviation in ice crystal size as a function of dasher and throughput rate are presented in Figure 4.4.39. While there was not a significant effect of throughput rate on ice crystal size, the relationship was trending towards significance (Table 4.4.28) for increased throughput rate decreasing ice crystal size. There has been one study that found there was no effect of throughput rate on ice crystal size (Arellano et al., 2013a), but most studies have concluded that increasing throughput rate decreases ice crystal

Table 4.4.28. Effects of dasher assembly and throughput rate on microstructural attributes of ice cream made at a dasher speed = 200 RPM, target overrun = 75%, and draw temperature = $-5.5 \pm 0.1^\circ\text{C}$.

Microstructural Attribute		Dasher Assembly	Throughput Rate		
			200 L/h	300 L/h	400 L/h
Draw Ice Crystal Diameter [†]	Mean (μm) Variance (μm)	Solid	19.0 \pm 2.3 ^{A,a} 6.7 \pm 0.5 ^{A,a}	19.1 \pm 1.0 ^{A,a} 5.4 \pm 0.3 ^{A,a}	17.1 \pm 1.2 ^{A,a} 5.9 \pm 0.3 ^{A,a}
		Multi + Solid	20.8 \pm 1.9 ^{A,a} 8.4 \pm 0.2 ^{AB,a}	20.8 \pm 0.7 ^{A,a} 6.3 \pm 0.5 ^{A,a}	19.0 \pm 5.4 ^{A,a} 7.3 \pm 1.6 ^{A,a}
		Standard + Solid	21.0 \pm 1.4 ^{A,a} 7.7 \pm 0.6 ^{AB,a}	22.0 \pm 2.6 ^{A,a} 6.1 \pm 0.4 ^{A,a}	19.3 \pm 1.8 ^{A,a} 6.9 \pm 0.8 ^{A,a}
		Multi + Wing	22.4 \pm 2.0 ^{A,a} 8.1 \pm 0.1 ^{AB,a}	21.3 \pm 1.7 ^{A,a} 6.3 \pm 0.3 ^{A,a}	17.9 \pm 2.2 ^{A,a} 6.6 \pm 0.3 ^{A,a}
		Standard + Wing	26.4 \pm 6.5 ^{A,a} 10.9 \pm 2.5 ^{B,a}	25.7 \pm 6.6 ^{A,a} 8.4 \pm 2.8 ^{A,a}	23.4 \pm 4.5 ^{A,a} 9.3 \pm 2.8 ^{A,a}
Hardened Ice Crystal Diameter [‡]	Mean (μm) Variance (μm)	Solid	29.1 \pm 2.1 ^{A,a} 11.2 \pm 1.3 ^{A,a}	30.7 \pm 0.7 ^{A,a} 9.4 \pm 0.3 ^{A,a}	28.9 \pm 2.0 ^{A,a} 10.2 \pm 0.9 ^{A,a}
		Multi + Solid	29.3 \pm 1.8 ^{A,a} 10.9 \pm 0.6 ^{A,a}	30.5 \pm 1.2 ^{A,a} 9.9 \pm 0.9 ^{A,a}	26.6 \pm 4.1 ^{A,a} 10.1 \pm 0.2 ^{A,a}
		Standard + Solid	29.6 \pm 2.4 ^{A,a} 10.6 \pm 1.2 ^{A,a}	30.2 \pm 0.7 ^{A,a} 10.1 \pm 0.2 ^{A,a}	28.3 \pm 2.2 ^{A,a} 10.0 \pm 0.8 ^{A,a}
		Multi + Wing	30.8 \pm 1.9 ^{A,a} 12.5 \pm 2.3 ^{A,a}	31.8 \pm 1.2 ^{A,a} 11.0 \pm 0.4 ^{A,a}	27.8 \pm 2.1 ^{A,a} 10.4 \pm 1.1 ^{A,a}
		Standard + Wing	33.3 \pm 1.0 ^{A,a} 13.0 \pm 1.0 ^{A,a}	32.2 \pm 0.8 ^{A,a} 11.3 \pm 0.2 ^{A,a}	28.7 \pm 0.5 ^{A,a} 11.8 \pm 1.6 ^{A,a}
Air Cell Diameter [‡]	Mean (μm) Variance (μm)	Solid	24.6 \pm 3.0 ^{A,a} 11.2 \pm 0.9 ^{A,a}	27.0 \pm 2.2 ^{A,a} 15.8 \pm 1.4 ^{A,a}	25.1 \pm 1.8 ^{A,a} 11.3 \pm 0.6 ^{A,a}
		Multi + Solid	26.3 \pm 3.0 ^{A,a} 13.5 \pm 1.8 ^{A,a}	23.1 \pm 1.4 ^{A,a} 9.9 \pm 0.8 ^{A,a}	26.5 \pm 0.9 ^{A,a} 12.6 \pm 1.3 ^{A,a}
		Standard + Solid	27.4 \pm 2.4 ^{A,a} 14.8 \pm 0.9 ^{A,a}	25.1 \pm 4.9 ^{A,a} 12.8 \pm 4.5 ^{A,a}	26.8 \pm 2.3 ^{A,a} 12.9 \pm 3.1 ^{A,a}
		Multi + Wing	26.7 \pm 3.8 ^{A,a} 13.8 \pm 2.4 ^{A,a}	26.6 \pm 2.0 ^{A,a} 13.4 \pm 2.3 ^{A,a}	26.4 \pm 1.0 ^{A,a} 13.3 \pm 0.2 ^{A,a}
		Standard + Wing	26.4 \pm 2.9 ^{A,a} 13.6 \pm 2.2 ^{A,a}	24.9 \pm 2.1 ^{A,a} 11.8 \pm 0.5 ^{A,a}	26.6 \pm 3.7 ^{A,a} 13.1 \pm 3.7 ^{A,a}
Fat	% Destabilization	Solid	70.9 \pm 3.2 ^{A,a}	57.0 \pm 7.4 ^{A,ab}	43.1 \pm 2.9 ^{A,b}
		Multi + Solid	70.1 \pm 4.8 ^{A,a}	57.3 \pm 3.7 ^{A,ab}	45.9 \pm 4.6 ^{A,b}
		Standard + Solid	71.9 \pm 4.9 ^{A,a}	50.6 \pm 6.5 ^{AB,b}	40.1 \pm 4.8 ^{A,b}
		Multi + Wing	62.7 \pm 6.5 ^{AB,a}	41.8 \pm 8.0 ^{AB,b}	45.3 \pm 4.2 ^{A,b}
		Standard + Wing	51.9 \pm 5.3 ^{B,a}	37.0 \pm 6.9 ^{B,a}	37.3 \pm 8.8 ^{A,a}

^{A-B} Within an attribute and column, means without a common uppercase superscript differ ($P < 0.05$) due to dasher.

^{a-b} Within a row, means without a common lowercase superscript differ ($P < 0.05$) due to throughput rate.

[†] Draw ice crystal diameter mean and variance evaluated at -5.5°C .

[‡] Hardened ice crystal/air cell diameter mean and variance evaluated at -15°C .

\pm Values indicate standard deviation for 3 replicates.

size (Russell et al., 1999; Koxholt et al., 2000; Drewett and Hartel, 2007; Inoue et al., 2008). There was a significant effect of throughput rate on the standard deviation in ice crystal size (Table 4.4.29); however, significant differences were not detected among individual treatments (Table 4.4.28). When data from all dashers was averaged, there was a wider spread in ice crystal size for ice cream made at 200 L/h than at 300 L/h, and the difference between the spread at 200 L/h and 400 L/h was trending toward significance ($P = 0.060$).

A significant effect of dasher on mean ice crystal size was identified (Table 4.4.28), with the standard + wing having a significantly larger ice crystal size compared to the solid dasher and multi + solid configurations. Additionally, the standard + wing dasher was trending toward generating significantly larger ice crystals than the standard + solid ($P = 0.067$) and multi + wing ($P = 0.0503$) configurations. However, these differences were not observed among individual treatments (Table 4.4.29), but only when data for all dasher speeds was averaged. Dasher assembly also had a significant effect on the standard deviation in ice crystal size. At a throughput rate of 200 L/h, the standard + wing assembly had a wider spread in ice crystal size than the solid dasher.

Table 4.4.29. ANOVA table assessing factors affecting ice crystal size at draw ($-5.5 \pm 0.1^\circ\text{C}$).

Attribute	Factor	F-value	P-value
Mean	Throughput Rate	2.78	0.078
	Dasher Assembly	4.96	0.003*
	Throughput Rate : Dasher Assembly	0.106	0.999
Standard Deviation	Throughput Rate	7.43	0.002*
	Dasher Assembly	8.75	<0.001*
	Throughput Rate : Dasher Assembly	0.12	0.998

* Denotes factors that are significant at $p < 0.05$.

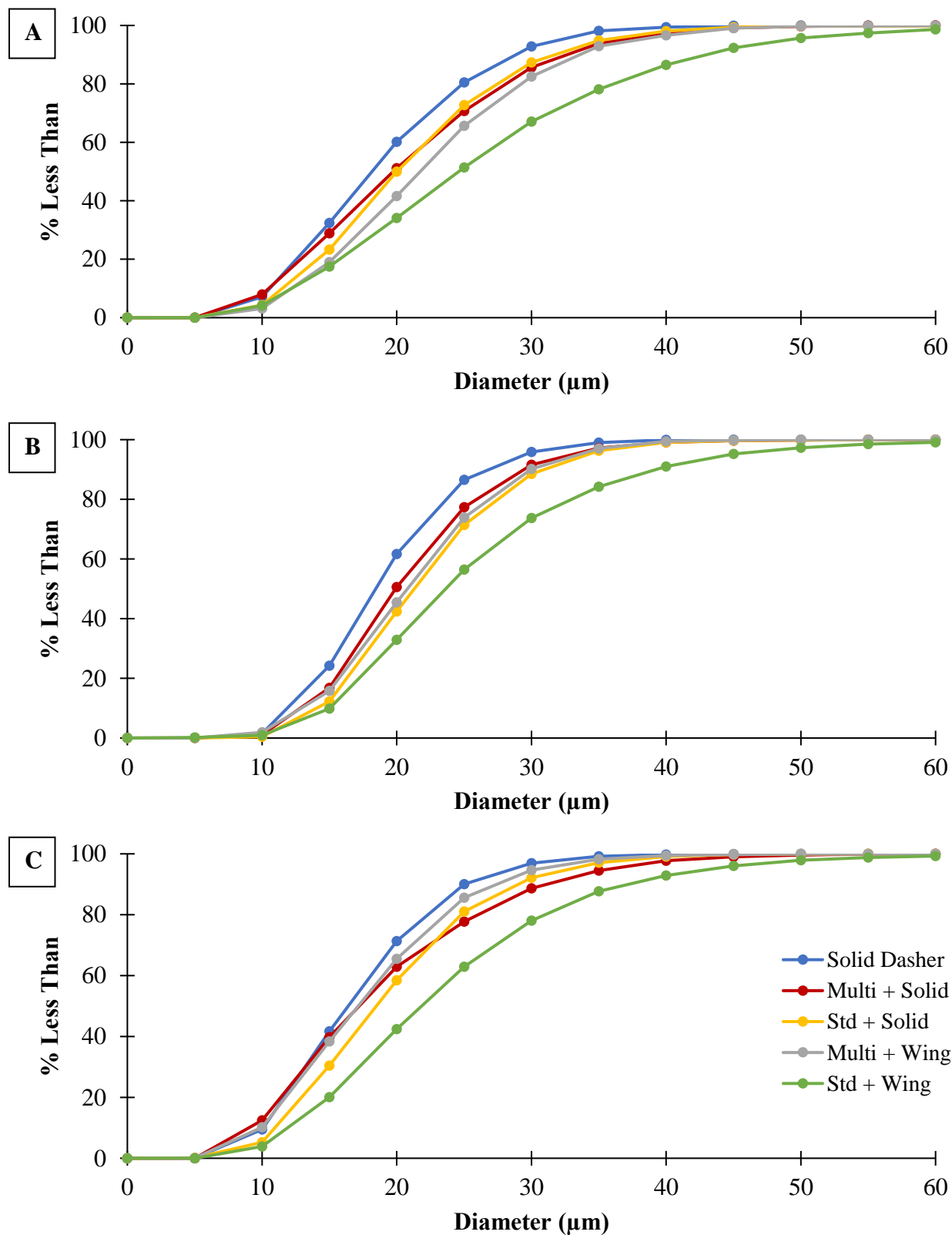


Figure 4.4.38. Cumulative ice crystal size distributions immediately after draw as a function of dasher assembly for ice cream made at a throughput rate of A) 200 L/h, B) 300 L/h, and C) 400 L/h. Dasher speed = 200 RPM, target overrun = 75%, draw temperature = $-5.5 \pm 0.1^\circ\text{C}$.

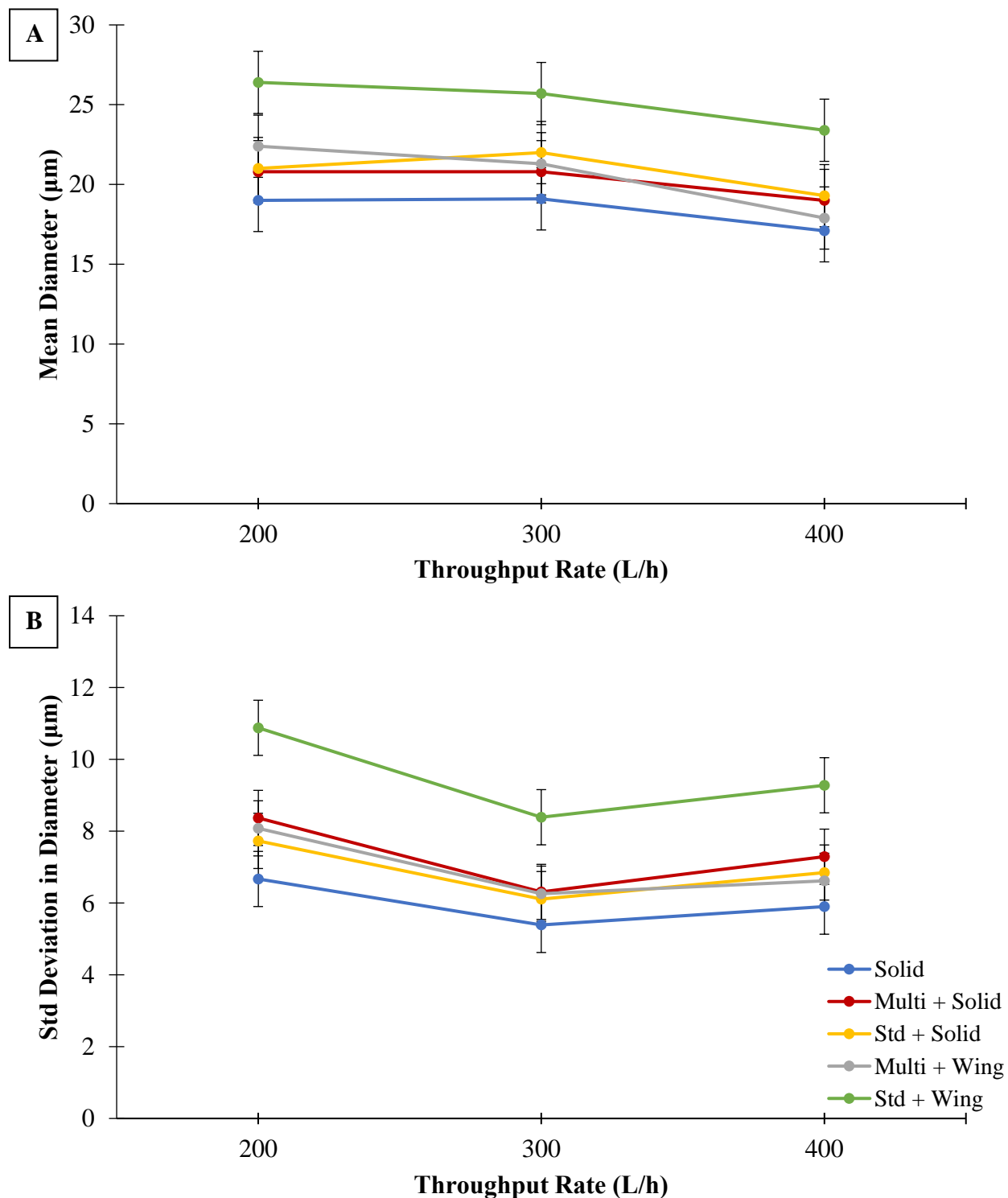


Figure 4.4.39. A) Mean ice crystal size and B) standard deviation in ice crystal size of ice cream immediately after draw as a function of dasher assembly and throughput rate. Dasher speed = 200 RPM, target overrun = 75%, draw temperature = $-5.5 \pm 0.1^\circ\text{C}$. Values represent the modeled averages for three replicates.

4.4.3.3.2 *Ice Crystal Size – Hardened*

The average ice crystal size in hardened ice cream ranged from 26.6 – 33.3 μm . Cumulative ice crystal size distributions for hardened samples are presented in Figure 4.4.40, and mean and standard deviations in ice crystal size as a function of throughput rate and dasher presented in Figure 4.4.41. A significant effect of throughput rate on average ice crystal size was identified (Table 4.4.30), with samples made at a throughput rate of 400 L/h having smaller mean ice crystal size than those made at 200 or 300 L/h when averaging across dasher assembly; however, no effect was observed among individual treatments (Table 4.4.28). Similarly, there was a significant effect of throughput rate on the standard deviation in ice crystal size (Table 4.4.30), with samples made at 200 L/h having a wider spread in ice crystal size than those made at 300 or 400 L/h, but again no significant differences were observed between individual treatments (Table 4.4.28).

There was not a significant effect of dasher assembly on mean ice crystal size, though the relationship was trending towards significance ($P = 0.067$). There was a significant effect of dasher assembly on the standard deviation in ice crystal size (Table 4.4.30). When data was averaged across throughput rate, the standard + wing assembly had a wider ice crystal size distribution than the solid dasher, multi + solid, and standard + solid configurations. However, there were again no significant differences found between individual treatments (Table 4.4.28).

Since there were distributions that appeared to have ice crystal sizes over the size of 50 μm , which is generally considered to be the size at which ice crystals become detectable and therefore can negatively impact ice cream texture (Goff and Hartel, 2013), the percentage of ice crystals in a treatment that were $\geq 50 \mu\text{m}$ was also calculated (Table 4.4.31). While no significant differences could be identified among individual treatments, a significant effect of throughput rate on the % of ice crystals $\geq 50 \mu\text{m}$ was detected (Table 4.4.30). At 400 L/h, the percentage of ice

crystals $\geq 50 \mu\text{m}$ was significantly lower than at 200 or 300 L/h, but practical differences were small ($\leq 3\%$). Additionally, a significant effect of dasher assembly was also detected (Table 4.4.30), where the standard + wing had a significantly higher proportion of ice crystals $\geq 50 \mu\text{m}$ relative to the solid dasher, multi + solid, and standard + solid configurations when averaging across throughput rates. Again, these differences were small ($\leq 3.5\%$) from a practical standpoint.

Table 4.4.30. ANOVA table assessing factors affecting ice crystal size in hardened ice cream.

Attribute	Factor	F-value	P-value
Mean	Throughput Rate	10.41	<0.001*
	Dasher Assembly	2.46	0.07
	Throughput Rate : Dasher Assembly	0.73	0.66
Standard Deviation	Throughput Rate	7.23	0.003*
	Dasher Assembly	5.57	0.002*
	Throughput Rate : Dasher Assembly	0.44	0.89
% >50 μm	Throughput Rate	10.41	<0.001*
	Dasher Assembly	2.46	0.067
	Throughput Rate : Dasher Assembly	0.73	0.66

* Denotes factors that are significant at $p < 0.05$.

Table 4.4.31. Percentage of ice crystals $> 50 \mu\text{m}$ in diameter as a function of dasher assembly and throughput rate for hardened ice cream made at dasher speed = 200 RPM, target overrun = 75%, and draw temperature = $-5.5 \pm 0.1^\circ\text{C}$.

Dasher Assembly	Throughput Rate		
	200 L/h	300 L/h	400 L/h
Solid	4.9 \pm 2.9 ^{A,a}	3.4 \pm 0.6 ^{A,a}	3.4 \pm 2.2 ^{A,a}
Multi + Solid	4.3 \pm 1.9 ^{A,a}	4.2 \pm 1.5 ^{A,a}	2.0 \pm 0.5 ^{A,a}
Standard + Solid	3.9 \pm 2.2 ^{A,a}	4.6 \pm 0.7 ^{A,a}	2.4 \pm 1.1 ^{A,a}
Multi + Wing	7.1 \pm 4.5 ^{A,a}	6.0 \pm 1.0 ^{A,a}	2.7 \pm 1.1 ^{A,a}
Standard + Wing	9.9 \pm 2.0 ^{A,a}	6.8 \pm 1.3 ^{A,a}	4.6 \pm 2.3 ^{A,a}

^A Within a column, means without a common uppercase superscript differ ($P < 0.05$) due to dasher.

^a Within a row, means without a common lowercase superscript differ ($P < 0.05$) due to throughput rate.

\pm Values indicate standard deviation for 3 replicates.

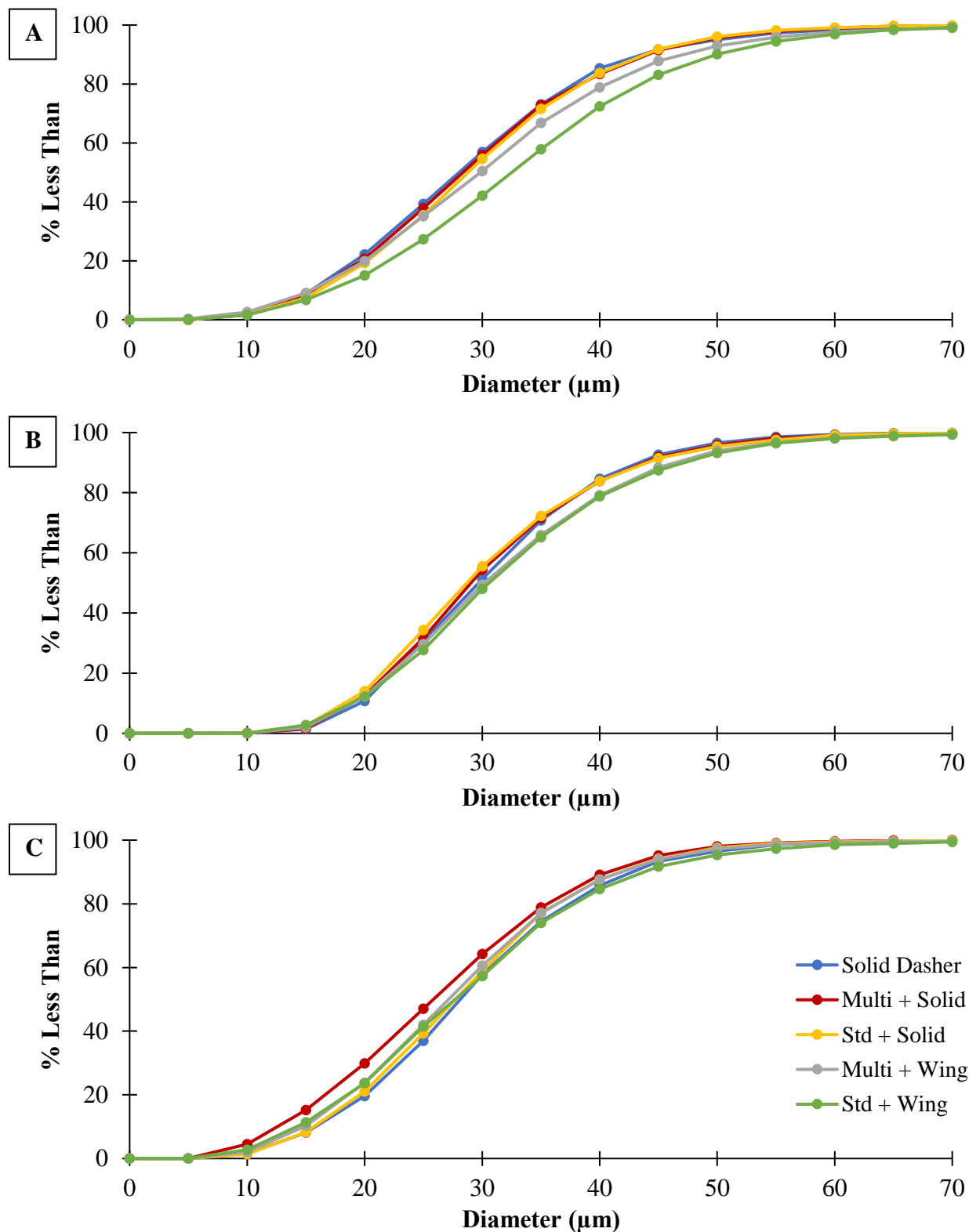


Figure 4.4.40. Cumulative ice crystal size distributions as a function of dasher assembly for hardened ice cream samples made at a throughput rate of A) 200 L/h, B) 300 L/h, and C) 400 L/h. Dasher speed = 200 RPM, target overrun = 75%, draw temperature = $-5.5 \pm 0.1^\circ\text{C}$. Samples were evaluated at -15°C .

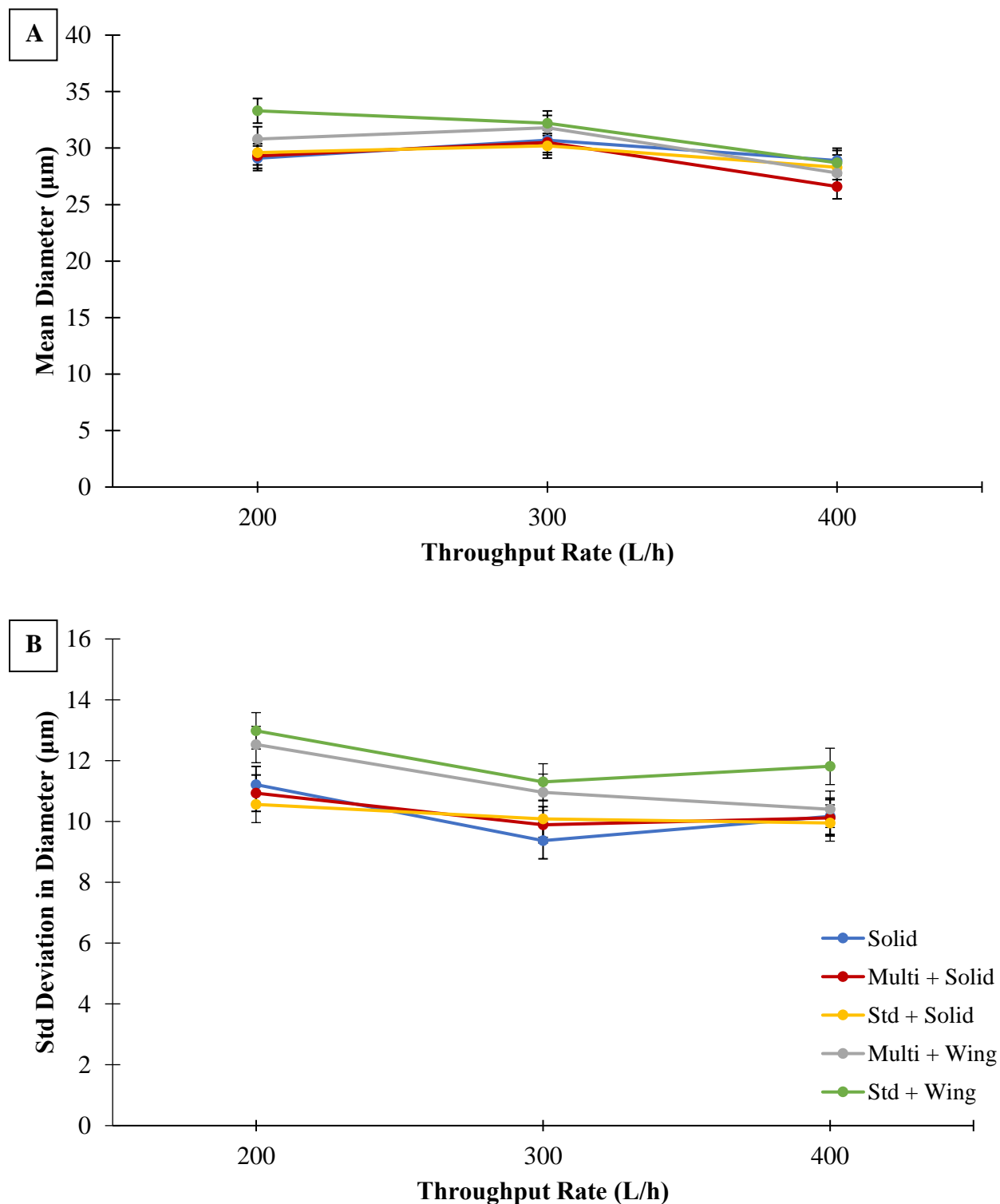


Figure 4.4.41. A) Mean ice crystal size and B) standard deviation in ice crystal size of hardened ice cream samples as a function of dasher assembly and throughput rate. Dasher speed = 200 RPM, target overrun = 75%, draw temperature = $-5.5 \pm 0.1^\circ\text{C}$. Samples were evaluated at -15°C . Values represent the modeled averages for three replicates.

4.4.3.3.3 Air Cell Size

The mean air cell size ranged from 23.1 – 27.4 μm . Cumulative air cell size distributions in hardened samples are given in Figure 4.4.42, with means and standard deviations for each treatment depicted in Figure 4.4.43. There was not a significant effect of throughput rate on the average or standard deviation in air cell size (Table 4.4.32). This is consistent with previous literature (Rohenkohl and Kohlus, 1999; Inoue et al., 2008). There was also not an effect of dasher assembly on average or standard deviation in air cell size (Table 4.4.32). Both of these findings support the theory that air cell distribution reaches an equilibrium relatively quickly (Kroezen and Wassink, 1987).

Table 4.4.32. ANOVA table assessing factors affecting air cell size in hardened ice cream.

Attribute	Factor	F-value	P-value
Mean	Throughput Rate	0.61	0.55
	Dasher Assembly	0.36	0.84
	Throughput Rate : Dasher Assembly	0.61	0.76
Standard Deviation	Throughput Rate	0.58	0.57
	Dasher Assembly	0.77	0.56
	Throughput Rate : Dasher Assembly	1.93	0.09

* Denotes factors that are significant at $p < 0.05$.

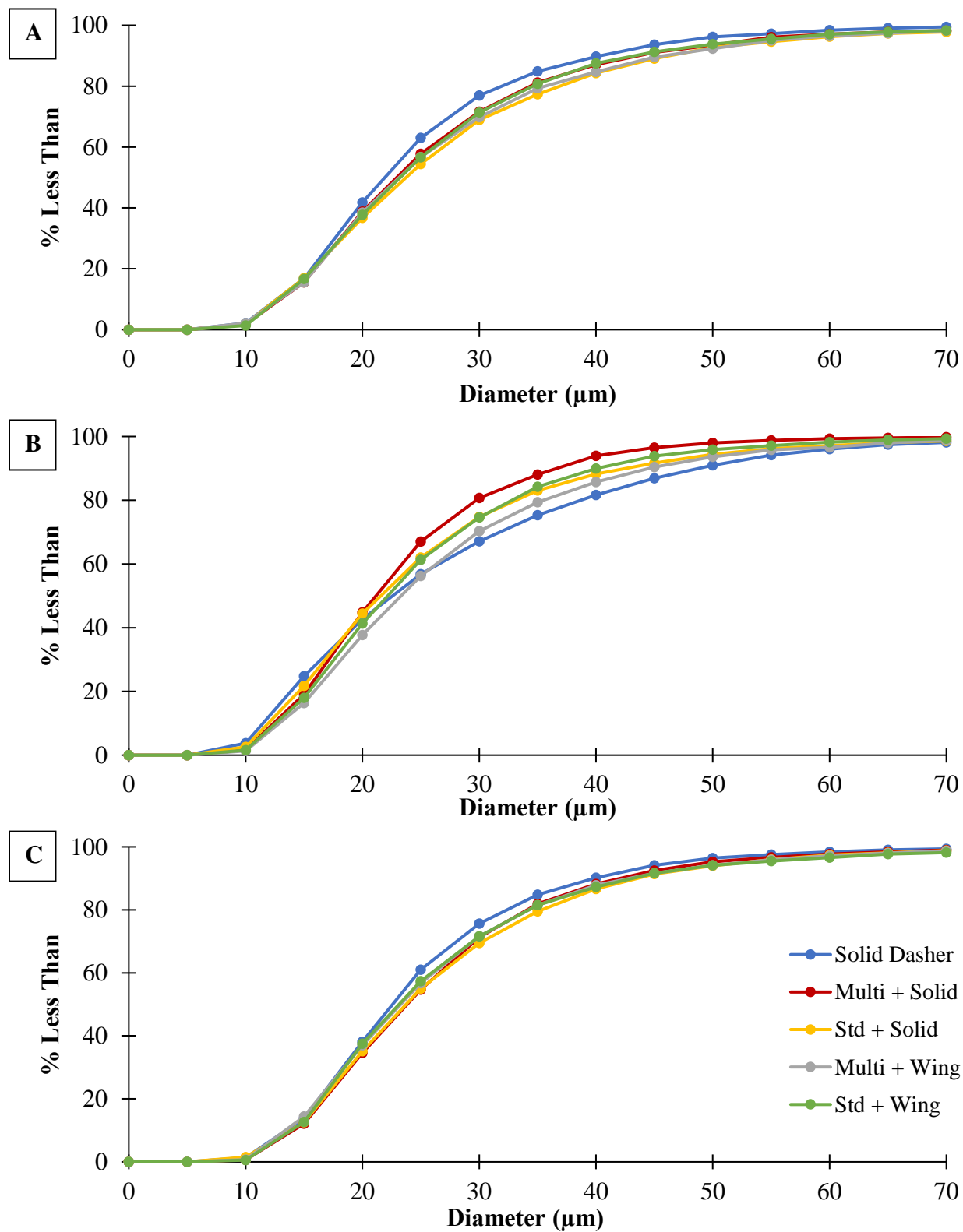


Figure 4.4.42. Cumulative air cell size distributions as a function of dasher assembly for hardened ice cream samples made at a throughput rate of A) 200 L/h, B) 300 L/h, and C) 400 L/h. Dasher speed = 200 RPM, target overrun = 75%, draw temperature = $-5.5 \pm 0.1^\circ\text{C}$. Samples were evaluated at -6°C .

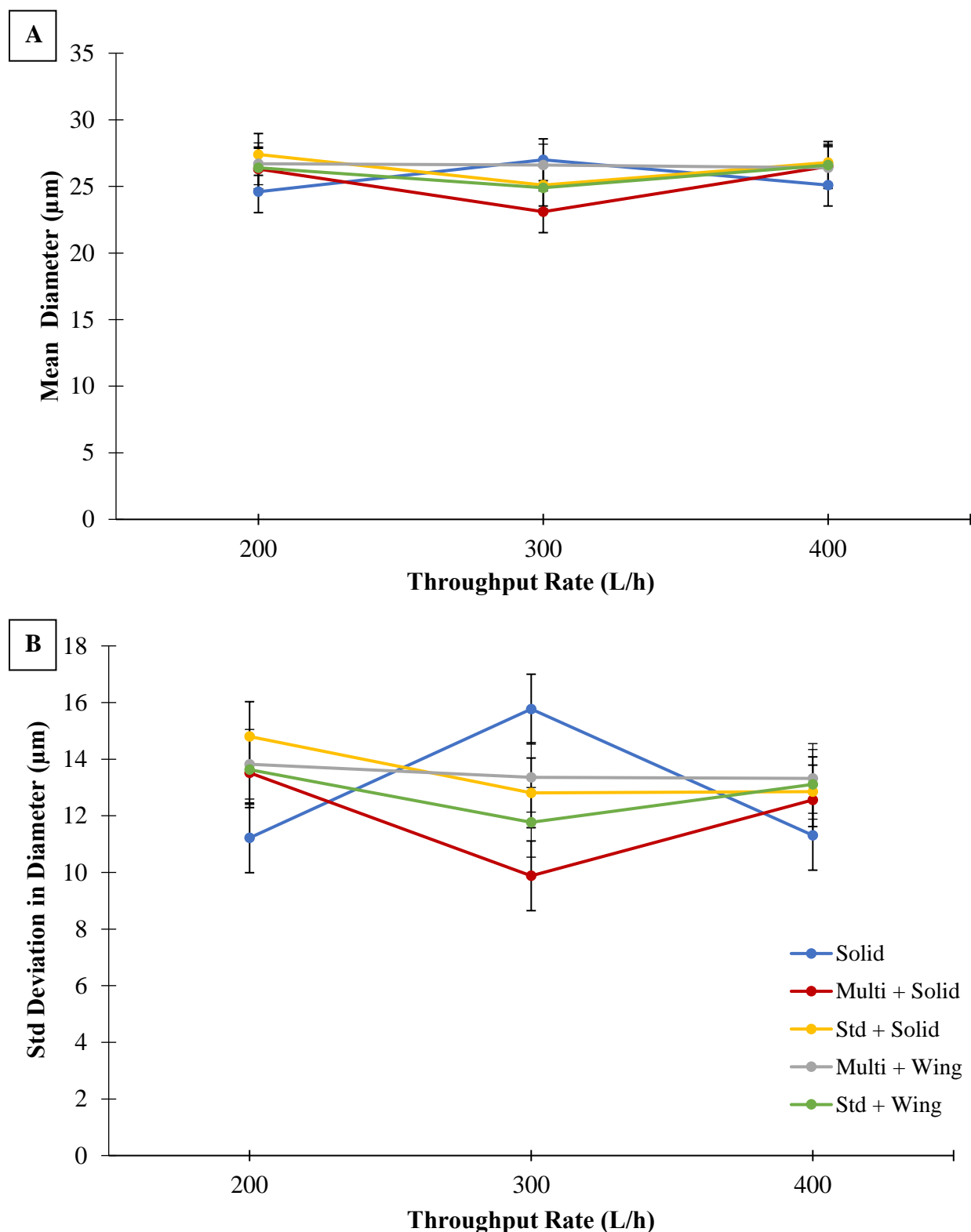


Figure 4.443. A) Mean air cell size and B) standard deviation in air cell size of hardened ice cream samples as a function of dasher assembly and throughput rate. Dasher speed = 200 RPM, target overrun = 75%, draw temperature = $-5.5 \pm 0.1^\circ\text{C}$. Samples were evaluated at -6°C . Values represent the modeled averages for three replicates.

4.4.3.3.4 Fat Destabilization

Fat destabilization ranged from 37.0 – 71.9%. Fat globule size distribution curves are provided in Figure 4.4.44. It can be observed that increasing throughput resulted in a smaller second peak, which would indicate a lower level of fat destabilization. This can also be observed in the microscopy images in Figure 4.4.45, where fat clusters become smaller as throughput rate increases. Indeed, there was a significant effect of throughput rate on fat destabilization, with increasing throughput rate resulting in a decrease in the level of fat destabilization (Table 4.4.33; Figure 4.4.46). This is likely because less total shear is imparted on the product due to the reduced residence time that results from a faster throughput rate. It appears that the decrease in fat destabilization with increasing throughput rate is approximately linear relationship for most dashers, particularly the solid dasher and configurations containing a solid beater (Figure 4.4.46).

There was also a significant effect of dasher assembly on the level of fat destabilization. The standard + wing assembly caused significantly less fat destabilization than the solid dasher, multi + solid, and standard + solid configurations (Figure 4.4.46). The multi + wing configuration was also trending toward causing significantly more fat destabilization than the standard + wing configuration ($P = 0.052$). While these differences were not detected at a throughput rate of 400 L/h, differences between dasher assemblies became more distinct with decreasing throughput rate (Table 4.4.28).

Table 4.4.33. ANOVA table assessing factors affecting fat destabilization.

Factor	F-value	P-value
Throughput Rate	64.69	<0.001*
Dasher Assembly	11.21	<0.001*
Throughput Rate : Dasher Assembly	1.92	0.09

* Denotes factors that are significant at $p < 0.05$

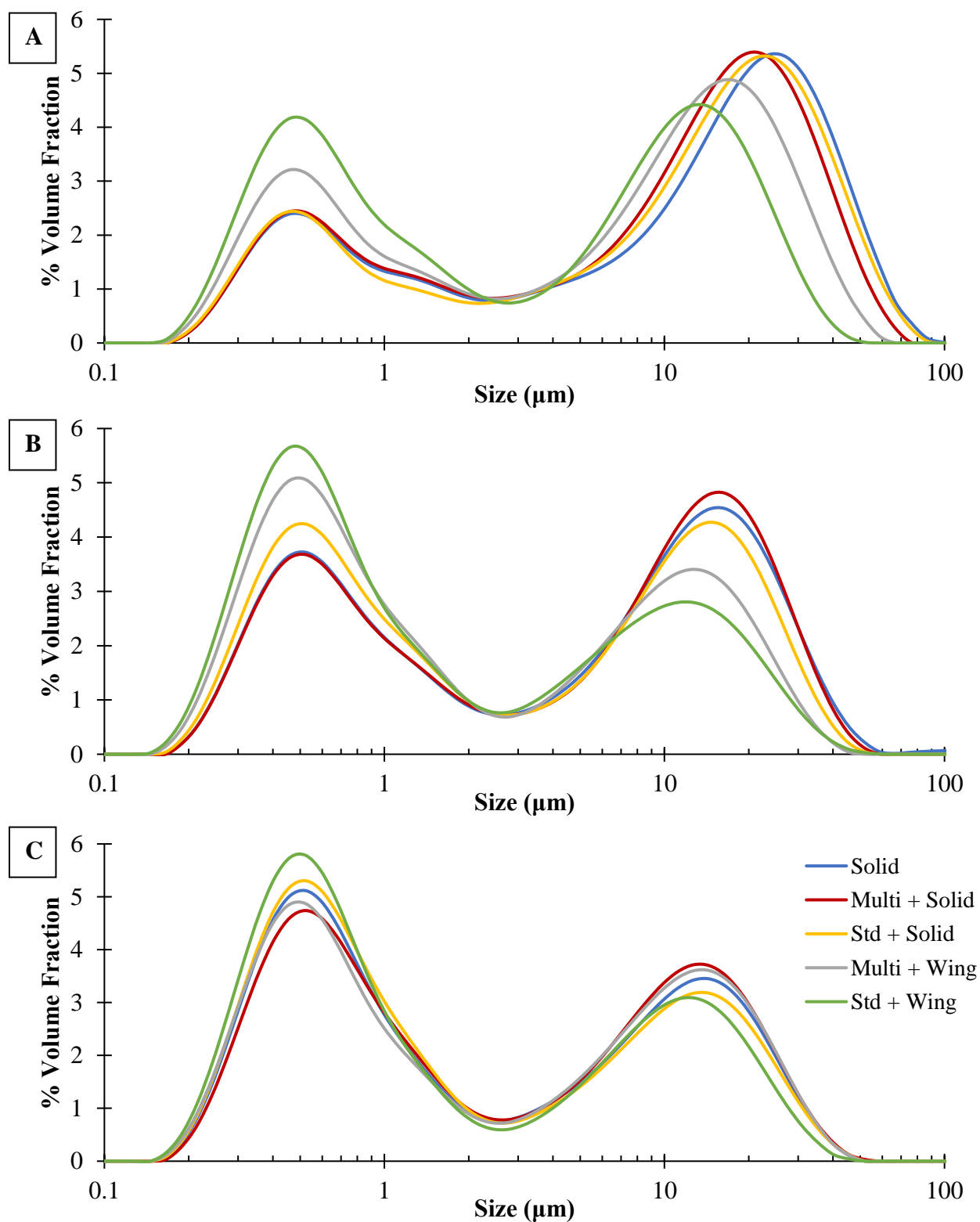


Figure 4.4.44. Fat globule size distributions as a function of dasher assembly for ice cream samples made at a throughput rate of A) 200 L/h, B) 300 L/h, and C) 400 L/h. Dasher speed = 200 RPM, target overrun = 75%, draw temperature = $-5.5 \pm 0.1^\circ\text{C}$. Curves represent the modeled averages for three replicates.

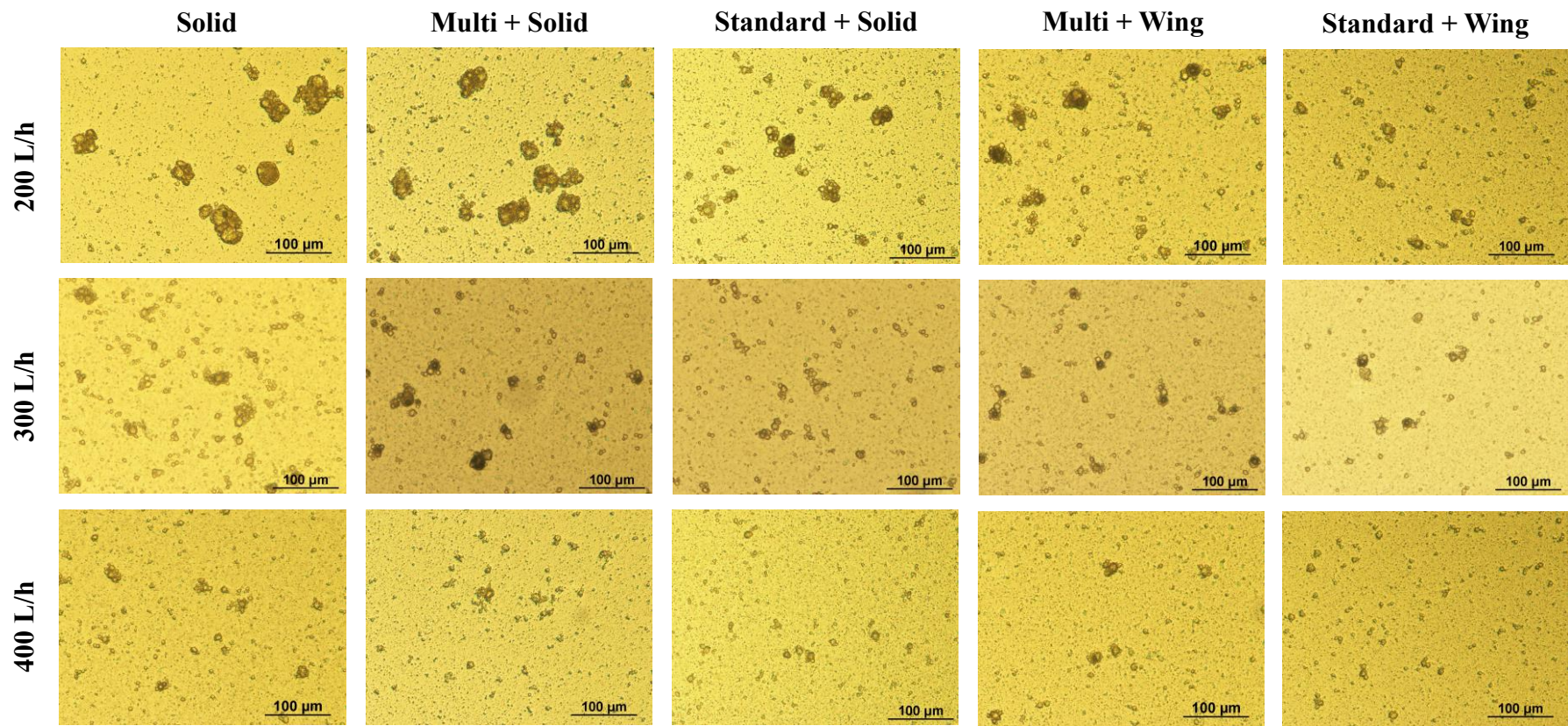


Figure 4.445. Optical microscope images (20x magnification) of destabilized fat clusters as a function of throughput rate and dasher assembly.

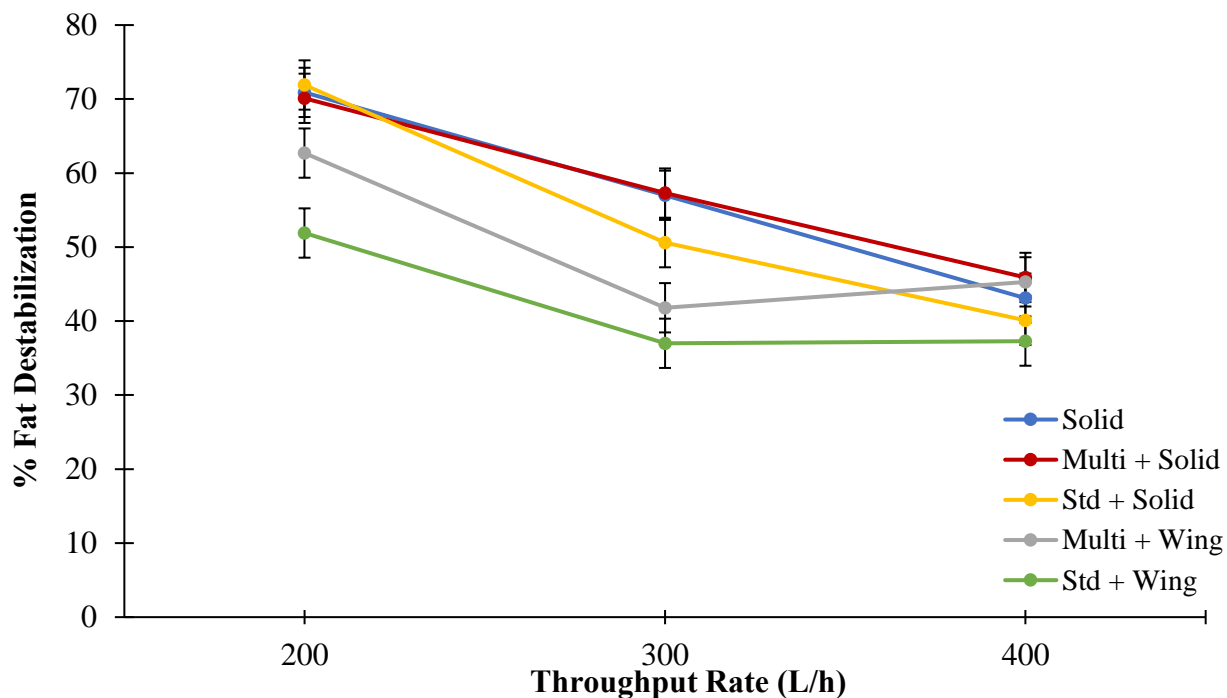


Figure 4.4.46. Mean fat destabilization (%) for ice cream samples as a function of dasher assembly and throughput rate. Dasher speed = 200 RPM, target overrun = 75%, draw temperature = $-5.5 \pm 0.1^\circ\text{C}$. Values represent the modeled averages for three replicates.

4.4.3.4 Correlations

Viscosity and residence time (both mean and standard deviation) were plotted against microstructural attributes to investigate if correlations existed. Table 4.4.34 provides the correlation coefficient R^2 when data for all dasher assemblies and throughput rates were included. Ice crystal size had a negative correlation with viscosity and a positive correlation with residence time. Mean ice crystal size was most highly correlated with viscosity and standard deviation in ice crystal size was most highly correlated with residence time, though correlations were low overall ($R^2 \leq 0.41$). A positive correlation with residence time can be attributed to an extended time for recrystallization to occur in the freezer, which would result in a larger ice crystal size. The relationship between viscosity and ice crystal size is less clear, since viscosity (or torque on the dasher motor) could indicate 1) increased cooling power was used, which could increase the

nucleation rate and thus the number of small ice crystals that are generated, or 2) greater shear forces in the freezer resulted in more breakup of ice crystal flocs, thereby creating smaller ice crystals. Correlations between air cell size and viscosity/residence time were weak ($R^2 \leq 0.03$), suggesting that air cell size is governed by factors other than viscosity and residence time. Fat destabilization correlations were weak ($R^2 \leq 0.11$) but positively correlated with both viscosity and residence time parameters.

Correlations were also tested for individual dasher assemblies to evaluate whether their behavior differs. Correlation coefficients between viscosity and microstructural attributes for individual dashers are given in Table 4.4.35. Generally, all dashers had a negative correlation between viscosity and mean ice crystal size. For hardened ice crystal mean size, dasher assemblies with a wing beater demonstrated the highest correlation with viscosity ($R^2 \geq 0.63$). Correlations between viscosity and the standard deviation in ice crystal size were inconsistent, and no clear trends were evident. While overall correlations were weak between air cell size and viscosity, the correlations for the solid dasher were negative and stronger than for other dasher assemblies ($R \leq 0.55$). Open dashers had a negative correlation between fat destabilization and viscosity, while the solid dasher had a positive weak correlation (Figure 4.4.47). Dasher configurations with a solid beater had the strongest correlation between viscosity and fat destabilization ($R^2 = 0.35 - 0.68$). This difference in correlation between the solid dasher and configurations containing the solid beater is somewhat difficult to parse. If shear was increased exclusively as a function of viscosity, a similar positive correlation between viscosity and fat destabilization would have been expected for the solid dasher. The difference could be related to the geometry of dasher configurations containing a solid beater, which have the narrowest annular gap between the dasher and beater. This would contribute to greater shear and therefore more fat destabilization. Configurations with

the solid beater also have the largest surface area (Table 3.1), which would not only increase shear stress applied to the product but also increase the fluid friction on the dasher assembly, thereby increasing the viscosity reading.

Table 4.4.34. Overall correlation coefficient R^2 between processing conditions and microstructural attributes.

Microstructural Attribute	Dasher Displacement	Viscosity	Average Residence Time	Std Dev in Residence Time
Draw Mean Ice Crystal Size	0.22 ⁽⁻⁾	0.31 ⁽⁻⁾	0.23 ⁽⁺⁾	0.21 ⁽⁺⁾
Draw Std Dev in Ice Crystal Size	0.23 ⁽⁻⁾	0.20 ⁽⁻⁾	0.30 ⁽⁺⁾	0.33 ⁽⁺⁾
Hardened Mean Ice Crystal Size	0.09 ⁽⁻⁾	0.33 ⁽⁻⁾	0.24 ⁽⁺⁾	0.22 ⁽⁺⁾
Hardened Std Dev in Ice Crystal Size	0.27 ⁽⁻⁾	0.24 ⁽⁻⁾	0.41 ⁽⁺⁾	0.33 ⁽⁺⁾
Mean Air Cell Size	0.01 ⁽⁻⁾	0.00 ⁽⁻⁾	0.01 ⁽⁺⁾	0.00 ⁽⁺⁾
Std Dev in Air Cell Size	0.01 ⁽⁻⁾	0.02 ⁽⁻⁾	0.03 ⁽⁺⁾	0.00 ⁽⁺⁾
% Fat Destabilization	0.16 ⁽⁺⁾	0.04 ⁽⁺⁾	0.11 ⁽⁺⁾	0.02 ⁽⁺⁾

* The symbol in parenthesis indicates the whether the correlation is positive⁽⁺⁾ or negative⁽⁻⁾.

Table 4.4.35. Correlation coefficient R^2 between viscosity and microstructural attributes as a function of dasher assembly.

Microstructural Attribute	Dasher Assembly				
	Solid Dasher	Multi + Solid	Standard + Solid	Multi + Wing	Standard + Wing
Draw Mean Ice Crystal Size	0.03 ⁽⁻⁾	0.04 ⁽⁻⁾	0.31 ⁽⁻⁾	0.46 ⁽⁻⁾	0.01 ⁽⁻⁾
Draw Std Dev in Ice Crystal Size	0.43 ⁽⁺⁾	0.00 ⁽⁺⁾	0.01 ⁽⁺⁾	0.13 ⁽⁻⁾	0.01 ⁽⁺⁾
Hardened Mean Ice Crystal Size	0.36 ⁽⁻⁾	0.35 ⁽⁻⁾	0.20 ⁽⁻⁾	0.63 ⁽⁻⁾	0.76 ⁽⁻⁾
Hardened Std Dev in Ice Crystal Size	0.40 ⁽⁺⁾	0.07 ⁽⁻⁾	0.02 ⁽⁻⁾	0.29 ⁽⁻⁾	0.00 ⁽⁻⁾
Mean Air Cell Size	0.31 ⁽⁻⁾	0.12 ⁽⁺⁾	0.02 ⁽⁺⁾	0.02 ⁽⁻⁾	0.11 ⁽⁺⁾
Std Dev in Air Cell Size	0.55 ⁽⁻⁾	0.02 ⁽⁺⁾	0.01 ⁽⁻⁾	0.04 ⁽⁻⁾	0.04 ⁽⁺⁾
% Fat Destabilization	0.15 ⁽⁺⁾	0.68 ⁽⁻⁾	0.35 ⁽⁻⁾	0.06 ⁽⁻⁾	0.04 ⁽⁻⁾

* The symbol in parenthesis indicates the whether the correlation is positive⁽⁺⁾ or negative⁽⁻⁾.

Correlations between mean residence time and microstructural attributes for individual dasher assemblies are given in Table 4.4.36, and correlations between the standard deviation in residence, or spread, in residence time and microstructural parameters are given in Table 4.4.37. The effects of mean and standard deviation in residence time were similar. Generally, all dashers had positive correlations between residence time and ice crystal size and standard deviation. Correlations between residence time and air cell size were weak for all dasher assemblies ($R^2 \leq 0.12$). Correlations between fat destabilization and mean residence time were strong, especially for the solid dasher ($R^2 = 0.84$) and dasher assemblies containing a solid beater ($R^2 \geq 0.86$). Similarly, the correlations between fat destabilization and standard deviation in residence time were strongest for the solid dasher ($R^2 = 0.69$) and dasher assemblies containing a solid beater ($R^2 \geq 0.71$). These correlations were positive, likely due to the extended time available for fat globule collisions to occur. The correlations for individual dashers were also stronger than the overall correlations of residence time and fat destabilization (Table 4.4.34). This suggests that there are likely other confounding factors that influence fat destabilization within each dasher assembly, such as shear rate, which could not be measured in this study.

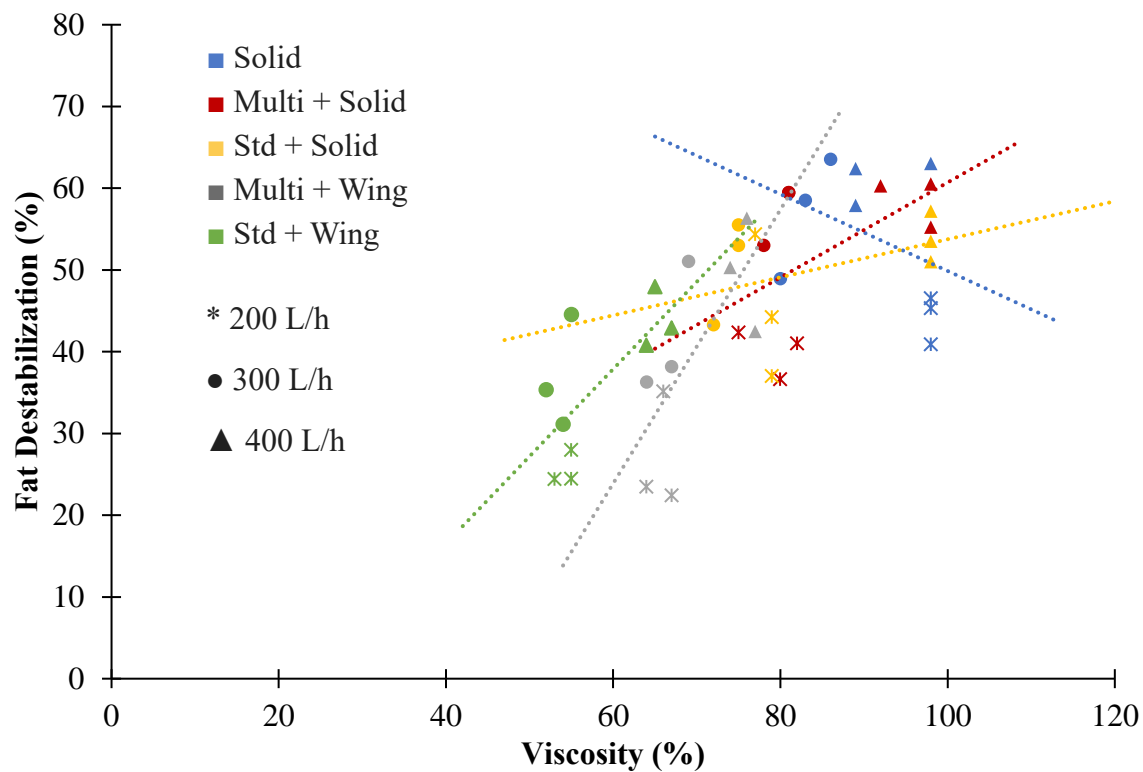


Figure 4.4.47. Correlation between fat destabilization and viscosity (i.e., torque on dasher motor as % of total capacity) as a function of dasher. Solid black line denotes the overall correlation and dotted lines indicate correlation for individual dashers.

Table 4.4.36. Correlation coefficient R^2 between mean residence time and microstructural attributes as a function of dasher assembly.

Microstructural Attribute	Dasher Assembly				
	Solid Dasher	Multi + Solid	Standard + Solid	Multi + Wing	Standard + Wing
Draw Mean Ice Crystal Size	0.20 (+)	0.06 (+)	0.06 (+)	0.46 (+)	0.05 (+)
Draw Std Dev in Ice Crystal Size	0.39 (+)	0.25 (+)	0.30 (+)	0.67 (+)	0.11 (+)
Hardened Mean Ice Crystal Size	0.01 (-)	0.13 (+)	0.06 (+)	0.16 (+)	0.65 (+)
Hardened Std Dev in Ice Crystal Size	0.21 (+)	0.30 (+)	0.12 (+)	0.38 (+)	0.22 (+)
Mean Air Cell Size	0.02 (-)	0.00 (+)	0.03 (+)	0.00 (+)	0.00 (+)
Std Dev in Air Cell Size	0.03 (-)	0.09 (+)	0.12 (+)	0.01 (+)	0.02 (+)
% Fat Destabilization	0.84 (+)	0.86 (+)	0.90 (+)	0.62 (+)	0.55 (+)

* The symbol in parenthesis indicates the whether the correlation is positive (+) or negative (-).

Table 4.4.37. Correlation coefficient R^2 between standard deviation in residence time and microstructural attributes as a function of dasher assembly.

Microstructural Attribute	Dasher Assembly				
	Solid Dasher	Multi + Solid	Standard + Solid	Multi + Wing	Standard + Wing
Draw Mean Ice Crystal Size	0.31 (+)	0.03 (+)	0.03 (+)	0.29 (+)	0.00 (+)
Draw Std Dev in Ice Crystal Size	0.46 (+)	0.21 (+)	0.36 (+)	0.69 (+)	0.03 (+)
Hardened Mean Ice Crystal Size	0.04 (-)	0.07 (+)	0.04 (+)	0.18 (+)	0.37 (+)
Hardened Std Dev in Ice Crystal Size	0.15 (+)	0.18 (+)	0.10 (+)	0.59 (+)	0.04 (+)
Mean Air Cell Size	0.00 (-)	0.00 (+)	0.03 (+)	0.00 (-)	0.03 (-)
Std Dev in Air Cell Size	0.04 (-)	0.09 (+)	0.08 (+)	0.00 (+)	0.01 (-)
% Fat Destabilization	0.69 (+)	0.71 (+)	0.87 (+)	0.60 (+)	0.40 (+)

* The symbol in parenthesis indicates the whether the correlation is positive (+) or negative (-).

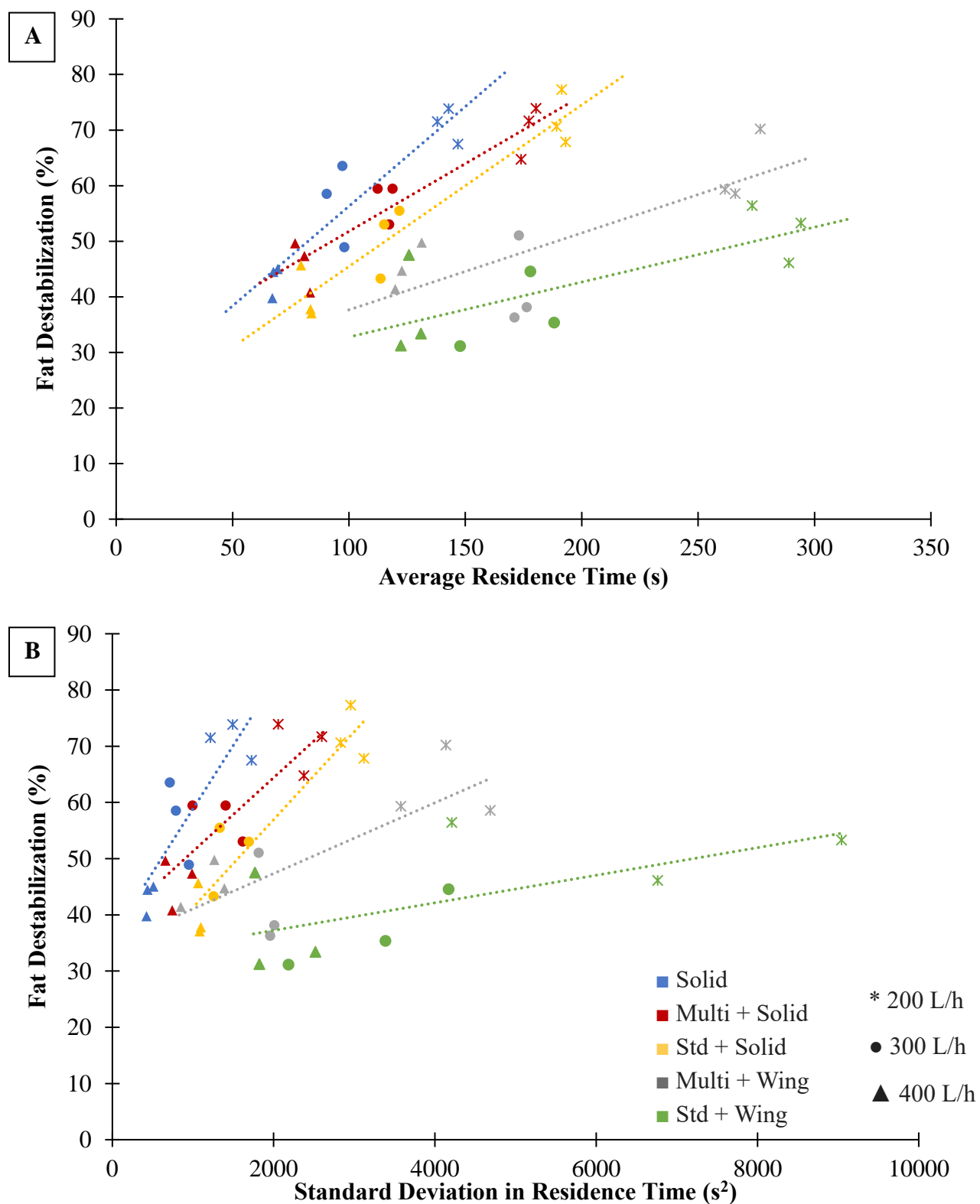


Figure 4.448. Correlation between fat destabilization and A) mean residence time and B) standard deviation in residence time as a function of dasher. Solid black line denotes the overall correlation and dotted lines indicate correlation for individual dashers.

4.4.4 Summary

Based on results from all three experiments, it can be determined that RTD is primarily driven by throughput rate, followed by dasher assembly, and then overrun. Dasher speed did not have an impact on residence time. Regarding microstructural parameters, air cell size was not affected by dasher assembly or throughput rate. Additionally, correlations between residence time and air cell size were very low, which suggests that the final air cell size distribution is reached quickly. Air cell size was reduced by increased overrun or dasher speed. Warren and Hartel (2018) noted that with decreasing in air cell size, there was a tendency of fat destabilization to increase. Indeed, increasing dasher speed and overrun also increased the level of fat destabilization. These effects are likely due to increased shear stresses in the freezer. Similarly, fat destabilization was increased when throughput rate was decreased.

It is difficult to surmise what the effect of dasher speed on ice crystal size is due to an increased draw temperature for high displacement dashers at increased dasher speeds. However, this does suggest that working volume as a result of dasher displacement influences the effect that frictional heat generation by the scraper blades has on the freezing process. Differences in ice crystal size due to dasher assembly were identified in ice cream samples at draw. In the overrun and throughput experiments, the solid dasher and multi + solid configuration had a smaller mean ice crystal size than the standard + wing configuration. As expected, ice crystal size increased upon hardening due to the decrease in temperature from -5.5°C at draw to a hardened ice crystal evaluation temperature of -15°C . However, when samples were hardened, differences in mean ice crystal size as a function of dasher assembly were eliminated. This might indicate that upon draw, ice cream made with the higher displacement dashers was not in thermal equilibrium. Drewett and Hartel (2007) observed that there was an increase in the product temperature after draw due to a

release of undercooling. As higher displacement dashers have a shorter residence time, a higher cooling rate and thus lower coolant temperature is necessary to achieve the target draw temperature (Russell et al., 1999); however, this will increase undercooling in the product. This would suggest that ice cream made with higher displacement dashers had a lower ice phase volume at draw. Therefore, more growth in ice crystal size would be expected as ice crystals are recrystallized upon hardening and storage to minimize the free energy of the system. That is, smaller ice crystals observed in ice cream made with higher displacement dashers would melt due to their lower freezing point, and the larger ice crystals would grow until the system approaches equilibrium (Cook and Hartel, 2010).

Correlations between processing parameters (dasher displacement, viscosity, mean and standard deviation in residence time) and the size of ice crystals and air cells were weak. This indicates that these processing parameters cannot be used to directly predict microstructural outcomes and highlights the complexity of structure formation of ice cream in SSFs. Fat destabilization could not be predicted well by dasher displacement; however, when data was broken out by dasher, correlations with other processing parameters were stronger. This suggests that dasher geometry, not just dasher displacement, plays a role in fat destabilization likely through the impact on shear.

5 CONCLUSIONS & RECOMMENDATIONS

5.1 CONCLUSIONS

Prior to this study, there was very limited knowledge regarding the impact of dasher design on the microstructure of frozen desserts (Kokubo et al., 1996; Russell et al., 1999; Helbig, 2021). This research provides new insights into the impact of dasher design on the flow performance and microstructure of frozen desserts made using a commercial scale continuous SSF.

The effect of dasher design on residence time was driven by the displacement, or the volume that a dasher occupies in the freezing cylinder. For both sorbet and ice cream, dashers with higher displacements had shorter mean residence times and lower standard deviations in residence times. While dasher speed did not affect residence time distribution, increasing overrun increased the average residence time due to the decreased mix flow rate needed to accommodate the additional air incorporated into the product. Changing the overrun had a larger impact on residence time for assemblies containing a wing beater. Increasing the throughput rate decreased the mean residence time across all dasher assemblies, but assemblies with the lower displacement beater (i.e., wing beater) saw more dramatic decreases in mean and variance in residence time with increasing throughput rate than higher displacement assemblies.

Differences in ice crystal size were observed at draw as a function of dasher design with higher displacement dashers, particularly the solid dasher, resulting in smaller ice crystal size and variance; however, dasher design did not have an impact on ice crystal size in hardened sorbet and ice cream. The disappearance of these differences with hardening is interesting. The mean residence time was shorter for higher displacement dashers. Shorter residence times require a lower coolant temperature to reach the draw temperature and thus subcooling and nucleation is enhanced, which promotes the formation of many small ice crystals. If the same amount of ice-

phase volume was generated during the dynamic freezing step for all dashers, these differences in ice crystal size would be observable even after hardening. However, once the ice cream reached equilibrium ice-phase volume at hardening and storage temperature, differences in ice crystal size disappeared. This suggests that less ice-phase volume was generated during the dynamic freezing step for higher displacement dashers. For this to occur, the product would need to experience a greater degree of subcooling without reaching ice-phase equilibrium at the draw temperature. Based on the rheology results as a function of freeze concentration, it would then be expected that the viscosity of products made using the higher displacement dasher would be lower within the SSF; however, the opposite was observed, with higher viscosity readings being registered for higher displacement dashers. This highlights one of the limitations of this study – that viscosity inside the barrel was measured as the torque placed on the dasher motor. Each dasher assembly had a different surface area and shear rates inside the freezer cannot be directly measured, meaning that the apparent viscosity of the product inside the barrel cannot be accurately determined (Eqn. 3.5). Therefore, to confirm the theory of greater subcooling in products made with higher displacement dashers, the temperature of the ice cream after draw would need to be monitored. Samples made with higher displacement dashers would be expected to experience a greater rise in temperature after draw relating to released subcooling.

No significant differences were observed in mean air cell size among individual treatments as a function of dasher assembly. Increased dasher speed and overrun tended to decrease air cell size, but throughput rate did not have an effect. Additionally, correlations between air cell size and dasher displacement, viscosity, and residence time, were generally weak. This suggests that shear may be a driver of air cell size, but that air cell size equilibrates quickly.

The microstructural attribute that was most impacted by changes in processing parameters was fat destabilization. Dasher assembly had a significant effect on fat destabilization across the dasher speed, overrun, and throughput experiments. Higher displacement dashers tended to result in more fat destabilization; however, dasher displacement did not correlate well with fat destabilization results. Increasing dasher speed tended to increase fat destabilization, but only for open dashers. Increasing overrun and decreasing throughput rate caused a greater amount of fat destabilization. The processing parameters that related to increased fat destabilization are also likely related to increased shear conditions, though this could not be measured directly. Correlations between fat destabilization and residence time or viscosity were generally weak when data from all dasher assemblies were included. However, when data were broken out by individual dasher assembly, correlations tended to improve. This suggests that residence time and ‘viscosity’ (as torque on the dasher motor) cannot be used to predict fat destabilization across dashers, and the shear forces caused by the geometry of each dasher likely have a key role in fat destabilization.

One of the limitations of this study is that the SSF automatically adjusts processing variables to achieve the processing setpoints set by the operator by using Proportional – Integral – Derivative (PID) controllers, which provide continuous feedback loops to regulate freezer conditions. For instance, changing the overrun throughput rate set point can cause the freezer to automatically change the volumetric flow rate of the pumps, the pump ratio (i.e., the ratio in volumetric flow rate between the mix pump and frozen product pump) that accounts for the addition of air after the mix pump, air mass flow rate, or the coolant temperature and opening/closing of the hot gas valve (which controls defrosting). While SSFs are a marvelous feat of engineering, designed for ease and consistency of operation, these control mechanisms make studying commercial freezers a challenge.

5.2 RECOMMENDATIONS

At present, this research can be used by frozen dessert manufacturers to make informed decisions on the dasher type best suited for their products based on desired product properties. For instance, a high level of fat destabilization is desirable in ice cream intended for use in extruded novelties where shape retention is integral to product properties. This study suggests that higher displacement dashers such as the solid dasher or assemblies containing a solid beater would be preferred to achieve a higher level of fat destabilization. However, it was also observed that the high displacement dashers could not be operated under as wide of a range of conditions as the lower displacement assemblies containing the wing beater. For manufacturers that may be looking for increased flexibility without needing to purchase separate dashers or change dasher assemblies between products, one of the assemblies containing the wing beater may be preferable.

The effect of dasher speed on ice crystal size remains unclear due in part to the current characterization of dasher speed within the literature. Dasher speed is usually reported in RPM; however, reporting the time between scrapes (i.e., ice removal events) would allow for direct comparison between studies utilizing different SSFs, as the time between scrapes is influenced by the dasher rotational speed, diameter of the freezing cylinder, and the number of blades supported on the dasher assembly. Reporting time between scraping events would enhance the understanding of ice crystallization within continuous SSFs. This gap of knowledge also highlights the importance of reporting dasher geometry, displacement, number of scraper blades, and freezing cylinder dimensions in studies focused on microstructure of frozen desserts.

There is also opportunity to further elucidate microstructural evolution upon start-up of continuous SSFs. The goal of evaluating microstructural evolution in this study was simply to determine the amount of time required after start-up to reach a microstructural steady state. A time

series study with several replicates and frequent sampling (approximately every 10 to 30s) during the first 15 min of freezing would provide a more comprehensive understanding of initial microstructure formation and stabilization after start-up.

It seems that microstructural properties, especially fat destabilization, may be primarily controlled by the amount of shear that the product undergoes. Due to the confined nature of SSFs, shear forces in the freezing cylinder are difficult to measure directly; however, computational fluid dynamics (CFD) offers an alternative method to study fluid flow and heat transfer within SSFs. Multiple studies have already successfully used CFD to model temperatures, velocity, viscosity, ice fraction, and shear rates in SSFs (Lian et al., 2006; Benkhelifa et al., 2008; Arellano et al., 2013b; Hernández-Parra et al., 2018b), including a study that created and experimentally verified a model for the freezer used in the present research study (Panditharatne, 2023). Some of these studies have also used population balance methods to predict ice crystal size of sorbet made with SSFs, with good agreement between model predictions and experimental values (Lian et al., 2006; Arellano et al., 2013b). Modeling the three-phase flow of ice cream using CFD will be a challenge, particularly with the phase change of water to ice; however, the capabilities of CFD are continually advancing. The rheological data collected in section 4.2 and the residence time distribution data collected in section 4.4 can be used for CFD model building and verification. Additionally, the shear estimates and mixing rates/efficiencies calculated by CFD can be compared to the microstructural outcomes observed in section 4.4 to further examine the drivers of microstructural development in SSFs. Ultimately, the goal is to use CFD to predict multiple microstructural outcomes and assist in efficiently designing dasher assemblies based on engineering principles rather than the current method of designing dashers by trial and error.

6 REFERENCES

- Adapa, S., K. A. Schmidt, I. J. Jeon, T. J. Herald, and R. A. Flores. (2000). Mechanisms of ice crystallization and recrystallization in ice cream: A review. *Food Rev. Int.* 16:259-271. <https://doi.org/10.1081/FRI-100100289>
- Adleman, R. and R. W. Hartel. (2001). Lipid crystallization and its effect on the physical structure of ice cream. Pages 329-355 in *Crystallization Processes in Fats and Lipid Systems*. N. Garti and K. Sato, ed. Marcel Dekker, Inc., New York, NY, USA.
- Amador, J., R. W. Hartel, and S. Rankin. (2017). The effects of fat structures and ice cream mix viscosity on physical and sensory properties of ice cream. *J. Food Sci.* 82:1851-1860. <https://doi.org/10.1111/1750-3841.13780>
- Arellano, M. H., 2012. H. Benkhelifa, D. Flick, and G. Alvarez. (2012). Online ice crystal size measurements during sorbet freezing by means of focused beam reflectance measurement (FBRM) technology. Influence of operating conditions. *J. Food Eng.* 113: 351-359. <https://doi.org/10.1016/j.jfoodeng.2012.05.016>
- Arellano, M., H. Benkhelifa, G. Alvarez, and D. Flick. (2013a). Experimental study and modelling of the residence time distribution in a scraped surface heat exchanger during sorbet freezing. *J. Food Eng.* 117: 14-25. <https://doi.org/10.1016/j.jfoodeng.2013.01.027>
- Arellano, M., H. Benkhelifa, G. Alvarez, and D. Flick. (2013b). Coupling population balance and residence time distribution for the ice crystallization modeling in a scraped surface heat exchanger. *Chem. Eng. Sci.* 102:502-513. <https://doi.org/10.1016/j.ces.2013.08.027>
- Baer, R. J. and K. R. Keating. (1987). Determination of ice cream mix freezing points: A comparison of methods. *J. Dairy Sci.* 70:555-558. [https://doi.org/10.3168/jds.S0022-0302\(87\)80040-1](https://doi.org/10.3168/jds.S0022-0302(87)80040-1)
- Barfod, N.M., N. Krog, G. Larsen, and W. Buchheim. (1991). Effects of emulsifiers on protein-fat interactions in ice cream mix during ageing I: quantitative analyses. *Fat Sci. Technol.* 93:24-29. <https://doi.org/10.1002/lipi.19910930104>
- Benkhelifa, H., A. Haddad Amamou, G. Alvarez, and D. Flick. (2008). Modelling fluid flow, heat transfer and crystallization in a scraped surface heat exchanger. *Acta Hort.* 802:163-170. <https://doi.org/10.17660/ActaHortic.2008.802.19>
- Ben-Yoseph, E. and R. W. Hartel. (1998). Computer simulation of ice recrystallization in ice cream during storage. *J. Food Eng.* 38:309-329. [https://doi.org/10.1016/S0260-8774\(98\)00116-2](https://doi.org/10.1016/S0260-8774(98)00116-2)
- Berger, K. G. and G. W. White. (1971). An electron microscopical investigation of fat destabilization in ice cream. *Int. J. Food Sci. Technol.* 6:285-294. <https://doi.org/10.1111/j.1365-2621.1971.tb01617.x>

- Bogdanova, E., A. M. Fureby, and V. Kocherbitov. (2022). Influence of cooling rate on ice crystallization and melting in sucrose-water system. *J. Pharm. Sci.* 111:2030-2037. <https://doi.org/10.1016/j.xphs.2022.01.027>
- Bolliger, S., H. D. Goff, and B. W. Tharp. (2000a). Correlation between colloidal properties of ice cream mix and ice cream. *Int. Dairy J.* 10:303-309. [https://doi.org/10.1016/S0958-6946\(00\)00044-3](https://doi.org/10.1016/S0958-6946(00)00044-3)
- Bolliger, S., H. Wildmoser, H. D. Goff, and B. W. Tharp. (2000b). Relationships between ice cream mix viscoelasticity and ice crystal growth in ice cream. *Int. Dairy J.* 10:791-797. [https://doi.org/10.1016/S0958-6946\(00\)00108-4](https://doi.org/10.1016/S0958-6946(00)00108-4)
- Boode, K. and P. Walstra. (1993). Partial coalescence in oil-in-water emulsions 1. Nature of the aggregation. *Colloids Surf. A Physicochem. Eng. Asp.* 81:121-137. [https://doi.org/10.1016/0927-7757\(93\)80239-B](https://doi.org/10.1016/0927-7757(93)80239-B)
- Boode, K., P. Walstra, and A. E. A. de Groot-Mostert. (1993). Partial coalescence in oil-in-water emulsions 2. Influence of the properties of the fat. *Colloids Surf. A Physicochem. Eng. Asp.* 81:139-151. [https://doi.org/10.1016/0927-7757\(93\)80240-F](https://doi.org/10.1016/0927-7757(93)80240-F)
- Brooker, B. E., M. Anderson, and A. T. Andrews. (1986). The development of structure in whipped cream. *Food Microstruct.* 5:277-285.
- Caillet, A., C. Cogné, J. Andrieu, P. Laurent, and A. Rivoire. (2003). Characterization of ice cream structure by direct optical microscopy. Influence of freezing parameters. *Lebensm.-Wiss. u.-Technol.* 36:743-749. [https://doi.org/10.1016/S0023-6438\(03\)00094-X](https://doi.org/10.1016/S0023-6438(03)00094-X)
- Caldwell, K. B., H. D. Goff, and D. W. Stanley. (1992). A low-temperature scanning electron microscopy study of ice cream. I. Techniques and general microstructure. *Food Structure.* 11:1-9. Available at: <https://digitalcommons.usu.edu/foodmicrostructure/vol11/iss1/1>
- Campos, R., S. S. Narine, and A. G. Marangoni. (2002). Effect of cooling rate on the structure and mechanical properties of milk fat and lard. *Food Res. Int.* 35:971-981. [https://doi.org/10.1016/S0963-9969\(02\)00159-X](https://doi.org/10.1016/S0963-9969(02)00159-X)
- Chang, Y. and R. W. Hartel. (2002a). Development of air cells in a batch ice cream freezer. *J. Food Eng.* 55:71-78. [https://doi.org/10.1016/S0260-8774\(01\)00243-6](https://doi.org/10.1016/S0260-8774(01)00243-6)
- Chang, Y. and R. W. Hartel. (2002b). Stability of air cells in ice cream during hardening and storage. *J. Food Eng.* 55:59-70. [https://doi.org/10.1016/S0260-8774\(01\)00242-4](https://doi.org/10.1016/S0260-8774(01)00242-4)
- Chang, Y. and R. W. Hartel. (2002c). Measurement of air cell distributions in dairy foams. *Int. Dairy J.* 12:463-472. [https://doi.org/10.1016/S0958-6946\(01\)00171-6](https://doi.org/10.1016/S0958-6946(01)00171-6)

- Chen, J. and E. Dickinson. (1993). Time-dependent competitive adsorption of milk proteins and surfactants in oil-in-water emulsions. *J. Sci. Food Agric.* 62:283-289. <https://doi.org/10.1002/jsfa.2740620312>
- Cogné, C., J. Andrieu, P. Laurent, A. Besson, and J. Nocquet. (2003). Experimental data and modelling of thermal properties of ice creams. *J. Food Eng.* 58:331-341. [https://doi.org/10.1016/S0260-8774\(02\)00396-5](https://doi.org/10.1016/S0260-8774(02)00396-5)
- Cook, K. L. K. (2010). Mechanisms of ice crystallization in ice cream. MS thesis. University of Wisconsin-Madison. Madison, WI, USA.
- Cook, K. L. K. and R. W. Hartel. (2010). Mechanisms of ice crystallization in ice cream production. *Compr. Rev. Food Sci. Food Saf.* 9:213-222. <https://doi.org/10.1111/j.1541-4337.2009.00101.x>
- Cook, K. L. K. and Hartel. (2011). Effect of freezing temperature and warming rate on dendrite break-up when freezing ice cream mix. *Int. Dairy J.* 21:447-453. <https://doi.org/10.1016/j.idairyj.2011.01.007>
- Cottrell, J. I. L., G. Pass, and G. O. Phillips. (1980). The effect of stabilisers on the viscosity of an ice cream mix. *J. Sci. Food. Agric.* 31:1066-1070. <https://doi.org/10.1002/jsfa.2740311015>
- Dahiya, P., A. DeBenedictis, T. J. Atherton, M. Caggioni, S. W. Prescott, R. W. Hartel, and P. T. Spicer. (2017). Arrested coalescence of viscoelastic droplets: triplet shape and restructuring. *Soft Matter.* 13:2686-2697. <https://doi.org/10.1039/C6SM02830F>
- Dankwerts, P. V. (1953). Continuous flow systems: Distribution of residence times. *Chem. Eng. Sci.* 2: 1-13. [https://doi.org/10.1016/0009-2509\(53\)80001-1](https://doi.org/10.1016/0009-2509(53)80001-1)
- Darling, D. F. and D. W. Butcher. (1978). Milk-fat globule membrane in homogenized cream. *J. Dairy Res.* 45:197-208. <https://doi.org/10.1017/S002202990001637X>
- de Cindio, S. Corraera, and V. Hoff. (1995). Low temperature sugar-water equilibrium curve by a rapid calorimetric method. *J. Food Eng.* 24:405-415. [https://doi.org/10.1016/0260-8774\(95\)90053-E](https://doi.org/10.1016/0260-8774(95)90053-E)
- Dincer, I. (2017). Refrigeration Systems and Applications. 3rd Ed. John Wiley & Sons Ltd. Chichester, West Sussex, UK.
- Donhowe, D. P., R. W. Hartel, and R. L. Bradley. (1991). Determination of ice crystal size distributions in frozen desserts. *J. Dairy Sci.* 74:3334-3344. [https://doi.org/10.3168/jds.S0022-0302\(91\)78521-4](https://doi.org/10.3168/jds.S0022-0302(91)78521-4)

- Donhowe, D. P. and R. W. Hartel. (1996a). Recrystallization of ice in ice cream during controlled accelerated storage. *Int. Dairy J.* 6:1191-1208. [https://doi.org/10.1016/S0958-6946\(96\)00029-5](https://doi.org/10.1016/S0958-6946(96)00029-5)
- Donhowe, D. P. and R. W. Hartel. (1996b). Recrystallization of ice during bulk storage of ice cream. *Int. Dairy J.* 6:1209-1221. [https://doi.org/10.1016/S0958-6946\(96\)00030-1](https://doi.org/10.1016/S0958-6946(96)00030-1)
- Drewett, E. M. and R. W. Hartel. (2007). Ice crystallization in a scraped surface freezer. *J. Food Eng.* 78: 1060-1066. <https://doi.org/10.1016/j.jfoodeng.2005.12.018>
- Ergun, R. (2011). Fat crystallization and mechanisms of partial coalescence. PhD Thesis. Department of Food Science, University of Wisconsin-Madison, Madison, WI, USA.
- Eisner, M. D., H. Wildmoser, and E. J. Windhab. (2005). Air cell microstructuring in a high viscous ice cream matrix. *Colloids Surf. A Physicochem. Eng. Asp.* 263:390-399. <https://doi.org/10.1016/j.colsurfa.2004.12.017>
- FDA. (1998). Requirements for specific standardized frozen desserts. 21 CFR part 135. Fed. Regist. 545-552.
- Fayolle, F., R. Belhamri, and D. Flick. (2013). Residence time distribution measurements and simulation of the flow pattern in a scraped surface heat exchanger during crystallisation of ice cream. *J. Food Eng.* 116: 390-397. <https://doi.org/10.1016/j.jfoodeng.2012.12.009>
- Fitzner, M., G. C. Sosso, S. J. Cox, and A. Michaelides. (2019). Ice is born in low-mobility regions of supercooled liquid water. *PNAS.* 116:2009-2014. <https://doi.org/10.1073/pnas.1817135116>
- Flores, A. A. and H. D. Goff. (1999a). Recrystallization in ice cream after constant and cycling temperature storage conditions as affected by stabilizers. *J. Dairy Sci.* 82:1408-1415. [https://doi.org/10.3168/jds.S0022-0302\(99\)75367-1](https://doi.org/10.3168/jds.S0022-0302(99)75367-1)
- Flores, A. A. and H. D. Goff. (1999b). Ice crystal size distributions in dynamically frozen model solutions and ice cream as affected by stabilizers. *J. Dairy Sci.* 82:1399-1407. [https://doi.org/10.3168/jds.S0022-0302\(99\)75366-X](https://doi.org/10.3168/jds.S0022-0302(99)75366-X)
- Fogler, H. S. (2016). Distributions of residence times for chemical reactors. Pages 767-806 in Elements of Chemical Reaction Engineering. 5th ed. Pearson Education, Upper Saddle River, NJ.
- Fredrick, E., P. Walstra, and K. Dewettinck. (2010). Factors governing partial coalescence in oil-in-water emulsions. *Adv. Colloid Interface Sci.* 153:30-42. <https://doi.org/10.1016/j.cis.2009.10.003>

- Fredrick, E., D. Van de Walle, P. Walstra, J. H. Zijtveld, S. Fischer, P. Van der Meeren, and K. Dewettinck. (2011). Isothermal crystallization behaviour of milk fat in bulk and emulsified state. *Int. Dairy J.* 21:685-695. <https://doi.org/10.1016/j.idairyj.2010.11.007>
- Freire, D. O., B. Wu, and R. W. Hartel. (2020). Effects of structural attributes on the rheological properties of ice cream and melted ice cream. *J. Food Sci.* 85:3885-3898. <https://doi.org/10.1111/1750-3841.15486>
- Fuller, G. T., T. Considine, M. Golding, L. Matia-Merino, A. MacGibbon, and G. Gillies. (2015a). Aggregation behavior of partially crystalline oil-in-water emulsions: Part I – Characterization under steady shear. *Food Hydrocoll.*43:521-528. <https://doi.org/10.1016/j.foodhyd.2014.07.032>
- Fuller, G. T., T. Considine, M. Golding, L. Matia-Merino, and A. MacGibbon. (2015b). Aggregation behavior of partially crystalline oil-in-water emulsions: Part II – Effect of solid fat content and interfacial film composition on quiescent and shear stability. *Food Hydrocoll.* 51:23-32. <https://doi.org/10.1016/j.foodhyd.2015.03.032>
- Gelin, J. L., L. Poyen, J. L. Courthaudon, M. Le Meste, and D. Lorient. (1994). Structural changes in oil-in-water emulsions during the manufacture of ice cream. *Food Hydrocoll.* 8:299-308. [https://doi.org/10.1016/S0268-005X\(09\)80342-1](https://doi.org/10.1016/S0268-005X(09)80342-1)
- Gelin, J. L., L. Poyen, R. Rizzotti, M. Le Meste, J. L. Courthaudon, and D. Lorient. (1996). Interactions between food components and ice cream. Part 1: unfrozen emulsions. *Food Hydrocoll.* 10:385-393. [https://doi.org/10.1016/S0268-005X\(96\)80017-8](https://doi.org/10.1016/S0268-005X(96)80017-8)
- Goff, H. D., M. Liboff, W. K. Jordan, and J. E. Kinsella. (1987). The effects of polysorbate 80 on the fat emulsion in ice cream mix: Evidence from transmission electron microscopy studies. *Food Struct.* 6:193-198.
- Goff, H. D. and W. K. Jordan. (1989). Action of emulsifiers in promoting fat destabilization during manufacture of ice cream. *J. Dairy Sci.* 72:18-29.
- Goff, H. D., B. Freslon, M. E. Sahagian, T. D. Hauber, A. P. Stone, and D. W. Stanley. (1995). Structural development in ice cream – Dynamic rheological measurements. *J. Texture Stud.* 26:517-536. <https://doi.org/10.1111/j.1745-4603.1995.tb00801.x>
- Goff, H. D., E. Verespej, and A.K. Smith. (1999). A study of fat and air structures in ice cream. *Int. Dairy J.* 9:817-829. [https://doi.org/10.1016/S0958-6946\(99\)00149-1](https://doi.org/10.1016/S0958-6946(99)00149-1)
- Goff, H. D. and R. W. Hartel. (2013). *Ice cream*. 7th ed. Springer, New York, NY, USA.
- Goff, H. D. (2016). Milk proteins in ice cream. Pages 329-345 in *Advanced Dairy Chemistry*. McSweeney, P. and J. O'Mahony, eds. Springer, New York, NY, USA. https://doi.org/10.1007/978-1-4939-2800-2_13

- Greaves, D., J. Boxall, J. Mullican, A. Montesi, J. Creek, E. D. Sloan, and C. A. Koh. (2008). Measuring the particle size of a known distribution using focused beam reflectance measurement technique. *Chem. Eng. Sci.* 63:5410-5419. <https://doi.org/10.1016/j.ces.2008.07.023>
- Haddad Amamou, A., H. Benkhelifa, G. Alvarez, and D. Flick. (2010). Study of crystal size evolution by focused-beam reflectance measurement during the freezing of sucrose/water solutions in a scraped-surface heat exchanger. *Process Biochem.* 45: 1821-1825. <https://doi.org/10.1016/j.procbio.2010.04.001>
- Hagiwara, T., J. Mao, T. Suzuki, and R. Takai. (2005). Ice recrystallization in sucrose solutions stored in a temperature range of -21°C to -50°C. *Food Sci. Technol. Res.* 11:407-411. <https://doi.org/10.3136/fstr.11.407>
- Härröd, M. (1986). Scraped surface heat exchangers: A literature survey of flow patterns, mixing effects, residence time distribution, heat transfer and power requirements. *J. Food Process Eng.* 9: 1-62. <https://doi.org/10.1111/j.1745-4530.1986.tb00116.x>
- Hartel, R. W. (1996). Ice crystallization during manufacture of ice cream. *Trends Food Sci. Technol.* 7:315-321. [https://doi.org/10.1016/0924-2244\(96\)10033-9](https://doi.org/10.1016/0924-2244(96)10033-9)
- Helbig, K. M. (2021). Effects of scraped surface freezer dasher design and operating parameters in ice crystal size in sorbet. MS Thesis. Department of Food Science, University of Wisconsin-Madison, Madison, WI.
- Hernández-Parra, O. D., F. -T. Ndoye, H. Benkhelifa, D. Flick, and G. Alvarez. (2018a). Effect of process parameters on ice crystals and air bubbles size distributions of sorbets in a scraped surface heat exchanger. *Int. J. Refrig.* 92:225-234. <https://doi.org/10.1016/j.ijrefrig.2018.02.013>
- Hernández-Parra, O. D., A. Plana-Fattori, G. Alvarez, F. -T. Ndoye, H. Benkhelifa, and D. Flick. (2018b). Modeling flow and heat transfer in a scraped surface heat exchanger during the production of sorbet. *J. Food Eng.* 221:54-69. <https://doi.org/10.1016/j.jfoodeng.2017.09.027>
- Herrera, M. L. and R. W. Hartel. (2000). Effect of processing conditions on crystallization kinetics of a milk fat model system. *J. Amer. Oil Chem. Soc.* 77:1177-1188. <https://doi.org/10.1007/s11746-000-0184-4>
- Hill, C. G. (1977). An Introduction to Chemical Engineering Kinetics & Reactor Design. John Wiley & Sons, Inc. New York, NY.
- Hindmarsh, J. P., A. B. Russell, and X. D. Chen. (2005). Measuring dendritic growth in undercooled sucrose solution droplets. *J. Crys. Gro.* 285:236-248. <https://doi.org/10.1016/j.jcrysgro.2005.08.017>

- Hinrichs, J. and H. G. Kessler. (1997). Fat content of milk and cream and effects on fat stability. *J. Food Sci.* 62:992-995. <https://doi.org/10.1111/j.1365-2621.1997.tb15022.x>
- Hinze, J. O. (1955). Fundamentals of the hydrodynamic mechanism of splitting in dispersion process. *AIChE J.* 1:289-295. <https://doi.org/10.1002/aic.690010303>
- Holden, M. A., T. F. Whale, M. D. Tarn, D. O'Sullivan, R. D. Walshaw, B. J. Murray, F. C. Meldrum, and H. K. Christenson. (2019). High-speed imaging of ice nucleation in water proves the existence of active sites. *Sci Adv.* 5:eaav4316. <https://doi.org/10.1126/sciadv.aav4316>
- Inoue, K., H. Ochi, M. Taketsuka, H. Saito, K. Sakurai, N. Ichihashi, K. Iwatsuki, and S. Kokubo. (2008). Modeling the effect of freezer conditions on the principal constituent parameters of ice cream by using response surface methodology. *J. Dairy Sci.* 91: 1722-1732. <https://doi.org/10.3168/jds.2007-0796>
- Jacobsen, J. A. (1999). Ice crystallization in a scraped-surface slush freezer. MS Thesis. Department of Food Science, University of Wisconsin-Madison, Madison, WI, USA.
- Janssen, J.J. M., A. Boon, and W. G. M. Agterof. (1994). Influence of dynamic interfacial properties on droplet breakup in simple shear flow. *AIChE J.* 40:1929-1939. <https://doi.org/10.1002/aic.690401202>
- Jaskulka, F. J., D. E. Smith, and K. Lartz. (1993). Comparison of the predictive ability of ice cream freezing point depression equations. *Milchwissenschaft.* 48:671-675.
- Jaskulka, F. J., D. E. Smith, and K. Larntz. (1995). Development of an empirical model to predict the freezing point of ice cream mix. *Milchwissenschaft.* 50:26-30.
- Kokubo, S., K. Sakurai, K. Hakamata, M. Tomita, and S. Yoshida. (1996). The effect of manufacturing conditions on the de-emulsification of fat globules in ice cream. *Milchwissenschaft.* 51:262-265.
- Kokubo, S., K. Sakurai, S. Iwaki, M. Tomita, and S. Yoshida. (1998). Agglomeration of fat globules during the freezing process of ice cream manufacturing. *Milchwissenschaft.* 53:206-209.
- Koxholt, M., B. Eisenmann, and J. Hinrichs. (2000). Effect of process parameters on the structure of ice-cream: Possible methods of optimizing traditional freezer technology. *European Dairy Magazine.* 27-30.
- Koxholt, M.M. R., B. Eisenmann, and J. Hinrichs. (2001). Effect of the fat globule sizes on the meltdown of ice cream. *J. Dairy Sci.* 84:31-37. [https://doi.org/10.3168/jds.S0022-0302\(01\)74448-7](https://doi.org/10.3168/jds.S0022-0302(01)74448-7)

- Kroezen, A. B. J. and J. G. Wassink. (1987). Bubble size distribution and energy dissipation in foam mixers. *JSDC*. 103:386-394. <https://doi.org/10.1111/j.1478-4408.1987.tb01090.x>
- Lakhdar, M. B., R. Cerecero, G. Alvarez, J. Guilpart, D. Flick, and A. Lallemand. (2005). Heat transfer with freezing in a scraped surface heat exchanger. *Appl. Therm. Eng.* 25: 45-60. <https://doi.org/10.1016/j.applthermaleng.2004.05.007>
- Leighton, A. (1927). On the calculation of the freezing point of ice cream mixes and of the quantities of ice separated during the freezing process. *J. Dairy Sci.* 10:300-308.
- Li, M., D. Wilkinson, and K. Patchigolla. (2005). Comparison of particle size distributions measured using different techniques. *Part. Sci. Technol.* 23:265-284. <https://doi.org/10.1080/02726350590955912>
- Li, C., X. Gao, and Z. Li. (2017). Roles of surface energy and temperature in heterogeneous ice nucleation. *J. Phys. Chem.* 121:11552-11559. <https://doi.org/10.1021/acs.jpcc.7b02848>
- Lian, G., S. Moore, and L. Heeney. (2006). Population balance and computational fluid dynamics modelling of ice crystallization in a scraped surface freezer. *Chem. Eng. Sci.* 61:7819-7826. <https://doi.org/10.1016/j.ces.2006.08.075>
- Linvey, T., H. D. Goff, and E. Verespej. (2003). On the calculation of ice cream freezing curves. *Milchwissenschaft*. 58:640-643.
- Liu, X., G. Sala, and E. Scholten. (2023). Structural and functional differences between ice crystal-dominated and fat network-dominated ice cream. *Food Hydrocoll.* 138:108466. <https://doi.org/10.1016/j.foodhyd.2023.108466>
- Luo, S., C. Li, F. Li, J. Wang, and J. Li. (2019). Ice crystallization in shear flows. *J. Phys. Chem.* 123:21042-21049. <https://doi.org/10.1021/acs.jpcc.9b06225>
- Martínez-Bazán, C., J. Rodríguez- Rodríguez, G. B. Deane, J. L. Montañes, and J. C. Lasheras. (2010). Considerations on bubble fragmentation models. *J. Fluid Mech.* 661:159-177. <https://doi.org/10.1017/S0022112010003186>
- Masuda, H., M. Sawano, K. Ishihara, and M. Shimoyamada. (2020). Effect of agitation speed on freezing process of ice cream using a batch freezer. *Food Proc. Eng.* 43:e13369. <https://doi.org/10.1111/jfpe.13369>
- Matsumoto, M., S. Saito, and I. Ohmine. (2002). Molecular dynamics simulation of the ice nucleation and growth process leading to water freezing. *Nature*. 416:409-413. <https://doi.org/10.1038/416409a>
- Méndez-Velasco, C. and H. D. Goff. (2012). Fat structure in ice cream: A study on the types of fat interactions. *Food Hydrocoll.* 29:152-159. <https://doi.org/10.1016/j.foodhyd.2012.02.002>

- Mintel. (2023). *US Ice Cream and Frozen Novelties Market Report 2023*.
<https://store.mintel.com/us/report/us-ice-cream-and-frozen-novelties-market-report/>
- Moens, K., I. Tavernier, and K. Dewettinck. (2018). Crystallization behavior of emulsified fats influences shear-induced partial coalescence. *Food Res. Int.*
<https://doi.org/10.1016/j.foodres.2018.07.005>
- Muse, M. R. and R. W. Hartel. (2004). Ice cream structural elements that affect melting rate and hardness. *J. Dairy Sci.* 87:1-10. [https://doi.org/10.3168/jds.S0022-0302\(04\)73135-5](https://doi.org/10.3168/jds.S0022-0302(04)73135-5)
- Ndoye, F. T. and G. Alvarez. (2014). Characterization of ice recrystallization in ice cream during storage using the focused beam reflectance measurement. *J. Food Eng.* 148:24-34.
<https://doi.org/10.1016/j.jfoodeng.2014.09.014>
- Ndoye, F. T., O. Hernández-Parra, H. Benkhelifa, G. Alvarez, and D. Flick. (2018). Influence of operating conditions on residence time distributions in a scraped surface heat exchanger during aerated sorbet production. *J. Food Eng.* 222: 126-138.
<https://doi.org/10.1016/j.jfoodeng.2017.11.018>
- Page, A. J. and R. P. Sear. (2006). Heterogeneous nucleation in and out of pores. *Phys. Rev. Lett.* 97:065701. <https://doi.org/10.1103/PhysRevLett.97.065701>
- Panditharatne, D. (2023). Application of computational fluid dynamics to improve scraped surface freezer operation for producing frozen desserts. MS Thesis. Department of Biological Systems Engineering, University of Wisconsin-Madison, Madison, WI, USA.
- Pawar, A. B., M. Caggioni, R. Ergun, R. W. Hartel, and P. T. Spicer. (2011). Arrested coalescence in Pickering emulsions. *Soft Matter.* 7:7710-7716.
<https://doi.org/10.1039/C1SM05457K>
- Pawar, A. B., M. Caggioni, R. W. Hartel, and P. T. Spicer. (2012). Arrested coalescence of viscoelastic droplets with internal microstructure. *Faraday Discuss.* 158:341-350.
<https://doi.org/10.1039/C2FD20029E>
- Pelan, B. M. C., K. M. Watts, I. J. Campbell, and A. Lips. (1997). The stability of aerated emulsions in the presence of small molecule surfactants. *J. Dairy Sci.* 80:2631-2638.
[https://doi.org/10.3168/jds.S0022-0302\(97\)76220-9](https://doi.org/10.3168/jds.S0022-0302(97)76220-9)
- Perrard, S., A. Rivière, W. Mostert, and L. Deike. (2021). Bubble deformation by a turbulent flow. *J. Fluid Mech.* 920:A15-1 – A15-27. <https://doi.org/10.1017/jfm.2021.379>
- Petzold, G. and J. M. Aguilera. (2009). Ice morphology: Fundamentals and technological applications in food. *Food Biophys.* 4:378-396. <https://doi.org/10.1007/s11483-009-9136-5>

- Rajesh Potineni, V., L. A. Dalby, J. N. Coupland, and R. F. Roberts. (2006). Sensory and microstructural properties of ice cream manufactured at a high draw temperature in a vertical barrel freezer at different dasher speeds. *J. Food Sci. Technol.* 43:242-246.
- Reid, D. S. and O. R. Fennema. (2008). Water and Ice. Pages 17-82 in Fennema's Food Chemistry. 4th Ed. S. Damodaran, K. L. Parkin, and O. R. Fennema, ed. CRC Press, Boca Raton, FL.
- Regand, A. and H. D. Goff. (2003). Structure and ice recrystallization in frozen stabilized ice cream model systems. *Food Hydrocoll.* 17:95-102. [https://doi.org/10.1016/S0268-005X\(02\)00042-5](https://doi.org/10.1016/S0268-005X(02)00042-5)
- Risso, F. and J. Fabre. (1998). Oscillations and breakup of a bubble immersed in a turbulent field. *J. Fluid Mech.* 372:323-355. <https://doi.org/10.1017/S0022112098002705>
- Rivière, A., W. Mostert, S. Perrard, and L. Deike. (2021). Sub-Hinze scale bubble production in turbulent bubble break-up. *J. Fluid Mech.* 917:A40. <https://doi.org/10.1017/jfm.2021.243>
- Rohenkohl, H. and R. Kohlus. (1999). Foaming of ice cream and the time stability of its bubble size distribution. Pages 45 – 53 in Bubbles in Food. G. M. Campbell, C. Webb, S. S. Pandiella, and K. Niranjana, ed. Eagan Press, St. Paul, MN, USA.
- Roos, Y. H. (2021). Glass transition and re-crystallization phenomena of frozen materials and their effect on frozen food quality. *Foods.* 10:447. <https://doi.org/10.3390/foods10020447>
- Rumscheidt, F. D. and S. G. Mason. (1961). Particle motions in sheared suspensions: XII. Deformation and burst of fluid drops in shear and hyperbolic flow. *J. Colloid. Sci.* 16:238-261. [https://doi.org/10.1016/0095-8522\(61\)90003-4](https://doi.org/10.1016/0095-8522(61)90003-4)
- Russell, A. B., S. S. H. Burmester, and P. J. Winch. (1997). Characterization of shear thinning flow within a scraped surface heat exchanger. *Food and Bioproducts Processing.* 75: 191-197. <https://doi.org/10.1205/096030897531540>
- Russell, A. B., P. E. Cheney, and S. D. Wantling. (1999). Influence of freezing conditions on ice crystallisation in ice cream. *J. Food Eng.* 39: 179-191. [https://doi.org/10.1016/S0260-8774\(98\)00161-7](https://doi.org/10.1016/S0260-8774(98)00161-7)
- Russo, J., K. Akahane, and H. Tanaka. (2018). Water-like anomalies as a function of tetrahedrality. *PNAS.* 115:E3333-E3341. <https://doi.org/10.1073/pnas.1722339115>
- Segall, K. I. and H. D. Goff. (2002). A modified ice cream processing routine that promotes fat destabilization in the absence of added emulsifier. *Int. Dairy J.* 12:1013-1018. [https://doi.org/10.1016/S0958-6946\(02\)00117-6](https://doi.org/10.1016/S0958-6946(02)00117-6)
- Sevik, M. and S. H. Park. (1973). The splitting of drops and bubbles by turbulent fluid flow. *J. Fluids Eng.* 95:53-60. <https://doi.org/10.1115/1.3446958>

- Si, W. (2000). Mechanisms of ice crystallization in scraped surface heat exchanger. MS Thesis. Department of Food Science, University of Wisconsin-Madison, Madison, WI, USA.
- Silva, S., A. Espiga, K. Niranjana, S. Livings, J-C. Gumy, and A. Sher. (2008). Pages 153-161 in Bubbles in Food 2: Novelty, Health and Luxury. G. M. Campbell, M. G. Scanlon, and D. L. Pyle, eds. AACC International, Inc., St. Paul, MN.
- Slade, L. and H. Levine. (1988). Non-equilibrium behavior of small carbohydrate-water systems. *Pure & Appl. Chem.* 60:1841-1864.
- Smith, K. E. and R. L. Bradley. (1983). Effects of freezing point of carbohydrates commonly used in frozen desserts. *J. Dairy Sci.* 66:2464-2467. [https://doi.org/10.3168/jds.S0022-0302\(83\)82112-2](https://doi.org/10.3168/jds.S0022-0302(83)82112-2)
- Smith, C. E. and H. G. Schwartzberg. (1985). Ice crystal size changes during ripening in freeze concentration. *Biotech. Progress.* 1:111-120. <https://doi.org/10.1002/btpr.5420010208>
- Sofjan, R. P., and R. W. Hartel. (2004). Effects of overrun on structural and physical characteristics of ice cream. *Int. Dairy J.* 14:255-262. <https://doi.org/10.1016/j.idairyj.2003.08.005>
- Stamatiou, E., J. W. Meewisse, and M. Kawaji. (2005). Ice slurry generation involving moving parts. *Int. J. Refrig.* 28:60-72. <https://doi.org/10.1016/j.ijrefrig.2004.07.016>
- Sung, K. K. and H. D. Goff. (2010). Effect of solid fat content on structure in ice creams containing palm kernel oil and high-oleic sunflower oil. *J. Food Sci.* 75:C274-C279. <https://doi.org/10.1111/j.1750-3841.2010.01539.x>
- Teraoka, Y., A. Saito, and S. Okawa. (2002). Ice crystal growth in supercooled solution. *Int. J. Refrig.* 25:218-225. [https://doi.org/10.1016/S0140-7007\(01\)00082-2](https://doi.org/10.1016/S0140-7007(01)00082-2)
- Thiel, A. E., R. W. Hartel, P. T. Spicer, and K. J. Hendrickson. (2016). Coalescence behavior of pure and natural fat droplets characterized via micromanipulation. *J. Am. Oil Chem. Soc.* 93:1467-1477. <https://doi.org/10.1007/s11746-016-2896-4>
- Thiel, A. (2020). Arrested coalescence, interfacial phenomena and stability of oil-water emulsions. PhD Thesis. Department of Food Science, University of Wisconsin-Madison, Madison, WI, USA.
- Vanapalli, S. A. and J. N. Coupland. (2001). Emulsions under shear – The formation and properties of partially coalesced lipid structures. *Food Hydrocoll.* 15:507-512. [https://doi.org/10.1016/S0268-005X\(01\)00057-1](https://doi.org/10.1016/S0268-005X(01)00057-1)
- van Boekel, M. A. J. S. and P. Walstra. (1981a). Stability of oil-in-water emulsions with crystals in the disperse phase. *Colloids Surf.* 3:109-118. [https://doi.org/10.1016/0166-6622\(81\)80071-6](https://doi.org/10.1016/0166-6622(81)80071-6)

- van Boekel, M. A. J. S. and P. Walstra. (1981b). Effect of Couette flow on stability of oil-in-water emulsions. *Colloids Surf.* 3:99-107. [https://doi.org/10.1016/0166-6622\(81\)80070-4](https://doi.org/10.1016/0166-6622(81)80070-4)
- Walstra, P. (2003). Physical chemistry of foods. Marcel Dekker, Inc., New York, USA.
- Walstra, P. and T. van Vliet. (2008). Dispersed systems: Basic considerations. Pages 783 – 847 in Fennema's Food Chemistry. 4th rev. ed. Damodaran, S., K. L. Parkin, and O. R. Fennema, ed. CRC Press, Boca Raton, FL, USA.
- Warren, M. M and R. W. Hartel. (2014). Structural, compositional, and sensorial properties of United States commercial ice cream products. *J. Food Sci.* 79:E2005-E2013. <https://doi.org/10.1111/1750-3841.12592>
- Warren, M. M. (2015). Understanding melt behavior of ice cream: Influence of the microstructure and composition on drip-through rate of ice cream products. PhD Thesis. Department of Food Science, University of Wisconsin-Madison, Madison, WI, USA.
- Warren, M. M. and R. W. Hartel. (2018). Effects of emulsifier, overrun, and dasher speed on ice cream microstructure and melting properties. *J. Food Sci.* 83:639-647. <https://doi.org/10.1111/1750-3841.13983>
- Whelan, A. P., C. Vega, J. P. Kerry, and H. D. Goff. (2008). Physicochemical and sensory optimisation of a low glycemic index ice cream formulation. *Int. J. Food Sci. Technol.* 43:1520-1527. <https://doi.org/10.1111/j.1365-2621.2007.01502.x>
- Wu, B., D. O. Freire, and R. W. Hartel. (2019). The effect of overrun, fat destabilization, and ice cream mix viscosity on entire meltdown behavior. *J. Food Sci.* 84:2562-2571. <https://doi.org/10.1111/1750-3841.14743>
- Wynn, E. J. W. (2003). Relationship between particle-size and chord-length distributions in focused beam reflectance measurement: stability of direct inversion and weighting. *Powder Technol.* 133:125-133. [https://doi.org/10.1016/S0032-5910\(03\)00084-6](https://doi.org/10.1016/S0032-5910(03)00084-6)
- Zhang, Z. and H. D. Goff. (2004). Protein distribution at air interfaces in dairy foams and ice cream as affected by casein dissociation and emulsifiers. *Int. Dairy J.* 14:647-657. <https://doi.org/10.1016/j.idairyj.2003.12.007>

A APPENDIX

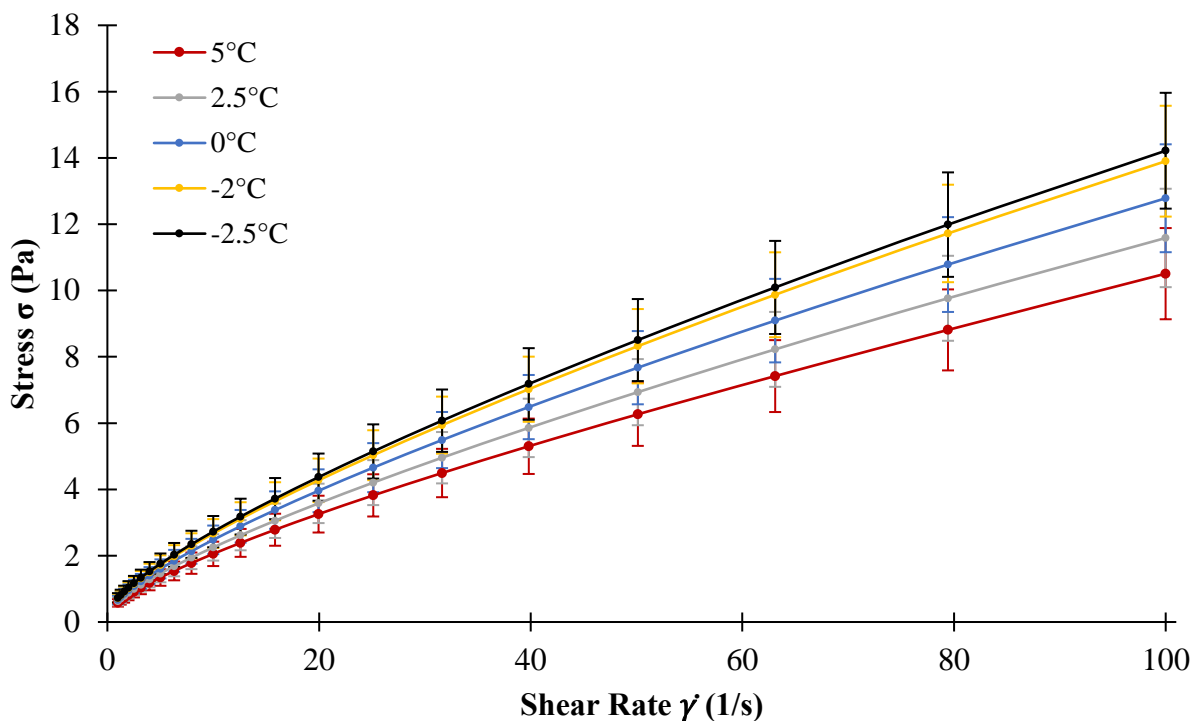


Figure A.1. Shear sweep curves for ice cream mix (0% water removed) as a function of temperature. Error bars represent standard deviation for 3 replicates.

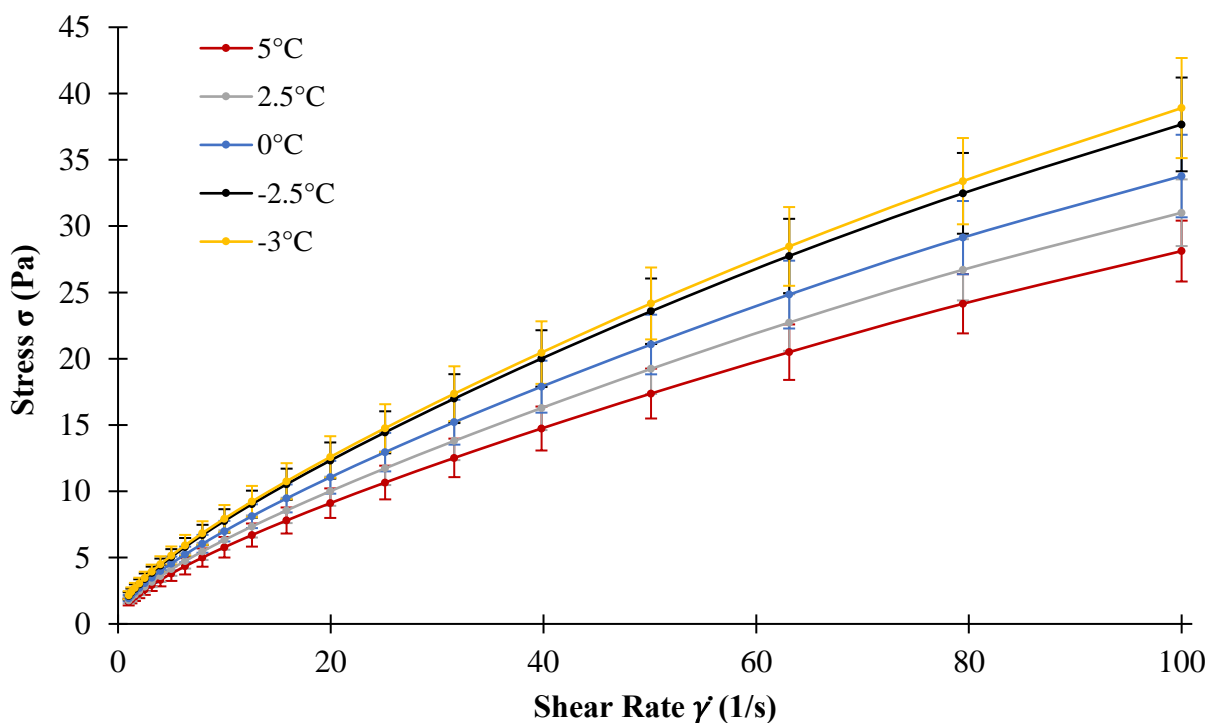


Figure A.2. Shear sweep curves for ice cream mix with 10% of water removed as a function of temperature. Error bars represent standard deviation for 3 replicates.

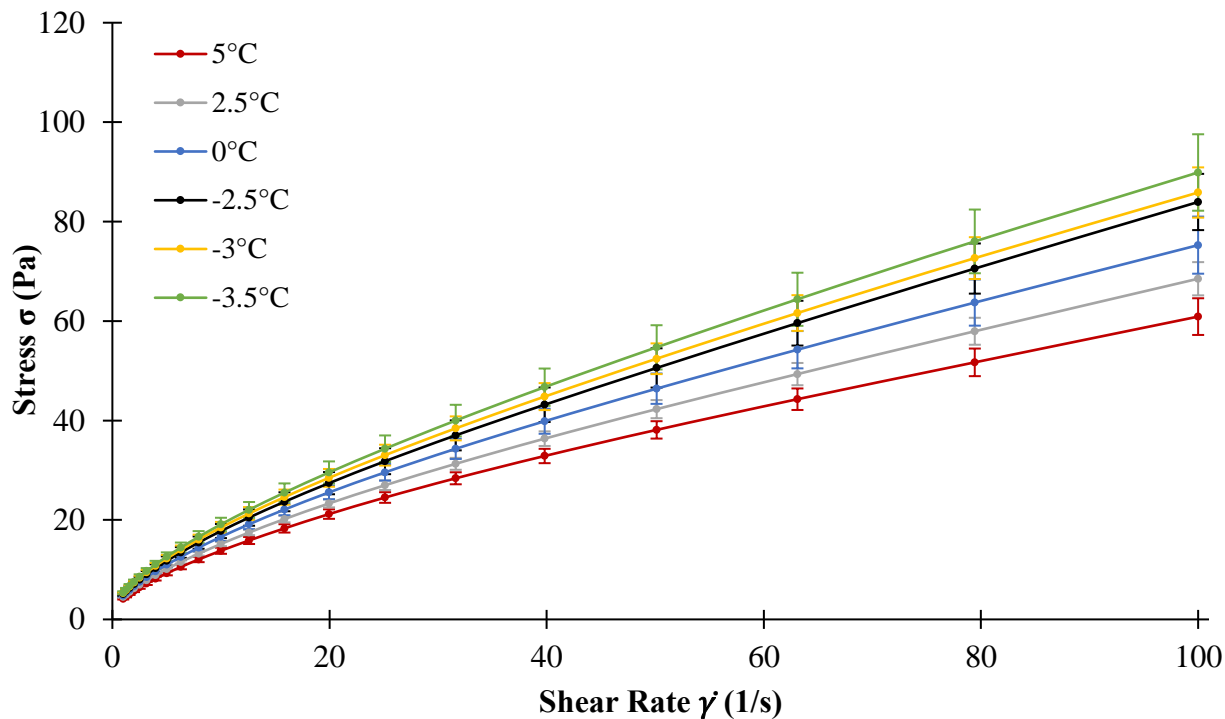


Figure A.3. Shear sweep curves for ice cream mix with 20% of water removed as a function of temperature. Error bars represent standard deviation for 3 replicates.

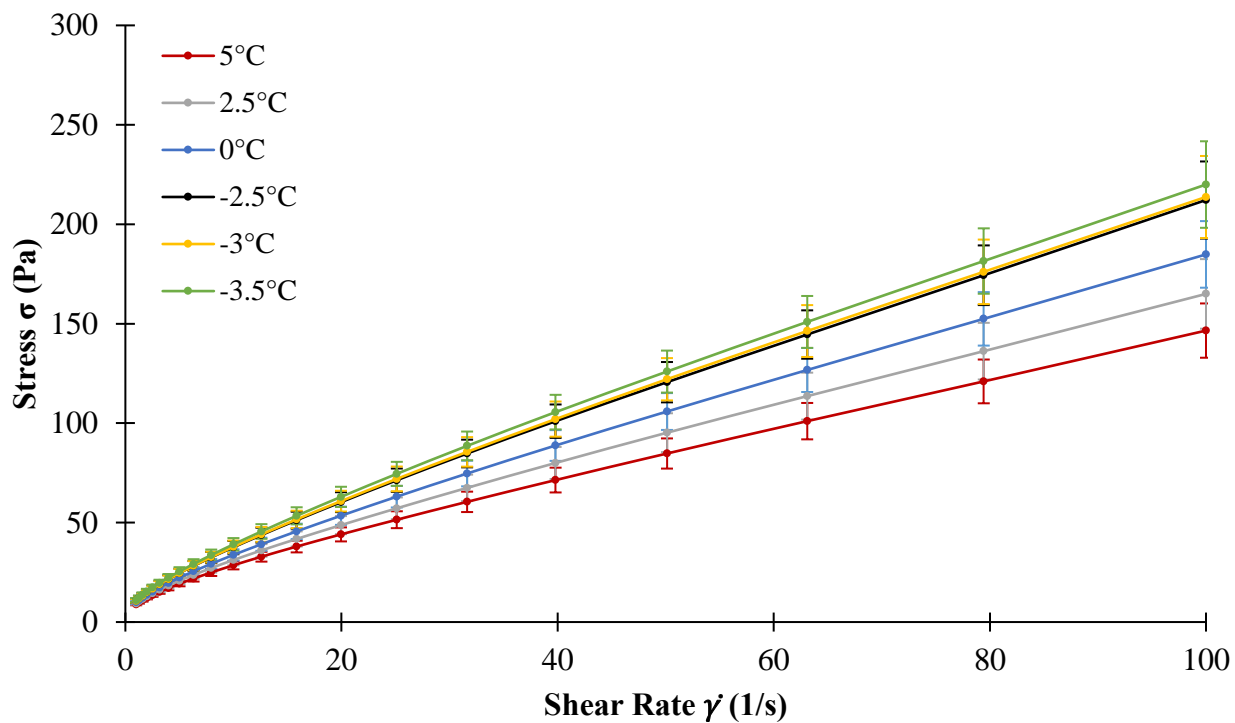


Figure A.4. Shear sweep curves for ice cream mix with 30% of water removed as a function of temperature. Error bars represent standard deviation for 3 replicates.

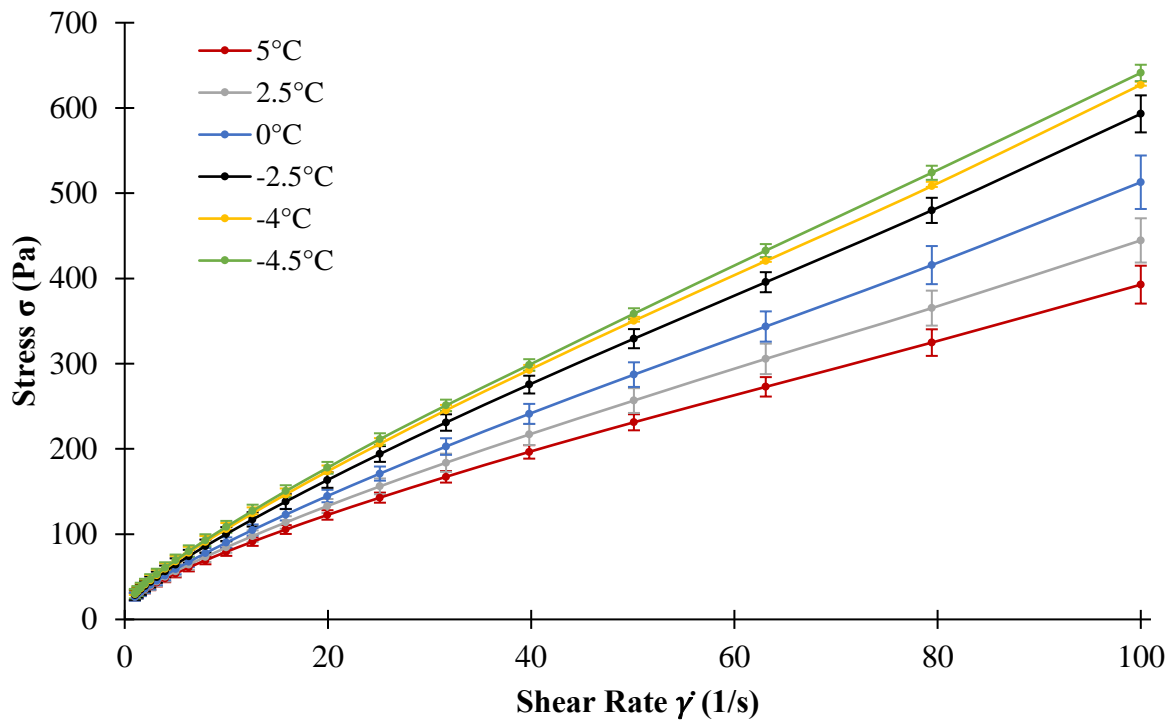


Figure A.5. Shear sweep curves for ice cream mix with 40% of water removed as a function of temperature. Error bars represent standard deviation for 3 replicates.

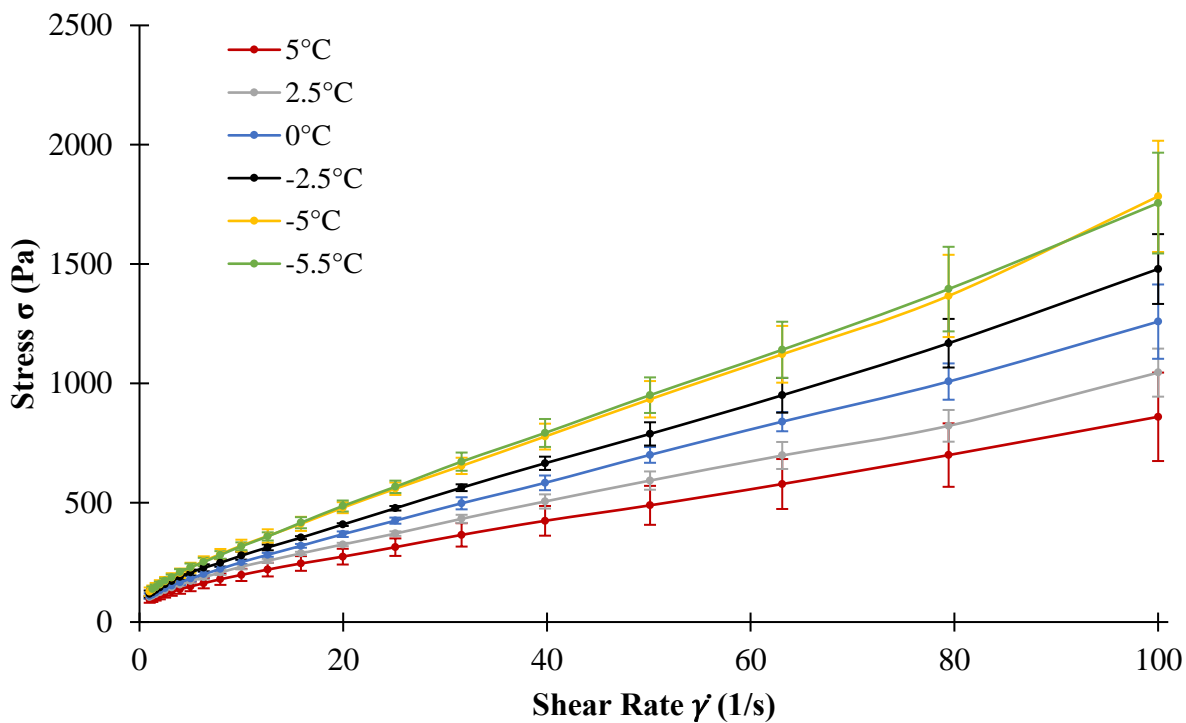


Figure A.6. Shear sweep curves for ice cream mix with 50% of water removed as a function of temperature. Error bars represent standard deviation for 3 replicates.